ABSTRACTS

May 16-19, 2023

JOHNS HOPKINS UNIVERSITY

AIR FORCE OFFICE OF SCIENTIFIC RESEARCH
UNITED STATES AIR FORCE

Ansys

Intelligent Light
Transformative Tools for Engineering

Contents

1 Session A: Aero-Hydrodynamics - 1

Dissecting 3D Vortex Dynamics of Pitching Wings Using the Force and Moment Partitioning Method

Yuanhang Zhu[†*] and Kenneth Breuer[*]
Center for Fluid Mechanics, Brown University, Providence, RI 02912, USA[1]
[†]Present address: University of Virginia, Charlottesville, VA 22904, USA
[*]Correspondence: *yuanhang_zhu@brown.edu, kenneth_breuer@brown.edu*

1 Introduction and Method

The recent development of the physics-based Force and Moment Partitioning Method (FMPM) provides us with a framework to determine vorticity-induced loads from the corresponding velocity fields [1, 2]. It has opened up new possibilities for correlating unsteady flow features with their resultant aerodynamic/hydrodynamic loads on bodies immersed in a flow. However, the current applications of the FMPM have mainly focused on data from numerical simulations. In the present study, we consider the application of FMPM to analyze 3D PIV measurements of unsteady pitching wings to demonstrate the powerful capability of the FMPM in providing new physical insights for vortex-dominated flows.

In the FMPM, the Navier-Stokes equation is projected onto the gradient of an auxiliary potential, ϕ - the "influence field" - which satisfies

$$\nabla^2\phi = 0, \ \frac{\partial\phi}{\partial \boldsymbol{n}} = \begin{cases} [(\boldsymbol{x}-\boldsymbol{x_p})\times\boldsymbol{n}]\cdot\boldsymbol{e_z} & \text{on body boundary} \\ 0 & \text{on outer boundary} \end{cases}, \tag{1}$$

where $\boldsymbol{n}$ is the unit vector normal to the body boundary, $\boldsymbol{x}-\boldsymbol{x_p}$ is the location vector pointing towards the rotation axis, and $\boldsymbol{e_z}$ is the spanwise unit vector. Note that Eqn. 1 is specifically constructed for *moment* partitioning. A different potential can be constructed to determine lift or drag, etc [1]. The vortex-induced force/moment *density* is expressed as $f_Q = -2\rho Q\phi$, where $Q = \frac{1}{2}(\|\boldsymbol{\Omega}\|^2 - \|\boldsymbol{S}\|^2)$ is the second invariant of the velocity gradient tensor, $\boldsymbol{\Omega}$ is the vorticity tensor, $\boldsymbol{S}$ is the strain-rate tensor, and ρ is the fluid density. The vortex-induced force/moment is then given by $M = -2\rho\int_V Q\phi \ dV$, where $\int_V$ represents volume integral over the field of interest. In this abstract, we focus on the vorticity-induced moment, M. However, with the appropriate influence field, ϕ, any force or moment can be computed in this manner.

We obtain the flow field data from multi-layer stereoscopic particle image velocimetry (PIV) experiments. A schematic of the setup is shown in Fig. 1. In the experiment, we have a NACA 0012 wing (span: s = 0.3 m, chord: c = 0.1 m) pitching sinusoidally (amplitude, $A = 60°$, frequency, $f = 0.255$ Hz) in a water tunnel, with the motion prescribed by a servo motor and the force/moment measured by a 6-axis transducer. With a freestream flow of $U_\infty = 0.3$ m/s, we conduct stereo PIV measurements at different spanwise layers to obtain phase-averaged 3D flow fields of three pitching wings. The three wings have sweep angles $\Lambda = 0°$, $10°$ and $20°$, respectively. A more detailed description of the experimental setup can be found in [3].

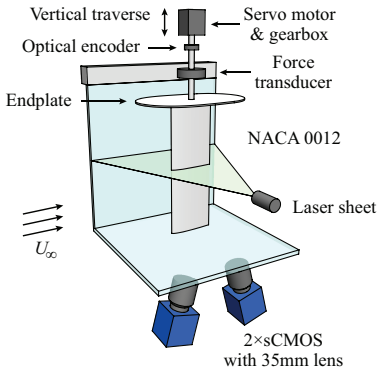

Figure 1: Schematic of the experimental setup.

There are many challenges and issues that are particularly relevant to applying FMPM to experimental data, including, for example, the effect of turbulence and measurement noise on the calculated Q-field. These issues have been explored in the context of two-dimensional geometries [4] and although they cannot be discussed in detail in this short abstract, they will be considered in the full conference presentation.

2 Results and Discussion

Fig. 2(a) first row compares the iso-$Q = 50$ surfaces colored by the spanwise vorticity for the three wings at $t/T = 0.14$, where $T = 1/f$ is the pitching period. Note that the figures are rotated in the spanwise direction to maintain a zero angle of attack, for a better view of the flow structures. We see that as the wings are pitching clockwise, at this time instant, the LEV mostly detaches from the wing surface for the $\Lambda = 0°$ wing except for a small portion near the wing

[1]This work was supported by AFOSR. We acknowledge the helpful discussions with Rajat Mittal and Sushrut Kumar at Johns Hopkins, and Karthik Menon at Stanford.

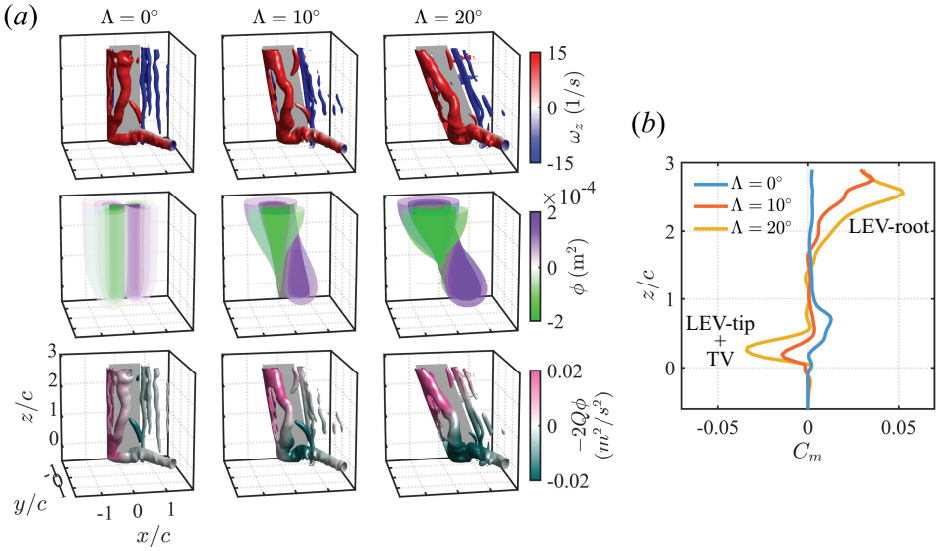

Figure 2: (*a*) 3D flow structures visualized with iso-$Q = 50$ surfaces colored by the spanwise vorticity, ω_z (1st row), and by the FMPM-based moment density, $-2Q\phi$ (3rd row), as well as the 3D ϕ field (2nd row) for the $\Lambda = 0^\circ$ wing (1st column), the $\Lambda = 10^\circ$ wing (2nd column), and the $\Lambda = 20^\circ$ wing (3rd column). (*b*) The corresponding spanwise distribution of the vorticity-induced moment.

tip, which stays attached. As Λ increases, this small portion of the attached LEV shrinks, whereas the top portion of the LEV near the wing root stays more attached. The tip vortex (TV) behaves similarly for the three wings.

The calculated 3D ϕ fields are plotted in the second row using iso-ϕ surfaces. For the unswept wing, the 3D ϕ field shows symmetry with respect to the pivot axis and the wing chord, forming a 3D quadrant pattern. The magnitude of ϕ peaks on the wing surface and decreases towards the far field. The iso-ϕ surfaces stay relatively constant in shape along the wing span, except at the wing tip, where the surfaces wrap around and seal the tube. As Λ is increased, we see that the quadrant pattern persists. However, the iso-ϕ surfaces form funnel-like shapes on the fore wing and resemble tear drops on the aft wing. This is presumably caused by the variation of the effective pivot axis along the wing span. The negative ϕ regions extend over the entire wing chord near the wing root, even behind the pitching axis. Similarly, the positive ϕ regions almost cover the entire wing tip and even spill to the front of the pitching axis.

From the third row, we see that for the $\Lambda = 0^\circ$ wing, the LEV generates negative moments near the wing tip, and near-zero moments near the wing root. The TV has almost no contributions to the moment. The LEV of the $\Lambda = 20^\circ$ wing generates more positive moments near the wing root as compared to the $\Lambda = 10^\circ$ wing, due to the combined effect of the LEV geometry and the magnitude of the ϕ field. Similarly, the TV of the $\Lambda = 20^\circ$ wing generates more negative moments than that of the $\Lambda = 10^\circ$ wing. The spanwise distributions of the vorticity-induced moment are calculated by integrating the moment density at different spanwise layers and the results are plotted in Fig. 2(*b*). They further interpret the 3D moment contributions from each vortical structure. Without FMPM, getting these useful physical insights would not have been possible.

3 Conclusion and Outlook

The above example has demonstrated the powerful capability of FMPM in providing new physical insights for vortex-dominated flows measured using PIV experiments. As hinted above, there remain challenges specific to using PIV data, such as measurement noise. Moreover, it is well-acknowledged that the accuracy of PIV measurements suffers close to the solid boundaries, which brings uncertainties to PIV-based load estimation methods. These will be addressed in the conference presentation, by comparing the FMPM-estimated force/moment with those measured using force/torque transducers.

References

[1] Menon, K. and Mittal, R. Quantitative analysis of the kinematics and induced aerodynamic loading of individual vortices in vortex-dominated flows: a computation and data-driven approach. *J. Comput. Phys.*, 443:110515, 2021.

[2] Menon, K. and Kumar, S. and Mittal, R. Contribution of spanwise and cross-span vortices to the lift generation of low-aspect-ratio wings: Insights from force partitioning. *Phys. Rev. Fluids*, 7(11):114102, 2022.

[3] Zhu, Y. and Breuer, K. Aeroelastic Instability Boundaries of Pitching Swept Wings. *AIAA SciTech Forum*, 2022-2328, 2022.

[4] Zhu, Y. et al. Force moment partitioning and scaling analysis of vortices shed by a 2D pitching wing in quiescent fluid. *Expt. Fluids*, (in review), 2023.

Force and velocity field fluctuations over static foils with surface roughness

Melike Kurt[a*], Rodrigo Vilumbrales-García[a], Gabriel Weymouth[a,b], and Bharathram Ganapathisubramani[a]
[a] School of Engineering and Physical Sciences, University of Southampton, Southampton, United Kingdom [1]
[b] Faculty of Mechanical, Maritime and Materials Engineering (3mE), TU Delft, NL
[*]Correspondence: *m.kurt@soton.ac.uk*

1 Introduction

There have been significant efforts to understand the hydrodynamic function of surface roughness due to large penalties in drag or potential performance enhancements [1–3]. Often, the research on this topic uses roughness elements with highly complex geometries, for example, by replicating morphological properties of shark denticles [2–4]. However, it is not clear here whether the highly complex geometry of these denticles has the main role in the reported force generation benefits or it is the generic roughness on the surface that causes a re-arrangement in the flow and enhances the hydrodynamic performance.

To better understand the role of roughness on propulsive surfaces, we used roughness elements with a simpler geometry and conducted force and flow measurements in a water channel with a cross section of 1.2 m width and 0.8 m depth, located at the University of Southampton Boldrewood Innovation Campus. Foils with rectangular planform and NACA0012 cross-section were 3d-printed, with a chord length of $c = 0.16$ m and aspect ratio of $AR = 2.5$. To enforce a nominally two-dimensional flow over the foils, the flow was constrained around the tips using a surface plate and the bottom wall of the channel (Figure 1a). Suction and pressure sides of the foils were covered with spherical-cap roughness elements that have a protrusion length of $H = 0.01c$ and a diameter of $W = 0.05c$. Two different roughness cases were considered with 75% (full-rough) and 36% (mid-rough) arae coverage ratios, as shown in Figure 1b. Additionally, a foil with a smooth surface (0% coverage, no roughness elements) was tested to establish a baseline. The free-stream velocity was fixed at $U = 0.085$, which gives a chord based Reynolds number of $Re = 12,000$. Foils' angle of attack were varied using a stepper motor, within the range of $-4^\circ \leq \alpha \leq 20^\circ$. Force measurements are conducted using an ATI Mini40 six-axis force sensor to measure the lift and drag generated from the foils with different roughness coverage ratios, at each prescribed angle of attack. Each test was conducted for at least 100 convection cycles ($T = c/U$) at each Re, and repeated for 5 times to ensure convergence in the root mean square (RMS) of the fluctuations for the measured lift and drag forces.

[1]This work was supported by the Engineering and Physical Sciences Research Council under Grant No: EP/R034370/1

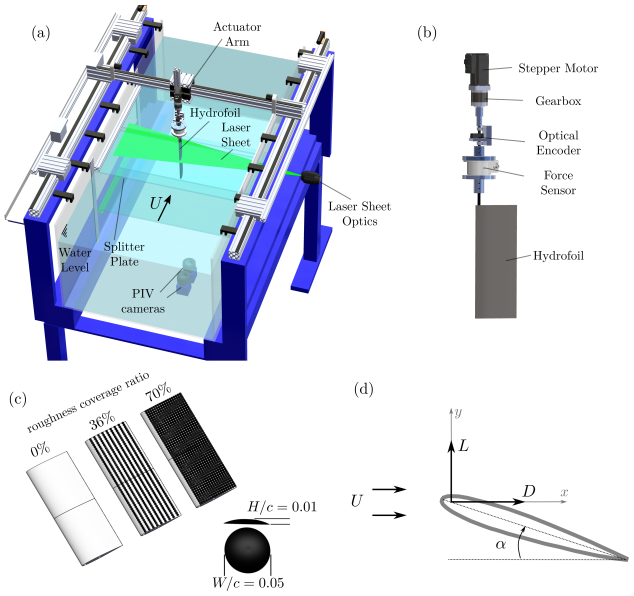

Figure 1: A schematic of the water channel setup with the flat plate constrained between the surface plate and bottom wall of the channel (a). A schematic of the actuation mechanism (b). Flat plates with spherical-cap roughness elements (bumpers) of different coverage ratios (c). A schematic of the forces acting on the foil (d).

2 Results

The flat plates with three different bumper coverage ratios have been tested for an angle of attack range of $-4^\circ \leq AoA \leq 20^\circ$, at $Re = 12,000$ and time-averaged lift coefficients have been calculated. Here, the definition of the lift coefficient is:

$$C_L = \frac{L}{0.5\rho U^2 c^2 AR} \quad C_D = \frac{D}{0.5\rho U^2 c^2 AR} \tag{1}$$

where L is the time-averaged lift force, and ρ is the density of water. Figure 2 presents C_L and the lift fluctuations ($C_{L,rms}$) as functions of angle of attack where the color of the lines is mapped to roughness ratios of 0% (smooth), 35%,

and 70%, respectively. As expected, the lift increases linearly against angle of attack up to $\alpha = 8°$, after which the lift curves become flatter. At this point, the onset of flow separation is expected to occur where the shear layers become completely detached from the foil's surface and the foil goes into stall. The lift generation does not show significant differences between the roughness coverages ($< 10\%$) for pre-stall conditions ($\alpha \leq 8°$). The lift slope shows dependency on roughness ratio. The lift slope decreases for roughness cases compared to smooth foil where the lift slope for the mid-rough foil is the lowest. As the angle of attack increases, the lift curves show a delay in stall for the full-rough foil compared to smooth and mid-rough cases. This may be related to an increase in the foil thickness that the flow sees due to the presence of roughness elements. The trend of the lift fluctuations ($C_{L,rms}$) is similar between different roughness coverages for pre-stall conditions. However, when the foils are at stall, at $\alpha = 12°$, there is a clear increase in lift fluctuations for smooth foil compared to mid-rough and full-rough cases.

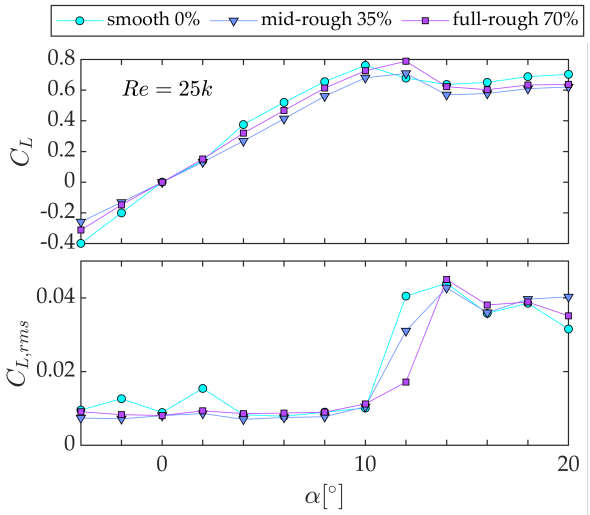

Figure 2: The lift (a) and lift fluctuations (b) acting on the foils with different roughness coverages as a function of angle of attack at $Re = 25,000$.

Figure 3 shows the changes in lift fluctuations for the mid-rough (top) and full-rough (bottom) cases relative to smooth foil across the Re and α range considered. For both mid-rough and full-rough foils, the addition of roughness generally decreases the fluctuations in lift forces compared to the smooth foil for $\alpha \leq 12°$, indicated by the negative values of the relative lift fluctuations marked by the shades of blue across the contours. However, this decrease in the lift fluctuations decreases as the roughness coverage ratio increases, with reduction in lift fluctuations up to 56% for mid-rough and 49% for full-rough foils. For both roughness cases, the highest decrease in lift fluctuations were obtained when the foils are in stall at $\alpha = 12°$.

Although, we have only shown the analysis on lift forces

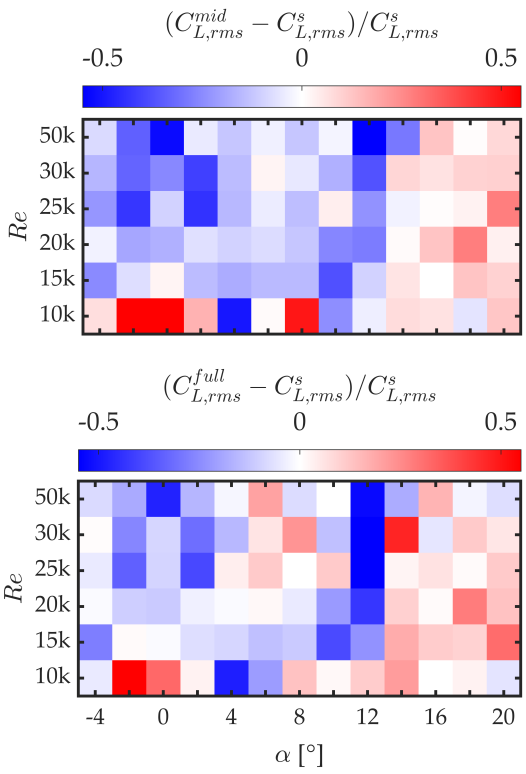

Figure 3: Changes in the lift fluctuations for the mid-rough (top) and full-rough (bottom) cases relative to smooth foil across the Re and α range.

here, a similar analysis has been conducted on drag forces as well. A further analysis on mid-span flow data revealed that the addition of roughness leads to a significant reduction in velocity fluctuations over foils with surface roughness compared to smooth foil. During the meeting, in addition to the data discussed here, we will talk about the pressure fields obtained from PIV data for different roughness cases and establish connections between lift and drag forces, and flowfields. We will also discuss findings by Vilumbrales-Garcia *et al.* [5], and compare surface roughness effects on force generation between static and sinusoidally pitching foils.

References

[1] Bechert, D. W., et al. Fluid mechanics of biological surfaces and their technological application. *Naturwissenschaften* 87.4 (2000): 157-171.

[2] Wen, Li, et al. Hydrodynamic function of biomimetic shark skin: effect of denticle pattern and spacing. *Bioinspiration & Biomimetics*, 10.6 (2015): 066010.

[3] Domel, August G., et al. Shark skin-inspired designs that improve aerodynamic performance. *Journal of the Royal Society Interface* 15.139 (2018): 20170828.

[4] Guo, Pengming, et al. On the influence of biomimetic shark skin in dynamic flow separation. *Bioinspiration & Biomimetics* 16.3 (2021): 034001.

[5] Vilumbrales-Garcia, R., et al. Effects of surface roughness on the propulsive performance of pitching foils. arXiv preprint arXiv:2301.03942 (2023).

A computationally-augmented wind tunnel with irrotational gust generation for low-speed aerodynamics

Diederik Beckers[a] and Jeff D. Eldredge[a*]
[a] University of California, Mechanical and Aerospace Engineering, Los Angeles, California, USA
[*]Correspondence: *jdeldre@ucla.edu*

1 Introduction

Large-amplitude flow disturbances, such as gusts, can drastically change the aerodynamic loads on machines. Active flow control can mitigate or exploit these disturbances, but developing an effective control strategy is challenging, partly because the interactions are often non-linearly dependent on the gust amplitude [1]. As a result, the parameter space is often too large to explore by wind tunnel experiments alone. One solution is to create a surrogate computational model (a digital twin) of the experiments that can augment the experimental data and model conditions outside the scope of the experiments. To ensure that the model is faithful to the true disturbed flow conditions, it should be able to assimilate data from experiments. We present a digital twin of a low-speed aerodynamics wind tunnel equipped with a system for irrotational gust generation.

2 Methodology

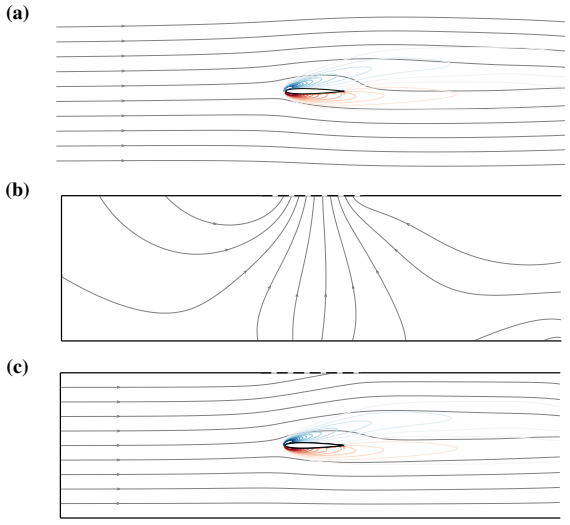

Figure 1: Streamlines and vorticity contours for (a) the external viscous flow $v_\omega + U_\infty$, (b) the potential flow correction v_ϕ, and (c) the combined velocity field v.

Consider the two-dimensional geometry in Figure 1 based on the Andrew Feijer Unsteady Wind Tunnel at IIT [2], which is equipped with controllable louvers to create a suction flow through the top wall. A transverse gust can be generated by rapidly opening and closing the louvers. We are interested in obtaining the aerodynamic forces on the test subject and a detailed description of the flow around it to augment experimental data.

We want to model the viscous flow in the vicinity of the test subject, satisfying the no-slip and no-flow-through conditions on its surface, and account for the influence of the wind tunnel walls on that flow. To avoid spending computational resources on accurately modeling the flow near the walls, we only enforce no flow through at the walls. The flow v that satisfies these boundary conditions can then be constructed from an external viscous flow v_ω (with non-zero vorticity) around the test subject in a freestream U_∞ and a potential flow correction $v_\phi = \nabla\phi$ according to the Helmholtz decomposition

$$v = v_\omega + v_\phi + U_\infty. \tag{1}$$

In this work, the viscous and potential flow are modeled using an immersed-layers solver [3, 4] and the lattice Green's function (LGF) to satisfy far-field boundary conditions automatically. By modeling the viscous flow as an external flow over the body using the LGF, the computational domain only has to be large enough to enclose the vorticity [5]. The LGF then still allows evaluating v_ω at the wind tunnel walls (far from the vorticity) such that the potential flow correction can be computed to cancel out the normal component. The potential flow contribution can also mimic the suction velocity at the top wall to create an irrotational suction flow, accurately representing the flow in the actual wind tunnel [2]. The suction velocity, and other unknown parameters, can be estimated through Bayesian inference from wind tunnel measurements.

3 Examples

We demonstrate the computational framework for a NACA0009 airfoil experiencing a gust with a Gaussian time profile. The force response is compared in Figure 2 to that of a flat plate and to the Wagner response for a vertical motion that matches the vertical velocity that the suction creates. The force contributions shown in Figure 3 reveal that the difference between the NACA airfoil and Wagner responses results from a different circulatory force response

due to non-linear effects during the vortex shedding. Snapshots of these vortices are shown in Figure 4. Furthermore, the difference between the NACA airfoil and the flat plate force responses is mostly a result of the buoyancy force on the non-zero volume of the NACA airfoil due to the accelerating external flow.

Other examples have been investigated and demonstrate that when the airfoil's angle of attack is increased or a stronger gust is created, non-linear effects and the wind tunnel confinement result in increasingly different behavior between the flow with and without the wind tunnel walls. Finally, gusts have been simulated that mimic the impulsive opening and closing of the suction louvers in the real wind tunnel used by He et al. [2].

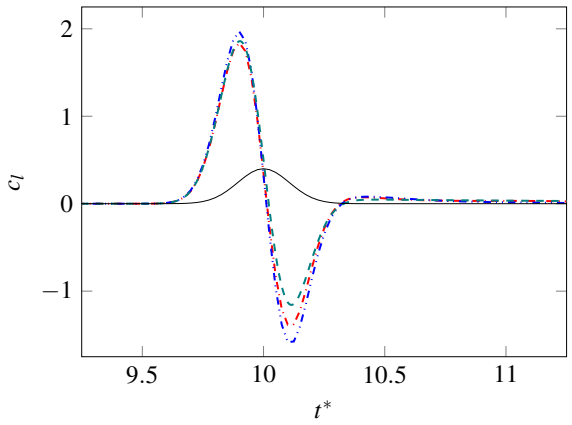

Figure 2: Lift coefficient for a NACA0009 airfoil (-·-·-), flat plate (-·-·-), and Wagner response (- - -), and the suction-to-inlet mass flow rate ratio (——) for a Gaussian gust.

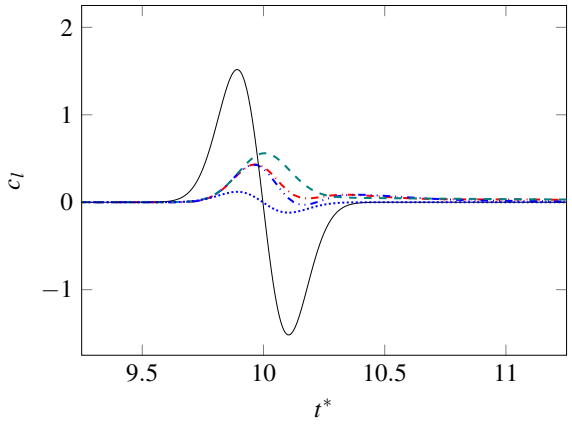

Figure 3: Contributions to the lift coefficient of the circulatory force for a NACA0009 airfoil (-·-·-), flat plate (-·-·-), and Wagner response (- - -), of the added mass force (——), and of the buoyancy force (·····) for a Gaussian gust.

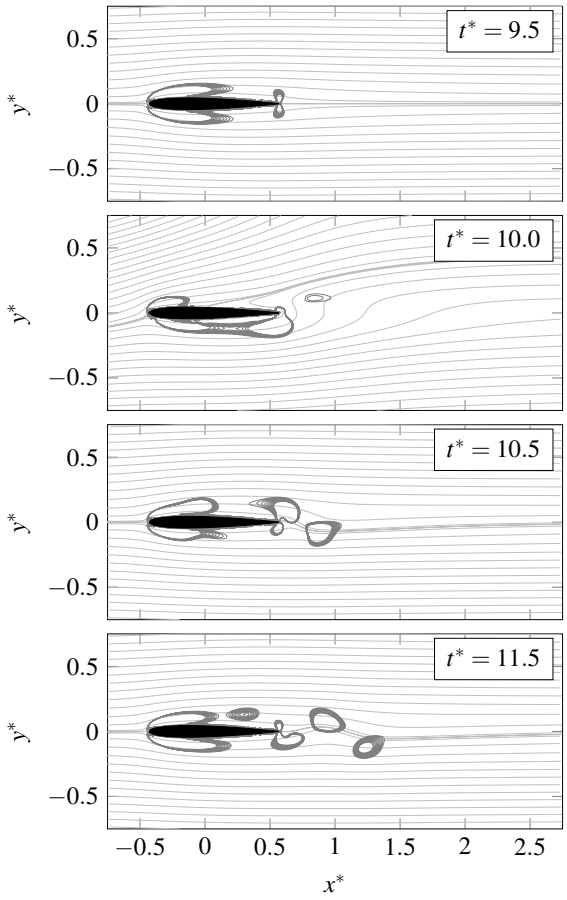

Figure 4: Streamlines and Q contours for a thick airfoil experiencing a Gaussian gust in a wind tunnel.

4 Conclusion

This work presents a computational framework for efficiently modeling the flow in a wind tunnel with irrotational gust generation by correcting a viscous flow solver with a potential flow. The simulations can be assimilated with experiments by inferring gust parameters from measurements. The force response of different airfoils is compared to analyze the wind tunnel and non-linear effects.

References

[1] A. R. Jones, O. Cetiner, and M. J. Smith. Physics and Modeling of Large Flow Disturbances: Discrete Gust Encounters for Modern Air Vehicles. *Annual Review of Fluid Mechanics*, 54:469–493, January 2022.

[2] X. He, D. R. Williams, and S. T. M. Dawson. Transverse gust generation in a wind tunnel: a suction-driven approach. *Experiments in Fluids*, 63(8):125, August 2022.

[3] J. D. Eldredge. A method of immersed layers on cartesian grids, with application to incompressible flows. *Journal of Computational Physics*, 448:110716, 2022.

[4] D. Beckers and J. D. Eldredge. Planar potential flow on cartesian grids. *Journal of Fluid Mechanics*, 941:A19, 2022.

[5] S. Liska and T. Colonius. A fast immersed boundary method for external incompressible viscous flows using lattice Green's functions. *Journal of Computational Physics*, 331:257–279, February 2017.

Prediction of transverse gust effects on airfoil vortex shedding and loads

Yi-Tsung Lee[a], Arun Vishnu Suresh Babu[b], and Ashok Gopalarathnam[a*]
[a] Mechanical and Aerospace Engineering, North Carolina State University, Raleigh, NC, USA
[b] Mechanical Engineering and Engineering Science, University of North Carolina at Charlotte
*Correspondence: *agopalar@ncsu.edu*

1 Introduction

With recent interest in the flight of small flight vehicles in urban environments, the effects of gusts is receiving increased attention. As a stepping stone to the effect on a flight vehicle, it is desirable to first characterize gust effects on an airfoil. Further, there is an interest in the effect of large gust-to-freestream ratios that are most relevant to the flight of small and slow vehicles in urban areas. A transverse gust is a region of flow disturbance normal to the freestream. When an airfoil flies through this region, the gust affects the airfoil bound circulation, vortex shedding, and the loads. Recent experimental and modeling efforts for this problem have used flat-plate geometries, and have studied gust effects, gust-mitigation approaches by pitch control, and experiment-model comparison [1]. In the current work, we use a new version of the LESP-modulated discrete-vortex method (LDVM) [2] that, unlike earlier models, can simulate transverse gust effects on round-leading-edge airfoils. Comparison of the results from this 2D-flow approach shows that the flow fields compare well with experimental results, but forces are over estimated as seen with the earlier models. However, when an aspect-ratio correction is applied to the 2D force results, the predicted forces are in better agreement with those measured in the experiments.

2 Methodology

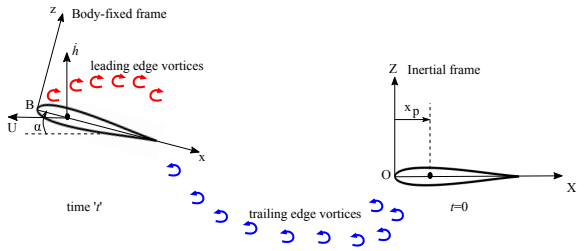

Figure 1: Illustration of the airfoil kinematics and the discrete vortices shed from it, along with the variables used in the unsteady aerodynamic model

In this work, the unsteady-airfoil prediction approach of Narsipur et al. [3] is used as the foundation. This approach uses lumped vortex elements to model the bound vortex sheet on the airfoil and discrete vortices to model shedding from leading and trailing edges. The shedding from the leading edge is intermittent, and is governed by the instantaneous leading-edge suction parameter (LESP) and whether or not it is greater than the critical LESP. Because the critical LESP depends on the leading-edge radius and it is an input to the simulation, the current approach can simulate flows over round-leading-edge airfoils. This formulation has been recast into a state-variable formulation [4]. The state-variable formulation casts the problem in a standard ordinary differential equation form, enabling the use of higher-order numerical integration methods for improved accuracy. The approach allows for easy integration of aerodynamic and structural dynamic models to study new problems.

The integration of the transverse gust effect to the unsteady solver is achieved by creating a gust velocity field, with a prescribed vertical flow velocity, over a region of the x coordinate. Whenever the airfoil or a free vortex is inside this region, the corresponding gust velocity will be added to the calculation. The contributions from the gust along with other induced velocities from the motion and other free vortices are summed to fulfill the zero-normal-flow boundary condition on the airfoil camber line. This affects the bound circulation on the airfoil. As the LESP is affected by the leading-edge bound circulation, the gust alters the shedding of vorticity from the leading edge. The gust also affects the velocity used in calculating the loads on this portion of the airfoil, which is done using the Kutta-Joukowski theorem. Thus the gust dynamically affects the vortex shedding and the loads as the airfoil moves in or out of the gust region. In future, this approach can be extended to study the effect of leading-edge shapes and pitching kinematics on gust effects and gust-mitigation strategies.

3 Results

Using our unsteady solver coupled with gust field function, an airfoil moving into a transverse gust region is studied for three different gust ratios (GR) . The lift history, $C_l(t)$, and the C_l normalized by the gust ratio (C_l/GR) between the three gust ratio cases are presented in figure 2. The results show how an airfoil with zero pitch angle can experience a lift increase followed by a decrease as the airfoil moves into and out of the gust region. The collapse of the C_l/GR plots shows that the lift increase due to gust is almost proportional to the strength of gust, and thus the normalized curve is similar between the cases with different gust ratios.

The simulation (Figs. 2 c,d) over predicts the lift when compared to the experimental results (Figs. 2 a,b, from Ref. [1]), as also observed in earlier works [1]. We hypothesized that this simulation-experiment discrepancy was due to the lack of 3D corrections in the simulation. To evaluate this hypothesis, we applied a simple lift-curve-slope correction based on Helmbold's equation for a low aspect ratio wing (Eq. 1). With the correction, the results from the simulation (Figs. 2 e,f) show much better agreement with the experimental results.

$$a = \frac{a_0}{\sqrt{1+(\frac{a_0}{\pi AR})^2}+\frac{a_0}{\pi AR}} \tag{1}$$

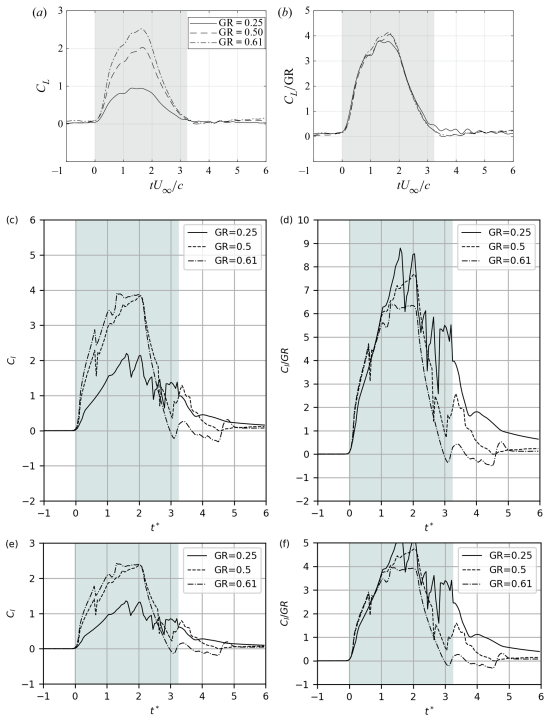

Figure 2: The load comparison: (a, b) Experimental results for C_l and C_l/GR, (c, d) Simulation results for C_l and C_l/GR, and (e, f) Simulation results with aspect-ratio correction for C_l and C_l/GR.

We are also interested in how well the simulation predicts the LEV shedding in the flow field. In figure 3, the flow predictions from the simulation are compared against PIV vorticity distributions from the experiments at different times during the gust encounter. The results are promising, indicating that the majority of the gust effects have been successfully modeled in the simulation. The vortex roll-up downstream the airfoil also shows very similar pattern when compared to the experimental results.

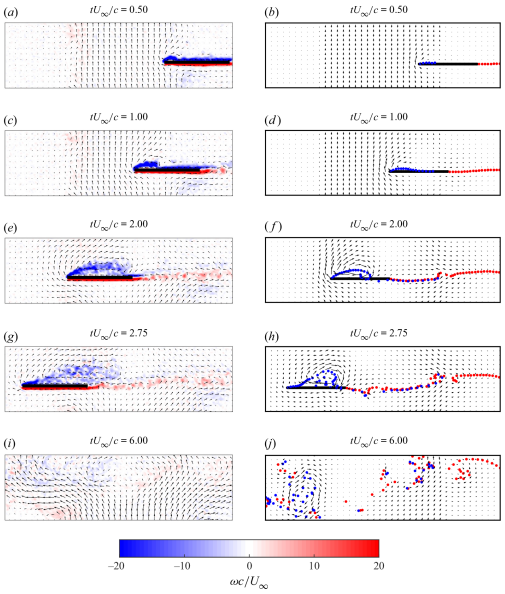

Figure 3: Vorticity distribution from experiment [1] (left) and discrete vortex distribution from simulation (right) for gust ratio of $GR = 0.25$.

4 Conclusions

The results presented here show that the current low-order model is capable of accurately predicting the LEV shedding pattern during gust encounters using the gust field function. The lift modulation is also captured by the model, but the solver does over-predict the lift compared to experiments. It was hypothesized that the discrepancy in lift was due to aspect-ratio effects. When an aspect-ratio correction was applied to the simulation, the lift history showed much better agreement with the experimental results, showing that it is important to account for aspect-ratio effects in such problems. One of the benefits of the current simulation approach is that it is possible to model round-leading-edge airfoils. Follow-on research efforts will focus on the effect of leading-edge radius and the design of motion kinematics to mitigate the effects of the gust. We expect to present some of these results at the conference.

References

[1] Sedky, G. and Lagor, F. D. and Jones, A.. Unsteady aerodynamics of lift regulation during a transverse gust encounter. *Physical Review Fluids*, Vol.5, 074701, 2020.

[2] Ramesh, K., Gopalarathnam, A., Granlund, K., Ol, M. V., and Edwards, J. R., Discrete-vortex method with novel shedding criterion for unsteady aerofoil flows with intermittent leading-edge vortex shedding. *Journal of Fluid Mechanics*, 751, 500-538, July 2014.

[3] Narsipur, Shreyas and Gopalarathnam, Ashok and Edwards, Jack R. Low-Order Model for Prediction of Trailing-Edge Separation in Unsteady Flow. *AIAA Journal*, Vol.57, 191-207, 2019.

[4] Lee, Yi Tsung and SureshBabu, ArunVishnu and Bryant, Matthew and Gopalarathnam, Ashok. State Variable Form of Unsteady Airfoil Aerodynamics with Vortex Shedding. *AIAA SCITECH 2022 Forum*, 2022-1667, 2022.

Laminar separated wakes around tapered wings: direct numerical simulations and triglobal resolvent analysis

Jean Hélder Marques Ribeiro[a*] and Kunihiko Taira[a]
[a] University of California, Los Angeles, Department of Mechanical and Aerospace Engineering, USA[1]
*Correspondence: *jeanmarques@g.ucla.edu*

1 Introduction

Understanding flow separation over lifting bodies is critical for supporting the design of aircraft. This flow problem has been a subject of research interests for decades [1]. The characterization of post-stall flows over finite wings is also fundamental to the understanding of biological flight [2]. To fly at high angle of attack post-stall, aerodynamicists aim to control and attenuate the detrimental effects of flow separation to the aerodynamic performance of the wing. To achieve this objective, we consider in this study the influence of the wing planform geometry on the separated wake features. This characterization remains a challenge, even in the absence of turbulence and has been largely unexplored for tapered wings.

In this work, we provide a detailed characterization of the wing taper effects on laminar separated wakes using direct numerical simulations (DNS). To further deepen our knowledge, we study the wake dynamics through triglobal resolvent analysis, which identifies the optimal forcing structures that can be amplified in the flow field [3]. Using those insights, we can further study the dynamics of self-sustained fluctuations that support unsteadiness on laminar separated flows using resolvent wavemakers [4,5]. These findings are crucial to the analysis of the wing taper effects on the wake dynamics and underpin future efforts to characterize flow separation in turbulent flow regimes.

2 Direct numerical simulations

We conduct DNS with a compressible flow solver *CharLES* [6]. The spatial coordinates are defined with (x,y,z) as the streamwise, transverse, and spanwise directions, respectively. The NACA 0015 profile is defined on the (x,y) plane at the wing root, which is then extruded in the spanwise direction to form the wingspan. We build half-span models with symmetry imposed at the wing root. Wing taper is defined by the taper ratio $\delta = c_{\text{tip}}/c_{\text{root}}$, where c_{tip} and c_{root} are the tip and root chord-lengths, respectively, as shown in figure 1(a). For all wings considered here, the chord length decreases linearly from root to tip. The mean chord length c at the quarter-span $b/2$ is used to scale all spatial variables. For all flows analyzed herein, we define the chord-based Reynolds number $Re_c = U_\infty c/\nu = 400$, where U_∞ is the freestream velocity and ν is the kinematic viscosity. The freestream Mach number is set to $M_\infty = U_\infty/a_\infty = 0.1$, where a_∞ is the freestream speed of sound. A schematic is shown in figure 1(a-c) for different tapered wing configurations. A close view on the near-wake computational grids is shown in figure 1(d,e).

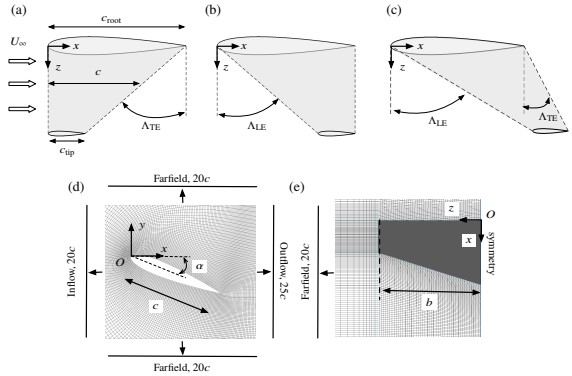

Figure 1: Problem setup for tapered wings. Wing planforms with $sAR = b/c = 2$, $\alpha = 18^\circ$, $\delta = 0.5$, and three different configurations (a) $\Lambda_{\text{LE}} = 0^\circ$, (b) $\Lambda_{\text{TE}} = 0^\circ$, and (c) $\Lambda_{\text{LE}} = 40^\circ$. Computational grids are shown on 2-D planes at (d) $z/c = 1$ and (e) $y/c = -0.5$.

Post-stall wakes around tapered wings exhibit a rich diversity of flow structures depending on the taper ratio, aspect ratio, angle of attack, and the leading and trailing edges sweep angles, as shown in figure 2. On the top left, we see the flow around an untapered and unswept wing, with streamwise tip vortices developing from the free end and spanwise roll structures located near the wing root. From the second to fourth rows, in the first column, we observe the effect of wing sweep over untapered wings. For swept wings, the region of shedding shifts towards the wing tip, and the amplitude of wake oscillations decreases for high sweep angles.

The flow over tapered wings is shown on the second and third columns of figure 2. In the top row, flows over forward-swept TE wings are presented. These planforms have fixed $\Lambda_{\text{LE}} = 0^\circ$, while $\Lambda_{\text{TE}} = -18.4^\circ$ and -30° for $\delta = 0.5$ and 0.27, respectively. In this manner, taper reduces the tip

[1]This work was supported by the Air Force Office of Scientific Research (program manager: Dr. G. Abate, grant: FA9550-21-1-0174)

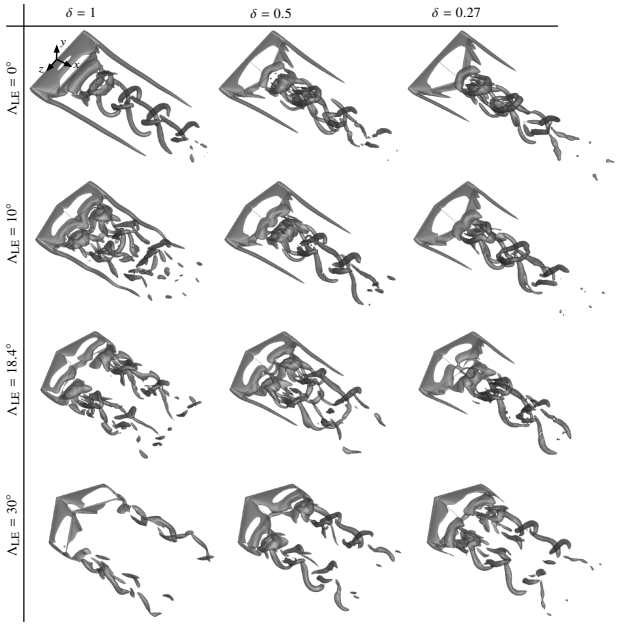

Figure 2: Isosurfaces of instantaneous flow fields around tapered wings with $sAR = 2$, at $\alpha = 18°$, taper ratios between $0.27 \leq \delta \leq 1$, and $0° \leq \Lambda_{LE} \leq 30°$, using gray-colored isosurfaces of $Q = 1$.

vortex length and affects the topology of the root shedding structures. Furthermore, we note flows over backward-swept LE tapered wings, with a fixed $\Lambda_{TE} = 0°$ while the LE is swept backwards with $\Lambda_{LE} = 18.4°$ and $30°$ for $\delta = 0.5$ and 0.27, respectively. This taper causes the wake shedding structures to appear towards the wing tip region. Lastly, for highly swept wings, shown at the bottom row of figure 2, with a fixed $\Lambda_{LE} = 30°$, wing taper increases the level of wake oscillations near the wing tip. These results show how taper affects wake oscillations, motivating us to study the dynamics of their flow perturbations through resolvent analysis.

3 Resolvent analysis

Triglobal resolvent analysis reveals how forcings are amplified in the flow field and the response they generate. To study wing taper effects on wake unsteadiness, we present an analysis of the forcing-response spatial overlap, named resolvent wavemaker, which highlights regions responsible for self-sustained oscillations in the flow field. In figure 3(a), wavemaker modes appear in the near-wake, encompassing the region where spanwise vortices are formed.

For the wing with forward-swept LE (figure 3b), the wavemaker support forms a triangular shape, starting from the wing root near the LE and expanding in spanwise rolls downstream and near the TE. Compared to the structures formed over the untapered wing, these modes show that the source of self-sustained oscillations near the LE is concentrated at the root region. In figure 3(c), for forward-swept LE, wavemakers appear far from the root region revealing that self-sustained oscillations arise from the tip region.

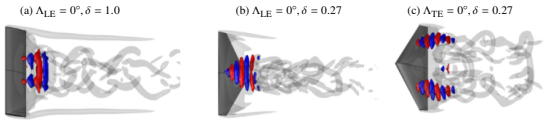

Figure 3: Resolvent wavemakers around tapered wings. (a) $\Lambda_{LE} = 0°, \delta = 1.0$, (b) $\Lambda_{LE} = 0°, \delta = 0.27$, and (b) $\Lambda_{TE} = 0°, \delta = 0.27$. For all modes, $\alpha = 22°$ and $St = 0.14$. Wavemaker modes shown in blue-red scale with y-velocity isusurfaces. Instantaneous flowfield shown in light gray colored isosurfaces of $Q = 2$.

4 Conclusion

We have presented the effect of wing taper on the wake dynamics using a comprehensive number od direct numerical simulations and resolvent analysis. Through DNS, we see that backward-swept TE concentrates flow oscillations near the wing root, while the forward-swept LE gives rise to the unsteadiness near the wing tip. To further study the emergence of unsteadiness, we use triglobal resolvent analysis and resolvent wavemakers, related to the regions with self-sustained oscillations due to the overlap of forcing and response modes. The wing planform alters the spatial support of wavemakers. For instance, the triangular-shaped wavemakers observed for forward-swept TE wings show that the self-sustained oscillations over this wing arise from the wing root. On the other hand, for forward-swept LE wings, the wavemakers appear near the wing tip, revealing the region where unsteadiness is supported around these wings. The present results reveal that the conflicting influence of LE and TE sweep angles pays a major role in defining the wake characteristics, steady, unsteady behavior, as well as the formation and maintenance of the tip vortex.

References

[1] J. D. Anderson. *Fundamentals of aerodynamics*. McGraw-Hill, 2010.

[2] J. J. Videler, E. J. Stamhuis, and G. D. E. Povel. Leading-edge vortex lifts swifts. *Science*, 306(5703):1960–1962, 2004.

[3] J. H. M. Ribeiro, C.-A. Yeh, and K. Taira. Randomized resolvent analysis. *Phys. Rev. Fluids*, 5(3):033902, 2020.

[4] J. H. M. Ribeiro, C.-A. Yeh, K. Zhang, and K. Taira. Wing sweep effects on laminar separated flows. *J. Fluid Mech.*, 950:A23, 2022.

[5] J. H. M. Ribeiro, C.-A. Yeh, and K. Taira. Triglobal resolvent analysis of swept-wing wakes. *J. Fluid Mech.*, 954:A42, 2023.

[6] G. A. Brès, F. E. Ham, J. W. Nichols, and S. K. Lele. Unstructured large-eddy simulations of supersonic jets. *AIAA J.*, 55(4):1164–1184, 2017.

LPT measurements around a hydrofoil close to the free surface

H. Bonnard[a*], P. Braud[a], L. Chatellier[a] and L. David[a]
[a] Pprime Institute, CNRS – University of Poitiers – ENSMA, UPR 3346, Futuroscope Cedex, France[1]
*Correspondence: *herve.bonnard@univ-poitiers.fr*

1 Introduction

The tips of wings have been a major design point for the wing's performance due to generation of trailing vortices close to the tips of finite span wings, leading to major change flow near the wing such as downwash and induced drag as shown by Prandtl [1]. While smoke visualizations were done at first to get a qualitative view of the trailing and tip vortices [2], Particle Image Velocimetry (PIV) and computational methods offer a quantitative study of them. PIV measurements were mainly done using two-dimensional measurements, being either two components or three components through stereographic PIV. Using tomographic PIV [3] or Particle Tracking Velocimetry [4] we can improve the understanding of 3D dominant flow topology, such as the ones occurring on a finite span wing.

Many studies have been done to optimize the shape of the tip as well as adding some appendages such as winglets to control the generation and behaviour of the wing tip vortices. Those design were commonly made for the wings of airplanes, but some studies were done specifically on hydrofoils due to their difference in operating conditions, such as the risk of cavitation as well as the influence of free-surface [5].

Thus, to study the influence of the free surface on the vortex formation and shedding, Lagrangian Particle Tracking (LPT) measurements have been carried out. The flow behaviour near the tip of a hydrofoil at low depth for different angles of attack and Reynolds numbers (Re) is investigated. The trajectory of the tip vortex and its intensity are identified and followed for the different configurations.

2 Methods

The experiments were carried out at the P' Institute in the Environmental Hydrodynamic Platform's open water channel which dimensions are 7 m × 0.385 m × 0.6 m (LxWxH). The channel is equipped with a PCM Moineau worm-drive pump controlled with a Schneider Electric variable-frequency drive up to flow rates of $Q = 65\ L/s^{-1}$. The flow rates are measured with an Endress+Hauser Promag55 electromagnetic flow-meter. The free-surface height can be modified by a spillway gate. An ABS 3D printed T-shaped hydrofoil (chord of c=40 mm and span of 200 mm) was placed inside the channel at a depth of d=1.75 chords in order to observe the influence of the proximity to the free-surface on the flow. Four cases were studied, using two different angles of attack α of 6° and 12° at two chord-based Reynolds numbers of about 20 000 and 6 500, thus using our fixed depth at depth-based Froude number of 0.63 and 0.21 respectively.

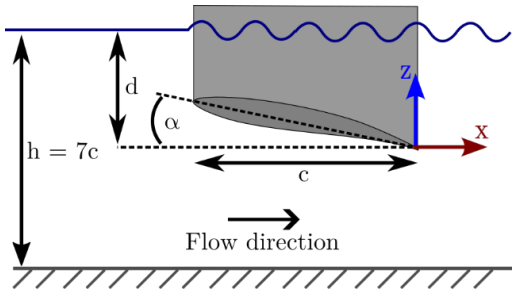

Figure 1: Schematic description of the experiment

Two Photron Fastcam SA-Z 1 MP 20 kHz cameras were used as well as two Photron Fastcam SA1.1 1 MP 5.4 kHz cameras, working at an acquisition frequency of 1 kHz and took 21 000 images. A 2 x 30 mJ Nd-YLF Continuum Terra PIV (527 nm, 10 kHz) laser was used with LaVision's Volume Optics laser generator. The measurements were recorded on a 100 mm x 100 mm x 40 mm volume downstream of the hydrofoil, streamwise starting just after the trailing edge and spanwise starting from 5 mm outside the wing.

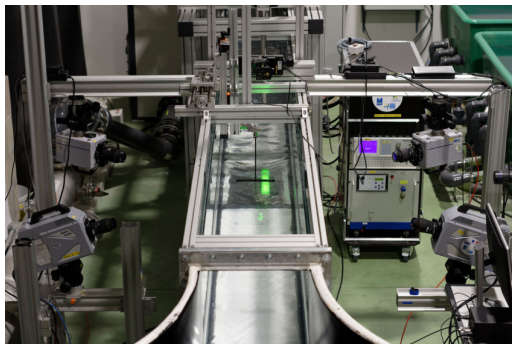

Figure 2: Experimental setup of the LPT measurements

[1]The authors would like to thank the Direction Générale de l'Armement for the funding of Hervé Bonnard's PhD thesis as well as the Plateforme Hydrodynamique Environnementale (PHE). This work pertains to the French government program "Investissements d'Avenir" (EUR INTREE, reference ANR-18-EURE-0010).

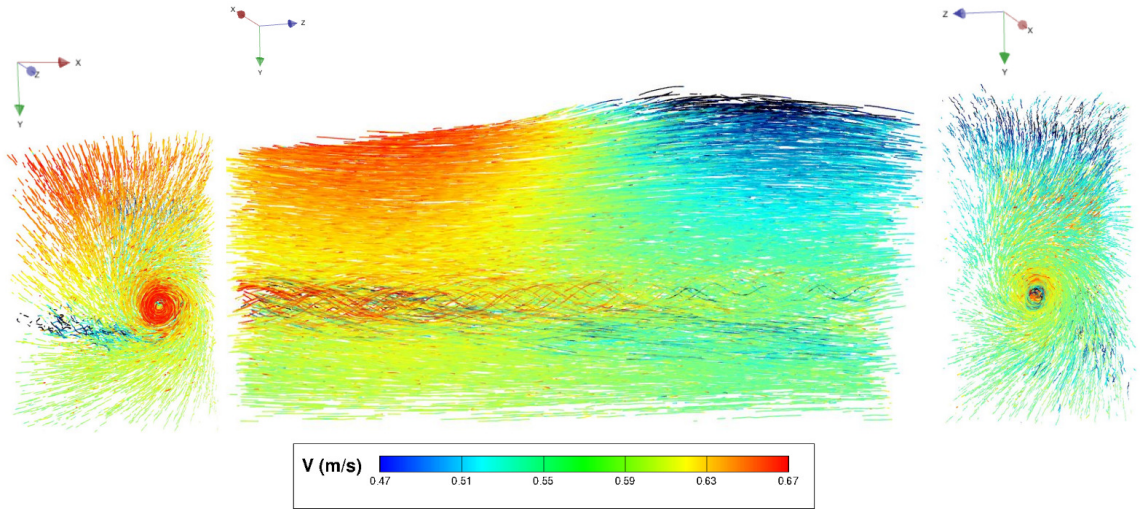

Figure 3: Front view, side view and back view of the trajectories close to the tip of the hydrofoil at an angle of attack of 12°, a Reynolds number of 20 000 and a depth-based Froude number of 0.63

Fluorescent particles have been used as PIV tracers. These 20 μm diameter particles are homemade with polyamide (density 1.04) doped with rhodamine 6G. The cameras equipped with a high pass filter only acquired the fluorescent signal avoiding the laser light reflections from the free surface.

The LPT was done using LaVision's software. The Shake-The-Box algorithm [6] is used to identify the particles in the volume from four images recorded simultaneously from different points of view and those particles are tracking in space at different times to follow their trajectories. An average of 20 000 active trajectories of 50 successive positions is obtained at each time.

3 Results

A previous study [5], showed the influence of the depth, Reynolds number and angle of attack on the flow topology at three different positions along the span of the T-shaped hydrofoil: at the symmetry plane (half span), at the quarter span and near the wing tip.

The free-surface proximity leads to important change in the flow topology, especially with the biggest depth-based Froude number (close to 0.9). Near the wing tip, the trailing edge vortices' wake is bent due to the proximity of the free-surface, as well as the wing tip vortices in a smaller way.

Another major difference can be observed over all the span of the hydrofoil when we decrease the depths, all other parameters being fixed, that is a decrease in the velocity gradient near the wing's leading edge. This will lead to a smaller pressure gradient and thus at a loss of lift which was confirmed using a 6-axis loads sensor during our experiments. Moreover, the wing tip vortices being strongly related to the pressure gradient of the wing will also see changes in its intensity.

The LPT measurements allowed us to observe the trailing vortices of the wing tip, which was missing in the previous study. The trajectories show us the vortices' spatial evolution depending on our parameters. An example is shown on Figure 3, where we can see the wing tip vortices moving closer to the hydrofoil when comparing the front and back views.

References

[1] Ludwig Prandtl. Applications of modern hydrodynamics to aerodynamics. Technical report, NACA, 1921.

[2] Myong Hwan Sohn and Jo Won Chang. Visualization and PIV study of wing-tip vortices for three different tip configurations. *Aerospace Science and Technology*, January 2012.

[3] L. David, T. Jardin, P. Braud, and A. Farcy. Time-resolved scanning tomography PIV measurements around a flapping wing. *Experiments in Fluids*, April 2012.

[4] I. Grant, G. McCutcheon, A.H. McColgan, and D. Hurst. Optical-velocimetry, wake measurements of lift and induced drag on a wing. *Optics and Lasers in Engineering*, March 2006.

[5] Hervé Bonnard, Ludovic Chatellier, and Laurent David. Investigation of 3D effects and free-surface proximity influence on the flow around a hydrofoil using PIV measurements. In *20th International Symposium on the Application of Laser and Imaging Techniques to Fluid Mechanics*, Lisbon, 2022.

[6] Daniel Schanz, Sebastian Gesemann, and Andreas Schröder. Shake-The-Box: Lagrangian particle tracking at high particle image densities. *Experiments in Fluids*, May 2016.

2 Session B: Flow Control & Energy Harvesting

Data-driven optimisation and control of pitching kinematics for vertical-axis wind turbine blades

Sébastien Le Fouest, Daniel Fernex, and Karen Mulleners*
École polytechnique fédérale de Lausanne, Institute of mechanical engineering,
Unsteady flow diagnostics laboratory, 1015 Lausanne, Switzerland[1]
*Correspondence: *karen.mulleners@epfl.ch*

Introduction

Vertical-axis wind turbines feature many advantages to complement traditional wind turbines in power production including omni-directionality, low noise production, and scalability. The inherent aerodynamic complexity of vertical-axis wind turbines has challenged their development for large-scale power production. The blades of these turbines undergo periodic variations in effective angle of attack and incident flow velocity, leading to the occurrence of dynamic stall. This phenomenon causes large cycle-to-cycle load fluctuations, jeopardising the turbine's structural integrity.

In this project, we investigate the potential of individual blade pitching to control the occurrence of dynamic stall on a single-bladed wind turbine. The optimal temporal evolution of the blade pitching angle has be determined through an open loop optimisation genetic algorithm based optimisation and through a cluster-based feedback control. Both strategies use experimental data from various measurement campaigns with a scaled-down vertical-axis wind turbine model with dynamic blade pitching capabilities and an instrumented blade shaft for load measurements [1]. The wind turbine blade is placed at the centre of the test section of a water channel and performs fully automated experiments to seek optimal blade pitching kinematics or control laws (fig. 1).

Genetic algorithm based optimisation

We performed an experimental optimisation of the blade's pitching kinematic at on and off-design operating conditions given by tip speed ratios $\lambda = 3.0$ and $\lambda = 1.5$. The tip-speed ratio $\lambda = U_b/U_\infty$ is the ratio between the blade's rotational velocity U_b and the incoming flow velocity U_∞.

We optimised the blade's pitching profile using a genetic algorithm [2] with two objectives: 1) maximising the net power production and 2) minimising load fluctuations related to flow separation. We performed over 1500 experiments visiting a large envelope of pitching kinematics. We obtain time-resolved aerodynamic force measurements using a customised load cell built into the blade's shaft and compute the wind turbine performance for each individual. The strongest individuals achieve a 300 % increase in net power production compared to a non-actuated wind turbine blade. Flow field measurements using time-resolved particle image velocimetry have been conducted for the strongest individuals to better understand how the pitching affects the development of dynamic stall.

An exemplary result of the open-loop optimisation for $\lambda = 1.5$ is presented in fig. 2. The non-actuated case in fig. 2a is characterised by the occurrence of dynamic stall. When the blade moves upwind, a leading-edge vortex forms that creates additional suction and allows for a peak in power production around $\theta = 80°$. Shortly thereafter, the large-scale stall vortex separates, leading to a significant drag excursion

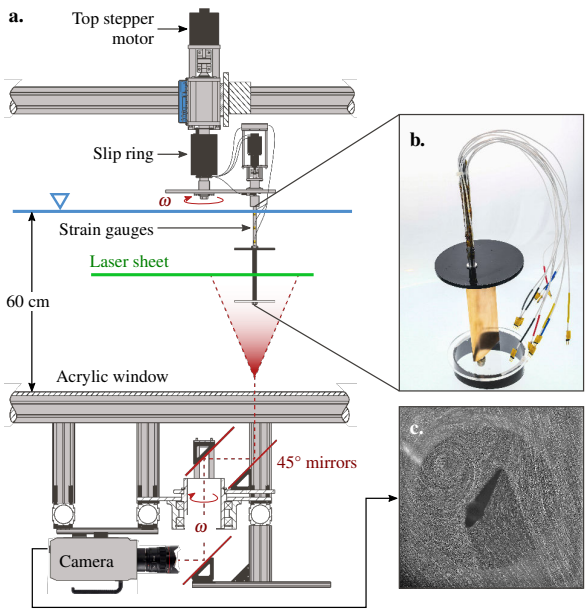

Figure 1: (a) Cross-sectional view of the experimental set-up including the wind turbine model, the light sheet, the rotating mirror system, and the high-speed camera for particle image velocimetry. (b) A close-up view of the blade sub-assembly, with installed strain gauges. (c) The camera's field of view indicated by a long exposure image of seeding particles in the flow.

[1]This work was supported by the Swiss National Science Foundation under grant number PYAPP2_173652

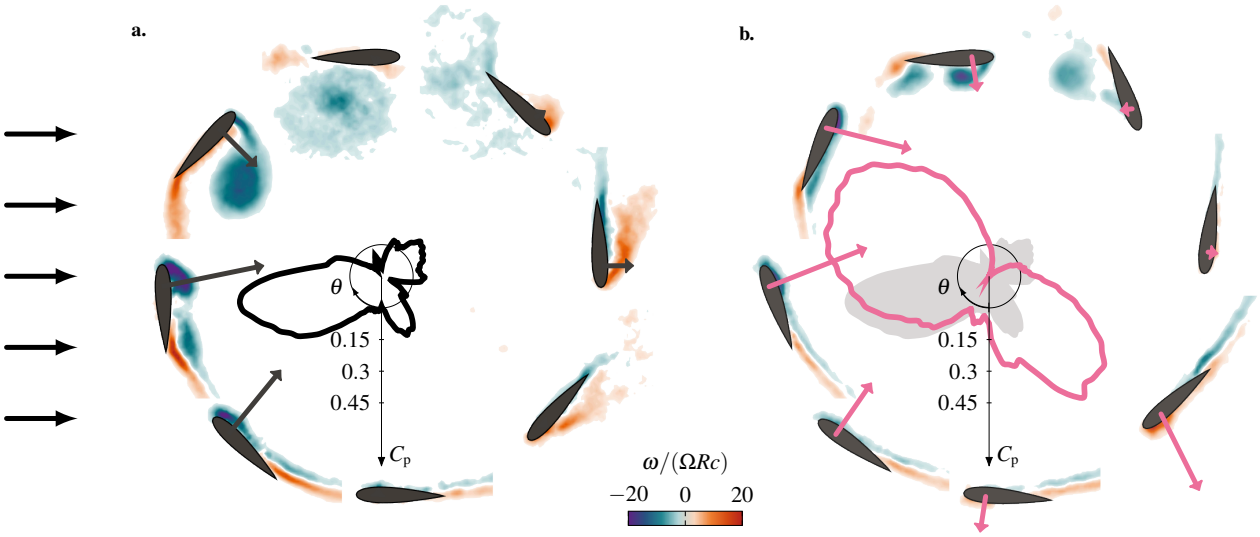

Figure 2: Evolution of the phase averaged velocity field and turbine power coefficient for (a) a single turbine without and (b) with pitch control for $\lambda = 1.5$. The cycle is divided into an upwind part $0° < \theta < 180°$ and a downwind part $180° < \theta < 360°$, with $\theta = 0$ referring to the blade in the bottom position. The power evolution without pitch control is added in grey in (b) for better comparison. The black circles in polar plots of the power coefficient correspond to $C_p = 0$.

and post-stall load fluctuations. In the downwind half of the motion, the flow remains fully separated, yielding sporadic small regions of positive power coefficient.

The optimised pitching kinematics presented a fig. 2b significantly improve the power production and limit the occurrence of dynamic stall. The blade pitching leads to an increase in the power production region during the upwind by delaying the onset of dynamic stall. The separation of the stall vortex is also delayed to $180° < \theta < 210°$ such that vortex is shed to the side. The reattachment is promoted and a significant second region of power production is present towards the end of the upwind part of the motion.

Cluster-based feedback control

In addition to the open loop optimisation of the blade's pitch angle evolution, we have applied cluster-based feedback control to continuously adjust the pitch angle in response to the measured blade loads. The control strategy builds upon the cluster-based feedback control presented by [3], which is a model-free approach that is especially well suited for complex systems without a known underlying model description.

Initial results for clean inflow conditions yield a control law that leads to an optimal blade pitching evolution that matches the optimal solutions obtained with the open loop optimisation. The added value of the closed loop control is its ability to adapt to perturbed and varying inflow conditions.

At the meeting, we will present a detailed comparison of the open and closed loop control of the blade pitching for steady inflow conditions. We will demonstrate the ability of the closed loop control to deal with varying and perturbed inflow conditions. The evolution of the power coefficients and the flow development under the various conditions will be analysed and guidelines for the safe control of vertical axis wind turbines will be presented.

References

[1] Sébastien Le Fouest and Karen Mulleners. The dynamic stall dilemma for vertical-axis wind turbines. *Renewable Energy*, 198:505–520, 2022.

[2] A.J. Chipperfield. The MATLAB Genetic Algorithm Toolbox. In *IEE Colloquium on Applied Control Techniques Using MATLAB*, volume 1995, pages 10–10. IEE, 1995.

[3] Aditya G. Nair, Chi-An Yeh, Eurika Kaiser, Bernd R. Noack, Steven L. Brunton, and Kunihiko Taira. Cluster-based feedback control of turbulent post-stall separated flows. 875:345–375.

Feather-inspired High-lift Flow Control Device for Stall Mitigation

Ahmed K. Othman*, Girguis Sedky, and Aimy Wissa

Princeton University, Princeton, NJ, USA
Correspondence: ahmed.othman@princeton.edu

Due to their speed, endurance, light-weight, and payload capabilities, small-scale unmanned aerial vehicles (sUAVs) are taking on more expansive roles in various applications, from search and rescue to cargo transport and mapping. However, such vehicles are still lacking in terms of agility and adaptability to be able to perform all these missions efficiently [1]. Stall is one of the limiting factors for sUAVs that prevents high angle of attack maneuvers, which are typically encountered during flight through gust and obstacle-filled environments or during takeoff and landing. These high angle of attack maneuvers are characterized by unsteady flow conditions due to the significant flow separation and vortex shedding[2]. Birds that operate in similar flight conditions and with the same constraints as sUAVs use some of their feather systems as passive-deployable flow control devices for stall mitigation; one of those feather systems is referred to as the coverts. In biology, the covert feathers are considered as aeroelastic flow-control devices for mitigating flow separation, enhancing lift, and delaying stall [3, 4]. The coverts are noticed to deploy during high angle of attack maneuvers such as perching, take-off, and landing as shown in Fig. 1a [5]. Two parameters affect the response of the covert feathers to the flow, namely the stiffness of the feather shaft determined by the material properties and the shaft area moment of inertia defined by the geometry.

Bio-inspired studies have investigated several covert-inspired flaps concepts to increase post-stall lift production and expand the flight envelope. Rigid metal flaps, feathered flaps, and elastic hair-like flaps are all examples of covert-inspired flaps that have been placed at various wing locations to augment aerodynamic performance. Furthermore, flaps with various mobility forms have also been studied, where some flaps were allowed to rotate freely (i.e. freely-moving flaps), others were attached to the surface of an airfoil at a static deflection angle, and some were connected to the airfoil surface via torsional hinges[6, 7, 8, 9]. Despite the different structural and mobility forms of the covert-inspired flaps, most studies confirmed that the flaps improve lift, especially at post-stall angles of attack. Two main flow control mechanisms have been identified for the coverts-inspired flaps to explain their aerodynamic benefits. The first mechanism is the "pressure dam" effect, which means that the flap acts as a dam to prevent reverse flow from advancing towards the leading edge of the airfoil, thus maintaining a lower suction pressure upstream of the flap as shown in the streamlines and vorticity contours in Fig. 1b & 1c [10, 11, 12]. The pressure dam effect was prominent in studies with both static and dynamic flaps; however, for some dynamic flaps, particularly torsionally hinged flaps, the pressure dam effect was accompanied by interaction with the vortex shedding processes [9]. This flap-vortex interaction represents the second flow control mechanism, and it was shown in a study by Nair and Goza [9]. In their study, the dynamic flaps obtain the largest lift benefits when the flap deflection is in phase with the vortex shedding. The flaps constructively interact with the lift-producing leading edge vortex (LEV) by allowing it to advect downstream with minimal resistance while countering the trailing edge vortex (TEV) and TEV-induced reverse flow by preventing it from propagating upstream, thus obtaining maximum lift benefits. However, this was only done numerically, and at a low Reynolds number ($Re = 1000$) that is characterized by significant regions of laminar flow and prone to early flow separation and vortex shedding due to the inability of the lower momentum flow to overcome the adverse pressure gradient aft of the point of maximum thickness.

This work expands on these studies by experimentally analyzing the physics of coverts-inspired torsionally hinged flaps at a higher Reynolds number ($Re = 2 \times 10^5$) which is relevant to both birds and sUAVs. This specific configuration was chosen since it is a more accurate representation of the coverts feathers compared to both the static and freely moving flaps. More specifically, using wind tunnel experiments, we measured the aerodynamic forces, flap deflection angles, and the flow field of a NACA 2414 airfoil with a passively deployable, torsionally hinged covert-inspired flap. The flap was mounted on the suction side of the airfoil and experiments were conducted at a post-stall angle of attack of 20°, where significant flow separation and vortex shedding are expected. The flap hinge location L_β (the chord-wise distance of the flap from the leading edge) was varied ($L_\beta = 70\%$c, 50%c, and 20%c). We also varied the moment of inertia of the flap, I_β and the stiffness of the torsional spring representing the hinge, K_β. These parameters were non-dimensionalized using flow properties, such as,

$$i_\beta = \frac{I_\beta}{\rho_f c^4}, \qquad k_\beta = \frac{K_\beta}{\rho_f U_\infty^2 c^2}, \qquad l_\beta = \frac{L_\beta}{c} \tag{1}$$

Here, the reference length scale is the airfoil chord c, velocity scale is the freestream velocity U_∞ and reference density is the fluid density ρ_f; i_β, k_β and l_β are the non-dimensional counterparts of I_β, K_β and L_β. In this work, the parameter l_β is reported as percentage of chord length from the leading edge.

The flap near the trailing edge (70%c) was found to be the most effective at improving lift post-stall with improvements up to 12% compared to the baseline flap-less

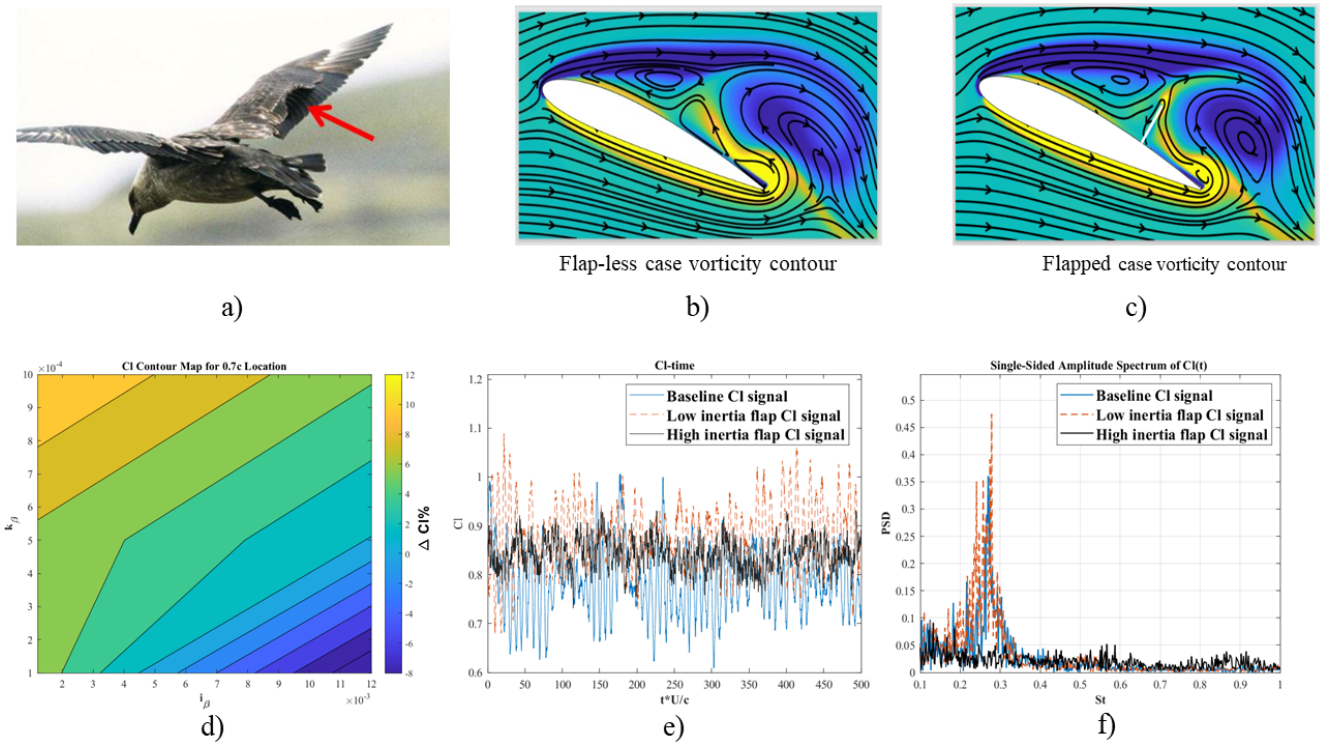

Figure 1: a) Upper wing coverts deploying in flight[5]. b) and c) Vorticity contours at Re=1000 for NACA2414 airfoil for the flap-less and flapped cases, respectively showing the pressure dam effect[12]. d) Contour plot of lift improvement percentage compared to the flap-less baseline at 70%c with respect to both stiffness and inertia. e) The time history of the lift coefficient for the flap-less and flapped cases with the highest lift improvement for both the low inertia and high inertia flap at $Re = 2 \times 10^5$. f) The power spectral density (PSD) of the lift coefficient for the flap-less and flapped cases for both the low inertia and high inertia flaps with the highest lift improvement at $Re = 2 \times 10^5$.

airfoil. At this location, the lower inertia flap is more effective at improving lift. Moreover, as the hinge stiffness increases, the lift improvement is found to increase as shown in Fig. 1d. The lift time signals of the case with the highest lift improvement for both the high and low inertia flaps are examined to understand the mechanism by which the flap improves lift. The highest lift-improvement case (i.e. the lower inertia flap) maintained the same vortex shedding frequency, non-dimensionalized and shown as Strouhal number, as the baseline flap-less case (Fig. 1f). On the other hand, the high inertia flap seems to remove this vortex shedding frequency, as shown by the lack of a peak in the power spectral density (Fig. 1f). Additionally, the fluctuations of the airfoil lift signal seem to decrease when the high inertia flap is deployed compared to the baseline and low inertia flap cases, as shown in Fig. 1e. In this work, we will also include recent flow field measurements of the airfoil with the flap at the location, stiffness, and inertia that show the lift improvements to better understand the flow physics involved behind the lift benefits observed and compare these to the baseline case and the previously reported numerical results at the lower Reynolds numbers [9, 12]. Using planar time-resolved particle image velocimetry, we will report the fluid-structure interactions that govern the flow physics and flap dynamics, and how they play a role in providing aerodynamic benefits.

References

[1] Johnny H Evers. Biological inspiration for agile autonomous air vehicles. Technical report, AIR FORCE RESEARCH LAB EGLIN AFB FL MUNITIONS DIRECTORATE, 2007.

[2] John David Anderson. *Fundamentals of aerodynamics*. McGraw-Hill Companies, 1984.

[3] Thomas Bachmann, Jens Emmerlich, Werner Baumgartner, Jochen M. Schneider, and Hermann Wagner. Flexural stiffness of feather shafts: geometry rules over material properties. *Journal of Experimental Biology*, 215(3):405–415, 02 2012.

[4] A.C. Carruthers, A.L.R. Thomas, and G.K. Taylor. Automatic aeroelastic devices in the wings of a steppe eagle aquila nipalensis. *Journal of Experimental Biology*, 210(23):4136–4149, 2007.

[5] Robert Meyer, Wolfram Hage, Dietrich W. Bechert, Markus Schatz, Thilo Knacke, and Frank Thiele. Separation control by self-activated movable flaps. *AIAA journal*, 45(1):191–199, 2007.

[6] D Bechert, M Bruse, W Hage, R Meyer, D Bechert, M Bruse, W Hage, and R Meyer. Biological surfaces and their technological application-laboratory and flight experiments on drag reduction and separation control. In *28th Fluid dynamics conference*, page 1960, 1997.

[7] Christoph Brücker and Christoph Weidner. Influence of self-adaptive hairy flaps on the stall delay of an airfoil in ramp-up motion. *Journal of Fluids and Structures*, 47:31–40, 2014.

[8] Marco E Rosti, Mohammad Omidyeganeh, and Alfredo Pinelli. Passive control of the flow around unsteady aerofoils using a self-activated deployable flap. *Journal of Turbulence*, 19(3):204–228, 2018.

[9] Nirmal J. Nair and Andres Goza. Fluid-structure interaction of a bio-inspired passively deployable flap for lift enhancement. *Physical Review Fluids*, 7:064701, June 2022.

[10] Chengfang Duan and Aimy Wissa. Covert-inspired flaps for lift enhancement and stall mitigation. *Bioinspiration & biomimetics*, 16(4), 2021.

[11] Gotz Bramesfeld and Mark D Maughmer. Experimental investigation of self-actuating, upper-surface, high-lift-enhancing effectors. *Journal of aircraft*, 39(1):120–124, 2002.

[12] Ahmed K. Othman, Nirmal J. Nair, Anushka Sandeep, Andres Goza, and Aimy Wissa. Numerical and experimental study of a covert-inspired passively deployable flap for aerodynamic lift enhancement. In *AIAA AVIATION 2022 Forum*, 2022.

Interactions of a Synthetic Jet with a Turbulent Boundary Layer

J. Straccia[a] and J. Farnsworth[a]
[a] University of Colorado Boulder, Boulder, Colorado, USA [1]
*Correspondence: *john.farnsworth@colorado.edu*

1 Introduction

Synthetic jets actuators (SJA) have been extensively studied for the purpose of controlling many different types of aerodynamic flows [1]. Their appeal comes from the fact that they are an active flow control device that can add momentum to the surrounding flow field without a net addition of mass. To generate this zero-net-mas-flux jet the driver draws external fluid into a cavity during the suction phase and then expels that fluid back out of the orifice during the blowing phase. The periodic expulsion of fluid by the actuator leads to the rapid formation of vortex rings which travel away from the orifice carrying the momentum introduced by the actuator outstorke. A vortex ring is formed with every actuation cycle, sometimes at a rate of thousands per second resulting in a train of vortex rings which constitute the early jet. As a result, vortex dynamics plays a critical role in not only establishing the synthetic jet flow, but also the interaction and evolution with an external cross-flow.

Not surprisingly the shape of the SJA orifice plays a critical role in formation and evolution of train of vortex rings. Pitched orifices have been specifically shown to produce vortex rings which have stronger circulation at the acute edge of the orifice than at the obtuse edge [2].

The interaction of a cross-flow with a synthetic jet issuing normal to the local surface can dramatically alter the vortex formation and distribution of circulation as well. Specifically, the vorticity generated on the upstream side of the orifice is of opposite sign of to the vorticity in the viscous boundary layer which results in the attenuation of the circulation along this edge. Simultaneously, the circulation along the downstream side of the orifice is strengthened by the cross-flow interaction, since the viscous boundary layer carries vorticity with the same sign.

Thus when an orifice is pitched in the downstream direction with respect to the cross-flow, the two modifying effects on the vortex circulation strength discussed above are in competition. On one hand, the interaction will cause vortex rings to form with lower circulation strength on the upstream side of the ring than on the downstream section, due to the rotational sign of the vorticity in the boundary layer. On the other hand, pitching the orifice downstream has the opposite effect, which is the enhancement of the circulation strength

[1] This work was supported by the National Science Foundation Graduate Research Fellowship Program under Grant No. (DGE 1144083).

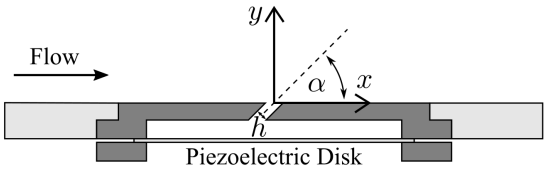

Figure 1: Side, cross-section view of SJA installed in boundary layer plate.

of the upstream or acute edge of the orifice. Therefore, a balance exists which is governed by the orifice pitch angle and the relative characteristics of the cross-flow (i.e., blowing ratio and boundary layer profile).

This means that wall attached vortices with different rotational sense can develop through the interaction of a synthetic jet with a cross-flow solely by altering the pitch angle of the the SJA orifice relative to the cross-flow direction. In this study the three-dimensional coherent vortex dynamics are experimentally investigated for two rectangular SJAs at pitch angles of $\alpha = 90^\circ$ and 45° as they interact with a canonical zero-pressure-gradient turbulent boundary layer.

2 Methods

The experiments were carried out within the low-speed wind tunnel at the University of Colorado Boulder. A boundary layer plate with a development length of 3.4 m was installed 0.31 m off of the test section floor and spanned the full width of the test section. The flow was tripped using a 0.0254 m wide strip of 36 grit distributed sand grain roughness installed 0.19 m downstream from the leading edge on the top surface of the boundary layer pate.

The SJA module was installed 1.62 m downstream from the leading edge of the boundary layer plate on the centerline of the plate in the transverse or z-direction. Figure 1 presents a simplified schematic of the SJA cavity and orifice orientation relative to the cross-flow. Numerous orifice configurations were evaluated as part of the experimental campaign, however the two primarily discussed here are rectangular orifices with an aspect ratio $AR = 18$ ($h = 0.001$ m) aligned with the minor axis parallel to the cross-flow direction ($\beta = 0^\circ$) at pitch angles of $\alpha = 90^\circ$ referred to as the "wall-normal orifice" and $\alpha = 45^\circ$ referred to as the "pitched orifice". For all experiments the volumetric flux out of the synthetic jets were matched by matching the mechanical stroke-length of the piezoelectric disk through ex-

perimental measurements of the disk displacement in time with a Polytec PDV 100 laser vibrometer. The average blowing velocity, U_o, was measured for the wall-normal orifice using a Dantec Dynamics miniature single-component hotwire probe with an A.A. Lab Systems AN-1003 constant-temperature anemometer system. Through matching the mechanical stroke length, the volumetric flux and thus average blowing velocity for the pitched orifice was assumed consistent with that of the wall-normal orifice. For the experiments discussed the blowing ratio was $C_b = U_o/U_e = 1$ where the boundary layer edge velocity was $U_e = 12$ m/s.

Volumetric reconstructions of the coherent vortical motions were carried out through the collection of three-component, two-dimensional velocity fields using a stereoscopic particle image velocimetry (SPIV) system from LaVision Inc. Twenty five SPIV measurement planes were collected across half of the orifice width ($0\ mm < z < 12\ mm$) at a spacing of $\Delta z = 0.5$ mm. The results were then mirrored to produce the full volume at four distinct phase angles in the synthetic jet actuation cycle: $\phi = 90°$, $180°$, $270°$, and $360°$. For each of these cases, 250 instantaneous phase-locked velocity fields were collected and ensemble averaged. For additional details related to the experiment and discussion of the results see Straccia and Farnsworth [3].

3 Results & Conclusions

The baseline (no actuation) flow conditions and boundary layer shape were characterized both using SPIV and hotwire anemometry at multiple locations within the synthetic jet turbulent boundary layer interaction region. For the cross flow speed of $U_e = 12$ m/s the boundary layer was found to exhibit the expected behavior for a canonical zero-pressure-gradient turbulent boundary layer [4]. More specifically, the boundary layer had a measured thickness of $\delta = 29.5$ mm and a measured shape factor of $H = 1.40$ at a friction velocity Reynolds number of $Re_\tau = 837$ (or a momentum thickness based Reynolds number of $Re_\theta = 1780$).

Evaluating the interaction of the wall-normal orifice SJA with the turbulent boundary layer cross-flow it is indeed found that circulation strength of the upstream side of the initial vortex ring is diminished while downstream side is strengthened. When the jet and free-stream velocities are matched, $C_b = 1$, the weak upstream side of the ring quickly decays, and the downstream flow field is dominated by a train of vortices which rotated clockwise in the spanwise direction as pictured in Figure 2. While the initial vortex structure is connected to the wall through legs which branched off from the primary vortex, downstream a new topology develops in the form of hairpin vortices which are connected to each other via their legs.

Pitching a spanwise-oriented orifice downstream has the opposite effect on the circulation strength of the vortex ring as the cross-flow did. Namely, the upstream side of the vortex ring becomes stronger and the downstream side weaker.

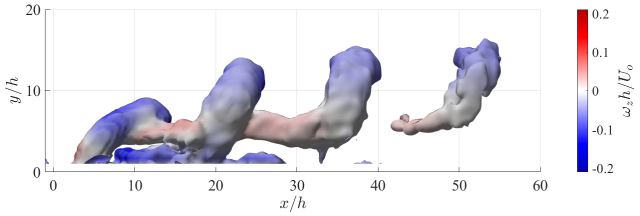

Figure 2: Isosurfaces of phased-locked $\lambda_{ci} = 0.25$ coloured by spanwise vorticity in the $\alpha = 90°$, $\beta = 0°$ jet at $\phi = 360°$ showing the train of hairpin vortices.

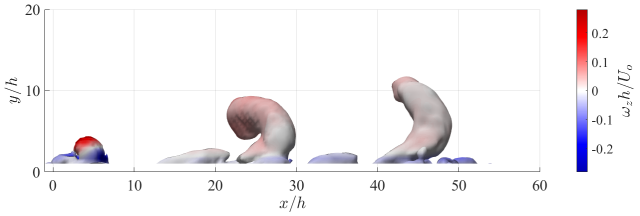

Figure 3: Isosurfaces of phased-locked $\lambda_{ci} = 0.3$ coloured by spanwise vorticity in the $\alpha = 45°$, $\beta = 0°$ jet at $\phi = 90°$ showing the train of arch-shaped vortices.

This results in the formation of a train of arch-shaped vortices with a counter-clockwise rotational sense (i.e. opposite to the sign of vorticity in the mean turbulent boundary layer) as pictured in Figure 3. In contrast with the hairpin vortices, the arch-shaped vortices remain connected to the wall as they advect downstream.

A clear difference in the advection speed between the trains of hairpin and arch-shaped vortices is visually apparent when directly comparing Figures 2 and 3. The coupling of the hairpin vortices with the image system below the surface slows their advection downstream, whereas the arch-shaped vortices are accelerated downstream by their interactions with the wall, increasing their spacing relative to the hairpin system. It is also worth noting that the wall-normal SJA induces mixing which transports low momentum fluid off of the wall depositing into a roughly circular wake higher up in the boundary layer. Off of the jet centerline though the vortical structures recirculate high momentum fluid towards the wall, accelerating the fluid there. Alternatively, the pitched SJA accelerates a thick layer of fluid near the wall through direct momentum injection by the train of arch-shaped vortices. Although a layer of fluid higher in the cross-flow was decelerated slightly by the pitched SJA, no localized wake is measured.

References

[1] Glezer, A. and Amitay, M. Synthetic Jets *Annual Review of Fluid Mechanics* 34, 503–529, 2002.

[2] Webster, D. and Longmire, E. Vortex rings from cylinders with inclined exits *Physics of Fluids* 10 (2), 400–416, 1998.

[3] Straccia, J. and Farnsworth, J. On the vortex dynamics of synthetic jet – turbulent boundary layer interactions *arXiv (physics.flu-dyn)*, 2022, https://arxiv.org/abs/2205.07370.

[4] Chauhan, K., Monkewitz, P., and Nagib, H. Criteria for assessing experiments in zero pressure gradient boundary layers *Fluid Dynamics Research* 41 (2), 021404, 2009.

Fluid-structure interaction between aerodynamic flows and phononic materials

Srikumar Balasubramanian[a], Arturo Machado Burgos[a], Sangwon Park[a],
Kathryn Matlack[a], and Andres Goza[a*]
[a]University of Illinois Urbana-Champaign, Aerospace Engineering, Urbana, IL, USA [1]
[*]Correspondence: *agoza@illinois.edu*

1 Introduction

Vortex dominated flows that involve fluid-structure interaction (FSI) between a compliant aerodynamic body and a surrounding flow provide both a hotbed of rich dynamics as well as a possible pathway for tuning the compliance of the structure to yield desirable changes to aerodynamic performance relative to a rigid aerodynamic body. We focus here on FSI dynamics involving a class of compliant structures referred to as *phononic materials*. These structures have a designed micro-structure which yields frequency dependent dynamics [1], making them natural candidates for passive, adaptive control of frequency-dominated flows. Indeed, studies have demonstrated a potential for phononic materials to modify the transition process of a wall-bounded flow [2, 3]. For the aerodynamic flows of interest here, phononic materials have been demonstrated to increase the mean lift on a flat plate (compared with a rigid plate) by as much as $\sim 25\%$ [4].

We use high-fidelity simulations to investigate the fluid-structure interactions involving an oncoming flow at a Reynolds number of $Re = 500$ and an aerodynamic body at a 15° angle of attack integrated with a phononic material. We consider two configurations: one where the body is a flat plate whose entire extent is comprised of a bi-layer phononic material, and the other where the body is an airfoil with a compliant section along the suction surface that is embedded with a phononic material subsurface. We describe the dimensionless parameters used to meaningfully traverse the parametric space, and indicate the nature of some of the results obtained for these configurations.

2 Results

We present in figure 1 a set of schematics for the two configurations considered. In the first configuration the entire plate is modeled as a bi-layer Euler Bernoulli beam, and in the second the phononic material is modeled as a diatomic spring-mass chain within the subsurface of a compliant portion of the airfoil.

The governing dimensionless parameters used to describe

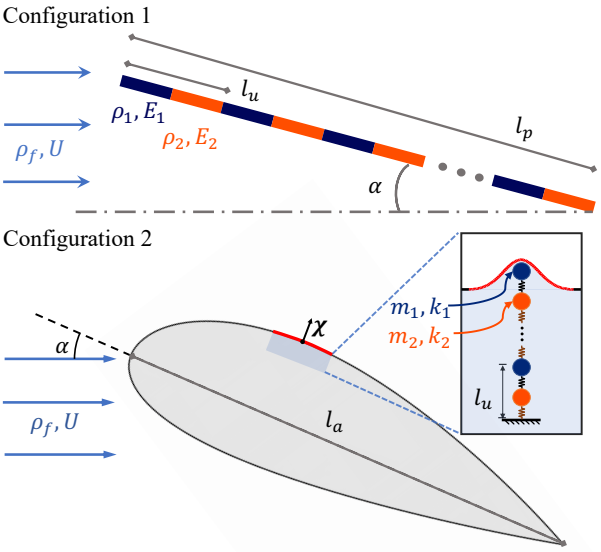

Figure 1: Schematics of the two phononic material configurations considered in this work.

the system, apart from the Reynolds number and angle of attack, are M, K, $k_r = \frac{k_1}{k_2}$, $m_r = \frac{m_1}{m_2}$, $l = \frac{l_u}{l_b}$. Here k_r and m_r are the corresponding stiffness and mass ratios between the 2 rods of a unit cell, where k_j, $j = 1,2$ is $E_j I$, $j = 1,2$ for the beam configuration and is the stiffness value associated with spring j, $j = 1,2$ in the second configuration. Similarly, m_j, $j = 1,2$ is $\rho_j h$, $j = 1,2$ where h is the beam thickness for the beam configuration and is the mass value associated with spring j, $j = 1,2$ in the second configuration. The ratio $\frac{l_u}{l_b}$ is the ratio between a single unit cell and the characteristic body length ($l_b = l_p$ for the flat plate, and $l_b = l_a$ for the airfoil). M, K are the *equivalent uniform-property* structure-to-fluid mass ratio and stiffness ratio, respectively, of the phononic material. The computation of these parameters is described in more detail in Balasubramanian et al. [4], and involves first identifying the ratio M/K of a uniform structure that has the same leading natural frequency as that of the phononic structure, then using a load test to unpack M and K separately by matching the amplitude of the response between the phononic and effective uniform structure. We demonstrated in Balasubramanian et al. [4] that for a fixed M, K, the global structural dynamics (encoded in the dis-

[1]This work was supported by AFOSR under grant number FA9550-21-1-0182.

persion behavior) are largely unchanged despite changes by orders of magnitude in the phononic material parameters, k_r, m_r, and l_u encode material nonuniformity. These parameters thus provide a means by which to systematically study the fluid-structure interplay: M and K may be chosen to align representative structural frequencies relative to the frequency of the underlying vortex shedding process in the reference (rigid body) case. For fixed values of these parameters, m_r, k_r, and l_u may be varied to assess how phononic behaviors such as band gaps alter the dynamics relative to the uniform material case.

To illustrate the nature of the FSI behavior, we show in figure 2 features of the dynamics for the flat plate configuration that arise from selecting M and K so that the second structural natural frequency is near the reference vortex shedding frequency of the baseline rigid case. The lift history (a) demonstrates a beating phenomenon (red curve, c.f., the rigid body dynamics in black), and the associated spectral density plot (b) demonstrates that this behavior is largely driven by dynamics at the vortex shedding frequency and its harmonic. A snapshot of the vorticity (c) hints at a possible reason for the appearance of the harmonic: the higher wavenumber deformation produces new vortex structures at higher spatial frequency than the reference case. The figure also demonstrates that this behavior of two dominant frequencies occurring at the shedding frequency and its harmonic were seen for all phononic material configurations considered (d).

3 Conclusion

We computed the fluid-structure interaction between an aerodynamic body equipped with a phononic material at a 15° angle of attack and an oncoming flow at a Reynolds number of $Re = 500$. We characterized the FSI dynamics by writing the governing dimensionless parameters in terms of an effective mass and stiffness of an analogous uniform structure along with stiffness and mass ratios that convey the departure from material uniformity. For illustration, we also provided a brief description of one of the behavioral regimes found for the flat plate configuration, where the effective uniform properties are chosen so that the second structural natural frequency aligns with (or is near) the vortex shedding frequency associated with the rigid flat plate. In this regime, the dynamics exhibit a beating behavior reflective of dominant FSI at the baseline shedding frequency and a signature at the harmonic frequency that arises from the higher mode spatial shape of the structural deformations. More details on many of these results can be found in found in Balasubramanian et al. [4]. We have also submitted an AIAA Aviation abstract and have two articles in preparation on these topics. The DisCoVor presentation will be a synthesis of these related efforts.

References

[1] M. I. Hussein, M. J. Leamy, and M. Ruzzene. "Dynamics of Phononic Materials and Structures: Historical Origins, Recent Progress, and Future Outlook". In: *Applied Mechanics Reviews* 66.4 (May 2014).

[2] M. I. Hussein, S. Biringen, O. R. Bilal, and A. Kucala. "Flow stabilization by subsurface phonons". In: *Proceedings of the Royal Society A: Mathematical, Physical and Engineering Sciences* 471.2177 (2015), p. 20140928. DOI: 10.1098/rspa.2014.0928.

[3] C. J. Barnes, C. L. Willey, K. Rosenberg, A. Medina, and A. T. Juhl. "Initial computational investigation toward passive transition delay using a phononic subsurface". In: *AIAA Scitech*. 2021.

[4] S. Balasubramanian, S. Park, K. Matlack, and A. Goza. "Harnessing Phononic Materials for Aerodynamic Flow Control". In: *AIAA Aviation*. 2022.

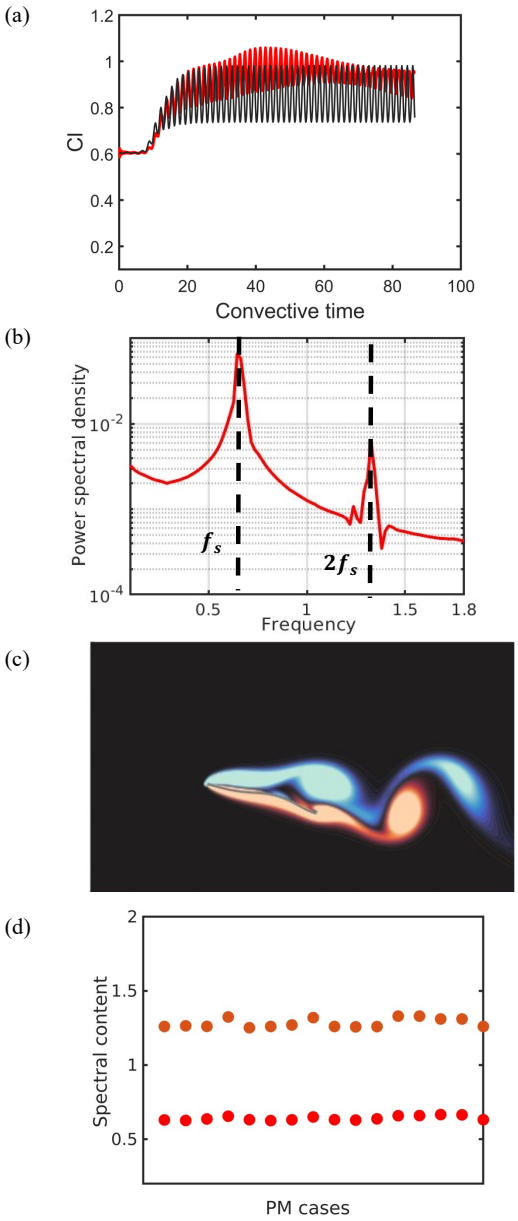

Figure 2: FSI dynamics for the flat plate configuration, with M and K chosen so the second structural natural frequency is near the baseline vortex shedding frequency.

Energy Extraction Potential in a Dual Oscillating-Foil System

Bernardo Luiz R. Ribeiro* and Jennifer A. Franck
University of Wisconsin—Madison, Department of Mechanical Engineering, Madison, WI, USA [1]
*Correspondence: *rocharibeiro@wisc.edu*

1 Introduction

This research investigates the energy extraction potential between oscillating foils based on the leading foil kinematics and the wake of a two-tandem foil array. Although commonly used in propulsive applications, oscillating foils can also extract energy from flow by tuning kinematic parameters, namely oscillating frequency, heave and pitch amplitude [1]. Unlike a traditional horizontal-axis turbine, the wake produced by an oscillating foil contains a nearly two-dimensional structured pattern of shed vortices that is directly correlated with the foil kinematics. In a two-turbine array, energy extraction potential differs between leading and trailing devices due to the reduced velocity downstream of the leading turbine. To design the control laws for foil-array performance optimization, it is important to quantify the impact of the wake and the oncoming unsteady vortices on the performance of a trailing foil as a function of flow conditions and foil kinematics.

When two foils are placed in a tandem array configuration and the same flapping kinematics for both foils are considered, two parameters dictate the parameter space, namely the inter-foil phase and the inter-foil spacing. Numerical and experimental work show that these two parameters can affect array performance due to the different wake-foil interactions [2,3]. To establish a relationship between the trailing foil motion and the wake from the leading foil, Kinsey and Dumas [3] defined a global phase parameter where it is assumed the wake is convecting with the freestream velocity. By quantifying the mean wake velocity from various leading foil kinematics, Ribeiro et al. [2] updated this definition as a wake phase parameter.

In a two-turbine array, the interaction between the unsteady wake vortices and trailing foil can increase or decrease the energy extraction potential depending on the timing of the vortex-foil interaction [4]. The proposed analysis decomposes the wake into a mean velocity field and an unsteady component to evaluate the energy extraction potential of the trailing foil compared to the leading foil. The resulting analysis of correlating the energy available between foils with the wake provides input to predictive wake-foil interaction models for energy harvesting.

[1]This work was supported by the National Science Foundation under Grant No. 1921594

2 Methods

This research is performed through numerical simulations of two-turbine arrays that computationally solve the incompressible Navier-Stokes equations at Reynolds number 1000 using OpenFOAM.

The two-foil array schematic in Figure 1 highlights the foil kinematics, the inter-foil spacing, S_x and swept area, Y_p. Since the oncoming flow velocity is different for foil 1 (leading foil) and foil 2 (trailing foil) due to the wake deficit, a mean wake velocity, $\overline{u}_w$, is defined [2] using the streamwise wake deficit at $x/c = 1$, depicted by a dashed line in Figure 1.

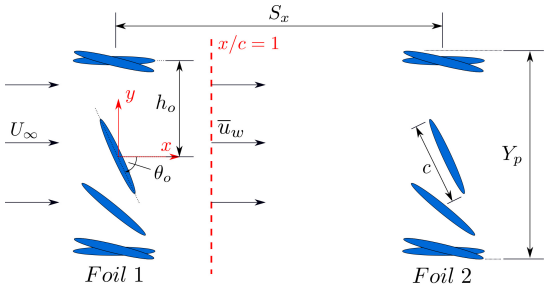

Figure 1: Two-tandem foil array schematic highlighting foil kinematics, inter-foil spacing and swept area.

A total of 16 unique sets of kinematics are prescribed to an elliptical foil. A sinusoidal foil motion in pitch and heave is utilized. Each kinematics is explored at 12 inter-foil phases sampled in increments of 30° from 0° to 330°, resulting in 192 simulations.

To evaluate foil performance, the total power generated, $P(t)$, is divided by the power available in the oncoming *mean* flow normalized by foil chord length. For foil 1, this quantity is $\frac{1}{2}\rho U_\infty^3 c$. For foil 2, rather than U_∞, the mean wake velocity is utilized ($\frac{1}{2}\rho \overline{u}_w^3 c$), resulting in the following definitions for the lead foil and trailing foil,

$$C_p(t) = \frac{P_1(t)}{\frac{1}{2}\rho U_\infty^3 c}, \qquad C_p'(\Phi,t) = \frac{P_2(\Phi,t)}{\frac{1}{2}\rho \overline{u}_w^3 c}, \tag{1}$$

where Φ is the wake phase which determines the timing of the second foil with respect to the spacing S_x, $\overline{u}_w$, and inter-foil phase.

Normalizing power by incorporating mean wake velocity enables a more direct comparison between the energy extracted by foil 1 and foil 2. This comparison can be quantified by the difference in performance between foils, defined as $\Delta C_p(\Phi,t)$. The difference between the two power profiles represents the effect on the trailing foil performance due to the unsteadiness within the wake between the two foils. Due to the timing of the unsteady wake-foil interactions, ΔC_p is strongly dependent on Φ, and can also be analyzed throughout the cycle as a function of non-dimensional time, t/T, where T stands for the cycle period.

3 Results

Depending on the foil kinematics and wake phase, the instantaneous power generated from the trailing foil can be higher or lower than the leading foil as illustrated by Figure 2.

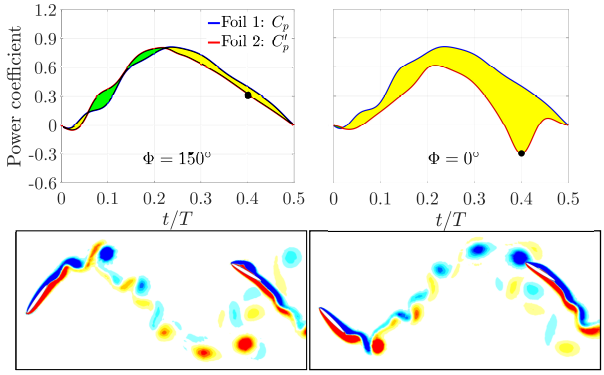

Figure 2: Power coefficient C_p and C_p' for the foil kinematics $fc/U_\infty = 0.12; h_o = 1.00; \theta_o = 55°$ at wake phases $\Phi = 150°$ and $\Phi = 0°$. The instantaneous vorticity fields at the times represented by the black circles are shown at the bottom row.

The colored region corresponds to the power difference between foils, $\Delta C_p(\Phi,t)$, where yellow and green represent the instances when the trailing foil's performance is lower and higher than the leading foil, respectively. For the kinematics $fc/U_\infty = 0.12; h_o = 1.00; \theta_o = 55°$ and $\Phi = 0°$, the trailing foil is performing worse than the leading foil throughout the cycle. The largest power difference is observed at $t/T = 0.40$, which corresponds to a destructive wake-foil interaction as illustrated by the instantaneous vorticity field. At $\Phi = 0°$, the trailing foil is oscillating in-sync with the wake from the leading foil and thus is continuously interacting destructively with the wake vortices, justifying the trailing foil's lower performance. In contrast, when the trailing foil is out-of-sync with the wake, which is represented by a wake phase close to 180°, its performance can follow the leading foil's performance throughout time since it is avoiding vortex-foil interactions. This is illustrated by the power curves and vorticity field at $\Phi = 150°$.

At higher pitch amplitudes, the unsteady vortices are stronger and the trailing foil's performance dependency with the wake phase is stronger. This is demonstrated in Figure 3.

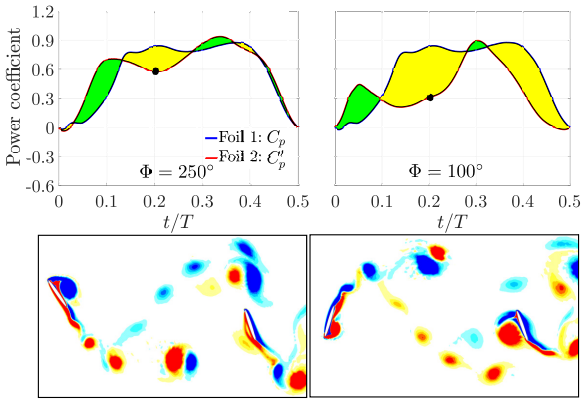

Figure 3: Power coefficient C_p and C_p' and instantaneous vorticity fields for the foil kinematics $fc/U_\infty = 0.12; h_o = 1.00; \theta_o = 75°$ at wake phases $\Phi = 250°$ and $\Phi = 100°$.

At both wake phases $\Phi = 250°$ and $\Phi = 100°$, the trailing foil power curves have a larger variation throughout time compared with those in Figure 2. This is due to stronger wake vortices interacting with the trailing foil which can significantly impact the vortex formation as shown by the vorticity fields. At the selected time $t/T = 0.20$, the vortex-foil interaction at $\Phi = 100°$ is enough to double the power discrepancy observed at $\Phi = 250°$. For kinematics with high pitch amplitude, the green regions indicating constructive wake-foil interactions are more significant than lower pitch amplitudes which demonstrates the feasibility of improving the energy extraction potential with the proposed power analysis.

4 Future Work

The energy extraction in a two-foil system is decomposed into mean and unsteady components to quantify the energy extraction potential between oscillating foils. This work is a step towards a predictive model to quantify the impact of the wake on trailing foil performance.

References

[1] Young, J., et al. A review of progress and challenges in flapping foil power generation. *Progress in Aerospace Sciences*, 67:2–28, 2014.

[2] Ribeiro, B. L. R., et al. Wake-foil Interactions and Energy Harvesting Efficiency in Tandem Oscillating Foils. *Physics Review Fluids*, 6(7):074703, 2021.

[3] Kinsey, T. and Dumas, G. Optimal tandem configuration for oscillating-foils hydrokinetic turbine. *Journal of Fluids Engineering*, 134(3):031103, 2012.

[4] Xiao, Q. and Zhu, Q. A review on flow energy harvesters based on flapping foils. *Journal of Fluids and Structures*, 46:174–191, 2014.

Cycle-to-cycle variations in cross-flow turbine performance and flow fields

Abigale Snortland [a*], Isabel Scherl[b], Brian Polagye[a] and Owen Williams[b]
[a] University of Washington, Mechanical Engineering, Seattle WA, USA[1]
[b] University of Washington, Aeronautics and Astronautics, Seattle WA, USA
[*]Correspondence: *abigales@uw.edu*

1 Introduction

Cross-flow turbines are able to harness the kinetic energy in wind, tidal currents, and rivers. Relative to axial-flow turbines, cross-flow turbines, referred to a "vertical-axis" turbines in the wind sector, operate at lower rotation rates, are insensitive to inflow direction, and may be able to achieve higher power output per unit area within an array [1]. However, because cross-flow turbines rotate perpendicular to the inflow, the blades encounter a continually fluctuating angle of attack and relative inflow velocity that can lead to the unsteady, non-linear phenomenon of dynamic stall [2, 3]. For cross-flow turbines, dynamic stall severity depends on the ratio of the blade tangential velocity to the inflow velocity – the dimensionless "tip-speed ratio". While cross-flow turbine hydrodynamics and performance are functions of both the blade azimuthal position and the tip-speed ratio, cycle-to-cycle variability is also observed. This variability is often implicitly neglected through time- and phase-averaging, but could arise from a variety of mechanisms – inflow fluctuations, the stochastic nature of dynamic stall, and cycle-to-cycle hysteresis. An in-depth cycle-to-cycle variation analysis has not yet been applied to cross-flow turbines. Our objective is to quantify the extent of cycle-to-cycle variation in cross-flow turbine performance and flow fields, its sources, and the relationships between performance and flow field variability. To do so, we have developed an unsupervised clustering/PCA pipeline that identifies physically meaningful flow field clusters with differing dynamics relevant to the dynamic stall process. We are also able to correlate these flow field clusters with performance and investigate the different sources of variability.

2 Methods

To contextualize experimental flow fields and performance, it is instructive to begin with a discussion of the kinematics and dynamic stall theory relevant to the hydrodynamics of cross-flow turbines. Two key factors which govern the near-blade hydrodynamics are the angle of attack, α and the blade-relative incident velocity, U_{rel}. Both depend on the blade azimuthal position, θ, and are functions of the non-dimenstional tip-speed ratio, $\lambda = r\omega/U_\infty$, where r is the turbine radius, ω is the rotation rate, and U_∞ is the freestream velocity. As such the phase, duration, and severity of dynamic stall are influenced by λ. A decrease in λ reduces $||U_{rel}||$ and increases the range of α across θ, which causes earlier vortex shedding, increased stall severity, and delayed flow recovery. Severe, or "deep" dynamic stall cases (low λ, large α ranges), are characterized by the formation of an energetic dynamic stall vortex that is on the order of the blade thickness. In contrast, any vortex growth in "light" dynamic stall cases (high λ, small α ranges) is prematurely terminated [4].

Experiments were performed in the Alice C. Tyler Flume at the University of Washington for a deep dynamic stall case, $\lambda = 1.5$. Two-dimensional, phase-locked particle image velocimetry flow fields, obtained inside the turbine swept area, are examined in concert with simultaneously-captured turbine performance measurements. A schematic of the performance measurement setup is shown in Figure 1a. Because turbine torque is measured at the center shaft, a one-bladed turbine is necessary to directly tie performance variations to the near-blade flow fields (i.e., with a multi-bladed turbine, the torque contribution from each blade is ambiguous). In these experiments, we hold ω constant. The hydrodynamic power produced by the turbine, P, is the product of the hydrodynamic torque and ω. This is non-dimensionalized as the coefficient of performance $\eta = \frac{P}{\rho U_\infty^3 L r}$ where ρ is fluid density and L is the blade span. The freestream velocity is measured upstream of the turbine with an acoustic Doppler velocimeter.

Before clustering, the flow field data were translated from the flume reference frame to that of the blade. These relative velocity fields, $\vec{\Phi}$, were then fed into a principle component analysis (PCA) preprocessor. The PCA preprocessor allowed for clustering based on all the dynamics present in the high-dimensional flow field data set, in an interpretable, low-dimensional subspace that is weighted by by contribution to overall velocity variance. The output was then fed into a hierarchical clustering algorithm that produced two clusters from 139 cycles in the data set. Each cycle is assigned to a cluster, which allows us to conditionally average the flow fields, as well as correlate clusters with cycle-specific inflow velocities and performance measurements.

[1]This work was supported by NAVFAC, NSF GRFP

3 Results

Figure 1 highlights flow field dependence on cluster assignment. The conditionally-averaged difference fields (b. and c.) highlight the deviation between the cluster conditionally-averaged fields (phase-average of all cycles in a specific cluster) and the phase-average of all the cycles (d.). These fields reveal opposing behaviors between the clusters (i.e., regions of lower-than-average velocities in one cluster are coincident with regions of higher-than-average velocities in the other and vice versa). This highlights distinctly different hydrodynamics between the flow field clusters, and indicates variations in timing and strength of the dynamic stall vortex. Specifically, cycles assigned to cluster 1 experience earlier shedding of a potentially stronger dynamic stall vortex.

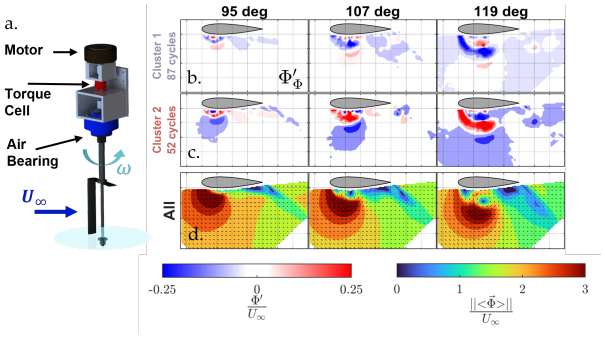

Figure 1: (a) schematic of the cross-flow turbine experimental setup, (b-c) cluster conditional difference fields, Φ', and (d) phase-averages, $||<\vec{\Phi}>||$, for selected θ. The grid spacing in (b-d) is $c/4$.

Hysteresis and dynamic stall stochasticity may contribute to variability, but freestream velocity perturbations are the most explanatory of the observed cycle-to-cycle variation in both the flow fields and performance. While we cannot completely disentangle the impacts of freestream velocity perturbations and dynamic stall stochasticity on the flow fields, the cycle-averaged freestream velocities are correlated with the flow field clusters, as shown in Figure 2a. Cycle-to-cycle variation in the rotation rate is negligible, so any perturbations in the freestream result in cycle-specific tip-speed ratios that differ from the average. Cluster 1 has higher inflows on average. As a result, the blade is effectively operating at a lower tip-speed ratio while also encountering more kinetic energy in the flow. As shown in Figure 2b-c, cluster 1 has a higher magnitude performance peak which occurs earlier in the cycle and a higher time-average, $\bar{\eta}$, relative to cluster 2. The earlier performance peak and the earlier and/or stronger stall for cluster 1 is consistent with the locally lower λ operation, but the higher performance observed is inconsistent with the known trend of lower λ correlating with lower peak and time-averaged performance. This contradiction arises because the velocity scale used to calculate non-dimensional performance (the mean of the cubes of all the velocities measured) does not account for differences in the inflow kinetic energy for the clusters. For cluster 1, this unaccounted for increase in inflow kinetic energy obscures the detrimental impacts expected for a lower cycle-specific tip-speed ratio.

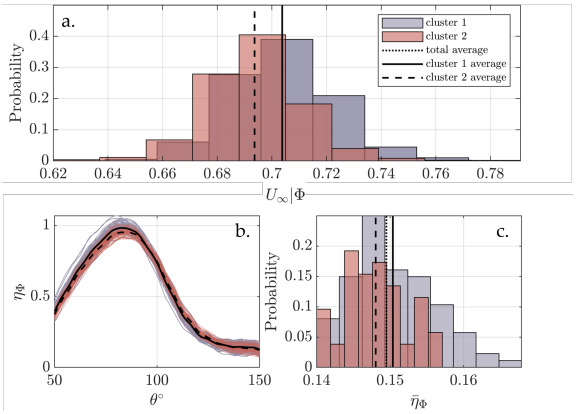

Figure 2: (a) Histogram of cycle-averaged freestream velocities conditional on flow field cluster, written as: $U_\infty|\Phi$. (b) Individual coefficient of performance trajectories at the peak conditional by cluster, written as: η_Φ. (c) Histograms of time-averaged coefficient of performance conditional on cluster, written as: $\bar{\eta}_\Phi$.

4 Conclusion

In this work, the extent and a source of cycle-to-cycle variability are explored experimentally using near-blade flow fields and performance metrics for a deep dynamic stall case, $\lambda = 1.5$. The flow field clustering technique developed for this purpose identifies cycle-to-cycle variations and highlights correlations between performance and flow field variability. We observe physically meaningful clusters representing a series of distinct flow field evolutions. These clusters reveal variations in timing and strength of the dynamic stall process, and are correlated with performance. Specifically, we show that the severity of dynamic stall, at a prescribed rotation rate, is correlated with perturbations in the inflow velocity, which also explains an apparent contradiction between cycle-to-cycle performance variations and global performance trends with tip-speed ratio. Overall, the flow field clustering technique contributes to our understanding of the sources of performance and flow field variability of cross-flow turbines, as well as providing a comprehensive picture of the phase-varying hydrodynamics.

References

[1] John Dabiri Simulations of Intracycle Angular Velocity Control for a Crossflow Turbine. *Journal of Renewable and Sustainable Energy*, 3(4):1–12, 2011.

[2] Mukul Dave et al. Simulations of Intracycle Angular Velocity Control for a Crossflow Turbine. *AIAA Journal*, 59(3):812–824, 2021.

[3] Sébastien Le Fouest and Karen Mulleners The dynamic stall dilemma for vertical-axis wind turbines, *Renewable Energy*, 198:505–520, 2022.

[4] Karen Mulleners and Markus Raffel The onset of dynamic stall revisited, *Experiments in Fluids*, 52:779–793, 2012.

Flow-energy harvesting by two fully passive flapping foils in tandem

Fuwang Zhao[#], Qian Jiang[#], Hui Tang[*]
Department of Mechanical Engineering, The Hong Kong Polytechnic University, Kowloon, Hong Kong[1]
[#]These authors contributed equally to this work; [*]Correspondence: *h.tang@polyu.edu.hk*

1 Introduction

Flapping foil-based energy harvesters are a type of unconventional concepts for air/water flow-energy harvesting. Compared to conventional rotary turbines, they have many advantages, such as having low cut-in speeds, better filling factor, scalable, operable in shallow water and environmentally friendly. From the practical perspective, this type of harvesters is usually arranged in arrays, so as to make the best from the flow at selected sites as well as to save the operation and maintenance costs. As the simplest configuration of harvester arrays, two-foil systems, especially arranged in tandem, are usually chosen to study the detailed foil-foil or wake-foil interactions and their influence on resulting energy harvesting.

Here we studied the interaction of two fully passive flapping foils arranged in tandem. Initially proposed by Platzer et al. (2009), each of the foil is able to do 2 degrees-of-freedom (DOFs) flapping motions in a uniform water flow by utilizing a group of heaving and pitching limiters to achieve continuous flapping motions. If two such foils are arranged in tandem, the total 4 DOFs in the system could generate very rich dynamics that makes impacts on the resulting energy harvesting performance, which motives the present study.

Both experimental and computational investigations were conducted. The experimental work was conducted in a water channel. The test rig is schematically shown in Fig. 1. Each foil system is equipped with a flat foil of chord $c = 140$ mm, span 200 mm, and mass 0.25 kg, which is mounted underneath a heaving platform through a long shaft located at $0.6c$ from the foil's leading edge (see Fig. 1(a)). Driven by a water flow of speed $U_\infty = 0.62$ m/s (corresponding to a chord-based Reynolds number 8.7×10^4), the foil can undergo both heaving and pitching motions. The ranges of these two motions can be pre-set by adjusting the heaving and pitching limiters, as depicted in Fig 1(b). CFD simulations were also concurrently conducted using ANSYS Fluent to provide complementing data.

2 Results

The dynamics and energy harvesting performance of a single-foil system has been systematically studied in our previous works (Mumtaz Qadri et al. 2020; Zhao et al. 2021). When two foils are placed in tandem, their initial states including the position and orientation may influence the dynamics of both foils. To study this influence, these two foils were separated by a distance of $L = 2c$ and simultaneously released with eight different initial states. It was found that, regardless the initial state, the two foils can always reach the same final state: nearly anti-phase motions, i.e., the phase shift $\phi \approx \pi$. This independence on the initial states was also confirmed at other tandem distances. It was further found that, independent of the initial state, the final phase difference ϕ between the tandem foils varies almost linearly with the distance L, as revealed by the data presented in Fig. 2. This implicates that the aft foil can be "captured" by the wake of the fore foil, leading to a phase difference ϕ that is independent of the initial phases.

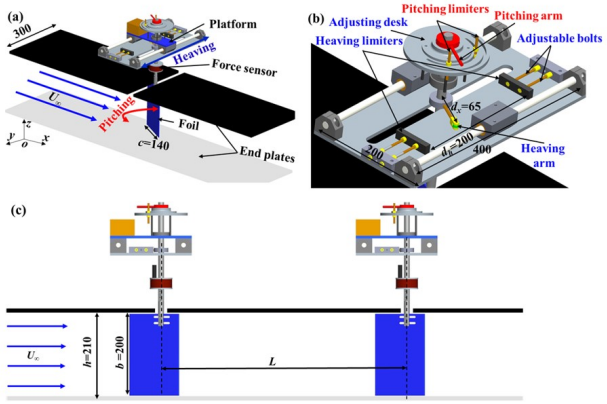

Figure 1: Schematics of the water-channel test rig for fully passive flapping foils arranged in tandem.

The wake capture is evidenced by the y-velocity contours during the aft foil's upstroke shown in Fig. 3. In the $L = 2c$ case, it is seen from Figs. 3(c2) to (c4) that a leading-edge vortex (LEV) shed from the fore foil convects towards the aft foil when the latter heaves up to cross the channel's centerline with its maximum allowed pitching angle. This convecting LEV induces a stronger upward flow just upstream of the aft foil, pushing the aft foil in its heaving direction. The same is also observed in the $L = 4c$ case, as evidenced in Figs. 3(d2) to (d4). These observations reveal that the kinematics of the aft foil is modulated and eventually locked up by the LEV generated by the fore foil. As such, the phase

[1]This work was supported by Natural Science Foundation of Guangdong Province (Project No. 2021A1515010337) and partially supported by Natural Science Foundation of China (Project No. 91952107)

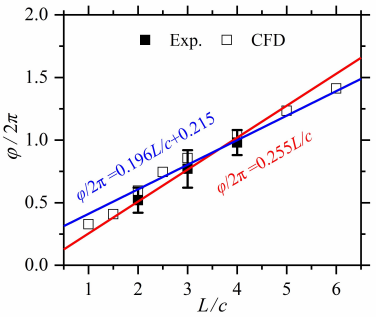

Figure 2: Variation of the steady-state phase difference between the two foils against the tandem distance.

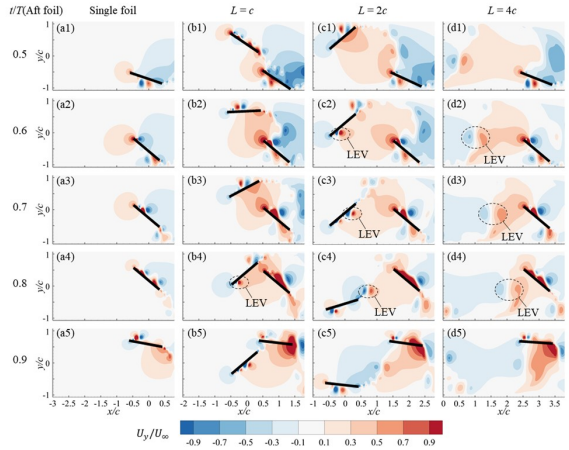

Figure 3: Evolution of flow fields near the flapping foils.

of the aft foil at the steady state is independent of its initial state. Instead, it is mainly related to the tandem distance L, through which the fore foil's LEV propagates.

Due to the extremely short tandem distance, the $L = c$ case (Fig. 3(b)) shows different wake-foil interaction from the other two cases. In this case, in addition to the LEV generated from the fore foil, a high-momentum flow "ejected" from the fore foil through its fast anti-clockwise rotation also contributes to the lock-up of the aft foil.

As the tandem distance is relatively small, i.e., $L < 3c$, the fore foil's dynamics can be affected by the aft foil. This interaction affects not only the dynamics but also the power extraction performance of both foils. Fig. 4 shows the overall power coefficients. It reveals that the fore foil is able to extract the maximum mean heaving power of $\overline{C}_{ph} = 0.223$ when the two foils are closest, i.e., $L = c$. $\overline{C}_{ph}$ quickly reduces with the tandem distance, reaching its minimum value 0.177 at $L = 2c$. As for the mean pitching power $\overline{C}_{p\theta}$, it monotonically increases with the tandem distance from its minimum value 0.022 at $L = c$ and gradually approaches to the value of the single foil. Since the variation in $\overline{C}_{ph}$ is larger than that in $\overline{C}_{p\theta}$, their summation, the mean total power $\overline{C}_p$, shows a similar variation trend with $\overline{C}_{ph}$.

Influenced by the fore foil's wake, the aft foil is able to extract in average 10.4% more heaving power $\overline{C}_{ph}$ than the single foil. This wake-foil interaction benefit could be more significant for the pitching power. With the smallest tandem distance, i.e., $L = c$, the aft foil can extract about twice the pitching power $\overline{C}_{p\theta}$ of the single foil. When the two foils are sufficiently far from each other, i.e., $L > 3c$, the aft foil's pitching power extraction achieves a stable performance, which is about 20% more than the single foil. As such, the mean total power $\overline{C}_p$ for the aft foil is in average about 15.2% larger than the single foil and the fore foil, showing a similar variation trend as $\overline{C}_{p\theta}$.

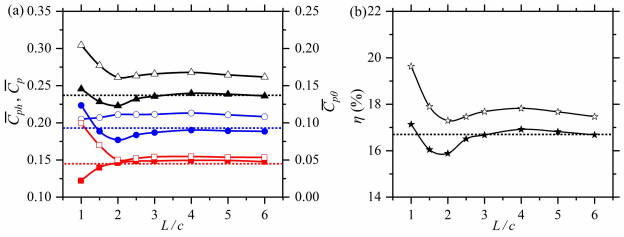

Figure 4: Power extraction performance of the two-foil system at different tandem distances.

The power conversion efficiency for both foils, η, follows similar trends of the respective $\overline{C}_p$, as shown in Fig. 4(b). The maximum efficiency 19.6% is achieved by the aft foil at $L = c$, whereas the minimum efficiency 15.9% is achieved by the fore foil at $L = 2c$. By adding the efficiencies of both foils, the total efficiency is in average 1% higher than twice the single foil's efficiency. The maximum total efficiency of 36.8% is achieved at $L = c$, the shortest tandem distance the two foils can be arranged.

3 Conclusion

We investigated the dynamics and energy harvesting performance of two fully passive flapping foil arranged in tandem. It was found that through the wake-foil interaction, the aft foil can be modulated and locked by the LEV generated by the flapping fore foil. The two foils can influence each other when $L < 3c$. The two foils can collectively achieve the best efficiency of 36.8% at $L = c$, more than the doubled value (33.4%) of the single foil's efficiency. More detailed results will be presented in the talk.

References

[1] Platzer M, Ashraf MA, Young J, et al. Development of a new oscillating-wing wind and hydropower generator. 47th AIAA Aerospace Sciences Meeting including the New Horizons Forum and Aerospace Exposition. AIAA 2009-1211, 2009.

[2] Qadri MNM, Zhao F, Tang H. Fluid-structure interaction of a fully passive flapping foil for flow energy extraction. *International Journal of Mechanical Sciences*, 177: 105587, 2020.

[3] Zhao F, Qadri MNM, Wang Z, et al. Flow-energy harvesting using a fully passive flapping foil: A guideline on design and operation. *International Journal of Mechanical Sciences*, 197: 106323, 2021.

3 Session C: Bio-Flight

Passive pitching and aperiodicity in the wake of flapping flights

Dipanjan Majumdar[a], Sridhar Ravi[b] and Sunetra Sarkar[a*]
[a] Indian Institute of Technology Madras, Department of Aerospace Engineering, Chennai, India
[b] University of New South Wales, School of Engineering and Information Technology, Canberra, Australia
*Correspondence: *sunetra.sarkar@gmail.com*

1 Introduction

Several experimental and numerical studies [1–8] with canonical models of flapping have overwhelmingly reported chaotic transitions at high dynamic plunge velocities ($\kappa h > 1.9$). In this parametric regime, despite the harmonic motion of the flapping foil, lift and thrust become aperiodic or fully chaotic. Aero(hydro)dynamic load generation in such regimes is inherently dictated by strong flow-separation and unsteady vortices' interactions in the near-field. It must however be noted that most previous studies considered fully actuated rigid flapping wing systems. Aperiodic flow is not desirable for flight platforms as this leads to unpredictability in the long-term behaviour of the fluid forces [5–7]. Furthermore, it is also not expected in natural and artificial flapping-wing flyers to exhibit chaos or aperiodicity, despite the observations made in the literature with canonical flapping models. The important question here is, what possible mechanisms could be responsible to prevent transition to aperiodicity/chaos in biological or bio-inspired flights, while such transitions seem unavoidable due to the complex interactions of the flow-field vortices [5–8] at certain parametric regimes. The current study will show that one of the likely mechanisms comes from the favourable effects of the passive movements of wings/fins. Passive dynamics was reported to play an important role in tuning the oscillation profile as well modifying/regularizing the flow-field/loads in earlier studies [9–11], though its role in inhibiting aperiodicity/chaos was not investigated. The two-way fluid-structure interaction effects associated with passive oscillations could be potentially instrumental is altering the leading-edge vortex (LEV) separation behaviour, which is one of the main agencies of aperiodicity, and thus possibly modify the dynamical transitions significantly to ensure a more regular flow-field.

2 Results

We considered a pitching-plunging flapping foil to investigate the effects of passive pitching on the fluid forces and dynamical states. Numerical simulations were performed using an in-house flow solver [6] considering an actively plunging-passively pitching (AP-PP) case. The results of the AP-PP foil were then compared with those of an actively plunging-actively pitching (AP-AP) foil, *i.e.* a fully actuated case. For the AP-PP foil, a harmonic plunging actuation was provided at the leading-edge, and along with that, the foil was allowed to freely oscillate in the pitch degree-of-freedom with the leading-edge being the pivot point. In the case of fully active situation, the foil was made to follow a set of pre-defined harmonic kinematics in both plunge and pitch directions. The amplitude, frequency and phase-offset of the active pitching was taken from the outcome of the AP-PP simulations. This equivalence was maintained to enable a suitable comparison between the AP-PP and AP-AP cases.

In comparison to the fully actuated foil, aperiodic transition was absent even at high κh when passive oscillations were allowed. Aerodynamic loads for the passive configuration exhibited perfect periodic signature (perfect close-loop orbits in $C_L - C_D$ phase portrait) across the tested range of κh (figures 1a-c). In comparison, a 'quasi-periodic like' toroidal band was seen at $\kappa h = 3.0$ (figure 1f) for the equivalent fully active case, signifying the lack of periodicity for AP-AP. In contrary to earlier literature [5–8] which reported the aperiodic transition to occur for $\kappa h > 1.5$, the present results with passive pitching revealed an absence of such transition even at significantly high κh of 3.0.

As reported in the earlier literature [5–8], aperiodic growth of strong LEVs and the subsequent vortex interactions are responsible for triggering aperiodicity/chaos in the flow-field. Present study revealed that these flow features were either absent or very weak/attached to the body for the AP-PP foil (figures 1a-c). Although weak LEVs were seen at high $\kappa h = 3.0$ (figure 1c), they remained attached to the body and could not undergo any interactions with the trailing-edge vortices (TEV). Hence, there were no obvious aperiodic agencies (such as aperiodic growth of LEVs and LEV-TEV interactions) present in the flow-field. Although the flow-field of the AP-PP and AP-AP cases looked very similar for $\kappa h = 1.0$ and 2.0 (figure 1), noticeable differences were seen for $\kappa h = 3.0$ (see figures 1c and 1f)). The primary LEV for the AP-AP foil was stronger (the circulation values should be noted in the figure), which approached the regime of aperiodicity [8]. These observations indicated that the delay/inhibition of aperiodic transition could be attributed to the absence of separation of strong LEVs in AP-PP foil.

3 Discussion

Aperiodic transition in the flow-field has been found to be significantly delayed/inhibited due to passive dynamics even

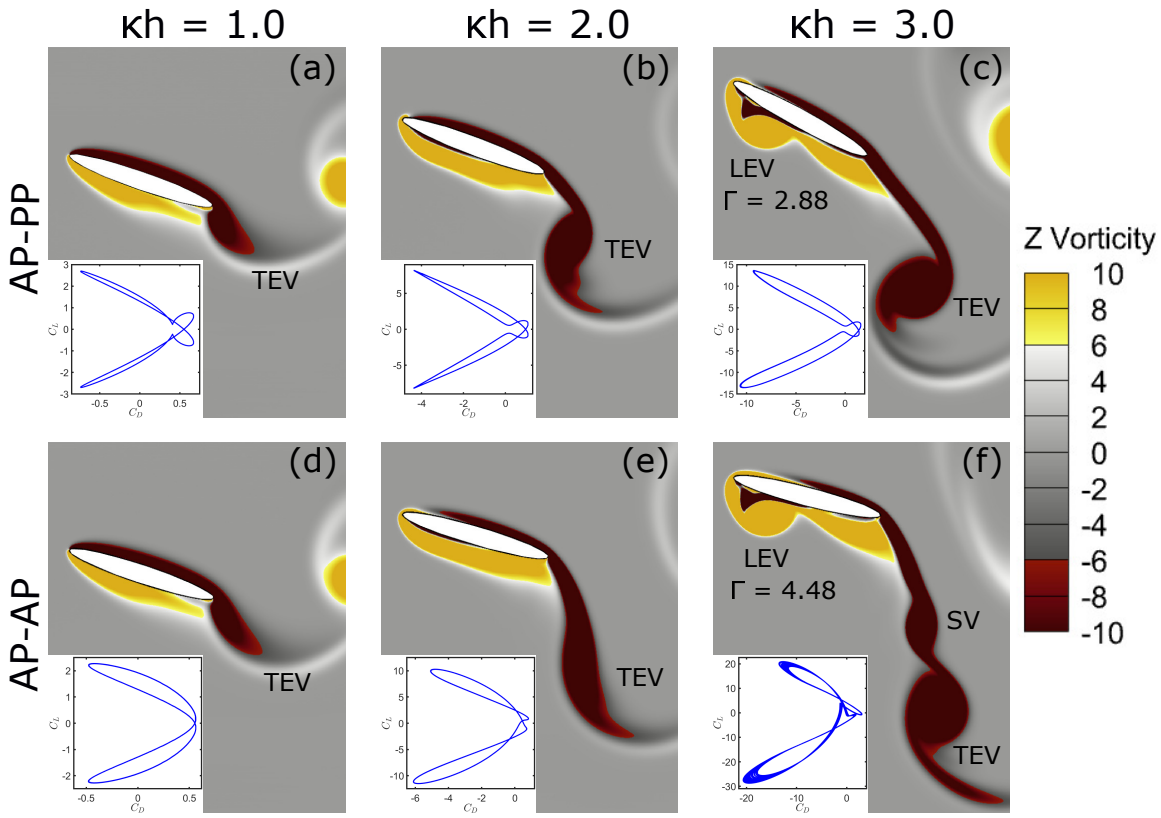

Figure 1: Near-field vorticity contours at a typical time instant of $t/T = 50.0$ when the foil completed the upstroke and about to commence downstroke in a typical flapping cycle. Γ indicates the strength of LEV in terms of its circulation. SV: secondary vortex. Inset box in each of the frames represents the corresponding $C_L - C_D$ phase portrait. (a - c) actively plunging-passively pitching and (d - f) actively plunging-actively pitching foil at different κh values.

at high amplitude-frequency kinematic ranges where aperiodic transition was observed in fully actuated foils. Passive pitching was able to modulate the flapping foil's movement in such a way that the leading-edge motion led the trailing-edge, and helped the foil "slice through" the incoming free stream so as to maintain a lower effective angle-of-attack throughout the stroke. This resulted in the attenuation of the LEV. Absence of aperiodic triggers such as separation of strong LEVs kept the wake periodic, thereby chaotic transition was averted. The favourable effects of passive dynamics will be further presented in terms of quantitative measures to capture the foil's orientation relative to the oncoming flow as well as the effective angle-of-attack. Notably, periodic dynamics through the introduction of passive oscillation did come at the cost of a reduction in load amplitudes, posing design challenges to balance the trade-off between the two.

References

[1] Paolo Blondeaux, et al. Chaotic Flow Generated by an Oscillating Foil. *AIAA Journal*, 43(4):918–921, 2005.

[2] David Lentink, et al. Vortex interactions with flapping wings and fins can be unpredictable. *Biology Letters*, 6(3):394–397, 2010.

[3] Muhammad Adeel Ashraf, et al. Oscillation frequency and amplitude effects on plunging airfoil propulsion and flow periodicity. *AIAA Journal*, 50(11):2308–2324, 2012.

[4] Jian Deng, et al. The correlation between wake transition and propulsive efficiency of a flapping foil: A numerical study. *Physics of Fluids*, 28(9):094101, 2016.

[5] Sandeep Badrinath, et al. Identifying the route to chaos in the flow past a flapping airfoil. *European Journal of Mechanics - B/Fluids*, 66:38–59, 2017.

[6] Dipanjan Majumdar, et al. Capturing the dynamical transitions in the flow-field of a flapping foil using immersed boundary method. *Journal of Fluids and Structures*, 95:102999, 2020.

[7] Chandan Bose, et al. Dynamic interlinking between near-and far-field wakes behind a pitching-heaving airfoil. *Journal of Fluid Mechanics*, 911:A31, 2021.

[8] Dipanjan Majumdar, et al. Transition boundaries and an order-to-chaos map for the flow-field past a flapping foil. *Journal of Fluid Mechanics*, 942:A40, 2022.

[9] Catherine Marais, et al. Stabilizing effect of flexibility in the wake of a flapping foil. *Journal of Fluid Mechanics*, 710:659–669, 2012.

[10] Eirik Bøckmann and Sverre Steen. Experiments with actively pitch-controlled and spring-loaded oscillating foils. *Applied Ocean Research*, 48:227–235, 2014.

[11] Sachin Y. Shinde and Jaywant H. Arakeri. Flexibility in flapping foil suppresses meandering of induced jet in absence of free stream. *Journal of Fluid Mechanics*, 757:231–250, 2014.

Unsteady pitching moment of heaving membrane wings

Sonya Tiomkin[a*] and Justin W. Jaworski[a]
[a] Lehigh University, Department of Mechanical Engineering and Mechanics, Bethlehem, PA, USA[1]
[*]Correspondence: *sot220@lehigh.edu*

1 Introduction

Mammalian fliers, such as flying squirrels and bats, are known for their use of extensible membranes for gliding and flight. These membrane wings adapt their shape passively to unsteady flow conditions, enabling several aerodynamic advantages over rigid wings. Recent studies have identified these advantages to be related to the onset of fluid-membrane oscillations, which enhance the mean lift coefficient in both steady and unsteady flow conditions [1].

In pursuit of a theoretical model to evaluate these benefits, our recent work [2] develops a theoretical framework to predict the lift and dynamic response of a membrane airfoil to unsteady flow conditions. An extensible membrane wing model is applied under the assumptions of small camber and constant membrane tension, and the aerodynamic load on the airfoil is obtained using unsteady thin airfoil theory, which permits the analysis of vertical gust encounters or prescribed flapping motions.

The present work extends this study to predict the unsteady pitching moment of a flapping membrane wing. We derive closed-form expressions for the moment coefficient and establish its role in the unsteady aerodynamic performance of heaving membrane wings. Implications of these results are discussed in relation to the propulsion potential of passively pitching membrane wings in prescribed heaving motions.

2 Methodology

We consider an extensible membrane airfoil of thickness $\tilde{h}$ and density ρ_m, which is held by simple supports at a distance $2b$ from one edge to the other. The membrane is immersed in a uniform and inviscid incompressible freestream of density ρ and speed U, and undergoes a harmonic heave motion $h(t)$ (see figure 1). Assuming small deformations of the membrane, $|y_x| \ll 1$, the nondimensional membrane dynamic equation is

$$4\mu\, y_{tt} = 2C_T\, y_{xx} + \Delta C_p, \tag{1}$$

where $\mu = \rho_m \tilde{h}/\rho c$ is the membrane mass ratio, C_T is the tension coefficient, and ΔC_p is the aerodynamic load on the membrane. The variables $b, b/U, \frac{1}{2}\rho U^2$, and $\rho U^2 b$ are used here as the units of length, time, pressure, and force (per unit span).

[1]This work was partially supported by the National Science Foundation under award 1846852.

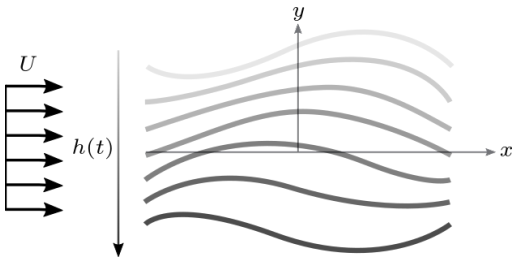

Figure 1: Schematic description of the problem: a compliant membrane wing deforms during the downstroke of a prescribed harmonic heaving motion.

The solution of the dynamic equation is obtained by expressing the membrane slope, y_x, as a Fourier cosine series expansion, following the method utilized by Nielsen [3] for a static membrane wing and augmenting it with time-dependent Fourier coefficients

$$y_x(t,\theta) = \frac{1}{2}F_0(t) + \sum_{n=1}^{\infty} F_n(t)\cos n\theta, \tag{2}$$

where the coordinate transformation $x = -\cos\theta$ is used.

The dynamic response of the membrane wing to harmonic heave motion, $h(t) = h_0 e^{ikt}$, is derived in frequency domain, following the method of [2]. Closed form expressions for the aerodynamic load on the membrane were derived in [2] and used to compute the unsteady lift of the airfoil. Here, we compute the pitching moment at location $x = a$ along the airfoil by substituting the aerodynamic load expression into

$$C_m(a,k) = -\frac{1}{4}\int_{-1}^{1} \Delta C_p(k,\theta)\cdot(x-a)\mathrm{d}x. \tag{3}$$

This integral leads to a closed-form expression for the pitching moment coefficient which depends only on the Fourier coefficients that decompose the membrane deformation and the classical Theodorsen function, $C(k)$, which is known to describe the mid-chord pitching moment of a rigid flat plate that undergoes a harmonic heave motion [4].

3 Results

The membrane moment coefficient in response to harmonic heave motions is examined next for a membrane wing of $\mu = 1$ and tension coefficients between 2.5 and 4, and compared against the rigid airfoil response. Figure 2 illustrates

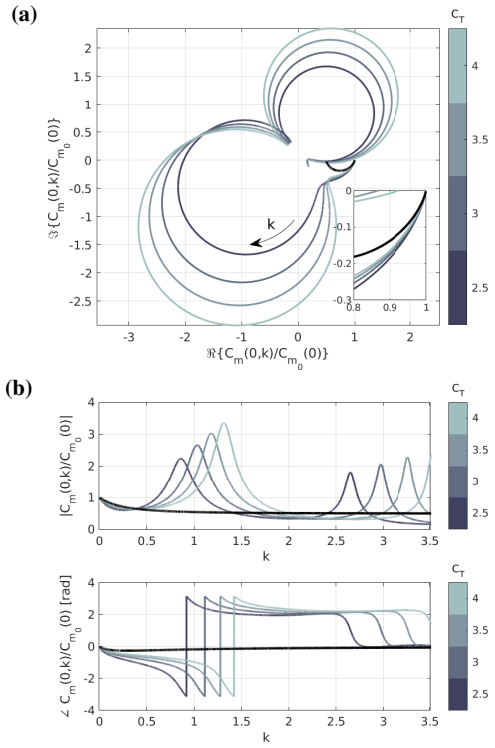

Figure 2: Pitching moment coefficient computed at mid-chord and normalized with respect to the quasi-steady coefficient, $C_{m_0}(0)$, in terms of: (a) Argand diagram; (b) modulus and phase. Membrane parameters: $\mu = 1, 2.5 \leq C_T \leq 4$. Black curve denotes rigid airfoil results.

this comparison in terms of an Argand diagram (figure 2a) and in terms of modulus and phase (figure 2b). For low reduced frequencies, the membrane moment coefficient follows the trend of the rigid airfoil response, but with reduced amplitude and increased phase lag. As the reduced frequency of the prescribed heave motion approaches the first resonance frequency of the fluid-loaded membrane, circular paths appear in the complex plane plot. These circles are due to the dynamic membrane response at resonance, as identified by [2] for the unsteady lift. However, the amplification of the mid-chord pitching moment is more significant than the enhancement of the lift coefficient reported in [2].

A key reason for our interest in the pitching moment of a heaving airfoil is its role in the passive pitching motion of the wing, which is known to produce thrust [5]. To this end, Moore [5] have studied the propulsive benefits of a heaving rigid airfoil that is elastically mounted to a torsional spring at the leading edge. We next focus on the pitching moment that is obtained at the leading edge (figure 3) with the intent to apply a similar model to study the propulsive benefits of a flapping membrane wing . We note that for low reduced frequencies the leading edge pitching moment responds similarly to the mid-chord moment when compared

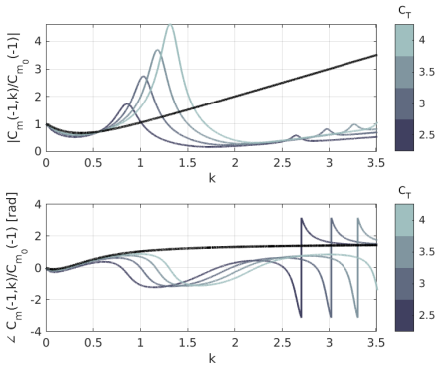

Figure 3: Modulus and phase of the moment coefficient computed at the leading edge and normalized with respect to the quasi-steady coefficient, $C_{m_0}(-1)$, obtained for $\mu = 1$.

to the rigid airfoil moment, whereas for higher frequencies beyond the first resonance peak, a strong reduction is evident in the leading-edge pitching moment amplitude relative to the rigid airfoil response.

4 Conclusion

We study analytically the aerodynamic pitching moment of membrane airfoils that are subject to small-amplitude heaving motions in a two-dimensional inviscid incompressible flow. The unsteady pitching moment is studied in the complex plane and compared to the classical rigid airfoil response. Preliminary results show that the membrane compliance reduces the pitching moment amplitude for low reduced frequencies below the first fluid-loaded resonance frequency. Higher (near-resonance) frequencies result with significant amplification in the pitching moment compared to the classical rigid airfoil moment.

In this talk we will discuss the effect of the different membrane parameters (e.g., tension coefficient and mass ratio) on the aerodynamic pitching moment of a flapping membrane wing and compare our results to the classical theory for rigid flat plates. We will also show how the closed-form expressions for the pitching moment can be applied to study the propulsion produced by heaving membrane wings due to an induced pitching motion. This result will be obtained by studying an elastically mounted membrane wing with a torsional spring at the leading edge, and by then deriving expressions for the resulting thrust.

References

[1] V. Mathai, G. Alon-Tzezana, A. Das, and K. S. Breuer. Fluid-structure interactions of energy-harvesting membrane hydrofoils. *Journal of Fluid Mechanics*, 942:R4, 2022.

[2] S. Tiomkin and J. W. Jaworski. Unsteady aerodynamic theory for membrane wings. *Journal of Fluid Mechanics*, 948:A33, 2022.

[3] J. N. Nielsen. Theory of flexible aerodynamic surfaces. *Journal of Applied Mechanics*, 30:435–442, 1963.

[4] T. von Kármán and W. R. Sears. Airfoil theory for non-uniform motion. *Journal of the Aeronautical Sciences*, 5(10):379–390, 1938.

[5] M. N. J. Moore. Analytical results on the role of flexibility in flapping propulsion. *Journal of Fluid Mechanics*, 757:599–612, 2014.

Surfing on Vortices: Bird flight and engineered wing responses to an unsteady vortex wake

S. Hao[a], S. I. Friman[b], A. R. Gerson[c], T. L. Hedrick[b], K. S. Breuer[a]
[a] Brown University, Center for Fluid Mechanics, Providence, RI[1]
[b] The University of North Carolina at Chapel Hill, Department of Biology, Chapel Hill, NC
[c] University of Massachusetts, Department of Biology, Amherst, MA[1]
*Correspondence: *kenneth_breuer@brown.edu*

1 Introduction

Birds are observed to interact with various unsteady flow structures during flight. While many groups have studied the vortex structure of the wake generated by a flapping animal (e.g., [1,2]), the interaction between flapping flight and an unsteady wake has not been quantitatively studied in a controlled environment. At the same time, recent research on the interaction of a fixed-wing with an unsteady vortex wake [3,4] provides a useful engineering model for understanding the wake interactions in animal flight. This work bridges these two approaches and uses wind tunnel measurements to study the interaction between a live bird flying in (i) the wake of another bird and (ii) the prescribed wake shed by a mechanical model.

2 Experimental Setup

Experiments are conducted in the Animal Flight and Aero-Mechanics Wind Tunnel at Brown University. The test section (Fig. 1) has a cross-section of 1.2m by 1.2m. For animal flights, the usable test section has a length of 2.8m. In bird flight experiments, European Starlings are flown in the test section with a freestream speed of $U = 11$m/s. The bird carries a lightweight "backpack" (Vesper, ASD Technologies, Haifa, Israel) to record body acceleration during flight. Four machine vision cameras (AlVIUM1800, Allied Vision Technologies, Stadtroda, Germany) are used to reconstruct the trajectory of the flights. We perform two kinds of bird flight experiments: (i) with two birds, in which one bird (the "follower") flies in the wake of a second bird (the "leader"), and (ii) with a single bird flying in the wake of an unsteady wake generator: a NACA 0012 airfoil with a 10 cm chord, spanning the entire test section and pitched in a sinusoidal motion about the quarter-chord at 10 Hz, with an amplitude of $\pm 15^\circ$ (Fig. 1). To better understand the unsteady aerodynamic force experienced by the bird, a second series of experiments was performed in which a fixed wing was positioned in the same unsteady wake. Here, a NACA 0012 wing (chord 27 mm, span 85 mm) was placed at the same height as the unsteady wake generator, 400mm downstream. The wing is mounted on a 6 DoF force/torque loadcell (Nano-17, ATI, Apex, NC) to measure the responses to the wake at 5000Hz (Fig. 2). For these experiments, the freestream velocity was set from 2m/s to 10m/s, and the flapping frequency varied between 2Hz and 8Hz, resulting in a range of non-dimensional Strouhal numbers, fc/U from 0.07 to 0.34. Two high-speed cameras (Nova R2, Photron Inc, San Deigo, CA) were positioned outside the test section and used to acquire Particle Image Velocimetry (PIV) images at 500 Hz ($50\times$ the flapping frequency) with a $300mm \times 500mm$ field of view positioned immediately downstream the wake-generating airfoil, and oriented parallel to the free stream.

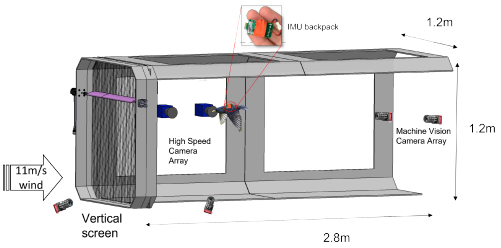

Figure 1: Wind tunnel setup for the bird flight experiments.

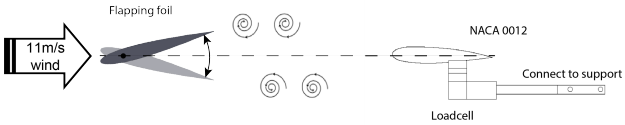

Figure 2: Schematic of the fixed wing experimental setup.

3 Results

3.1 Flapping foil wake structure

Phase-averaged snapshots of the flow field downstream of the flapping airfoil are shown in Fig. **??** for three representative times. The wake comprises a deflected reverse von Karman Street with a stronger CCW vortex (red) that convects downstream. This asymmetric wake structure agrees with previous observations [5,6] and is due to the obliquely propagating dipolar structure triggered at this flapping am-

[1]This work was supported by NSF Grant 1930924

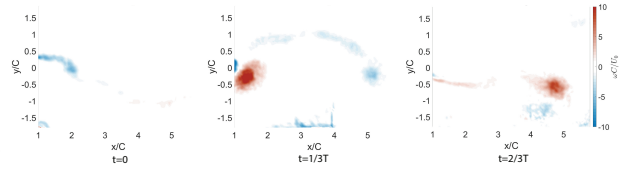

Figure 3: Phase-averaged PIV Snapshots on a flapping cycle

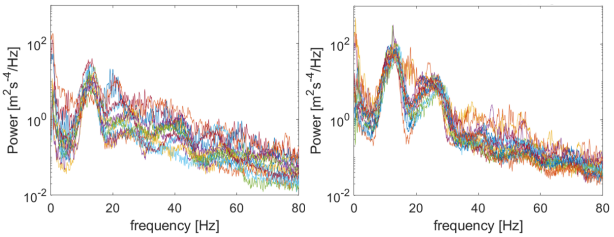

(a) Flight in clean flow **(b)** Flight in wake

Figure 4: A comparison of the power spectrum of the acceleration data during the flight.

plitude. This wake structure serves as a background for both the bird and fixed-wing experiments.

3.2 Bird flight frequency lock-in

Figure **??** shows power spectra of the acceleration experienced by the birds during flight; note that each color represents an individual flight. For the flights in the clean flow (Fig. 4a), there is a peak corresponding to the primary flapping frequency near 10 Hz as well as a prominent second harmonic; the spectra are loosely distributed both in frequency and amplitude. In contrast, for the flights behind the flapping airfoil (Fig. 4b), the main peak and the first harmonic are centered much more tightly around the prescribed flapping frequency and with a higher amplitude than observed in the clean flow.

3.3 Wing model force response

For the fixed-wing experiment, the spectrum of the aerodynamic force response is comparable to the acceleration data of the birds' flights. As shown in figure 5a, the dominant frequency of the aerodynamic response scales with the flapping frequency of the airfoil, confirming that the response is induced by this vortex-shedding frequency. This agrees well with the shedding frequency-related peak observed in the acceleration spectrum of bird flights.

The intensity of the wing response can be quantified by a narrow-band integration:

$$P_1 = \int_{0.95}^{1.05} PSD_{Force} d\frac{f}{f_0}. \tag{1}$$

We observe a linear relationship between P_1 and the product of the free-stream speed and driving frequency (Fig 5b). $U_\infty f_0$ has the dimensions of acceleration and can be interpreted as the intensity of flow disturbance shed by the oscillating airfoil. Dividing by dynamic pressure, $0.5\rho U_\infty^2$, equation 1 yields

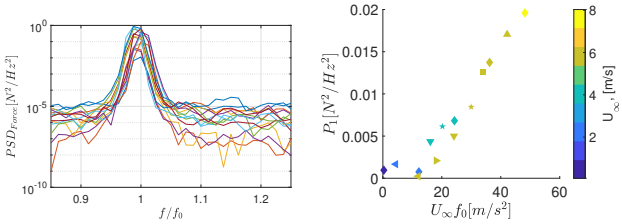

(a) Responding spectrum **(b)** First responding peak intensity

Figure 5: Force response on airfoil model

$$\frac{P_1}{1/2\rho U_\infty^2} \propto \frac{f_0 c}{U_\infty} = St, \tag{2}$$

where c is the chord of the fixed wing.

4 Conclusion

We have seen evidence that the starlings interact with the prescribed wake structure. From dynamic aspects, the acceleration spectrum is distributed tighter on the frequency domain in the wake but excited at the wake's corresponding frequency. We also compare the acceleration spectrum with the force response on an airfoil model, which also surfs in the prescribed wake. The responding force is aligned with the wake-shedding frequency on the frequency domain, which agrees with the wake-excited peak in the acceleration spectrum of bird flight. And the intensity of this response shows a proportional relation with the *St* number.

The full paper will present extended measurements of the fixed wing response over a broader range of forcing *St* and downstream positions, as well as a more detailed analysis of the accelerations experienced by the birds.

References

[1] Spedding, G. R., Rosén, M., & Hedenström, A. (2003), A family of vortex wakes generated by a thrush nightingale in free flight in a wind tunnel over its entire natural range of flight speeds, *Journal of Experimental Biology* **206**, 2313–2344.

[2] Hubel, T. Y., Hristov, N. I., Swartz, S. M., & Breuer, K. S. (2009), Time-resolved wake structure and kinematics of bat flight, *Experiments in Fluids* **46**, 933–943.

[3] Turhan, B., Wang, Z., & Gursul, I. (2022), Interaction of vortex streets with a downstream wing, *Physical Review Fluids* **7**.

[4] Sureshbabu, A. V., Medina, A., Rockwood, M., Bryant, M., & Gopalarathnam, A. (2021), Theoretical and experimental investigation of an unsteady airfoil in the presence of external flow disturbances, *Journal of Fluid Mechanics* **921**.

[5] Deng, J. & Caulfield, C. P. (2015), Three-dimensional transition after wake deflection behind a flapping foil, *Physical Review E - Statistical, Nonlinear, and Soft Matter Physics* **91**.

[6] Godoy-Diana, R., Aider, J. L., & Wesfreid, J. E. (2008), Transitions in the wake of a flapping foil, *Physical Review E - Statistical, Nonlinear, and Soft Matter Physics* **77**.

The influence of trailing edge shape on the time-averaged wakes of bio-inspired pitching panels

Justin T. King[a] and Melissa A. Green[a]
[a] University of Minnesota, Aerospace Engineering and Mechanics, Minneapolis, MN, USA
*Correspondence: *king1526@umn.edu*

1 Introduction

Recently, engineers working on swimming and flying vehicles have looked to nature for motivation and have incorporated their findings into man-made vehicles [1, 2]. Bio-inspired vehicles have the potential to be valuable in applications like surveillance, oceanic sampling, and reconnaissance [3, 4]. Crucial to the design of such vehicles and the understanding of biological propulsion, is comprehension of the unsteady fluid flows they generate and the time-varying forces acting on them.

For some swimming animals, thrust is generated primarily by a caudal fin, which may display a range of planforms and different trailing edge shape [5]. Geometric abstractions of some caudal fins are shown in Fig. 1, which illustrates the diversity in leading and trailing edge shapes. The top row of Fig. 1 displays high aspect ratio (*AR*) fins that are typically associated with improved performance [6], and fins of low *AR* and reduced performance are in the bottom row. Increases in *AR* are due to reductions in area, increases in span, or both. Smits stated that, although the effects of changing *AR* may be well understood, "we are far from understanding the effects of changing the planform shape" [7]. Experiments in the current work focus on three shapes from Fig. 1: forked, truncate, and pointed. This work explores the influence of propulsor planform on vortex dynamics and performance of bio-inspired swimmers.

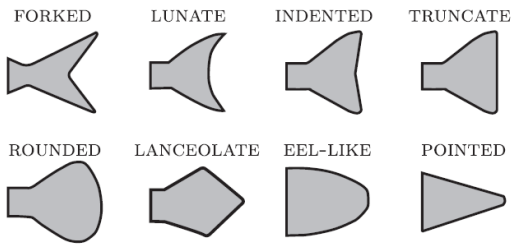

Figure 1: Geometric abstractions of caudal fins from a variety of fish species. ***Adapted from Van Buren et al. [8].***

2 Results

The thrust production of a pitching propulsor is often linked to the formation of a time-averaged jet in the wake [9]. A momentum analysis of the time-averaged wake can be used to provide an estimate of the thrust, although failure to account for time-varying factors like velocity fluctuations and pressure may result in overestimation of mean forces [10]. Changes to trailing edge shape and Strouhal number (*St*) have significant impact on the spatial distribution of the streamwise component of momentum.

Behaviors of the time-averaged streamwise momentum is explored using isosurfaces of $\bar{u}/U$ in Figure 2, where $\bar{u}$ is the time-averaged value of local streamwise velocity. For the sake of brevity, isosurfaces $\bar{u}/U$ for only the most forked planform (Panel 1), a trapezoidal planform (Panel 3), and the most pointed planform (Panel 5) at select *St* are displayed in Figure 2. At low pitching amplitudes, when $St \approx 0.1$, increases in trailing edge convexity result in a relatively weak dual jet that is symmetric about $z/2b = 0$. The appearance of this dual jet is consistent with an increase in thrust production between Panel 5 at $St = 0.14$ and Panel 1 at $St = 0.09$ that has been observed in other work. Not shown in Figure 2 are the time-averaged wakes of Panel 1 at $St = 0.17$ and Panel 3 at $St = 0.22$, which also display dual jets symmetric about the midspan plane. The wake of Panel 1 at $St = 0.17$ also displays a single, central jet that lies close to and within the midspan plane. When *St* is low and the trailing edge is forked or straight, the wake is *only* comprised of momentum deficit regions along the centerline that may cover a significant portion of the wake volume in the spanwise direction. If *St* is kept small, a dual jet will result from increases to trailing edge convexity, while the same structure, sometimes accompanied by a single jet, can also emerge through slight increases to *St* for forked and straight trailing edge shapes.

When $St = 0.25$, Figure 2(d) shows that Panel 1 produces a single jet along the wake centerline with a large spanwise extent. While maintaining intermediate *St*, increases to trailing edge convexity result in the appearance of a quadfurcated jet for Panel 3 in Figure 2(h). The quadfurcated wake structure was first described by Van Buren *et al.*, where it was linked to improved performance [8]. These four tubular jets are inclined away from the wake centerline and compress in the spanwise direction, behaviors displayed more clearly in the wake of Panel 5 at $St = 0.40$. A quadfurcated jet never develops in the wake of Panel 1; however, the structure occurs in the wake of Panel 2 at $St = 0.38$. The wake of Panel 1 at $St = 0.41$ in Figure 2(g) may show evidence of an incipient quadfurcated jet, but the structure does not clearly emerge

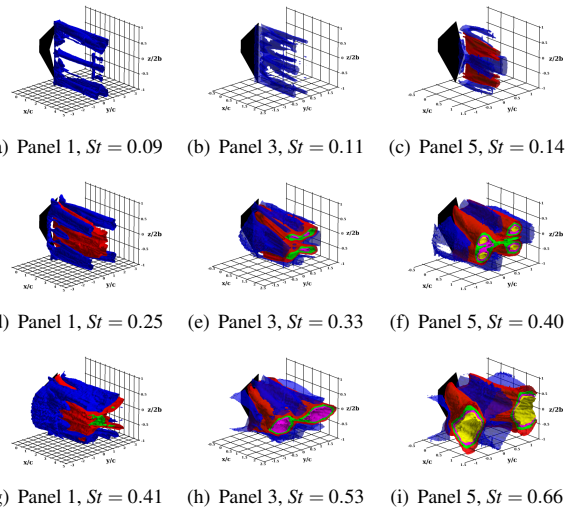

(a) Panel 1, $St = 0.09$ (b) Panel 3, $St = 0.11$ (c) Panel 5, $St = 0.14$

(d) Panel 1, $St = 0.25$ (e) Panel 3, $St = 0.33$ (f) Panel 5, $St = 0.40$

(g) Panel 1, $St = 0.41$ (h) Panel 3, $St = 0.53$ (i) Panel 5, $St = 0.66$

Figure 2: Isometric views of isosurfaces of $\bar{u}/U$ for Panel 1, Panel 3, and Panel 5 at select St. Isosurfaces are thresholded to $\bar{u}/U = 0.95$ (blue), 1.1 (red), 1.2 (green), 1.3 (purple), and 1.4 (yellow).

within the St range explored. The wake behaviors of Panel 2 indicate that a quadfurcated jet may emerge through increases to trailing edge convexity while maintaining St, or through increases to St for a fixed geometry. Additional results, not shown here, demonstrate that the momentum contained within time-averaged jets, let alone their shape and number, do not provide all the information necessary to carry out a complete control volume analysis that would quantify swimming performance. A complete analysis of this type would also require information about quantities such as the time-varying pressure and velocity fields acting on the control volume boundary [10]. Without information about forces acting on the propulsor surface, it can be difficult to reconcile observations in the current like decreasing jet size and strength occurring for cases of improved performance. Ultimately, as with recent findings on links between the instantaneous wake and performance [11], performance characteristics gleaned from the time-averaged wake should be viewed with caution.

3 Conclusion

Experiments in a recirculating water tunnel are used to investigate the performance and wakes of bio-inspired pitching panels of varying trailing edge shape. Measurements of time-averaged propulsive performance reveal that changes to trailing edge shape and Strouhal number can have significant impacts on thrust and propulsive efficiency. For panels with either a straight or pointed trailing edge, thrust increases with Strouhal number and can become rather large as the trailing edge becomes more pointed, while thrust never becomes positive for forked panels and tends to decrease with increases to Strouhal number. Velocity vectors captured using multiple planes of stereoscopic particle image velocimetry indicate that the structure of the time-averaged wake is also altered through changes to planform shape and Strouhal number. Future work will explore what is can be attributed to changes only in trailing edge shape, and what should be considered the effect of planform area changes.

Wake results show that prior descriptions in the research literature that link specific jet structures to performance are not generally applicable to the wakes of oscillating propulsors. Relatively strong, centralized jets of streamwise momentum are observed in drag-producing cases, while jets are large inclination angles are prominent in wakes corresponding to conditions of large thrust. Furthermore, although quadfurcated jets may be present for scenarios of peak propulsive efficiency and moderate thrust, they also appear when the panel fails to generate positive thrust. Similar to the results of recent work that indicate caution must be taken when making direction connections between patterns within the instantaneous wake and swimming performance [7, 11, 12], discretion must similarly be applied whenever characteristics of the time-averaged wake are used to draw inferences about performance.

References

[1] D.T. Roper, S. Sharma, R. Sutton, and P. Culverhouse. A review of developments towards biologically inspired propulsion systems for autonomous underwater vehicles. *Proc. IMechE*, 225:77–96, 2010.

[2] R. Siddall and M. Kovac. Launching the aquamav: bioinspired design for aerial–aquatic robotic platforms. *Bioinspiration & Biomimetics*, 9, 2014.

[3] Edwin F. S. Danson. *Technology and Applications of Autonomous Underwater Vehicles*, chapter AUV tasks in the offshore industry, pages 127–138. Taylor and Francis, London, 2003.

[4] Simon Corfield and Christopher Hillenbrand. *Technology and Applications of Underwater Autonomous Vehicles*, chapter Defence applications for unmanned underwater vehicles, pages 161–178. Taylor and Francis, London, 2003.

[5] M. J. Lighthill. Hydromechanics of aquatic animal propulsion. *Annual Review of Fluid Mechanics*, 1:413–446, 1969.

[6] Michael Sfakiotakis, David M. Lane, and J. Bruce C. Davies. Review of fish swimming modes for aquatic locomotion. *IEEE Journal of oceanic engineering*, 24(2):237–252, 1999.

[7] Alexander J Smits. Undulatory and oscillatory swimming. *Journal of Fluid Mechanics*, 874, 2019.

[8] Tyler Van Buren, D. Floryan, D. Brunner, U. Senturk, and Alexander J. Smits. Impact of trailing edge shape on the wake and propulsive performance of pitching panels. *Physical Review Fluids*, 2(1):014702, Jan 2017.

[9] G.S. Triantafyllou, M.S. Triantafyllou, and M.A. Grosenbaugh. Optimal thrust development in oscillating foils with application to fish propulsion. *Journal of Fluids and Structures*, 7:205–224, 1993.

[10] Douglas G. Bohl and Manoochehr M. Koochesfahani. Mtv measurements of the vortical field in the wake of an airfoil oscillating at high reduced frequency. *J. Fluid Mech.*, 620:63–88, 2009.

[11] Daniel Floryan, Tyler Van Buren, and Alexander J Smits. Swimmers' wake structures are not reliable indicators of swimming performance. *Bioinspiration & biomimetics*, 15(2):024001, 2020.

[12] A.W. Mackowski and C.H.K. Williamson. Direct measurement of thrust and efficiency of an airfoil undergoing pure pitching. *J. Fluid Mech.*, 765:524–543, 2015.

Aerodynamics and inertial steering mechanisms in hummingbird's escape maneuver

Mohammad Nasirul Haque[a] and Haoxiang Luo[a*] and Bo Cheng[b], Bret W. Tobalske[c]
[a] Vanderbilt University, Department of Mechanical Engineering, Nashville, TN 37235, USA.[1]
[b] Pennsylvania State University, Department of Mechanical and Nuclear Engineering, University Park, PA 16802, USA.
[c] University of Montana, Field Research Station at Fort Missoula, Division of Biological Sciences, Missoula, MT 59812, USA.
[*]Correspondence: *haoxiang.luo@vanderbilt.edu*

1 Introduction

Hummingbirds are one of nature's most remarkable flyers, capable of not only fast cruise flight like most other birds but also sustained hovering and rapid aerobatic maneuvers to fly in a cluttered environment or to prey on insects. To enable these different flight modes, their flapping wings have to provide the necessary forces and moments for propulsion, linear accelerations, and three degrees-of-freedom body rotations in addition to maintaining weight support. On other hand, each hummingbird wing has only three primary degrees of freedom at the shoulder, unlike larger birds whose wings may have additional degrees of freedom at the finger joint. Nevertheless, hummingbirds outperform larger birds in terms of agility, especially at low speeds. Previous studies hummingbird aerodynamics have primarily focused on hovering flight or cruising flight, where the wing kinematics is periodic and body motion is steady. There have been few studies that addressed the aerodynamics and flight mechanics of hummingbird maneuvers, even though hummingbirds obviously have amazing maneuvering skills.

For a hovering-to-escape maneuver, a hummingbird can evade the perceived threat, reorient its body, and accelerate toward the escaping direction in less than 0.2 second (about 5 or 6 wingbeat cycles). In this process, the hummingbird body may pitch and roll simultaneously, and it can reach desired rotational velocities with one or two wingbeats. The question is, how are hummingbirds able to execute such a complex maneuver on a dime? In the current study, a high-fidelity CFD analysis has been performed for a Rivoli's hummingbird based on the full-body kinematics reconstructed from the high-speed videos of the escape maneuver Fig. 1 to simulate the 3D flow and obtain the details of the wing aerodynamic and inertial forces, as well as the torques on the bird body due to these forces. From the simulation results, we have investigated how these forces and moments enabled the bird's body acceleration and rotation to accomplish the escape maneuver.

[1]This work was supported by ONR under grant No. N00014-19-1-2540

2 Results

The CFD simulation provided all the aerodynamic forces (Fig. 2). We also calculated the wing inertial forces based on the wing kinematics and mass distribution scaled from measurement data of the Ruby-throated hummingbird. The simulation results show that from hovering to escape, the bird changed its wing kinematics dramatically in addition to increasing the wingbeat frequency from 25 Hz to around 33 Hz. As a result, not only the aerodynamic force magnitude greatly increased, but also the force vectoring with respect to the bird body changed significantly to redirect toward the direction of escape (backward away from the threat).

Fig. 3 shows the pitching torques on the bird body produced by the two wings together with the forces on the wings at selected time frames. From these results, it could be seen that the wing inertial forces generated a great pitch torque at pronation, which drove the body pitch acceleration (around t=60 and 90 ms). On the other hand, the aerodynamic forces generated pitch torque during downstroke to counteract the opposite inertial torque caused by wing reversal. In combination, the inertial and aerodynamic forces enabled fast body rotation for the maneuver. A similar strategy was found for roll rotation as well.

3 Conclusion

Inertial steering was found in hummingbirds for fast maneuver, which distinguishes them from insects and aircraft who primarily rely on aerodynamics for maneuvering. In the presentation, we will discuss details of aerodynamics, as well as the body acceleration and rotation that includes pitch, roll, and yaw. Furthermore, we will discuss the power consumption of the escape maneuver.

References

[1] B. Cheng, et al., Flight mechanics and control of escape manoeuvres in hummingbirds. I. Flight kinematics. *J. Exp. Bio.*, 219, 3518–3531, 2016.

[2] B. Cheng, et al., Flight mechanics and control of escape manoeuvres in hummingbirds. II. Aerodynamic force production, flight control and performance limitations. *J. Exp. Bio.*, 219, 3532–3543, 2016.

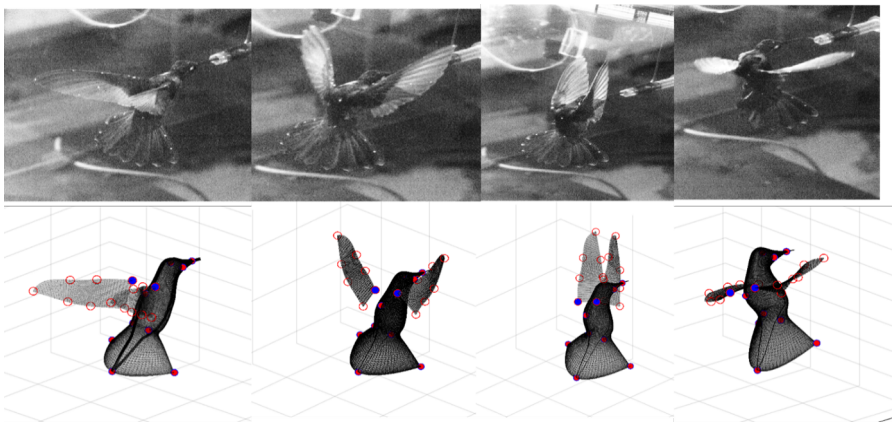

Figure 1: Top: snapshots from one of the camera views (videos data from a previous study of hummingbird escape maneuver by Cheng et al. [1]), and bottom: the corresponding reconstructed model with the marker points labelled on the bird.

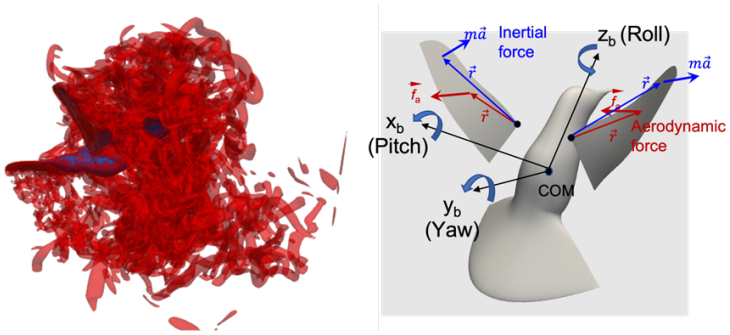

Figure 2: Left: Flow field from the CFD simulation. Right: illustration of the rotational dynamics.

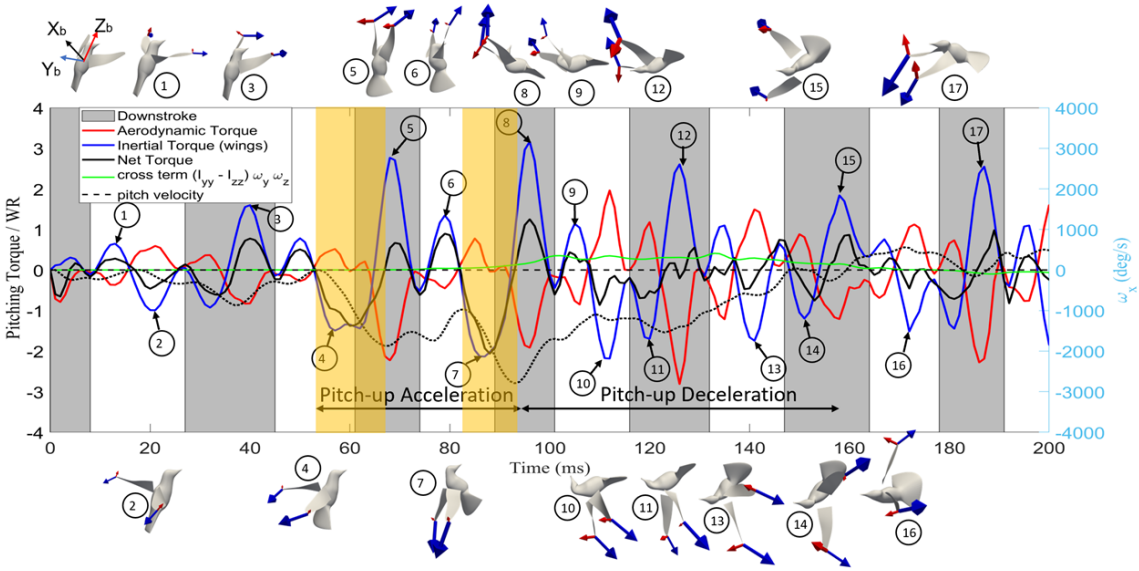

Figure 3: Instantaneous pitching torques (normalized by the body weight × wing length); Insets showing the aerodynamic (red arrows) and inertial forces (blue arrows) on the wings.

Discovering optimal flapping wing kinematics using active deep learning

Baptiste Corban, Michael Bauerheim and Thierry Jardin
ISAE-SUPAERO, Toulouse, France

1 Introduction

The aim of this study is to perform a multi-objective-optimization of flapping wing kinematics. Such an optimization has been conducted experimentally by [1], where input samples to the evolutionary algorithm are cheap to obtain. Here, we perform a similar optimization based on numerical simulations which are comparatively much more expensive. Thus, we build and use a surrogate model of the unsteady forces experienced by the wing using deep, active learning and identify the Pareto front of optimal solutions. The flow and forces resulting from a selection of optimal kinematics are then analyzed.

1.1 Building a dataset of motions

Two angles are used to describe the kinematics: the stroke angle ϕ and the pitch angle ψ, as shown in figure 1.

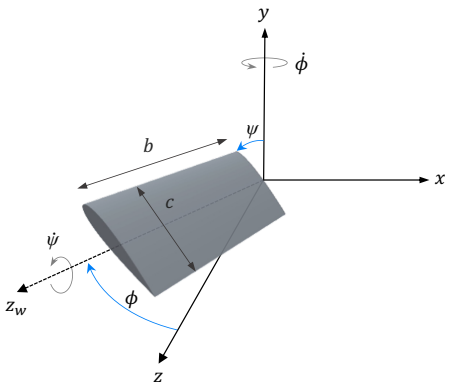

Figure 1: Definition of stroke ϕ and pitch ψ angles used to describe the wing motion

The motions are defined by $\psi(t) = a_1\cos(2\pi ft) + b_1\sin(2\pi ft) + b_3\sin(6\pi ft)$ and $\phi(t) = \phi_0\sin(2\pi ft - \delta)$. This definition allows to approximate real insect wing kinematics with reasonable accuracy. The Reynolds number Re is fixed to 1000, and defined using the mean velocity at the tip of the wing during a stroke $\overline{U}_\phi = 4bf\phi_0$. The flapping frequency f is deduced from the Reynolds number. The performance of a given motion are assessed by its mean lift coefficient $\overline{C_L}$ and efficiency η.

Real hovering kinematics from the Hawkmoth, Fruit fly and Honeybee [2] are used as a basis to generate the dataset used for neural network training. 294 other kinematics are generated by varying the Fourier coefficients of ψ, the stroke amplitude ϕ_0 and the phase shift δ. Direct numerical simulations (DNS) of the 297 flapping motions are performed and used to train the neural networks.

1.2 Unsteady aerodynamics deep learning model

Lift, rotation torque and revolution torque are needed to compute η and $\overline{C_L}$ and assess a motion performance. Thus, three neural networks are trained to predict those three outputs. The neural network take as input $\mathbf{X} = [\mathbf{x}(t), \mathbf{x}(t - 9\mathrm{d}t), \mathbf{x}(t - 18\mathrm{d}t)]$ with $\mathbf{x} = [\psi, \dot{\psi}, \ddot{\psi}, \dot{\varphi}]$ to predict one of the three outputs at the instant t. $\mathrm{d}t = T/250$ is the time discretization of the simulations, with T the flapping period. The size of the input vector and the sampling was chosen by first performing a grid search. Once trained, these networks can predict the instantaneous values of the lift and torques, given sparse information about the kinematics up to $18\mathrm{d}t$ before. These predictions of the unsteady aerodynamics take the order of 0.5s to run. This makes the neural networks suitable to be used as a surrogate model for an optimization of the kinematics.

1.3 Multi-objective optimization and active learning

The surrogate model is used to perform a multi-objective optimization of the flapping motions, using the NSGA II genetic algorithm. The objectives are the lift coefficient $\overline{C_L}$ and efficiency η. Each motion is represented by its 5 parameters $[a_1, b_1, b_3, \phi_0, \delta]$.

In order to improve the accuracy of the multi-objective optimization and of the model, an active learning algorithm is used. One issue affecting the performance of deep learning surrogate models is that the training dataset is generated before the optimization step, and the data points may be very different from the Pareto optimal points. The *Iterative Surrogate Model Optimization* (ISMO) algorithm [3] allows for an iterative construction of the dataset with data points from successive optimization steps.

In this study, an original dataset of 297 motions is generated for neural networks training. Then, the deep learning surrogate model is used in conjunction with the NSGA II algorithm to generate a Pareto front of optimal solutions. $N = 7$ motions from the predicted Pareto front are arbitrarily selected and numerical simulations are performed to check the accuracy of the surrogate model on kinematics unseen

during the training. New data from these simulations are then added to the dataset for another step of neural network training and multi-objective optimization.

2 Results

Three iterations of the active learning algorithm were needed to obtain an accurate prediction of the Pareto front. The corresponding Pareto fronts are displayed in figure 2, showing both the prediction by the neural network and results from DNS of the 7 arbitrarily selected kinematics. The predicted Pareto front from step 1 is not accurate in regions of high lift, but the highest lift obtained (and later confirmed) is showing an increase of 52% in $\overline{C_L}$ from the dataset. The deep learning model from step 1 was thus able to discover new high lift kinematics, and predict their performance with a prediction error of 11% on the lift coefficient. Steps 2 and 3 improve the accuracy of the prediction throughout the front, without improving the best performing individuals in each objective.

The most efficient motion from the Pareto front is resembling the reference kinematics, characterized by a high stroke amplitude (55°) and a low average angle of attack (37°). The flow is weakly unsteady with the formation of an attached leading edge vortex that reaches a quasi-steady state and relatively weak wing-wake interactions.

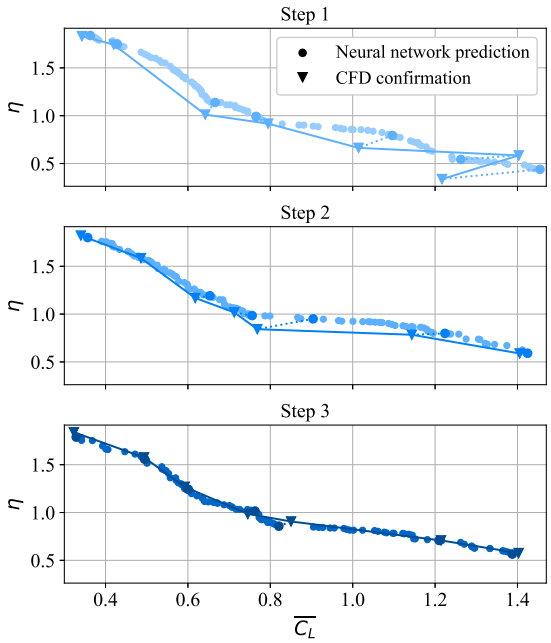

Figure 2: Pareto fronts from the three steps of the active learning algorithm, circles represent the predicted Pareto front by the deep learning surrogate model and triangles the DNS of selected individuals

On the other hand, the highest lift motion has a low stroke amplitude (10°), with a high amplitude pitching motion during the stroke, shown in figure 3. Due to the phase shift between stroke and pitch motions, the pitch angle ψ changes sign during a stroke, meaning that the leading edge is oriented backward at the end of the stroke.

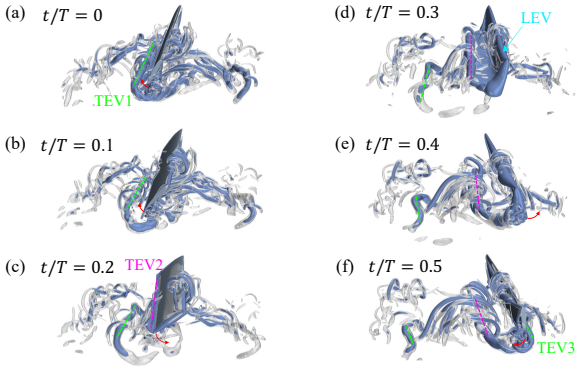

Figure 3: Non-dimensional Q-criterion isosurfaces obtained at different instants t/T for the highest-lift-generating motion. The grey isosurfaces correspond to a value of 60, and the blue to a value of 200

The complex pitching motion during a stroke can be split in two phases: a main pitching motion ($t/T \in [0.2-0.4]$), and smaller pitching variations between strokes. The main motion generates lift by a combination of added mass effects and Kramer effect, investigated by implementing the quasi-steady model by Sane & Dickinson [4]. A strong trailing edge vortex TEV2 is produced, combined to a smaller leading edge vortex. The smaller variations allow for the shedding of two trailing edge vortices between strokes.

3 Conclusion

This study demonstrates the interest of using deep learning to predict the unsteady aerodynamics of a flapping wing. Using this surrogate model for optimization allowed to discover new flapping motions and significantly improve the performance from the kinematics in the original dataset. This model is able to make accurate predictions on a wide range of motion : from high-stroke-amplitude conventional flapping motions to short amplitude high lift generating motions. Those short-stroke motions are studied in detail to isolate the mechanisms creating lift, in a trailing-edge-vortex dominated flow.

References

[1] GHERKE, A. & MULLENERS, K. 2021 Phenomenology and scaling of optimal flapping wing kinematics, *Bioinspiration & Biomimetics*,Vol 16 **2**

[2] LIU, H. & AONO, H., 2009 Size effects on insect hovering aerodynamics : an integrated computational study, *Bioinspiration and Biomimetics*, Vol 4, **1**

[3] LYE, K., MISHRA, S., RAY, D. & CHANDRASHEKAR, P. 2021 Iterative surrogate model optimization (ISMO): An active learning algorithm for PDE constrained optimization with deep neural networks, *Computer Methods in Applied Mechanics and Engineering*, 374. 113575.

[4] SANE, S. P. & DICKINSON, M. H. 2002 The aerodynamic effects of wing rotation and a revised quasi-steady model of flapping flight. *J. Expl Biol.*, 205 (8): 1087–1096.

4 Session D: Bio-Hydrodynamics

Kinematics, vortex dynamics and thrust estimation in swimming snakes

R. Godoy-Diana[a], V. Stin[a,b], G. Fosseries[d], E. Gautreau[c], S. Lombardo[d], A. Herrel[b] and X. Bonnet[d]
[a] PMMH, CNRS, ESPCI Paris-PSL, Sorbonne Université, Université Paris Cité, Paris, France [1]
[b] MECADEV, Département Adaptation du Vivant, MNHN, CNRS, Paris, France
[c] Pprime Institute, CNRS - University of Poitiers -ENSMA, Poitiers, France
[d] Centre d'Études Biologiques de Chizé, CNRS, Villiers-en-Bois, France

1 Introduction

Snakes are anguilliform swimmers, characterized by an undulation of the body with an increasing amplitude from the head to the tail. We estimate the thrust force production of a swimming snake using Lighthill's elongated-body theory [1]. Following Piñeirua et al. [2], in addition to the reactive force of Lighthill's theory, we include a resistive term arising from the local quadratic drag endured by each section of the animal's body as it oscillates laterally (see also [3, 4]). Real swimming kinematics, characterized by the deformation of the body mid-line, were obtained from video recordings of dice snakes (*Natrix tessellata*) in a swimming flume. The swimming kinematics is characterized by the deformation of the body midline, whose local position can be described by the $x(s,t)$, $y(s,t)$ coordinates, where s is the curvilinear coordinate following the midline and t is time (see Fig. 1). During the swimming motion, each slice of the swimmer is thus subjected to local forces corresponding to both reactive and resistive contributions that read (see [2]):

$$t_{\mathbf{react}} = -\mathscr{M}(h)(\ddot{y}+2U\dot{y}'+U^2y'')y' , \quad (1)$$

$$t_{\mathbf{resist}} = -\frac{1}{2}\rho C_d|\dot{y}+Uy'|(\dot{y}+Uy')y' , \quad (2)$$

where $h(s)$ is the local height of the body (i.e. its dimension in the direction perpendicular to the xy-plane, C_d is a local drag coefficient, and U is the average swimming speed.

2 Results

A typical example of the undulation kinematics and the corresponding calculation of the total thrust represented over the midline at several successive times is shown in Fig. 2. Recalling the framework of elongated-body theory, it can be seen from Fig. 2 that the contribution to the thrust of each portion of the body is very dynamic, with some parts along the midline contributing positively while others negatively, in a proportion that changes with time.

[1] This work was supported by the Paris Sorbonne IPV doctorate program and the ANR DRAGON2 (ANR-20-CE02-0010)

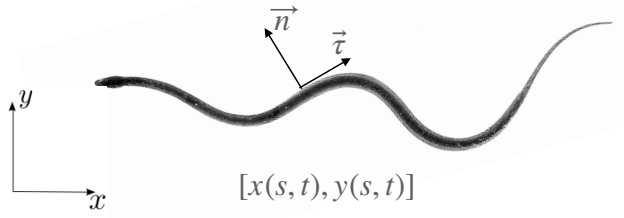

Figure 1: Elongated-body theory framework. $[x(s,t),y(s,t)]$ describe the undulation of the midline of the snake. The local unit vectors $\vec{n}$ and $\vec{\tau}$ are, respectively, normal and tangential to the body at each section. Inn the reference frame represented the snake is swimming with an average speed U in the negative x direction.

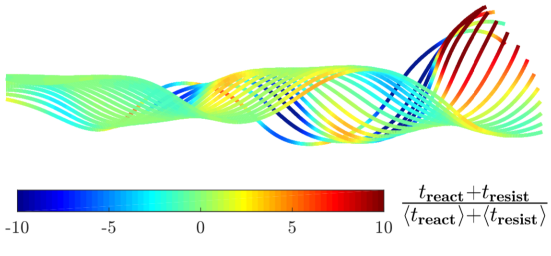

Figure 2: Snapshots of total thrust over the midline at several successive times.

3 Conclusion

Because the whole body of a swimming snake undulates, an intense vortex dynamics is active at each section of the body (see [5]), governing the quadratic local drag. This drag constitutes the resistive term (Eq. 2) in the elongated-body framework that we have used to predict the thrust produced by a swimming snake. For elongated animals, this term is crucial to estimate the force correctly, it being of the same order of magnitude than the added-mass term [2]. Ongoing work is dedicated to the use of these propulsive force estimates from a large dataset of swimming snakes to examine the question of swimming energetics.

References

[1] M. J. Lighthill, Note on the swimming of slender fish, *J. Fluid Mech.* **9**, 305?317 (1960).

[2] M. Piñeirua, R. Godoy-Diana, and B. Thiria, Resistive thrust production can be as crucial as added mass mechanisms for inertial undulatory swimmers, *Phys. Rev. E* **92**, 021001 (2015).

[3] Taylor, G. I. Analysis of the swimming of long and narrow animals. *Proceedings of the Royal Society of London. Series A. Mathematical and Physical Sciences*, **214**(1117), 158-183 (1952).

[4] R. Godoy-Diana and B Thiria, On the diverse roles of fluid dynamic drag in animal swimming and flying, *Journal of The Royal Society Interface* **15**, 20170715 (2018).

[5] V. Stin, R. Godoy-Diana, X. Bonnet, A. Herrel, Measuring the 3D wake of swimming dice snakes using volumetric velocimetry *bioRxiv preprint* 2022.11.04.515204; doi: https://doi.org/10.1101/2022.11.04.515204

Parameterizing tail-first swimming in mosquito larvae

Karthick Dhileep[a*], Qiuxiang Huang[a], John Young[a], Joseph C.S. Lai[a], Fang-Bao Tian[a+], and Sridhar Ravi[a]
[a] School of Engineering and Information Technology, UNSW Canberra, ACT 2612, Australia
[*]Presenter: *k.dhileep@adfa.edu.au*; [+]Correspondence: *f.tian@adfa.edu.au*.

1 Introduction

Natural swimmers are believed to have developed refined kinematics due to evolutionary pressure [1] being able to inspire novel designs of autonomous underwater vehicles [2]. Through rhythmic/reciprocating motion of their body and/or appendages, aquatic swimmers transfer momentum to the surrounding fluid thereby propelling themselves forward. In body caudal fin (BCF) swimmers, which constitute 85% of fishes(vertebrates) [3], thrust production has been directly associated with the momentum carried in the wake jets [4,5] and the wake pattern primarily depends on the Strouhal number (St) [6].

Compared with aquatic vertebrates, invertebrates such as insects undergo significant morphological changes during their life cycle and can often be amphibious. As a result, invertebrates display a variety of propulsive gaits and mechanisms from pulsatile swimming mode that produces vortex rings in jellyfish [7] to rhythmic paddling in crustaceans [8]. While a comprehensive understanding of vertebrate swimming exists in literature, invertebrate swimming has not received similar consideration. Among invertebrates, the larvae of mosquito display a unique side-to-side high amplitude flexural motion resulting in a tail-first gait where the posterior end of the larvae leads the anterior end in the direction of locomotion (see illustrations in Fig. 1). Previous literature on swimming in mosquito larvae [9, 10] have shown the presence of periodic vortex shedding, but fall short in investigating the provenance of these vortical structures and their significance in thrust generation. Importantly, questions on the energetics of this gait and how it compares to the more common head-first swimming remain unanswered. The scale and swimming speed of this animal place them in the intermediate Reynolds number where both viscous and inertial effects are significant. Hence, a comprehensive study encompassing flow mechanism, energetics and significance of this unique gait is required.

Here, we attempt to investigate the propulsive mechanism behind tail-first swimming by using numerical and experimental methods.

2 Results

In order to experimentally capture the flow field, larvae of mosquitoes were placed in a petri-dish under a microscope with tracers. Cyclic swimming bouts were recorded and

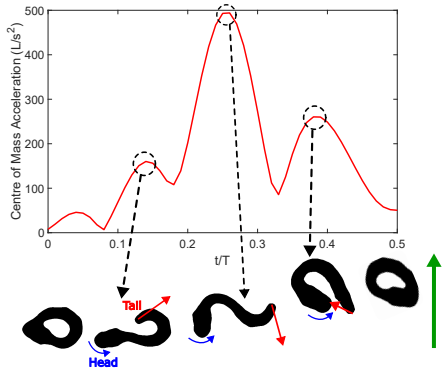

Figure 1: Centre of mass acceleration over a stroke with illustrations of the larva at various stroke phases. The blue, red and green arrows indicate the direction of motion of the head, tail and centre of mass.

2D2C particle image velocimetry (PIV) analysis was done. The centre of mass was estimated by tracking the mid-line (or centres of body parts) of the larvae using a deep neural network-based marker-less tracker.

The flow field from PIV analysis revealed the presence of multiple vortices around the larva during the stroke (see Fig. 2). Progressing through the stroke from start to mid-stroke (see $t/T = 0$ to 0.27 in Fig. 2), vortical structures were formed near the tail (positive), the inflexion point on the body close to the tail (negative) and head (positive), respectively. At mid-stroke, the larva experienced maximum hydrodynamic force as indicated by the peak in the centre of mass acceleration (see Fig. 1). Past the mid-stroke point, the larva begins to move upward and vortical structures near the tail seen earlier in the stroke were shed (see $t/T = 0.50$ in Fig. 2). The shed vortices have an opposite sense of rotation thereby inducing a jet flow between them. This is correlated to the generation of thrust. Tracking the mid-line of the larvae allowed for the estimation of relative angles (θ) between line segments connecting each body part of the larvae. This data was parameterized using a simple sinusoidal equation (see Eq. 1) to capture the kinematics of the tail-first gait,

$$\theta = \theta_0 \sin \omega t + \phi, \tag{1}$$

where θ_0 and ϕ are respectively the relative angle amplitude and the phase difference along the body of the parameterised swimmer. The frequency of the cyclic motion is represented by ω.

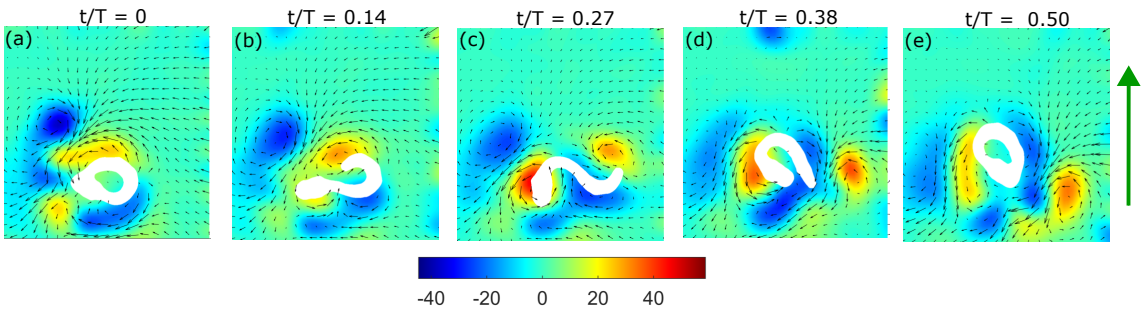

Figure 2: Vorticity field of mosquito larva. The green arrow indicates the direction of locomotion.

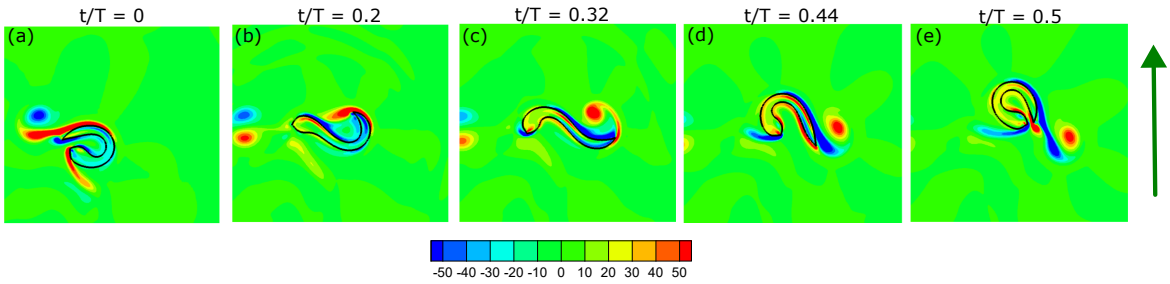

Figure 3: Vorticity field of the parameterized tail-first swimmer. The green arrow indicates the direction of locomotion.

Simulations of 2D self-propelled parameterised swimmer was conducted by an immersed boundary–lattice Boltzmann method (IB-LBM) (see e.g., [11]) and compared with the experimental results. The flow field of the parameterized tail-first swimmer shown in Fig. 3 closely resembled the experimentally obtained flow field (see Fig. 2). For instance, the vortex shedding from the tail as observed in experiments was also seen in the simulations. This reveals that the parameterized swimmer agrees well with the natural tail-first swimmer.

Furthermore, as a result of this parameterization, various other gaits can be obtained by the modifying parameters of Eq. 1, namely amplitude (θ_0) and phase difference (ϕ) of relative angles. This would allow for transitioning from head-first to tail-first kinematics through the manipulation of the parameterization and enable closer comparisons in flow mechanisms and energetics between these two types of swimming gaits by using the IB-LBM. This would also aid in determining the critical parameters responsible for the transition.

3 Conclusion

Tail-first swimmers such as mosquito larvae display a unique tail-first swimming gait involving high amplitude side-to-side flexural motion. In this type of gait, the posterior end of the body leads the anterior end. The swimming of mosquito larvae was recorded and analysed through particle image velocimetry analysis. A parametric model of tail-first locomotion was developed using an IB-LBM method, and the flow field was compared to that of the natural counterpart. The results reveal the presence of multiple vortices around the natural swimmer and a similar flow field for the parameterized swimmer. This enables the capabilities of such parameterization and its application in further investigation of tail-first gaits.

References

[1] Fish, F. and Lauder, G.V. Passive and Active Flow Control by Swimming Fishes and Mammals. *Annual Review of Fluid Mechanics*, 38:193–224, 2006.

[2] Krishnamurthy P., et al. A Multi-Body Approach for 6DOF Modeling of Biomimetic Autonomous Underwater Vehicles with Simulation and Experimental Results. *In 2009 IEEE Control Applications,(CCA) & Intelligent Control,(ISIC),IEEE*, 1282–1287, 2009.

[3] Videler, J.J. Fish Swimming (Vol. 10). *Springer Science & Business Media*, 1993.

[4] Muller, U.K., et al. Fish Foot Prints: Morphology and Energetics of the Wake Behind a Continuously Swimming Mullet (Chelon Labrosus Risso). *The Journal of Experimental Biology*, 200(22):2893–2906, 1997.

[5] Muller, U.K., et al. How the Body Contributes to the Wake in Undulatory Fish Swimming: Flow Fields of a Swimming Eel (Anguilla anguilla). *Journal of Experimental Biology*, 204(16):2751-2762, 2001.

[6] Borazjani, I. and Sotiropolous, F. Numerical Investigation of the Hydrodynamics of Anguilliform Swimming in the Transitional and Inertial Flow Regimes. *Journal of Experimental Biology*, 212(4):576-592, 2009.

[7] Costello, J. H, et al. The Hydrodynamics of Jellyfish Swimming. *Annual Review of Marine Science*, 13:375-396, 2021.

[8] Granzier-Nakajima, S., et al. A Numerical Study of Metachronal Propulsion at Low to Intermediate Reynolds numbers. *Fluids*, 5(2):86, 2020.

[9] Brackenbury, J. The Vortex Wake of the Free-swimming Larva and Pupa of Culex Pipiens (Diptera). *Journal of Experimental Biology*, 204(11):1855-1867, 2001.

[10] Kikuchi, K. and Mochizuki, O., Consideration of Thrust in Escaping Motion of a Mosquito Larva. *Journal of Aero Aqua Bio-mechanisms*, 1(1):111–116, 2010.

[11] Huang, Q., et al. Streamline penetration, velocity error and consequences of the feedback immersed boundary method. *Physics of Fluids*, 34:097101, 2022.

Swimming in Interactions: Hydrodynamic Analysis of Fish Schools in Low-speed Flows

Alec Menzer[a], Pan Han[a], George Lauder[b] and Haibo Dong[a*]
[a] University of Virginia, Department of Mechanical and Aerospace Engineering, Charlottesville VA, USA[1]
[b] Harvard University, Department of Organismic and Evolutionary Biology, Cambridge MA, USA
[*]Correspondence: *hd6q@virginia.edu*

1 Introduction

Collective swimming is a feature of fish behavior that is though to provide many social, protective, and hydrodynamic benefits. The fixed positions of some model three-dimensional (3D) fishes has been studied, with some important mechanisms such as caudal fin (CF) leading-edge vortex (LEV) enhancement as well as trunk (TK) drag reduction for the downstream placed fish [1]. 2D works have identifed the role of body-body interactions in dense schooling configurations, and even drawn connections between the wake characteristics and the fish performance within the school [2]. Real fishes may undertake many configurations, including dynamically changing positions, though, which we aim to explore in this work involving a real biological fish schooling arrangement.

For this study of the bioloigcal fish school, some modeling and computational techniques are required. First, the bio-data is collected using high-speed videography in which which 2 perspective views of the collective swimming are captured at 100 frames per second. Using Autodesk Maya, we extract the geometry of the giant danios trunk, caudal fin, anal fin (AF), and dorsal fin (DF) to create polygonal surfaces whose motion is governed by a binded skeletal structure. Then, the skeleton is manipulated on a frame-by-frame basis so that the motion of the digital danios matches the real danios in the videos.

To simulate this biological flow scenario, the incompressible Navier-Stokes equations are discretizedon non-conformal Cartesian grids. Solid (TK) and membrane (CF, DF, and AF) representation on this domain is handled by an immersed boundary method (IBM) [3]. A consequence of studying the unsteady bio-data is fish position changes and translations. A tree-topological mesh refinement technique is implemented to parallelize solution convergence on the indicated domain refinement regions immediately surrounding the group of fish [4]. A table of the geometric, kinematic, and flow parameters is outlined in Table 1.

[1]This work was supported by funding by NSF CNS-1931929, ONR N00014-15-1-2234 and the UVA SEAS Carlos and Esther Farrar Fellowship

Table 1: Morphological, kinematic, and flow parameters

	BL	A	T	U_∞	St	Re
Simulation	1.0	0.287BL	1.0	$0.676\frac{BL}{T}$	0.424	8000

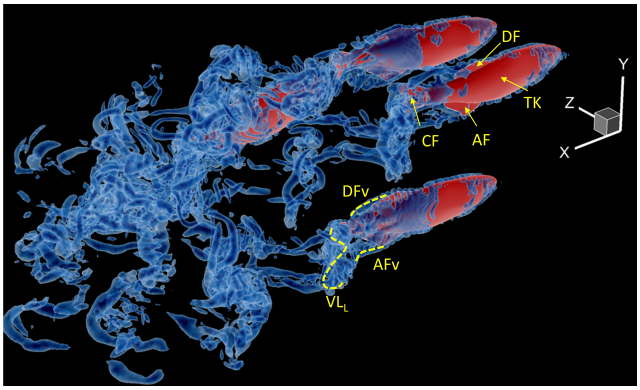

Figure 1: Giant danio bodies & fins with labelled vortex topology

2 Results

The goals of this research are to study the body positioning and hydrodynamic interactions of a real fish school. We will take particular interest in fish 4, (F4), as it traverses across the downstream wakes of the leading fishes 1-3 (F1-3). While the video contains 9 danios, the 4 fish indicated are selected for simulations for their close proximity to each other and expected rich hydrodynamic interactions. Figure 1 identifies the TK, CF, AF, and DF as well as some key flow features generated by the danios, such as the CF shed VL and AF and DF generated AFv and DFv, respectively.

First, preliminary results on the performance of F4 and flow environment are provided. As the undulation kinematics are not periodic we present averaged CF C_T, TK+AF+DF C_D, and total C_{pw} (denoting normalized thrust, drag, and power coefficients respectively) on a stroke-by-stroke basis in Table 2. As F4s position within the school changes on a stroke by stroke basis, this will allow for connections to be drawn between the time varying position and time varying performance.

Table 2: Stroke averaged hydrodynamic coefficients for F4 with all fish present

	1	2	3	4	5
C_T	4.2×10^{-3}	6.4×10^{-3}	8.5×10^{-3}	1.3×10^{-2}	1.6×10^{-2}
C_D	7.4×10^{-3}	7.5×10^{-3}	7.6×10^{-3}	5.1×10^{-3}	4.7×10^{-3}
C_{PW}	2.5×10^{-2}	2.9×10^{-2}	2.7×10^{-2}	4.6×10^{-2}	3.8×10^{-2}

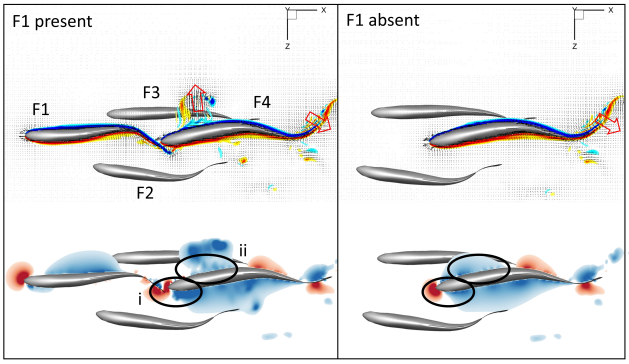

Figure 2: Slice cut of vorticity and velocity (top) and pressure (bottom) around F1 & F4

For the 1st 3 captured strokes, F4 experiences large drag forces, evident in Table 2. F4 is positioned in a dense tandem configuration to the leader, F1, and the removal in F1 leads to a C_D reduction of 18% on average over the 1st 3 strokes. From Figure, where slice cuts of vorticity, pressure and velocity gradients are shown, we observe that a major portion of the drag increase originates from the anterior (head) region. Specifically dominant causes are decrease in thrust inducing low pressure in region (i) due to shed vortex loop from F1 interference and increase in drag inducing low pressure in region (ii) of Figure 2.

Without the leader fish, the F4 C_T does decrease by 3% on average, though, but while CF C_T thrust enhancements do occur in the dense tandem arrangement the C_D penalties are far more significant and consequently, schooling hydrodynamic benefits may be realized at other positions.

Interestingly, F4 performs and undulatory maneuver causing lateral translation out of the wake of the leading F1 and in a vertically stacked, laterally staggered position relative to F2. To study the hydrodynamic function of this out-of-plane arrangement, we perform a simulation with F2 absent. F2s hydrodynamic effect on F4 is minimal for the 1st 3 strokes, however, as the F4 assumes its vertical arrangement the benefit of F2 becomes clear. F4 experiences on average a 13% C_D reduction due to the presence of the vertical/staggered interaction with F2 with. This is accompanied by only slight increases in C_T, though, so the main function of F2s hydrodynamic interaction is drag reduction. The reason for this is stronger suction pressure on the anterior of F4 when F2 is present, evident from the pressure iso-surfaces, slice cuts and surfaces pressure in Figure 3

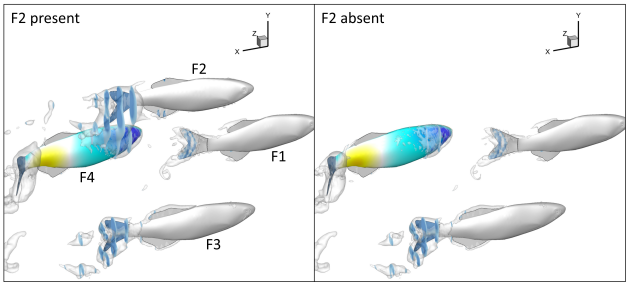

Figure 3: Pressure iso-surfaces (P=-0.05) with slice cut and surface pressure surrounding F4

3 Conclusion

To study the hydrodynamic interactions of fish schooling, this study uses model giant danio geometry and kinematics derived from bio-data. The traversal of F4 was of particular interest due to its position and motion behind the leader fish, while the positions of F1-3 stayed comparatively similar relative to each other.

While the exact behavioral reasons of F4s swimming motion is unknown, the hydrodynamic benefits of its movement are clarified. As previously established, despite C_T enhancements in the tandem arrangement with F1, significant TK+DF+AF C_D penalties are associated. The motion to a vertical/staggered arrangement with F2 provides significant C_D decrease with minimal effect on C_T. In this biological fish school, we have observed an interesting dynamic fish position change which corresponds to a transition from a detrimental to a beneficial hydrodynamic interaction with another fish.

This results described in this extended abstract represent preliminary findings. While many previous works address configurations with just TK/CF, we modelled the AF and DF as well and our next steps will involve quantifying fin-fin and fin-body interactions in this complex schooling environment. Additionally, we are taking advantage of the bio-data to construct model problems to study fish schooling arrangements and kinematics in a more controlled, periodic/steady environment while also collecting more bio-data in which the schooling patterns are steady as well.

References

[1] Jung-Hee Seo and Rajat Mittal. Improved swimming performance in schooling fish via leading-edge vortex enhancement. *Bioinspiration & Biomimetics*, 17:066020, 2022.

[2] Yu Pan and Haibo Dong. Effects of phase difference on hydrodynamic interactions and wake patters in high-density fish schools. *Physics of Fluids*, 34:111902, 2022.

[3] Rajat Mittal and et al. A versatile sharp interface immersed boundary method for incompressible flows with complex boundaries. *Journal of Computational Physics*, 227(10):4825-4852, 2008.

[4] Wei Zhang and et al. An efficient tree-topological local mesh refinement on Cartesian grids for multiple moving objects in incompressible flow. *Journal of Computational Physics*, NEED INFO HERE, 2023.

Optimizing propulsive efficiency at stable positions of in-line schooling by unmatched kinematics

Tianjun Han[a*], Amin Mivehchi[a] and Keith Moored[a]
[a] Lehigh University, Department of Mechanical Engineering and Mechanics, Bethlehem, USA
[*]Correspondence: *tih216@lehigh.edu*

1 Introduction

In nature, many underwater animals propel themselves in schools [1–5]. In-line schooling is a simple configuration of underwater propulsion. Inspired by this biological behavior, thrust and efficiency enhancement has been found to be achieved for underwater propulsors, which can benefit the design of advanced underwater robots with higher cruising speed and lower energy consumption [6–11].

Most of previous research about in-line schooling focuses on swimmers constrained in the stream-wise direction. For pure pitching swimmers, it was found that the follower's thrust and efficiency enhancement or drag reduction can be boosted by more than 50% [9, 12–14]. In addition, Kurt *et al*. [12] and Boschitsch *et al*. [13] both observed band structures in performance maps where the performance enhancement is maximized, which indicates that the optimal phase synchrony varies with gap distance between swimmers.

Real autonomous underwater robots are free to swim, so it's important to explore the hydrodynamics of unconstrained in-line schooling. The most prominent phenomenon that occurs during in-line schooling when swimmers freely swim in the stream-wise direction is the stable position, which is school cohesion driven by fluid-mediated forces when swimmers travel together in a stable configuration. The gap distance under stable positions was found to vary linearly with the phase synchrony between swimmers [7, 15, 16].

However, the fundamental mechanism behind stable positions is still unknown. Also, no one has explored what kinematics control stable position's location like the Lighthill number Li or dimensionless amplitude θ_0. Furthermore, can freely-swimming foils' stable positions be tuned to lie within a desirable performance band structure observed in constrained foil studies? To answer these issues, we will employ our advanced boundary element method (ABEM) to examine two pure pitching foils in an in-line configuration that are free to swim in the streamwise direction.

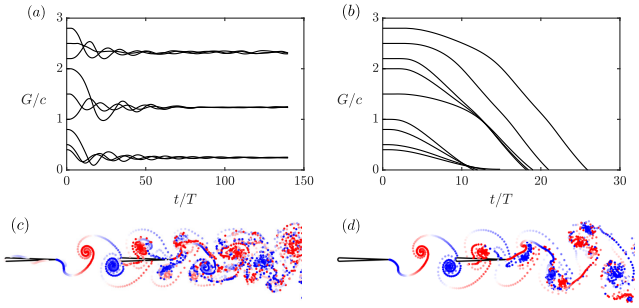

Figure 1: Stable positions disappear when there is no leading-edge separation. (a) Gap distance G normalized by chord length c for simulations with leading-edge separation. (b) Gap distance G normalized by chord length (c) for simulations without leading-edge separation. (c) Wake plots with leading edge separation. (d) Wake plots without leading edge separation.

2 Results

Simulations were performed for cases with a fixed pitching amplitude of $\theta_0 = 7.5°$ and varying Lighthill number and, *vice versa*, with a fixed Lighthill number of $Li = 0.36$ and varying pitching amplitude. The Lighthill number indicates the amount of drag imposed on the swimmer. Here we present results for a typical case ($\theta_0 = 7.5°$ and $Li = 0.36$) in Figure 1. It can be seen that the follower always collides into the leader, in other words, there are no stable positions if there is no leading-edge separation. Also, this phenomenon applies to all kinematics examined in this study.

Figure 2(a) shows stable positions scaled by default wavelength $\lambda_d = U/f$ for varying Li, where f is the oscillating frequency and U is the cruising speed. λ_d has been widely used in previous literature. However, λ_d doesn't provide good collapse of the stable positions. Figure 2(b) shows that a good collapse can be achieved by normalizing stable positions by the actual wake wavelength, λ_a, measured as the distance between two vortices of the same sign in the isolated foil's wake (Figure 2(c)). Also, in Figure 2(d), the actual wavelength makes stable positions with both varying Li and varying θ_0 collapse to the same line, which indicates

[1]This work was supported by MURI program on the hydrodynamics of fish schooling

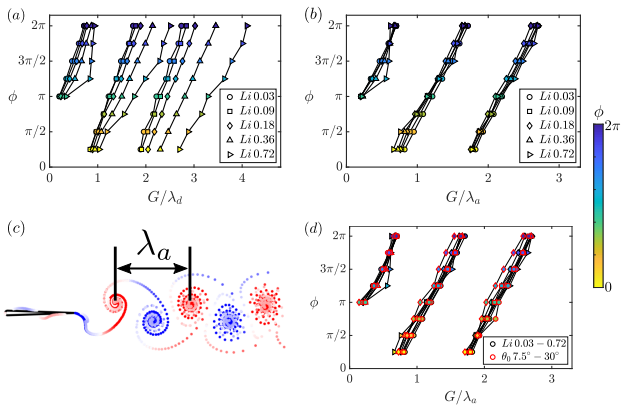

Figure 2: Actual wave length λ_a provides good scaling for stable positions under various control parameters. (a) Gap distance normalized by default wavelength λ_d for varying Li. (b) Gap distance normalized by actual wavelength for varying Li. (c) Illustration about actual wavelength. (d) Gap distance normalized by actual wavelength for both varying Li and varying θ_0.

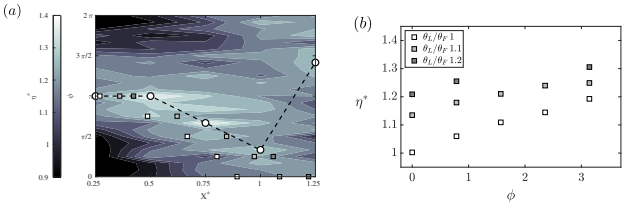

Figure 3: Utilizing unmatched kinematics can push the follower into the desirable band structure and optimize efficiency. (a) stable positions on constrained experimental data. (b) efficiency enhancement under different ratios of leader's amplitude over follower's amplitude.

that the actual wavelength is able to scale stable positions under various control parameters.

Most research examines leaders and followers with the same Lighthill number and pitching amplitude. In one such case [12] experimentally examines two constrained pitching foils in an in-line configuration with $Li = 0.18$ and $\theta_0 = 7.5°$. Figure 3 overlays the stable positions from freely-swimming simulations onto the experimental efficiency data of Kurt & Moored [12]. It can be seen that when swimmers are free to swim they don't swim on the desirable high-efficiency band structure. By increasing the ratio of leader's amplitude to the follower's amplitude from 1 to 1.2, we show that the follower can be pushed into the optimal band structure and increase its efficiency enhancement.

3 Conclusion

In this study, we find that leading-edge separation is a key element to formation of in-line stable positions and stable positions are scaled by the actual wake wavelength. Furthermore, at stable positions, swimmer's propulsive efficiency can be optimized by using unmatched amplitudes between the leader and follower.

References

[1] Liang Li, Máté Nagy, Jacob M. Graving, Joseph Bak-Coleman, Guangming Xie, and Iain D. Couzin. Vortex phase matching as a strategy for schooling in robots and in fish. *Nature Communications*, 11(1):1–9, 2020.

[2] I. Ashraf, R. Godoy-Diana, J. Halloy, B. Collignon, and B. Thiria. Synchronization and collective swimming patterns in fish (Hemigrammus bleheri). *Journal of the Royal Society Interface*, 13(123), 2016.

[3] D. Weihs. Hydromechanics of fish schooling [24]. *Nature*, 241(5387):290–291, 1973.

[4] Intesaaf Ashraf, Hanaé Bradshaw, Thanh Tung Ha, José Halloy, Ramiro Godoy-Diana, and Benjamin Thiria. Simple phalanx pattern leads to energy saving in cohesive fish schooling. *Proceedings of the National Academy of Sciences of the United States of America*, 114(36):9599–9604, 2017.

[5] George V Lauder. In-line swimming dynamics revealed by fish interacting with a robotic mechanism. 2022.

[6] N. S. Lagopoulos, G. D. Weymouth, and B. Ganapathisubramani. Deflected wake interaction of tandem flapping foils. *Journal of Fluid Mechanics*, 903, 2020.

[7] Xingjian Lin, Jie Wu, Tongwei Zhang, and Liming Yang. Phase difference effect on collective locomotion of two tandem autopropelled flapping foils. *Physical Review Fluids*, 4(5):1–20, 2019.

[8] Melike Kurt, Amin Mivehchi, and Keith Moored. High-efficiency can be achieved for non-uniformly flexible pitching hydrofoils via tailored collective interactions. *Fluids*, 6(7):10–14, 2021.

[9] Leif Ristroph and Jun Zhang. Anomalous hydrodynamic drafting of interacting flapping flags. *Physical Review Letters*, 101(19):1–4, 2008.

[10] Melike Kurt, Azar Eslam Panah, and Keith W. Moored. Flow Interactions Between Low Aspect Ratio Hydrofoils in In-line and Staggered Arrangements. *Biomimetics*, 5(2):13, 2020.

[11] Xingjian Lin, Jie Wu, Liming Yang, and Hao Dong. Two-dimensional hydrodynamic schooling of two flapping swimmers initially in tandem formation. *Journal of Fluid Mechanics*, 941:1–17, 2022.

[12] Melike Kurt and Keith W. Moored. Flow interactions of two- and three-dimensional networked bio-inspired control elements in an in-line arrangement. *Bioinspiration and Biomimetics*, 13(4), 2018.

[13] Birgitt M. Boschitsch, Peter A. Dewey, and Alexander J. Smits. Propulsive performance of unsteady tandem hydrofoils in an in-line configuration. *Physics of Fluids*, 26(5), 2014.

[14] Pan Han, Yu Pan, Geng Liu, and Haibo Dong. Propulsive performance and vortex wakes of multiple tandem foils pitching in-line. *Journal of Fluids and Structures*, 108:103422, 2022.

[15] Joel W. Newbolt, Jun Zhang, and Leif Ristroph. Flow interactions between uncoordinated flapping swimmers give rise to group cohesion. *Proceedings of the National Academy of Sciences of the United States of America*, 116(7):2419–2424, 2019.

[16] Sophie Ramananarivo, Fang Fang, Anand Oza, Jun Zhang, and Leif Ristroph. Flow interactions lead to orderly formations of flapping wings in forward flight. *Physical Review Fluids*, 1(7):1–9, 2016.

Tip vortex dynamics in metachronal paddling: effects of varying number of paddles

Mitchell P. Ford and Arvind Santhanakrishnan*
School of Mechanical and Aerospace Engineering, Oklahoma State University, Stillwater, USA
*Correspondence: *askrish@okstate.edu*

1 Introduction

Metachronal paddling is a common strategy used for locomotion and fluid transport in numerous aquatic animals [1–5]. Sequential, reciprocating motion of multiple appendages (or cilia) are used to displace ambient water near the animal, starting from the posterior to the anterior (see Figure 1 for example). The coordinated motion generates a metachronal wave that travels in the direction opposite fluid motion. Aquatic animals that use metachronal paddling for locomotion show wide variation in body and appendage shapes, as well as in the number of appendages. Even within the same species, individuals often undergo drastic changes in body form throughout their development. An example of this is the transition from larval to adult stages in marine copepods, which grow additional body segments (with additional legs on these segments) during the copepodite stages of development.

Previous studies have shown that relative to synchronous motion, pure metachrony (metachronal power and recovery strokes) [3,6] or hybrid metachrony (metachronal power stroke and near-synchronous recovery) [7] can help to augment the propulsive forces. These two locomotion strategies are widely employed by crustaceans. These crustaceans have a number of closely spaced swimming legs (ranging from 2-38) and swim across a wide range of Reynolds numbers (ranging from 40-5000) [8]. The phase lag [9] and spacing [6] between these paddles have both been shown to affect swimming performance, so it is believed that interactions between tip vortices on adjacent paddles are essential to the metachronal paddling strategy. However, the dynamics of these interactions, and the effects of changing the Reynolds number and number of paddles on these interactions are not well understood.

In order to investigate the effect of varying number of paddles on the tip-vortex interactions that occur during metachronal paddling, we used a programmable robotic paddling model (nicknamed the 'krillbot') on which it is possible to prescribe a wide variety of paddling kinematics [7], and which we modified to accommodate a variable number of paddles. First, the effect of paddle tip-speed based Reynolds number (which was varied from 21-54,700) on the swimming performance and the tip vortex circulation was determined using a fixed set of kinematics but varying the stroke frequency and fluid kinematic viscosity. Then, the model was programmed to perform a metachronal paddling stroke with a stroke amplitude of $\theta = 70^\circ$ and variable phase lags between adjacent paddles ranging from $\phi = 0\%$ to $\phi = 15\%$ of the total stroke time. The number of paddles in the system was varied from 1 to 7, and Reynolds numbers from 50 to 200 were achieved by varying the stroke frequency. The test conditions for determining the effects of phase lag and number of paddles are given in Table 1.

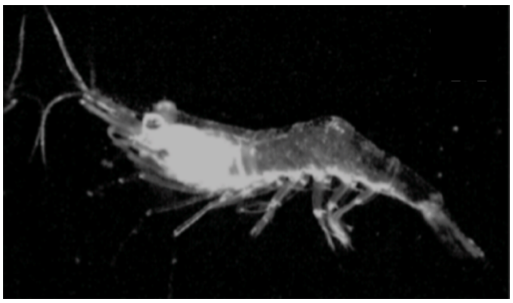

Figure 1: Ghost shrimp swimming. Five pairs of closely spaced swimming legs are stroked metachronally to generate propulsive forces.

Table 1: Experimental test conditions used in the study on the effects of phase lag and number of paddles on tip vortex dynamics.

	No. paddles	Phase lag ϕ (%)	Reynolds number (Re_L)
Conditions	$1,3,5,7$	$0,5,10,15,$	$50,100,200$

2 Results

From the initial study on the effects of Reynolds number on the swimming performance and tip vortex circulation, it was found that both the Reynolds number based on the swimming speed and the Reynolds number based on tip vortex circulation both scale linearly with the Reynolds number based on paddle tip speed. These Reynolds numbers are plotted against each other in Figure 2.

For the second portion of this study, we performed two-dimensional (2D), two-component, time-resolved particle

[1]This work was supported by the National Science Foundation awards CBET 1706762 and OCE 2023675 to A.S.

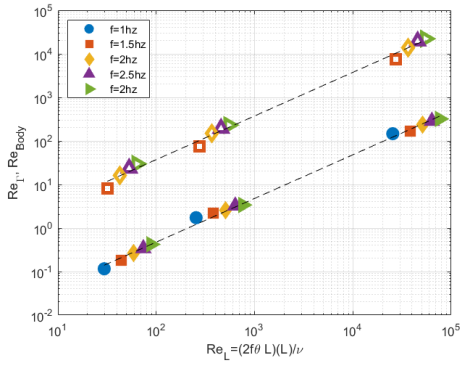

Figure 2: Scaling of Reynolds numbers calculated based on the swimming speed (Re_{Body}) and the tip vortex circulation (Re_Γ) as a function of the Reynolds number based on the prescribed kinematics (Re_L). Solid markers represent Re_Γ while hollow markers represent Re_{Body}.

image velocimetry (2D-2C TR-PIV) on the wake generated by the metachronal paddling robotic model operating under the test conditions given in Table 1. By testing with odd numbers of paddles, we were able to compare flow characteristics around the central paddle on the robotic model, and the interactions that the tip vortex from the central paddle has with the vortices generated at the tips of the adjacent paddles.

Figure 3 shows the velocity field of the paddling system with 1 and 5 paddles at the mid-point of the power stroke. The metachronal nature of the stroke causes adjacent paddles to all be at different points in their stroke cycle, which results in interactions between the tip vortices on the paddles. Figure 3 shows how the vortex generated on the tip of the center paddle in the 5-paddle case differs from the tip vortex in the 1-paddle case. When more paddles are added, the tip vortex stretches and separates from the paddle tip, which helps to dissipate the counter-rotating vortex that was formed on the adjacent (upstream) paddle during the previous recovery stroke. This could help to minimize the drag which is experienced by the adjacent paddle during the recovery stroke, thereby improving the paddling performance. For a given number of paddles, varying inter-appendage phase lag can be used to modulate the hydrodynamic interactions for different needs such as cruising, escaping and feeding.

3 Conclusions

In this study, it was found that Re_{Body}, Re_Γ, and Re_L all scale linearly with each other for a given set of paddle kinematics. Additionally, the number of paddles and the phase lag between adjacent paddles can significantly affect the interactions between the tip vortices, and therefore the swimming performance. Interactions between the wakes of adjacent paddles results in the formation of a large-scale paddling wake, with these interactions changing based on the phase lag and the number of paddles.

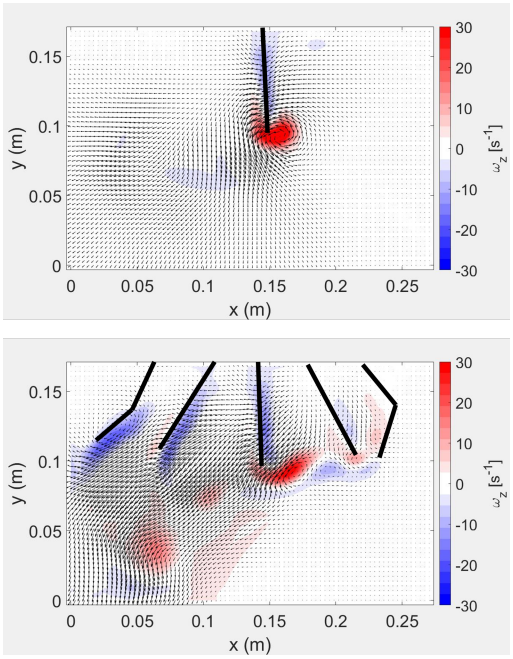

Figure 3: Velocity vectors overlaid on vorticity fields for the 1-paddle and 5-paddle cases at $Re_L = 200$ and $\phi = 15\%$. The shown velocity fields are sampled from the time point where the middle paddle has completed 50% of its respective power stroke.

Further information on the swimming performance and flow field will be presented on the full range of variation of Reynolds number, phase lag, and number of paddles.

References

[1] AT Sensenig, KT Kiger and JW Shultz. Hydrodynamic pumping by serial gill arrays in the mayfly nymph *Centroptilum triangulifer*. *J Exp Biol*, 213:3319-3331, 2010.

[2] MA Sleigh, JR Blake and N Liron. The propulsion of mucus by cilia. *Am Rev Respir Dis*, 137:726-741, 1988.

[3] C Zhang, RD Guy, B Mulloney, Q Zhang and TJ Lewis. Neural mechanism of optimal limb coordination in crustacean swimming. *Proc Natl Acad Sci USA*, 111:13840-13845, 2014.

[4] WL Heimbichner Goebel, SP Colin, JH Costello, BJ Gemmell and KR Sutherland. Scaling of ctenes and consequences for swimming performance in the ctenophore *Pleurobrachia bachei*. *Invert Biol*, 139:e12297, 2020.

[5] LA van Duren and JJ Videler. Excape from viscosity: the kinematics and hydrodynamics of copepod foraging and escape swimming. *J Exp Biol*, 206:269-279, 2003.

[6] MP Ford and A Santhanakrishnan. Closer Appendage Spacing Augments Metachronal Swimming Speed by Promoting Tip Vortex Interactions. *Integr Comp Biol*, 61(5):1608–1618, 2021.

[7] MP Ford, WJ Ray, EM DiLuca, SN Patek and A Santhanakrishnan. Hybrid Metachronal Rowing Augments Swimming Speed and Acceleration via Increased Stroke Amplitude. *Integr Comp Biol*, 61(5):1619–1630, 2021.

[8] M Ruszczyk, DR Webster and J Yen. Dual Phase-Shifted Ipsilateral Metachrony in *Americamysis bahia*. *Integr Comp Biol*, 61(5):1644-1657, 2021.

[9] MP Ford, HK Lai, M Samaee, and A Santhanakrishnan Hydrodynamics of metachronal paddling: effects of varying Reynolds number and phase lag. *R Soc Open Sci*, 6:191387, 2019.

Establishing upstream obstacle-wake-signal correlation in seal whisker array sensing using interpretable neural network

Dariush Bodaghi [a], Yuxing Wang[b], Geng Liu[c],Qian Xue[a,d], Dongfang Liu[b] and Xudong zheng[a,d*]
[a] University of Maine, Department of Mechanical Engineering, Orono, USA[1]
[b] Rochester Institute of Technology, Department of Computer Engineering, Rochester, USA
[c] King's College, Department of Engineering, Wilkes-Barre, USA
[d] Rochester Institute of Technology, Department of Mechanical Engineering, Rochester, USA
*Correspondence: *xxzeme@rit.edu*

1 Introduction

Seal whisker inspired flow sensing is receiving increasing research attention owing to its extraordinary sensitivity, accuracy, and intelligence. Phocid seals can detect and track artificial and biogenic hydrodynamic trails generated 30s ago solely based on the mechanical signals on their whisker arrays [1]. Behavior studies showed that by using the collective array signals resulting from the interactions with oncoming vortices, seals can locate and distinguish upstream obstacles of different sizes and shapes down to 4 cm. It was postulated that seals can correlate temporal-spatial patterns of whisker array signals with surrounding flow patterns and use the correlations for intelligent perception. A few recent studies tried to uncover what flow features may be used by seals for perception. By visualizing the flow fields in a behavior study, Wieskotten et al. [2] suggested that seals might use the combined information of the highest velocities, the steepness of velocity gradients, and the spatial extension of wake to discriminate the size and shape of upstream objects. Using bio-inspired artificial whisker arrays, Glick et al. [3] suggested that the cross-correlation of the bending signals from tandem pairs of whiskers may be used to detect vortices and their passages. Our recent computational study [4] showed that the signal patterns on whisker arrays can reflect the strength, timing, and moving trajectories of upstream vortex-induced jets. Another recent study [5] showed that a supervised deep-learning model is able to infer the position of an upstream object from the tip displacements of whiskers in an artificial whisker array.

Despite the previous studies, signal patterns on entire whisker arrays remains largely unexplored. It remains unclear what wake characteristics are captured by whisker array signals and how seals interpret the signals to perceive surrounding environments. In this study, we aimed to develop an interpretable neural network model for establishing the correlations between the upstream stimulation, wake characteristics and whisker array signals. The acquired knowledge is critical for developing smart flow sensors for accurately perceiving complex flow environments.

[1]This work was supported by NSF under grant number 2144217. The computation was supported by XSEDE project TG-CTS180004.

2 Results

Data Collection: Flow-structure interaction simulations were conducted to generate training data. Figure 1(a) shows the simulation setup. A circular plate of 40 mm in diameter is placed 30 cm in front of the nasal tip of a realistic harbor seal head. A uniform incoming flow of 20 cm/s was applied. An in-house sharp-interface immersed-boundary-method based flow solver was used to simulate the hydrodynamic wake structures. One-way flow-structure interaction simulations were then conducted to obtain the dynamics of each whisker. The details of the computational model can be found in our previous study [4]. Parametric simulations were conducted by systematically varying the plate's location defined by the center coordinates (X, Y) and orientation defined by the two angles (α, β) shown in figure 1(a). Considering the geometric symmetries, five different values are assigned to each parameter as follows: $X = \{-120, -60, 0, 60, 120\}$, $Y = \{0, 50, 100, 150, 200\}$, $\alpha = \{-45^o, -22.5^o, 0^o, 22.5^o, 45^o\}$, $\beta = \{-45^o, -22.5^o, 0^o, 22.5^o, 45^o\}$. This results in a total of 625 parametric cases.

Figure 1 (b) shows the vortex structures induced by the plate in five representative cases: baseline, X=60, Y=50, α = 22.5, and β = 22.5. The wake of the baseline is dominated by two vortex rings alternatively shed with a 180° phase difference. Varying the plate's location only translates the wake. Titling the plate changes the direction of the wake. The wake is directed upward by a positive β which also generates a stronger upper vortex ring and a weaker bottom vortex ring. The wake is directed leftward by a positive α. The translated and oriented wakes interact with the downstream whisker arrays, generating distinct mechanical signals at their roots. The phased-averaged bending moments at the root of each whisker was first calculated, and then averaged in four subzones of the whisker arrays for analysis, as illustrated in figure 1 (c). Figure 1 (c) also shows the obtained time history of the signals at the four subzones in

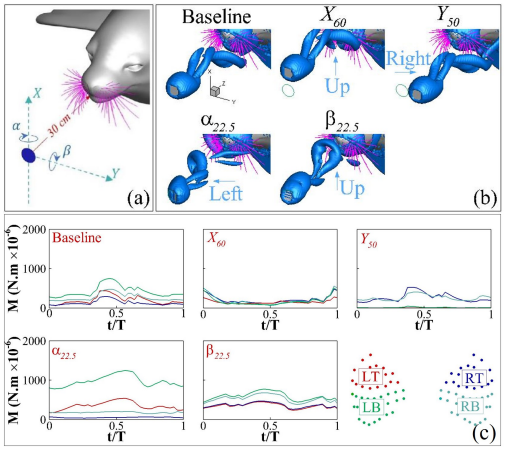

Figure 1: (a) Schematics of simulation setup, (b) Vortex structures in 5 representative cases, (c) time history of the averaged root bending moment signals in each case

the five representative cases. Both the temporal and spatial development of the signals are clearly different among the cases. Overall, the X60 and Y50 cases show weaker signals than the other three case. The α22.5 case has the strongest signal located at the left bottom region.

Neural Network prediction The temporal evolution of the whisker array signals was converted into a series of images in time. In each image, each pixel represents a single whisker, and its color is rendered by the X and Y components of the bending moment at each time instant. A video transformer-based neural network was constructed which takes the images as inputs and outputs the X, Y, α, and β of the corresponding case. The five-fold cross-validation is used to train and validate the network. A Vision Transformer (ViT) [6] network architecture and a factorized self-attention model [7] were employed. The techniques have the advantages of capturing both temporal and spatial changes of the inputs and more importantly, evaluating the importance of each pixel in capturing the changes. Therefore, it enables constructing attention maps consisting of important whiskers from which the major signal patterns for decision making can be recognized for interpretation. The interpretable learning is essential for understanding the fundamental sensing mechanisms.

Figure 3 (a) compares the network outputs to their ground truth in all the validation cases. The prediction accuracy is 94.4%, suggesting that the location and orientation of the upstream obstacle is successfully inferred by the network. Figure 3(b) plots the attention map of the whisker arrays in the five representative cases with the darkness of the blue color representing the level of importance of each whisker. In the baseline case, the importance is more evenly distributed among the whiskers. In the cases of X60 and β22.5, the important whiskers are in the upper tip of the two whisker arrays, corresponding to the translation and tilting of the wakes. In the cases of Y50 an α22.5, the important

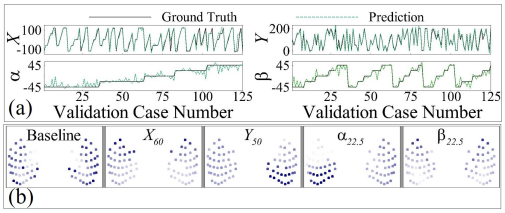

Figure 2: (a) Network prediction of locations and orientations of the plate against the ground truth. (b) The inferred attention map of the whisker arrays in the five cases.

whiskers are at the bottom of the whisker arrays, also corresponding to the changes of the wake trajectories.

3 Conclusion

In this study, an interpretable neural network based deep learning model was developed for predicting an upstream obstacle's location and orientation by using the bending moment signals on the whisker arrays induced by the wake of the obstacle. A vision transformer network architecture and a factorized self-attention model were employed for capturing attention maps of whiskers from which major signal patterns in decision making can be identified for establishing correlations between upstream obstacle information, wake characteristics and signal patterns, which is essential for understanding the fundamental mechanisms of smart flow sensing of seal whisker.

Flow-structure interaction simulations were performed to generate the training data of the wake and whisker array dynamics induced by an upstream plate with varied location and orientation. The neural network was successfully trained and shows a 94.4% accuracy using five-fold cross validation. The inferred attention maps of the important whiskers correspond well to the changes of the wake structures and trajectories. The results suggest that the proposed neural network algorithm can perceive important characteristics of an upstream object with hydrodynamic sensing as well as to decode complex signal-disturbance correlations for intelligent flow sensing.

References

[1] Dehnardt, et al. Hydrodynamic trail-following in harbor seals(Phoca vitulina). *Science*, 293(5527):102-104, 2001.

[2] Wieskotten, et al. Hydrodynamic discrimination of wakes caused by objects of different size or shape in a harbour seal. *J. Exp. Biol*, 214:1992-30, 2011.

[3] Glick, et al. Fluid-structure interaction of flexible whisker-type beams and its implications for flow sensing by pair-wise correlation. *fluids*, 6(3):102, 2021.

[4] Liu, et al. Flow-signal correlation in seal whisker array sensing. *Bioinspiration & Biomimetics*, 17(1):016004–14, 2021.

[5] Elshalakani, et al. A deep-learning model for underwater position sensing of a wake's source using artificial seal whiskers. *Sensors*, 20(12):3522–19, 2020.

[6] Dosovitskiy, et al. An image is worth 16x16 words: Transformers for image recognition at scale. *arXiv*, 2010.11929, 2020.

[7] Arnab, et al. Vivit: A video vision transformer. *ICCV*, (pp. 6836-6846), 2021.

Propulsive performance of oscillating plates with time-periodic flexibility

David Yudin[a], Tyler Van Buren[a*], and Daniel Floryan[b*]
[a] University of Delaware, Department of Mechanical Engineering, Newark, DE, USA
[b] University of Houston, Department of Mechanical Engineering, Houston, TX, USA
*Correspondence: *vanburen@udel.edu*, *dfloryan@uh.edu*

1 Introduction

The grace and beauty displayed by swimming animals have captivated biologists and engineers alike for many decades. Through over 500 million years of evolutionary pressure, swimmers have converged on common features and behaviours different from traditional human-made swimming machines. There is the possibility that animals' propulsive mechanisms are inherently highly efficient, maneuverable, and stealthy, which has led to intense study of the fluid dynamics of biological swimmers [1].

Through observations and measurements of animals, it is known that swimmers can control their fin curvature, displacement, area, and stiffness [2, 3]. It stands to reason that swimmers may be able to utilize their muscles on the time scale of the oscillation of their propulsors to tune performance, e.g., by dynamically changing the stiffness of their propulsors. In this work we will show that, from a purely hydrodynamic perspective, time-varying stiffness leads to propulsive benefits over constant-stiffness propulsors [4, 5].

2 Problem setup

Consider a two-dimensional, inextensible plate in a fluid flow, as sketched in Figure 1. The plate has thickness d and length L, and we assume that it is thin ($d \ll L$) and that its maximum deflection is small, with its slope $|Y_x| \ll 1$. The deflection Y of the plate is then governed by the Euler-Bernoulli beam equation. The plate has density ρ_s, time-varying Young's modulus $E(t)$, and second moment of area $I = wd^3/12$, where w is its width. The plate is immersed in an inviscid and incompressible fluid with density ρ_f and freestream speed U. The fluid imparts a hydrodynamic load onto the plate, given by the pressure difference across the plate, Δp. The perturbation velocity is assumed small, and the flow is attached.

We heave and pitch the plate at its leading edge at a frequency f with amplitudes h_0 and θ_0, respectively. We also let the stiffness vary in time, with twice the frequency of actuation. Key dimensionless parameters are

$$R = \frac{\rho_s d}{\rho_f L}, \quad S(t) = \frac{E(t)d^3}{\rho_f U^2 L^3}, \quad \sigma = \frac{\pi f L}{U}, \quad h_0^* = \frac{h_0}{2L}, \quad \theta_0. \tag{1}$$

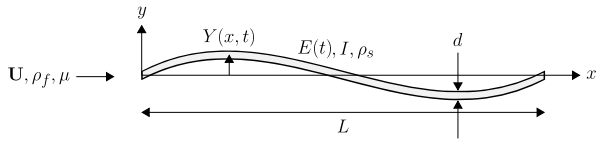

Figure 1: A two-dimensional plate with time-varying Young's modulus moving through a fluid.

We will investigate the effect of the amplitude of the stiffness oscillation in depth. This amplitude is denoted by S_0; $S_0 = 0.5$ means that the stiffness oscillates with an amplitude that is 50% of the mean stiffness. The phase of the stiffness oscillation relative to the leading-edge actuation is ϕ_S.

We solve for the motion of the plate by adapting the method in [6]. The main quantities of interest are the dimensionless thrust, C_T, and the efficiency, η.

3 Results

For brevity, we only describe representative results for a heaving plate here. When the time-varying stiffness is in phase with the motion ($\phi_S = 0$), the plate is stiffer at the extremity of the heave motion and softer at the mid-stroke. Conversely, when the time-varying stiffness is out of phase with the motion ($\phi_S = \pi$), the plate is softer at the extremity of the heave motion and stiffer at the mid-stroke. Both phase differences lead to an increased trailing edge amplitude around the first resonant frequency of the plate, at least in a region of parameter space where Euler-Bernoulli-type behaviour is observed. When $\phi_S = 0$, the motion lags that of the equivalent constant-stiffness plate, while when $\phi_S = \pi$, the motion leads that of the equivalent constant-stiffness plate.

The thrust and efficiency are shown in Figures 2 and 3, respectively. Both plots show the effect of time-varying stiffness. The frequency range is centered about the first resonant frequency of a plate with a mean stiffness of $\overline{S} = 20$. Generally, adding periodic stiffness leads to a continuous and substantial increase in thrust as the stiffness oscillation amplitude increases, with up to a 35% increase in thrust when $|S_0| = 0.5$. For $\phi_S = 0$, the resonance is shifted to higher frequencies, while for $\phi_S = \pi$ the resonance is

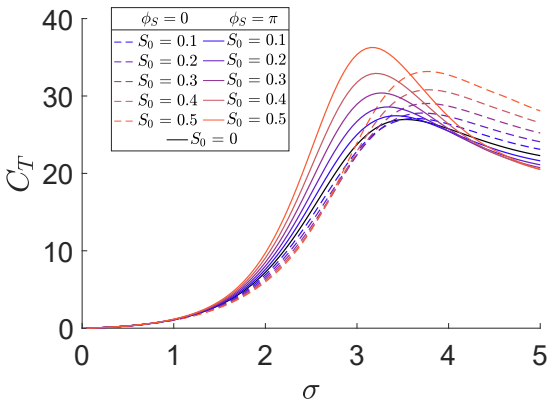

Figure 2: Thrust for a heaving plate with gradually increasing stiffness oscillation amplitude. The mean stiffness is $\overline{S} = 20$, $h_0^* = 1$, and $R = 0.01$.

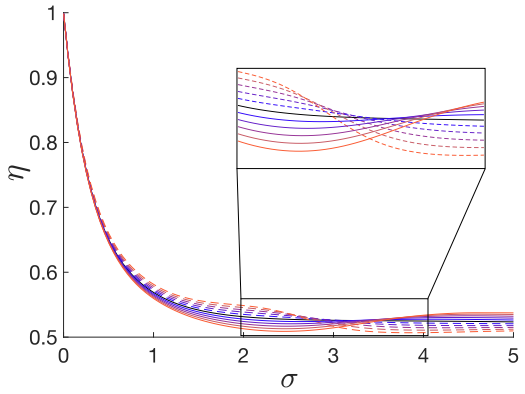

Figure 3: Same as Figure 2, but for efficiency.

shifted lower. Past the resonant frequency, the $\phi_S = \pi$ case yields slightly lower thrust than the baseline case. The trailing-edge amplitude follows nearly the same pattern as the thrust does, suggesting that the main mechanism through which time-varying stiffness increases thrust is an increase in trailing-edge amplitude. For constant-stiffness plates, thrust also generally displays the same behaviour as trailing-edge amplitude.

For efficiency, we observe the opposite behavior. Performance benefits for $\phi_S = 0$ occur below the baseline resonant frequency, while for $\phi_S = \pi$ they occur above the baseline resonant frequency. For both phases of the stiffness oscillation, there are frequencies yielding greater efficiency than the constant-stiffness plate, as well as frequencies yielding lower efficiency. The effect of time-varying stiffness on the efficiency is much milder than it is for thrust, however, as time-varying stiffness only changes the efficiency by $\Delta\eta \leq 0.05$. This suggests that time-varying stiffness may be a strategy to substantially increase thrust without much, if any, penalty in efficiency.

The time-varying stiffness leads to cross-frequency coupling in the kinematics, which does not occur for a constant-stiffness plate in the low-amplitude regime that we consider. The timing of the stiffness oscillation is crucial in determining the resulting propulsive performance. We find that thrust generally increases the most relative to the constant-stiffness case when $\pi/2 < \phi_S < 2\pi/3$, and efficiency boosts peak near $\phi_S \approx 3\pi/2$. However, it is important to note that time-varying stiffness may also lead to performance hindrances depending on the frequency.

Lastly, we note that when σ and S_0 are large enough, a Floquet analysis reveals the emergence of tongues of instability in the S_0-$\overline{S}$ plane. Such tongues are characteristic of parametrically excited systems. While instability usually has a negative connotation in engineering applications, these unstable regions could potentially lead to greatly enhanced propulsive performance since an instability would produce large deflections from small actuation. Our linear method cannot capture the saturation of the instabilities, but we believe that exploring the unstable regions via experiments or nonlinear simulations is a promising direction.

4 Conclusion

In this work, we explored the impact of time-periodic stiffness on an oscillating plate in a free stream—a model for swimmers. We found that the oscillation in stiffness has a significant impact on the thrust and kinematics. The impact on thrust is most prominent, with time-periodic stiffness increasing thrust by up to 35% at the first resonant peak. The impact on efficiency is, on the other hand, mild, with the efficiency changing by $\Delta\eta \leq 0.05$. The changes in thrust and efficiency are often negatively correlated. These performance changes are consistent across heaving, pitching, and combined pitch-and-heave motions.

While there may not yet be concrete evidence of biological swimmers actively changing their stiffness on the time scale of their kinematic frequency, we have presented strong evidence that there would be a hydrodynamic benefit to doing so. This may be a promising avenue to pursue when designing robotic swimmers.

References

[1] A. J. Smits. Undulatory and oscillatory swimming. *Journal of Fluid Mechanics*, 874:P1, 2019.

[2] D. S. Adams and F. E. Fish. Odontocete peduncle tendons for possible control of fluke orientation and flexibility. *Journal of Morphology*, 280(9):1323–1331, 2019.

[3] F. E. Fish and G. V. Lauder. Passive and active flow control by swimming fishes and mammals. *Annual Review of Fluid Mechanics*, 38:193–224, 2006.

[4] G. Shi, Q. Xiao, and Q. Zhu. Effects of time-varying flexibility on the propulsion performance of a flapping foil. *Physics of Fluids*, 32(12):121904, 2020.

[5] H. Hu, J. Wang, Y. Wang, and H. Dong. Effects of tunable stiffness on the hydrodynamics and flow features of a passive pitching panel. *Journal of Fluids and Structures*, 100:103175, 2021.

[6] M. N. J. Moore. A fast Chebyshev method for simulating flexible-wing propulsion. *Journal of Computational Physics*, 345:792–817, 2017.

5 Session E: Vortex Dynamics - 1

Turbulence Interaction with Re-configurable Fractal Tree Canopies

Aojia Jiang[a] Oluwafemi Ojo[a] and Kourosh Shoele[a*]
[a] Department of Mechanical Engineering, Florida State University, Tallahassee, FL, USA[1]
*Correspondence: *kshoele@fsu.edu*

1 Introduction

The interaction between crops and wind is continuous and strongly coupled process. Crop plants move in the wind and show a wave-like movement pattern. The wave is oftentimes visible as it is represented as a bending progressive motion over the plants known as Honami for crops and Monami motion for underwater vegetation. In Dupont's paper in 2010 [1], universal characteristics of turbulent flow over vegetation canopies are identified from the flow simulations, following the previous observations in situ and wind tunnel experiments [2]. Later, He *et al.* [3] and Wang *et al.* [4] numerically studied the submerged vegetation canopy as a single object or a group of connecting spherical units. Yet, most numerical analyses on this topic focus on homogeneous unbranched flexible stems while real vegetated canopies have much more complex shapes and follow particular fractal behavior.

In this study, we employ a new computational modeling approach to study flow interaction with branched trees. The computational model contains three components to represent this complex fluid-structure interaction problem. We use the large eddy simulation to model the flow. For the structural system, the trees are represented as a multilink system and its connecting rotational joints. The geometrical pattern of trees is assumed to be similar and follows a self-similar fractal law while their placement and orientations are considered to be random. By formulation of the tree dynamics based on joint angles, a compact dynamic representation is formulated using the Newton-Euler technique. The aerodynamic drag forces are computed and expressed as normal and tangential force components over the length of each branch. The communication between the fluid and solid domains is accomplished using the regularized kernel delta function.

The validation of the model is done by comparison with results in Dupont 2011 [1]. Overall, similar parameters to this study are assumed and the only difference between studies is that in the current work rather than the use of a rigid cylinder and one mode of vibration to model a crop, a four-link crop model is employed. The results of the streamwise velocity component, the momentum flux, and Reynolds stress, etc. from the new model compare well with the previously reported values.

[1]This work was supported by funding_NSF under grant number CBET-1943810

The canopy deformation pattern and turbulent flow statistics are investigated by varying the flexibility and the branching ratio. In addition, the distance between the trees is modified in both spanwise and streamwise directions to explore the role of canopy configuration on mean energy transfer.

2 Results

Table 1 and figure 1 show the computational setup and sample snapshots of streamwise velocity are shown in figure 2 for three different tree flexibility represented with non-dimensional Cauchy number Ca.

We first investigate the turbulent boundary layer interaction over rigid fractal trees to study its intrinsic flow properties. It is observed that the canopy ($z/H_T \leq 1$) is enveloped by a wake region of reduced velocity in the streamwise direction, which is typical of flows over bluff bodies. Above the canopy, a strong mixing process occurs characterized by the presence of turbulent sweeps and ejections. At the canopy top, the flow is dominated by sweep events that penetrate the canopy [1], causing effective momentum and turbulent energy transfer into the canopy. At $z/H_T \leq 0.8$, the time-averaged flow velocity clearly shows a reduced streamwise velocity region in the canopy region, while at $0.8 \leq z/H_T \leq 1$, the flow velocity rapidly increases, signifying the region where the bulk of momentum transfer between the atmosphere and canopy occurs.

Furthermore, to account for the effect of flexibility, three cases are investigated based on our previous investigation of fractal trees [5]. Semi-rigid tree case ($Ca = 0.1, \lambda_A = 2.6$) with limited flexibility, flexible case with optimal tree branching ($Ca = 0.5, \lambda_A = 2.6$), and flexible trees with more deflection at the trunk ($Ca = 0.5, \lambda_A = 2.0$). Here $\lambda_A = A_M/A_D$ is the fractal law between the mother branch and one of its daughter branches. The bulk of the momentum transfer between the environment and the canopy occurs just above the canopy. In order to further dissect the fluid-structure interaction of the problem, we separate the velocity into three regions (gust, fast, and slow) based on velocity fluctuation (u') similar to [6] and quantify the deformation of trees below those regions. When $u' > 2\alpha u_{rms}$ the velocity is classified into gust regions, velocity within $\alpha u_{rms} < u' < 2\alpha u_{rms}$ is classified as fast flow, and when $u' < -\alpha u_{rms}$, the flow is tagged as the slow flow condition. Here, u_{rms} is the root mean square of u' and α is the threshold value. In this study, we fix α as 1.5.

Table 1: Computational setup.

	Non-dimensional paradmeters
Domain size	$17H_T \times 7H_T \times 7H_T$
Fluid grid	$401 \times 161 \times 161$
Separation Distance (S_x, S_y)	$0.8H_T$
Slenderness Ratio (D_T/L_T)	0.3
Ca	$0.2, 0.66, 2$
Branching Ratio (λ_A)	$2.6, 2.0$

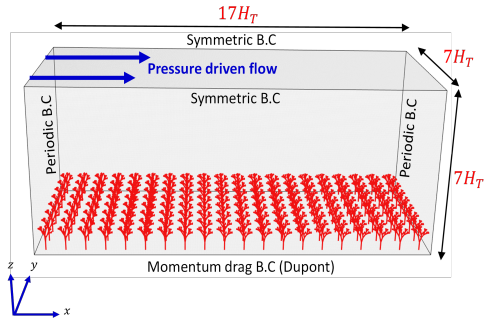

Figure 1: Comuputional setup.

A Honami phenomenon is observed and further investigated. It is found that the tree canopies are bending and extending in the gust flow region, starting to come back in the fast flow region and returning to the original position in the slow flow.

The gust region has the highest streamwise velocity magnitude and it is evident from the vertical velocity that gust and fast velocity satisfy the sweep condition ($u' > 0$, and $w' < 0$), while the slow flow satisfies the outward interaction condition ($u' > 0$, and $w' > 0$). The flow velocities also show the same trends for more flexible tree cases ($Ca = 0.5$, at $\lambda_A = 2.0$, and 2.6). However, with increased tree flexibility, the gust profile becomes more uniform above the canopy. Also, all the velocity profiles show less modification at the top of the canopy with increased tree flexibility, which signifies that larger intermittent eddies have sufficient energy to penetrate deep into the canopy.

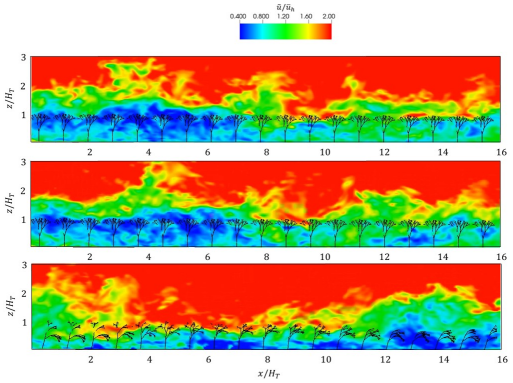

Figure 2: Streamwise velocity with Ca number at 0.2, 0.66 and 2 and the tree patterns.

3 Conclusion

The LES-fractal canopy model effectively captures the turbulent characteristics within and above the canopy. Trees within the gust regions undergo more elevated static and dynamic deflections than those within fast and slow flow regions. Energetic large intermittent eddies penetrate flexible canopies better than rigid ones. The dominance of sweeps at the canopy top signifies the importance of gusts in canopy flows and this modifies the momentum transfer in flexible canopies.

It was observed that trees within the gust region experienced the most significant deformation, followed by trees in the fast-flow region. Also, sweeps dominate the gust and fast flow regions, while the slow flow region is dominated by outward interaction.

Furthermore, this study shows that the momentum transfer in a flexible tree canopy differs from rigid canopies and is affected by the fractal nature of the branching trees. The momentum flux and streamwise Reynolds stress of flexible trees present a mild gradient around the canopy top, signifying more momentum absorption from the inertial sublayer. The energy budget and spectral analysis reveal how the energy is exchanged between the flow and flexible trees and explain why sweeps over flexible trees penetrate further down the canopy, up to half the tree height, significantly different from rigid cases. Further exploration of different separation distances between trees also discloses how the trees' arrangement affects the energy transfer between the different layers and canopies.

References

[1] S Dupont, F Gosselin, Charlotte Py, Emmanuel De Langre, Pascal Hemon, and Yves Brunet. Modelling waving crops using large-eddy simulation: comparison with experiments and a linear stability analysis. *Journal of Fluid Mechanics*, 652:5–44, 2010.

[2] Kyaw Tha Paw U, Yves Brunet, Serge Collineau, Roger H Shaw, Toshihiko Maitani, Jie Qiu, and Lawrence Hipps. On coherent structures in turbulence above and within agricultural plant canopies. *Agricultural and Forest Meteorology*, 61(1-2):55–68, 1992.

[3] Sida He, Han Liu, and Lian Shen. Simulation-based study of turbulent aquatic canopy flows with flexible stems. *Journal of Fluid Mechanics*, 947:A33, 2022.

[4] Jianyu Wang, Guojian He, Subhasish Dey, and Hongwei Fang. Fluid–structure interaction in a flexible vegetation canopy in an open channel. *Journal of Fluid Mechanics*, 951:A41, 2022.

[5] Oluwafemi Ojo and Kourosh Shoele. Branching pattern of flexible trees for environmental load mitigation. 17(5):056003, 2022. Publisher: IOP Publishing.

[6] Li-Hao Wang, Guo-Zhen Ma, Chun-Xiao Xu, Hyung Jin Sung, and Wei-Xi Huang. Wall-attached structures over a traveling wavy boundary: Scalar transport. *Physics of Fluids*, 33(10):105115, 2021.

[7] E Inoue. Studies of the phenomena of waving plants ("honami") caused by wind part 1. mechanism and characteristics of waving plants phenomena. *Journal of Agricultural Meteorology*, 11(1):18–22, 1955.

Clarifying the timescales of starting vortex pinch-off and formation

Ilambharathi Govindasamy[a] and Abel-John Buchner[a*]
[a] Laboratory for Aero- and Hydrodynamics, Delft University of Technology, The Netherlands[1]
*Correspondence: *a.j.buchner@tudelft.nl*

1 Introduction

Acceleration of a body in a fluid causes circulation shedding, which impacts the forces on the object and the final characteristics of the vortex wake; the timing of dissociation, or vortex "pinch-off", is of particular interest. A timescale of $T_f^* = U_p t/c \approx 4$ has been observed [1], beyond which a vortex no longer accepts additional circulation. This has been explained in terms of the Kelvin-Benjamin variational principle that requires the kinetic energy provided by the generating body to be greater than that in the forming vortex [2]. Typically an impulse-normalised energy, $E^* = E_v/\sqrt{\mathbf{\Pi}^3}$ [1], where I is the vortex's hydrodynamic impulse, Γ is the circulation, and the vorticity-based kinetic energy is given by the integral of the product of the stream function and vorticity, $E_v = \pi \iint_{core} \Psi\omega \; dxdr$, has been used to indicate this energy ratio. In propulsive vortices, the moments of maximum circulation and vortex separation are simultaneous with minimal E^*. A recent study [3] assessed the relevance of T_f^* to the case of drag vortices, concluding that E^* relates to the spatial arrangement of vorticity in the wake, and its plateau does not coincide with vortex pinch-off. A key difficulty in studying vortex pinch-off is the ambiguity in defining the moment of vortex dissociation with the generating body. Often, this ambiguity is rooted in the Eulerian flow classification methods used, which lack objectivity due to their frame and threshold dependence. A more useful pinch-off definition can be obtained by employing Lagrangian Coherent Structures to separate the flow field into dynamically distinct regions based on the finite time Lyapunov exponent (FTLE). The dynamical dissociation of a starting vortex with the generating body, or pinch-off, can be demarcated by a topological saddle point, identified by the intersection of positive and negative FTLE ridges. The initial motion of this saddle point serves as an indicator of the pinch-off event [4].

In this study, we revisit the order of events associated with starting vortex pinch-off from an accelerated body. Three possible signifiers of pinch-off are assessed: The initiation of motion of the FTLE saddle point, a minimum value of E^* being attained, and the cessation of growth of the ratio, $\hat{E} = 2E_{core}/E_{plate}$, where the kinetic energy, $E_{core} = \frac{1}{2}\rho \iint_{core}(u^2+v^2)dA$, per unit span within the starting vortex structure was integrated over a region of positive Q-criterion bounded upstream by the topological saddle point in the FTLE field (fig. 1B) and the kinetic energy per unit span supplied by the plate is given by $E_{plate} = \frac{1}{2}\rho U_{plate}^2(\frac{\pi}{4}c^2)$ [5]. By combining Eulerian and Lagrangian views, our work supports the idea that E_{min}^* does not signify pinch-off, and clarifies its significance as a measure of compactness of the starting vortex and thus of the shear layer's roll-up timescale. We highlight the importance of $\hat{E}$, in determining vortex pinch-off as a phenomenon of dissociation from the generating body, distinct to, and preceding the roll-up of the circulation into a starting vortex. Our data additionally suggest qualitative variation in starting vortex topology at very low accelerations. When $\hat{E}$ has not yet reached unity by the vortex roll-up timescale, $T^*(E_{min}^*)$, the shear layer rolls up nevertheless, followed shortly thereafter by pinch-off.

[1]This work was supported by NWO VENI Grant 18176

2 Method

A $60 \times 30 \times 3$mm flat plate was started from rest in a $500 \times 240 \times 135$mm tank (fig. 1A) of $69V/V\%$ glycerol/water mix. The plate underwent constant acceleration until a target Reynolds number, $Re_c = U_p c/\nu$. Accelerations chosen were such that each of two target Reynolds numbers, $Re_c = 150$, 225, were achieved within a dimensionless acceleration time of $T_a^* = 0.3$, 1.0, or 4.0. Acceleration was non-dimensionalised as $\alpha = ac^3/\nu^2$, and expressed as $\sqrt{\alpha} \sim Re_c(t)/\sqrt{T^*}$. The wake was measured at the plate's centreplane, using two-component, planar particle image velocimetry (PIV). Hollow glass spheres (Sphericel 110-P8, $\rho = 1100\text{kg/m}^3$, $\bar{d} = 11.7\mu\text{m}$) were used as seeding. Particle images were recorded using a single LaVision Imager pro HS camera (2016×2016 pixel CMOS sensor, Nikon-35mm lens) at a rate of between $200-400$Hz, depending on motion case. Illumination at wavelength, $\lambda = 527nm$, was provided by a pulsed Nd-YAG laser (Quantronix, Darwin Duo). The images were analysed using multi-grid cross-correlation with initial and final interrogation window sizes of 48×48 and 24×24 pixels, respectively, with 50% overlap, resulting in 17 vectors per chord length.

3 Results

Time-series of vorticity are plotted in fig. 1C, for each of $\sqrt{\alpha} = 290$ and 80. In the higher acceleration case, a starting vortex rapidly forms, while in the lower acceleration case the circulation remains elongated in the form of a shear-layer until at least $T^* > 5$. The FTLE saddle point location is indicated in each panel. As in [4], the saddle point is observed to remain in the vicinity of the generating body for a time before suddenly departing downstream. For $\sqrt{\alpha} \geq 100$, saddle point motion begins at $T^* \approx 3$, but is observed to be delayed at lower accelerations (fig. 1D, bottom).

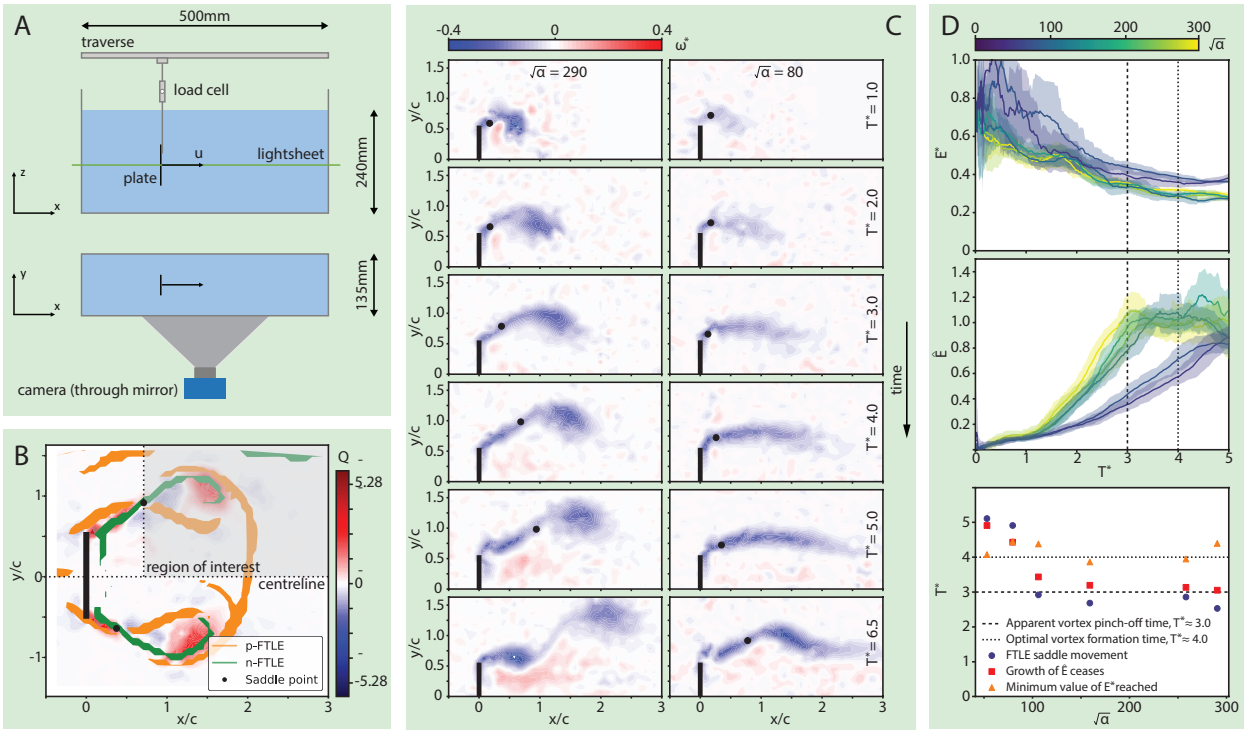

Figure 1: (A) Experimental setup, (B) Example field combining Q-criterion with FTLE ridges, and indicating saddle point locations, (C) Example time series, with FTLE saddle marked, indicating qualitative topological difference between high and low $\sqrt{\alpha}$ cases. (D) E^* (top) and $\hat{E}$ (middle) variation with T^*. Bottom: Observed temporal locations of critical events.

The impulse-normalised energy, E^*, is plotted in fig. 1D (top). The solid curves represent a moving average, across a window of 21 datapoints, with shaded regions indicating ± 1 standard deviation within the averaging window. In agreement with the observations of de Guyon and Mulleners [3], the magnitude of E^* diminishes with time before reaching a minimum of $E^* \approx 0.3$. This occurs consistently at $T^* \approx 4$ (fig. 1D, bottom), in agreement with the universal optimal vortex formation time widely discussed in the literature [1] but is delayed compared to the beginning of FTLE saddle point motion. The higher plateau value, $E^* \approx 0.4$, observed in low acceleration cases is indicative of the qualitatively different vortex topology at these accelerations, in which the circulation is more spread in the direction of motion as compared with the higher acceleration cases where the shear layer rolls up into a starting vortex much earlier (fig. 1C).

Although, E^*_{min} at $T^* \approx 4$ is in line with optimal vortex formation time, it is unclear why the FTLE saddle moves earlier, around $T^* \approx 3$. The kinetic energy ratio, $\hat{E}$ provides an answer: Its value increases monotonically until it reaches approximately unity. In accordance with the Kelvin-Benjamin principle, the vortex can at this point no longer absorb energy from the generating body, and $\hat{E}$ subsequently ceases to grow. The rate of increase of $\hat{E}$ with respect to T^* is only weakly dependent on acceleration for high acceleration cases, but is significantly reduced at lower accelerations. This results in unity being reached at roughly $T^* \approx 3$ for acceleration, $\sqrt{\alpha} \geq 100$. At lower accelerations, unity is not reached until after T^* (E^*_{min}). Across all cases measured, the moment at which $\hat{E}$ reaches unity and ceases to grow is more closely associated with the moment of initial FTLE saddle point motion than with the time of minimum E^*. This indicates that energy arguments, as per Kelvin-Benjamin, are indeed the reason for vortex pinch-off. After $\hat{E}$ has saturated at $T^* \approx 3$ and the saddle point motion has begun, the kinetic energy of the vortex core and feeding shear-layer are dissociated from the plate. This pinch-off precedes a rearrangement of the downstream circulation, which continues to roll up into a compact starting vortex on a formation timescale of $T^* \approx 4$, as indicated by E^*. In low acceleration cases, our data indicate that the shear layer downstream of the FTLE saddle grows slowly and does not roll up until after the formation time of $T^* \approx 4$, when roll-up occurs spontaneously and is followed shortly by pinch-off leading to qualitatively different vortex wake structure.

References

[1] M. Gharib, E. Rambod, K. Shariff. A universal time scale for vortex ring formation. *J. Fluid Mech.*, 360:121–140, 1998.

[2] M. Shusser, M. Gharib. Energy and velocity of a forming vortex ring. *Phys. Fluids*, 12(3):618–621, 2000.

[3] G. de Guyon, K. Mulleners. Scaling of the translational velocity of vortex rings behind conical objects. *Phys. Rev. Fluids*, 6 024701, 2021.

[4] Y. Huang, M. Green. Detection and Tracking of Vortex Phenomena Using Lagrangian Coherent Structures. *Exp. Fluids*, 56(147):1–12, 2015.

[5] P. Saffman. Vortex Dynamics. *Cambridge University Press*, 1995.

Cluster-based predictive model for nonlinear dynamics

Nitish Arya[a*] and Aditya Nair[a]
[a] University of Nevada, Department of Mechanical Engineering, Reno, NV 89557[1]
[*]Correspondence: *narya@unr.edu*

1 Introduction

In the last decade, data-driven modeling has played a crucial role for the real-time prediction and control of engineering systems such as aircraft wings and wind turbines. The complexity of the model and their predictive accuracy vary on the methodology adopted to construct them. In applications involving high-dimensional fluid flows, techniques such as proper orthogonal decomposition (POD) [1] and dynamic mode decomposition (DMD) [2] are used to distill physically important energetic or dynamically important features (spatial modes) of the flow. By projecting these features onto the governing equations, reduced-order ordinary differential equation models for the temporal evolution of the features have been successfully constructed [3]. However, rare short-term events tend to be ignored by the above modal decomposition techniques as they primarily rely on the frequency content of the features.

An alternate approach to building reduced-order models was pioneered by Kaiser et al. [4] in which important features of the system were coarse-grained into K clusters, each with a representative centroid. The transitions between the clusters were then modeled as a probabilistic Markov process providing a linear evolution of the probability distribution. The simplicity of the cluster-based representation enables the identification of important transitions in amplitude and phase of the time-series signals that make up the feature space and is modular enough to incorporate full high-dimensional snapshots to limited sensor measurements. This formulation has led to the development of deterministic–stochastic network models [5] and suppression of extreme drag events in the turbulent bluff body flows [6].

In the present work, a novel cluster-based decomposition method is presented for describing the nonlinear (forced) dynamics of complex systems. The time-series measurement data is collected by simulating the dynamical system with added external forcing and coarse-grained using k-means clustering. This process results in K centroids that serve as basis vectors for our decomposition method, akin to spatial modes in modal decomposition methods. By projecting the feature space time series onto the centroids, the associated cluster coefficients (akin to modal temporal coefficients) are deduced using a sparse regression. This results in a deterministic nonlinear predictive model for the evolution of the time-series measurements as opposed to probabilistic linear Markov models as in the previous works. The present formulation is especially attractive for model-based control of the system dynamics. The decomposition method is presented for the canonical model for chaotic dynamics, the Lorenz system, and then applied to time-series data from a fluid-structure interaction system.

[1]This work was supported by Department of Energy Early Career Research Award (Award no: DE-SC0022945, PM: Dr. William Spotz) and the National Science Foundation AI Institute in Dynamic systems (Award no: 2112085, PM: Dr. Shahab Shojaei-Zadeh)

2 Results

The collection of measurements in an $n-$dimensional feature space: $x_1(t), x_2(t), x_3(t), ..., x_n(t)$ is segmented via k-means clustering to obtain K centroids. For each feature space co-ordinate x_r, the cluster basis vector is given by $C^{x_r} = [C_1^{x_r}\ C_2^{x_r}\ C_3^{x_r} \cdots C_K^{x_r}]^T \in \mathbb{R}^{K\times 1}$, where $r = 1,2,3...n$. We can then describe each feature space co-ordinate as

$$x_r(t) = P^{x_r}(t) C^{x_r} \quad \text{where } r = 1,2,3....n \tag{1}$$

where $P^{x_r} \in \mathbb{R}^{1\times K}$ are trainable coefficients describing the feature space evolution. The cluster coefficients P^{x_r} are trained from the data and the obtained centroids using a sparse regression procedure [7]. In this procedure, a library of polynomial functions of the input data $\Theta(X,U)$ is created, where $X = [P^{x_1}\ P^{x_2} \cdots P^{x_r}]$ are the cluster coefficients for feature space co-ordinates and U is the input forcing. The derivative of the coefficients are regressed with the library functions to obtain optimum value of the coefficients Ξ as

$$\dot{X} = \Theta(X,U)\Xi. \tag{2}$$

As in the SINDy method, sequential thresholding is used to construct a sparse model for the dynamics of the cluster coefficients.

2.1 Lorenz System

The Lorenz system with external forcing u is given by

$$\frac{dx}{dt} = \sigma(y-x) + u, \quad \frac{dy}{dt} = x(r-z) - y, \quad \frac{dz}{dt} = xy - bz \tag{3}$$

where $\sigma = 10, b = 8/3, r = 28$. The characteristic butterfly attractor of the Lorenz system is divided into 10 clusters by k-means clustering as shown in Fig. 1. The first lobe consists of clusters 4, 1, 7, 5, and 2 and the second lobe consists of clusters 8, 6, 10, and 3 with a transition cluster 9 through which switching between the two lobes occurs.

The data collected from the numerical simulation, the cluster centroids and the forcing term are used to predict the cluster coefficient dynamics via a SINDy model as shown in Fig. 1. The model is trained for 10 seconds with a Schroeder-phased harmonic forcing and then validated for the next 10 seconds with a sinusoidal forcing. For the present case, the polynomial order for the library Θ is taken as 4.

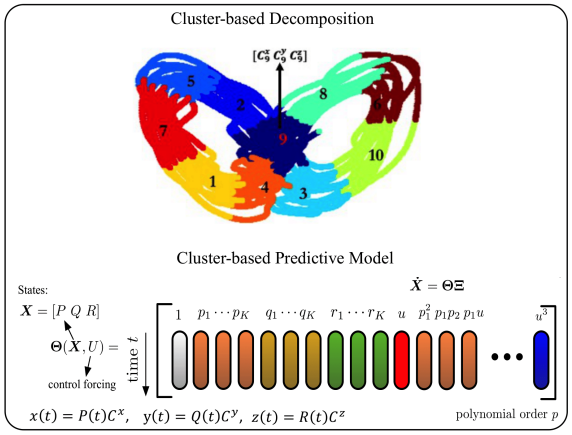

Figure 1: Cluster-based predictive model for a Lorenz system.

The cluster transition matrix P_{ij} representing the probability of transition from cluster i to cluster j and the cluster residence time τ_{ii}, representing the probability of the trajectory to remain in a particular cluster, are presented in Fig. 2. The highest residence time is obtained for cluster 9. We see a good agreement of transition probabilities and the cluster residence time between the simulated system and the predictive model.

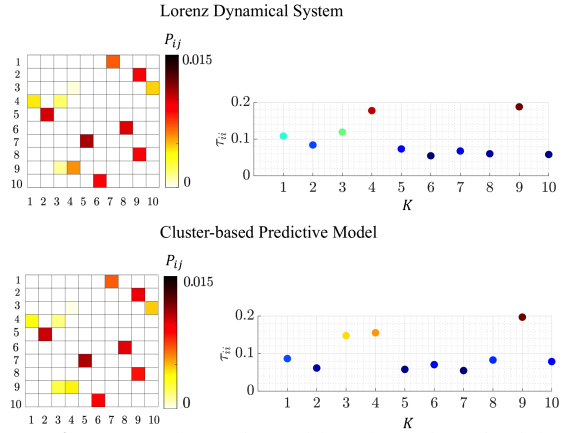

Figure 2: Comparison of transition dynamics of original Lorenz System (top) and SINDy model (bottom).

2.2 Fluid Structure Interaction

We also employ the current methodology for data collected from a numerical simulation of 2D laminar flow over a compliant flat plate [8]. Here, we consider an Euler-Bernoulli beam at an angle of attack of 35 degree with compliance, $K_b = 0.3125$. The Reynolds number of the incoming flow is 100. We add a sinusoidal localized force to the Navier-Stokes equation to mimic a blowing/suction type actuator near the separation location over the plate. Cluster decomposition is applied over the time-series data of aerodynamic forces C_L,C_D and strain energy(S) as seen in Fig. 3. Separate SINDy models are trained for fluid and structure properties by employing C_L and C_D for fluid and strain energy S and its time derivative,$\dot{S}$, for structure. It is clear from Fig. 3 that the model prediction is in good agreement with the DNS results.

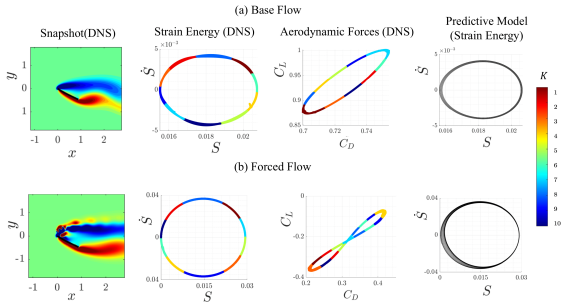

Figure 3: Cluster-based prediction for a unsteady baseline and forced fluid-structure interaction system.

3 Conclusion

We presented a cluster-based model for predicting the nonlinear dynamics of complex systems. The method was demonstrated for a (forced) Lorenz system and then for a 2D laminar flow over a compliant flat plate with momentum injection external forcing. The dynamics of both systems are efficiently captured by the predictive model. As the data is obtained by employing a time-dependent forcing for both systems, coupling of the present framework with a model-predictive control strategy is currently in progress.

References

[1] Gal Berkooz, Philip Holmes, and John L Lumley. The proper orthogonal decomposition in the analysis of turbulent flows. *Annual review of fluid mechanics*, 25(1):539–575, 1993.

[2] Peter J Schmid. Dynamic mode decomposition of numerical and experimental data. *Journal of fluid mechanics*, 656:5–28, 2010.

[3] Bernd R Noack, Marek Morzynski, and Gilead Tadmor. *Reduced-order modelling for flow control*, volume 528. Springer Science & Business Media, 2011.

[4] Eurika Kaiser, Bernd R Noack, Laurent Cordier, Andreas Spohn, Marc Segond, Markus Abel, Guillaume Daviller, Jan Östh, Siniša Krajnović, and Robert K Niven. Cluster-based reduced-order modelling of a mixing layer. *Journal of Fluid Mechanics*, 754:365–414, 2014.

[5] Hao Li, Daniel Fernex, Richard Semaan, Jianguo Tan, Marek Morzyński, and Bernd R Noack. Cluster-based network model. *Journal of Fluid Mechanics*, 906, 2021.

[6] Aditya G Nair, Chi-An Yeh, Eurika Kaiser, Bernd R Noack, Steven L Brunton, and Kunihiko Taira. Cluster-based feedback control of turbulent post-stall separated flows. *Journal of Fluid Mechanics*, 875:345–375, 2019.

[7] Steven L Brunton, Joshua L Proctor, and J Nathan Kutz. Discovering governing equations from data by sparse identification of nonlinear dynamical systems. *Proceedings of the national academy of sciences*, 113(15):3932–3937, 2016.

[8] Andres Goza and Tim Colonius. A strongly-coupled immersed-boundary formulation for thin elastic structures. *Journal of Computational Physics*, 336:401–411, 2017.

Dynamics of a flexible sheet interacting with the vortices in the wake of a cylinder forced to rotate

Adrian Carleton[a] and Yahya Modarres-Sadeghi[a*]
[a] University of Massachusetts, Department of Mechanical and Industrial Engineering, Amherst, MA, USA[1]
*Correspondence: *modarres@umass.edu*

1 Introduction

We discuss how desired dynamical responses can be imposed on a flexible sheet placed in flow without directly interacting with the structure but by manipulating the frequency and strength of vortices that are generated upstream. We do this by controlling the shedding and strength of vortices that interact with the flexible sheet through imposing a forced rotation to a cylinder that is placed upstream.

When a flexible structure is placed in flow it could oscillate due to its interactions with the incoming flow of fluid (the response of a flag in wind, for example) (a summary is found in [1–3].) The incoming flow that interacts with the flexible structure could be uniform (i.e., non-disturbed and with a uniform flow velocity across the field) resulting in problems such as Vortex-Induced Vibrations (VIV) (e.g., [4, 5], galloping and flutter [6]), or it could be the already-disturbed flow due to its previous interactions with an object placed upstream, resulting in Wake-Induced Vibration (WIV) problems [8], in which the downstream structure interacts with vortices that are shed from the upstream object and reacts to those vortices. Naturally, the frequency of vortices that are shed from the upstream object dictates the response of the downstream flexible structure.

If, however, the cylinder is externally forced to rotate, then the shedding of vortices in its wake can be controlled. For example, if the cylinder is forced to rotate in one direction, the wake can be deflected to one side, and for larger rotation rates, the vortices can be entirely suppressed. If the cylinder is forced to rotate periodically, the frequency and strength of the shed vortices can be controlled by the rotation of the cylinder, and sometimes vortices much larger than the cylinder diameter can be shed in the wake. By forcing the cylinder to rotate at different frequencies or following different waveforms, one can create several other shedding patterns in the wake. Then it can be expected that if an object is placed in this controlled wake, its motion can be controlled as well.

In our recent work [7], we conducted a series of experiments in which we placed a hydrofoil in the wake of a cylinder and controlled its motion by imposing rotations on the cylinder.

[1]This work is partially supported by the National Science Foundation under grant number CMMI 2024409.

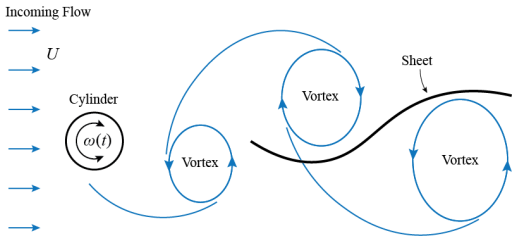

Figure 1: A schematic of a flexible sheet placed in the wake of a cylinder forced to rotate. By forcing the rotation of the upstream cylinder, we control the frequency and strength of the vortices that interact with the flexible structure, thereby controlling the response of the flexible sheet.

The vortices that were shed from the cylinder were shed at a frequency equal to the rotation frequency. Then the hydrofoil that was placed in the wake found its way in between the vortices that were shed and whose frequency and strength were imposed by the rotation of the upstream cylinder.

Here, we discuss how the response of a flexible sheet that is placed in the wake of a cylinder forced to rotate can be influenced by controlling the shedding of the upstream vortices.

2 Results

For these experiments, a 1.9 cm diameter, 46 cm long aluminum cylinder was fixed to a Velmex PK245 stepper motor through a Vex VersaPlanetary 5:1 reduction gearbox and suspended vertically in the test section of a recirculating water tunnel. A flexible sheet was placed in the wake of the cylinder (figure 1). The sheet was attached to a string at its leading edge and the string was fixed at the two ends of the test section of the water tunnel. The rotation of the motor, and in turn the cylinder, was controlled by the stepper motor controller, programmed in MATLAB. Position of the cylinder was measured by an encoder, and response of the sheet was captured using a high speed camera. The sheet edge was tracked using the object tracking feature in Adobe After Effects and the collected data were processed in MATLAB. Flow visualization was conducted using Bubble Image Velocimetry technique.

We conducted a series of experiments using this setup to study the response of a flexible sheet in the wake of a cylin-

der forced to rotate periodically. Sample results of these experiments are shown in figure 2. We first considered the case where the cylinder was fixed. In this case, as expected, vortices were shed in the wake of the cylinder at a frequency predicted by the Strouhal law (which says the shedding frequency increases linearly with the incoming flow velocity). The flexible sheet placed in the wake then interacted with these vortices and found its way in between them. Since the shedding frequency was governed by the incoming flow velocity (which was kept constant in these experiments) the interactions between the flexible sheet and the vortices could not be controlled by the user. We then applied a known frequency of rotation to the upstream cylinder (we picked 1 Hz, only as a sample). By forcing the upstream cylinder to rotate at 1 Hz, we then controlled the shedding frequency of the vortices in its wake, which were shed at 1 Hz as well. Then an external force with a frequency of 1 Hz was applied to the downstream sheet, and the sheet oscillated at that frequency (the middle plot in the figure), resulting in relatively large-amplitude oscillations at a prescribed frequency. We then increased the frequency to 2 Hz as another sample point and as a result shed vortices at the frequency of 2 Hz in the wake, which then excited the sheet at that same frequency and resulted in very small amplitude oscillations in the sheet (the plot on the right in the figure). The differences in the responses in the right two plots of figure 2 are very obvious. They have been obtained at the same incoming flow velocity, and only by changing the frequency of rotation of the upstream cylinder.

We also investigated the influence of asymmetric forcing, which would impose asymmetric response on the flexible sheet. We conducted experiments with an asymmetric input waveform in which the forcing frequency in the counter-clockwise rotation was four times that in the clockwise rotation. The result was that the response of the sheet switched from oscillations to almost static within each cycle of cylinder's rotation, i.e., a combination of responses similar to those shown in the two right plots of figure 2, but obtained within the same cycle.

3 Conclusion

We have conducted a series of experiments to show how the response of a flexible sheet placed in the wake of a cylinder can be controlled by forcing the cylinder to rotate at prescribed frequencies. By doing so, the vortices that are shed in the wake of the cylinder follow the prescribed frequency of the rotating cylinder and therefore the sheet responses at a desired frequency. We also investigated the response of a flexible sheet in the wake of a cylinder forced to rotate with a 4:1 ratio between the CCW and CW rotations, thereby creating an asymmetric response in the sheet and we showed that using this method, non-trivial responses can be imposed on the sheet.

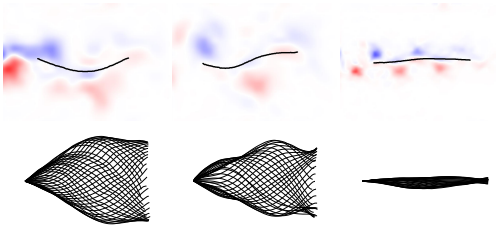

Figure 2: A flexible structure in the wake of a rotating cylinder: left: the cylinder is fixed and the sheet navigates its way in between the vortices that are shed from the fixed cylinder. Middle: The cylinder is forced to rotate at a given frequency and the shed vortices impose the same frequency on the sheet. Right: The cylinder is forced to rotate at a higher frequency, resulting in a higher shedding frequency, which then imposes a higher frequency oscillation on the sheet and decreases its amplitude of oscillations.

References

[1] Païdoussis, M.P. *Fluid-Structure Interactions: Slender Structures and Axial Flow, Vol. 1*, San Diego, CA: Academic Press Inc, 1998.

[2] Païdoussis, M.P. *Fluid-Structure Interactions: Slender Structures and Axial Flow, Vol. 2*, Academic Press, London, 2004.

[3] Païdoussis, M.P., Price, S.J., de Langre, E. *Fluid-structure interactions: cross-flow-induced instabilities*, Cambridge University Press, 2010.

[4] Bourguet, R., Modarres-Sadeghi, Y., Karniadakis, G.Em, Triantafyllou, M.S. Wake-body Resonance of Long Flexible Structures is Dominated by Counterclockwise Orbits, *Physical review letters*, 107(13), 134502, 2011.

[5] Bourguet, R. Flow-induced vibrations of a rotating cylinder in an arbitrary direction *Journal of Fluid Mechanics*, 860, 739-766, 2019.

[6] Blevins, R.D. *Flow-induced vibration*, Krieger Pub. Co., Malabar, Fla., 1990.

[7] Currier, T.M., Carleton, A.G., Modarres-Sadeghi, Y. Dynamics of a hydrofoil free to oscillate in the wake of a fixed, constantly rotating or periodically rotating cylinder, *Journal of Fluid Mechanics*, 923, A21, 2021.

[8] Assi, G.R.S., Bearman, P.W., Meneghini, J.R. On the wake-induced vibration of tandem circular cylinders: the vortex interaction excitation mechanism, 661 *Journal of Fluid Mechanics*, 365–401, 2010.

Vortex formation in an instationary rotating cylinder with barrier

Lyke E. van Dalen[a*], Edwin F.J. Overmars[a] and Jerry Westerweel[a]
[a] Laboratory for Aero-and Hydrodynamics, Delft University of Technology, The Netherlands[1]
[*]Correspondence: *l.e.vandalen@tudelft.nl*

1 Introduction

Recent experiments [1] have indicated inconsistencies with the current force estimation of impulsively started objects. It seems evident that more research is needed to fully understand the behavior of fluids a high rate of change in their motion. Gaining knowledge on the behavior and resulting forces of these unsteady flows is important for numerous applications; impact forces on structures, propulsion in sports [1], but also insect flight [2] are relevant examples.

The current work focuses on the the influence of acceleration in rotational systems. Few movements that we see around us are purely rectilinear, and to be able to understand more complicated flows and paths it is important to study purely rotational flows. An example of a pure rotational movement can be found in the inner ear. Forces resulting from the angular acceleration of a sudden head movements, rather than from the rotation itself, have shown to be leading for deformation of the *cupula* [4]. This is the structure responsible for movement to signal conversion in the vestibular system [3]. A result from this research can be seen in fig. 1a, which, when presented in a rotating frame of reference, shows us the vortex partially responsible for this deflection.

To further study these kind of vortices and the forces they exert in rotational systems an experimental setup is designed. We use a simplified representation of the inner ear, consisting of a cylinder with a partial barrier, shown in fig. 1b.

2 Experimental setup

The designed setup consists of a cylinder with radius r of 7.2 cm on a turntable (Zaber X-RSB120AD-E01). The cylinder has no lid (and thus a free surface), and the camera (GoPro HERO7) is pointed down. Within the cylinder there is a barrier fixed at the cylinder wall. The camera is mounted to the cylinder, moving along with it. Hence, we observe the flow in a rotating frame of reference with non-stationary angular velocity $\Omega(t)$.

An initial rotational velocity Ω_0 is chosen and we wait for the flow to reach a steady state. At t_0 the rotational velocity is increased as $\Omega(t) = \Omega_0 + at$, with rotational acceleration a. This initiates spin-up and the formation of a tip vortex.

[1]This work was supported by ERC-AdG Grant 884778 'Impulsive Flows'

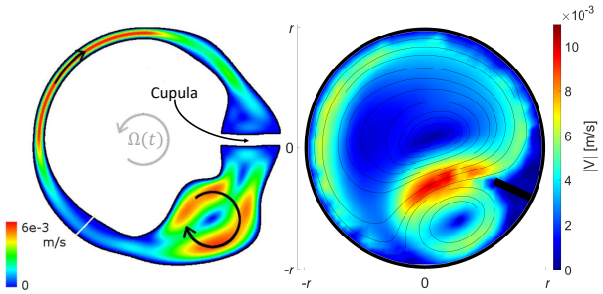

(a) **(b)**

Figure 1: **(a)** Simulations (CFD, FEM and FSI) of the flow in the vestibular system due to a non-stationary angular velocity $\Omega(t)$. Results from [4]. **(b)** The velocity field including streamlines in a rotating cylinder with barrier ($t = t_0 + 22$s). Both **(a)** and **(b)** are in a rotational frame of reference.

3 Results and future work

Using particle tracking velocimetry (PTV), we are able to estimate the particles paths and with that the local particle velocities. PTV allows for a high spatial resolution even in presence of strong shear [5], which is crucial considering the velocity field around the barrier is our main focus.

In fig. 2 the formation and breakdown of the tip vortex is shown, including the steady state solution for $t < t_0$ in fig. 2a. It can be noticed that the velocity field is divided into cells of which the size is determined by the barrier. This is something that is commonly seen with nonaxisymmetric geometries [6, 7]. When the rotational velocity is increased a vortex appears at the tip of the barrier, with the total circulation Γ_{total} and tip velocity $|\mathrm{V}|_{\text{tip}}$ reaching a maximum around $t = t_0 + 7$s. After this, while continuing to grow in size, the vortex reaches the wall and later detaches from the barrier while breaking down.

In fig. 3 a comparison is made of our experiments with the potential flow solution [7]. For $t = t_0 + 2$s the streamlines are plotted in the relative frame of reference, as seen in fig. 3a. The cellular structure is still clearly visible and, except for the flow around the barrier, the change in comparison to the steady state solution is not directly clear. In fig. 3b the steady state solution is subtracted, and there is a clear agreement of these streamlines with the potential flow solution in fig. 3c. However, from fig. 2b it can be noticed that the

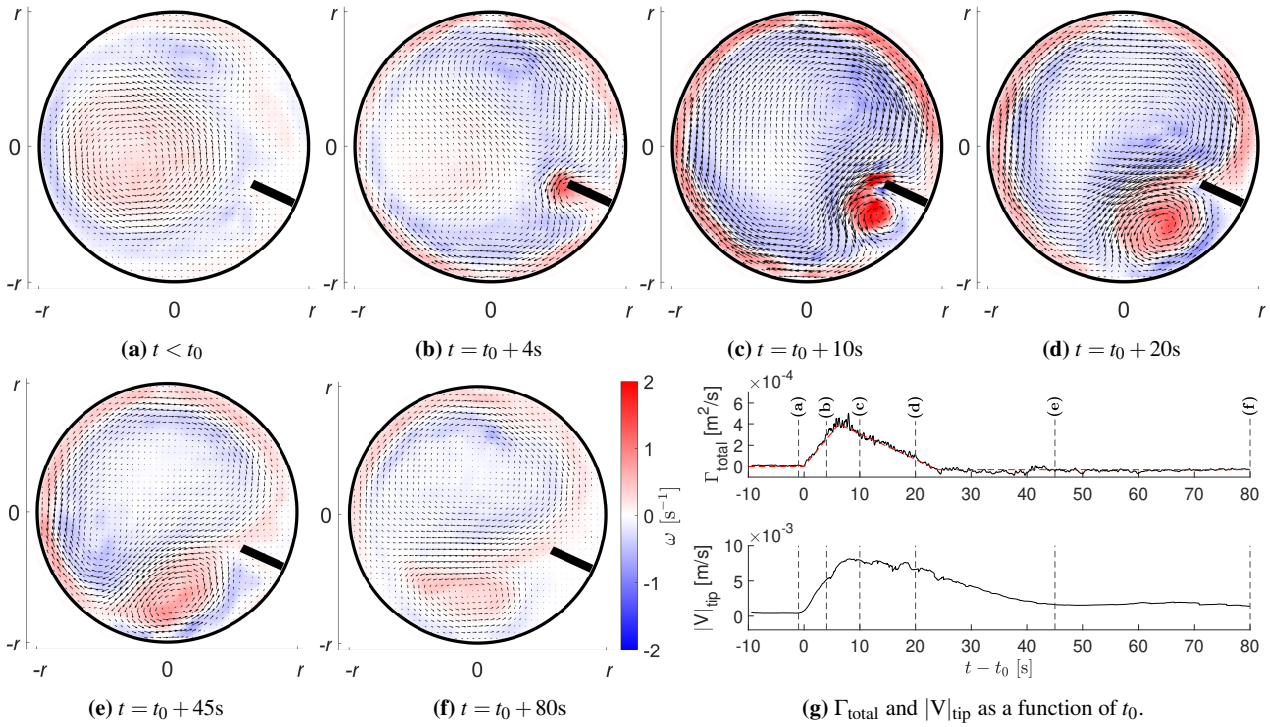

(a) $t < t_0$ **(b)** $t = t_0 + 4$s **(c)** $t = t_0 + 10$s **(d)** $t = t_0 + 20$s

(e) $t = t_0 + 45$s **(f)** $t = t_0 + 80$s **(g)** Γ_{total} and $|\text{V}|_{\text{tip}}$ as a function of t_0.

Figure 2: (a)-(f) The velocity field and vorticity during the formation and breakdown of the tip vortex. At $t = t_0$ the angular velocity is changed. The colorbar in **(f)** represents the vorticity ω in all figures, including fig. 3. **(g)** Here the total circulation (Γ_{total}) and tip velocity ($|\text{V}|_{\text{tip}}$) is shown over time. An asymmetrical ramp profile is observed in the circulation.

solutions start to differ.

We are currently investigating how long and in what situations the comparison in fig. 3 holds, with the extension to other quantities, e.g. the forces. For a straight path these have shown to be clearly deviating from potential flow theory, even at high Reynolds numbers, as well as being affected by the magnitude of the acceleration [1].

References

[1] E.J. Grift, N.B. Vijayaragavan, M.J. Tummers and J. Westerweel. Drag force on an accelerating submerged plate. *Journal of Fluid Mechanics*, 866:369–398, 2019.

[2] J.D. Eldredge and A.R. Jones. Leading-Edge Vortices: Mechanics and Modeling. *Annual Review of Fluid Mechanics*, 51:75–104, 2019.

[3] J. Goyens and P. Aerts. Why the semicircular canals are not stimulated by linear accelerations. *Bioinspiration & Biomimetics*, 14(5):056004, 2019.

[4] J. Goyens, M.J.B.M. Pourquie, C. Poelma and J. Westerweel Asymmetric cupula displacement due to endolymph vortex in the human semicircular canal *Biomechanics and Modeling in Mechanobiology* 18:1577–1590, 2019.

[5] R.J. Adrian and J. Westerweel. Particle image velocimetry. *Cambridge university press*, 2011.

[6] P.W. Duck and M.R. Foster. Spin-Up of Homogeneous and Stratified Fluids. *Annual Review of Fluid Mechanics*, 33:231–263, 2001.

[7] J.A. van de Konijnenberg, T.L. Wessels and G.J.F. van Heijst. Spin-up in a circular tank with a radial barrier. *Physics of Fluids*, 8(8):, 2048–2059, 1996.

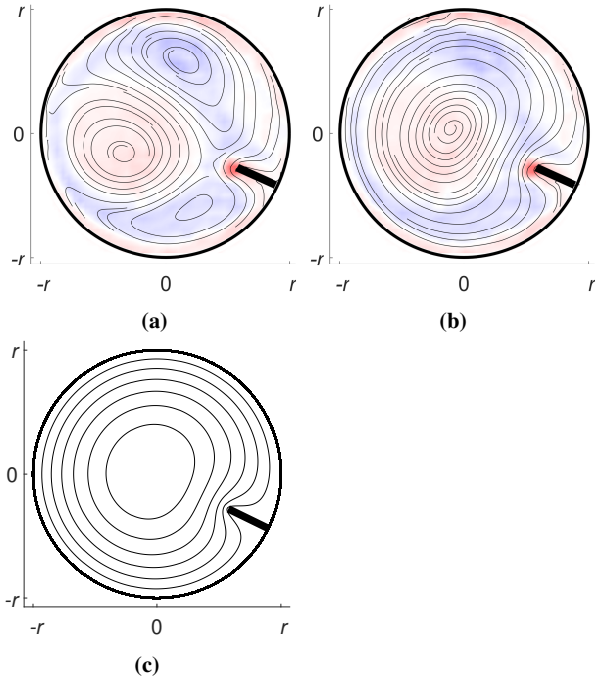

Figure 3: Streamlines and vorticity at $t = t_0 + 2$ s. **(a)** As measured in the rotational frame of reference. **(b)** After subtraction of the steady state flow solution for $t < t_0$. **(c)** Streamlines of the potential flow solution for spin-up in a cylinder with barrier [7].

Geometrical influence on decay rates of low-order azimuthal modes in axisymmetric wakes

Dylan Caverly[a*] and Jovan Nedić[a]
[a] McGill University, Department of Mechanical Engineering, Montréal, Canada [1]
[*]Correspondence: *dylan.caverly@mail.mcgill.ca*

Introduction

The dynamics of coherent structures in wakes are of particular interest in aero- and hydrodynamic applications, as they have a relationship with the drag on a body. Understanding the primary coherent structures within a wake and their dynamics can help us further understand and develop models, which can be used for practical design considerations, such as reducing the drag on vehicles, or vehicle identification. If structures within vortex-dominated flows contain specific characteristics, we may also be able to use this information for identification, spatialization, and localization applications.

One approach to modelling a wake is through modal decomposition. Reduced-order models can, and have, been used to estimate the turbulent kinetic energy and Reynolds stresses in a wake, by considering only a finite amount of modes, reducing computation demands. The wake is typically dominated by two azimuthal modes: the vortex shedding $(m = 1)$ mode, and the double-helix $(m = 2)$ mode, which contains roughly $20-35\%$ of the total fluctuating energy of the wake [1, 2]. Each azimuthal mode has distinct characteristics, such as a peak at a specific Strouhal number $St = flU^{-1}$, where f is the frequency, l is a characteristic length, and U is the free-stream velocity. The $m = 1$ mode, for example, is associated with vortex shedding. In the near field, these structures dominate the flow and have a Strouhal number of $St \approx 0.11$. Far downstream, the $m = 2$ mode eventually dominates the flow. This mode has its maximum energy at very low frequencies $St \longrightarrow 0$ [3].

Johansson & George experimentally examined the wake behind a disk with Reynolds number $Re = 26,400$ using pairs of hot-wire measurements at fixed radial distances and angular separations at different downstream locations [2]. By examining the cross-correlations of these measurements, they extracted the energy associated with each azimuthal mode of the wake. They found that the two modes were equally important around $x/D = 30$. The authors note that soon after the $m = 1$ and $m = 2$ modes have similar strength, the wake approaches equilibrium similarity, as the mean deficit and turbulence intensity collapse in similarity variables. Nidhan *et al.* numerically examined the axisymmetric wake behind a disk at $Re = 50,000$ [1]. Using spectral proper orthogonal decomposition (SPOD), they extracted the azimuthal energy from planes of data. Similar to Johansson & George [2], they found that the intersection of the $m = 1$ and $m = 2$ azimuthal modes occurs around $x/D = 35$. Nedić *et al.* examined the wake behind flat plates of various geometries at Reynolds number $Re = 82,000$ [4]. Using pairs of hot-wire measurements at a fixed radial distance, they extracted azimuthal energy at the radial distance where vortex energy is at its strongest. They found that the relative amount of fluctuating energy contained in the $m = 1$ mode depends on flat plate geometry. For example, at $x = 10l$, where $l = \sqrt{A}$ is the square root of the area of the plate, the relative amount of fluctuating energy in the $m = 1$ mode is 73% for a disk, while for $D_f = 1.5$ fractal plates (fig. 1), it decreases from 63% to 55% with increasing fractal iteration.

The vast majority of our understanding of the underlying dynamics of axisymmetric wakes are from wakes generated by disks, which themselves are axisymmetric. It is known, however, that other vehicles and shapes also produce axisymmetric wakes which have a different structure than those created by disks. We will investigate to what degree the initial geometry of a body generating an axisymmetric wake affects the spatial behaviour of the large-scale structures that are generated. Specifically, our objective is to determine the rates at which the first two azimuthal modes decay in the near wake region, and to understand what aspects of the initial geometry drive any observed changes. We will begin our study by examining the wake decay of disks.

Experimental Setup

Preliminary analysis has been performed on the hot wire measurements from Nedić *et al.* [4]. This data was acquired with disks, square plates, and fractal plates of various fractal dimensions. All plates had a characteristic length $l = \sqrt{A} = 50$ mm, with increasing perimeter P_n with increasing fractal dimension. Hot wire measurements were taken at thirteen pairs of angular separation a fixed radial distance of $r \approx \delta$, where δ is the integral width of the wake, which is where vortex shedding energy is at its strongest. Unlike the experiments of Johansson *et al.* [3], who measured velocity fluctuations at several radial distances, all measurements were gathered at a fixed radial distance. For all measurements, the velocity was fixed at 12.8 m/s, corresponding to a Reynolds number of $Re = 82,000$.

[1]This work was supported by the FRQNT under grant number 287781.

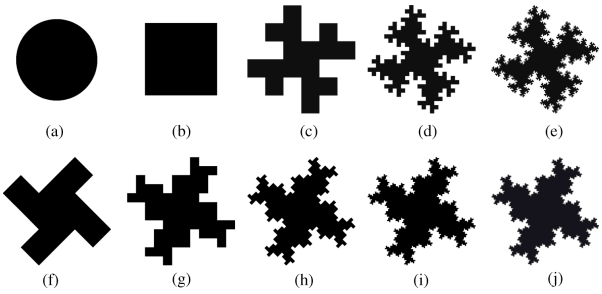

Figure 1: Plate geometries used in [4].

The streamwise velocity fluctuations $u_1(t)$ and $u_2(t)$, where "1" and "2" denote two signals at a fixed radial distance and azimuthal separation $\Delta\varphi$, were used to separate the flow into azimuthal modes with Fourier decomposition. The amount of fluctuating energy found in each azimuthal mode is

$$C_{12,m}(f,m) = \frac{1}{\pi}\int_0^{\pi} C_{12}(f,\Delta\varphi)\cos(m\Delta\varphi)\mathrm{d}(\Delta\varphi), \qquad (1)$$

where C_{12} is the coincident spectra, the real component of the cross-power spectral density E_{12} between signals $u_1(t)$ and $u_2(t)$, and $C_{12,m}$ the discrete coefficients of a Fourier series of C_{12}, such that $C_{12}(f,\Delta\varphi) = \sum_{m=0}^{\infty} C_{12,m}(f,m)\cos(m\Delta\varphi)$.

Results and Conclusions to Date

The Fourier decomposition shown in Eq. 1 was applied to the Nedić *et al.* [4] data for each plate at downstream positions of $x/l = \{5, 10, 20\}$. For each disk and location, the peak fluctuating energy $C_{12,m}$ and its corresponding Strouhal number was recorded for each azimuthal mode. For each plate, a power law was fit to the peak fluctuating energy of each mode to observe their decay. The intersection of the $m = 1$ and $m = 2$ decays was observed, where both modes contain equivalent energy, is shown in fig. 2.

In the case of the circular disk, the $m = 1$ and $m = 2$ modes have equal strength at $x/l = 35$, which is consistent with the aforementioned studies. Similarly, the wake of a square disk has a crossover point at $x/l = 33$. However, once we consider the wakes of fractal plates, the decay of both modes changes. Consider the $D_f = 1.5$ fractal plates; as noted by Nedić *et al.* [4], the amount of fluctuating energy contained in the $m = 1$ is less than that of a circular disk. As the fractal number increases, the crossover point occurs later downstream, as the $m = 1$ mode appears to decay at a lower rate, while the $m = 2$ mode tends to decay at a steeper rate than in the wake of the disk. Similarly, when isolating for a fixed P_n/l, the $D_f = 1.5$ plates tend have intersection points further downstream than $D_f = 1.3$ plates.

Future Work

Although these plates generate axisymmetric wakes, it is evident that the spatial decay of the two dominant modes in the wakes is significantly altered. Moreover, there appears to be an apparent trend in terms of the downstream distance where the double-helix mode dominates over the vortex shedding mode. In order to accurately compare these results to those in the literature, time-resolved Particle Image Velocimetry (PIV) will be used to analyze the velocity field and investigate the decay of each azimuthal mode. These measurements will be taken in a newly built water tunnel, with dimensions $0.5\text{m} \times 0.5\text{m} \times 3\text{m}$. Experiments will be gathered over Reynolds numbers $Re = 5{,}000 - 26{,}000$, which the upper bound is consistent with the works of Johansson & George [2]. We plan to compare and contrast the decay rate of the modes over a larger streamwise extent, incorporating all radial locations. We will extend this over a large range of Reynolds numbers to investigate low- and high-turbulent activity on the wake decay dynamics.

Table 1: Wake properties of various plate geometries.

Plate	$m = 1$ decay	$m = 2$ decay	Intersection (x/l)
Disk (●) (a)	1.82	0.91	35
Square (■) (b)	1.79	0.95	33
$D_f = 1.5(1)$(▲) (c)	1.82	1.02	65
$D_f = 1.5(2)$(►) (d)	1.50	1.19	83
$D_f = 1.5(3)$(▼) (e)	1.55	1.16	101
$D_f = 1.3(1)$(△) (f)	1.47	1.13	174
$D_f = 1.3(2)$(▷) (g)	1.69	0.95	36
$D_f = 1.3(3)$(▽) (h)	1.78	0.94	36
$D_f = 1.3(4)$(◁) (i)	1.73	1.02	48
$D_f = 1.3(5)$(◊) (j)	1.73	1.05	53

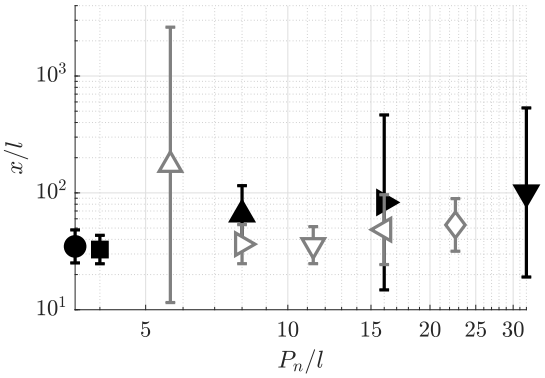

Figure 2: Downstream location of crossover points vs P_n/l for various flat plate geometries. Legend provided in table 1.

References

[1] S. Nidhan, K. Chongsiripinyo, O. T. Schmidt, and S. Sarkar. Spectral proper orthogonal decomposition analysis of the turbulent wake of a disk at Re = 50 000. *Phys. Rev. Fluids*, 5(12):124606, 12 2020.

[2] P. B. V. Johansson and W. K. George. The far downstream evolution of the high-Reynolds-number axisymmetric wake behind a disk. Part 2. Slice proper orthogonal decomposition. *Journal of Fluid Mechanics*, 555:387, 5 2006.

[3] P. B. V. Johansson, W. K. George, and S. H. Woodward. Proper orthogonal decomposition of an axisymmetric turbulent wake behind a disk. *Physics of Fluids*, 14(7):2508–2514, 6 2002.

[4] J. Nedić, O. Supponen, B. Ganapathisubramani, and J. C. Vassilicos. Geometrical influence on vortex shedding in turbulent axisymmetric wakes. *Physics of Fluids*, 27(3):35103, 2015.

6 Session F: Aero-Hydrodynamics - 2

Effect of wing transients on the leading-edge vortex dynamics over a rotating wing

Abbishek Gururaj[a*], Sarah Morris[a], Brian Thurow[a], and Vrishank Raghav[a]
[a] Auburn University, Aerospace Engineering Department, Auburn, USA[1]
[*]Correspondence: *azg0100@auburn.edu*

1 Introduction

The development of efficient biomimicking micro-air vehicles in recent years has renewed interest in studying the forces and flowfield evolving over an insect wing. Insect wings have been observed to have enhanced aerodynamic performance, primarily due to the formation of a stable leading-edge vortex (LEV) [1–3]. In hovering conditions, the flapping motion of an insect wing consists of a pitching motion and a rotational motion. Past studies have observed that the stable LEV, responsible for increased aerodynamic performance, is formed during the rotational phase of the wing motion [1, 2]. A comprehensive study by Lentink and Dickinson [4] showed that the rotational accelerations (centripetal, Coriolis, and Euler acceleration) mediate the LEV stability over a rotating wing. Among these, centripetal and Coriolis accelerations dominate in the quasi-steady phase, whereas the Euler acceleration is dominant during the transient phase of the rotational motion.

Various studies have been conducted to understand the evolution and stability of LEVs in the quasi-steady phase. Studies conducted by Jardin and David [5] suggested that rotational accelerations are a key factor in anchoring the LEV closer to the wing and thus generating high lift over a rotating wing. The vorticity transport equation has also been used to understand the mechanisms responsible for the stability of the LEV. Different mechanisms, such as planetary vorticity transport [6], radial-tangential vorticity balance [7], and vorticity annihilation [8], among others, have been found to be responsible for the stability of the LEV under different *Re* conditions. In addition, several other studies have been conducted to understand the LEV dynamics and stability in the quasi-steady phase. However, it has been observed that some insects might have small stroke amplitude and hence might operate in the transient phase. As suggested by Lentink and Dickinson [4], Euler acceleration dominates in the transient phase of the wing motion and might influence the LEV dynamics. As such, it is important to understand the influence of Euler/wing acceleration on the LEV dynamics over a rotating wing. Hence, this study aims to understand the influence of wing acceleration on the loads experienced and the flowfield evolving over a rotating wing. This aim is achieved by performing experiments over a rotating wing in a hydrodynamic hover rotor facility [9]. In this study, force measurements and flow field measurements were performed using particle image velocimetry in the rotating frame of reference. Wing acceleration ($\dot{\Omega}$) was varied as shown in Table 1, while the Reynolds number ($Re_g = 1500$), Rossby number ($Ro_g = 4.5$), aspect ratio ($AR = 5$), and pitch angle ($\theta = 45°$) were held constant.

[1]This work was supported by the Army Research Office under grant numbers W911NF-19-1-0052 and W911NF-19-1-0124.

Table 1: Summary of the experimental conditions.

Measurement	Wing acceleration (rad/s^2)	Reynolds number
Force	0,1, 0.25, 0.5, 1.0, 1.5, 2.0	1500
PIV	0,1, 0.25, 0.5, 1.0, 1.5, 2.0	1500

2 Results and Discussion

The results in this section are presented in terms of the non-dimensional acceleration (α^*), where α^* is defined as the ratio of wing acceleration to the convective acceleration of the fluid ($\alpha^* = \dot{\Omega}c^2/(\Omega^2 R_g^2)$). Figure 1 shows the lift coefficient (C_L) variation with non-dimensional time ($t^* = t\Omega R_g/c$) for different α^* conditions. It can be observed that an increase in α^* results in a higher lift at any given time ($t^* < 1.5$). This behavior is observed as a higher α^* results in a higher non-circulatory (due to wing inertia) and circulatory (due to LEV) force. Hence, it can be inferred that a higher α^* results in a higher lift due to a stronger LEV generated over the rotating wing. This correlation between wing acceleration, lift force, and LEV evolution will be elucidated in the following discussion.

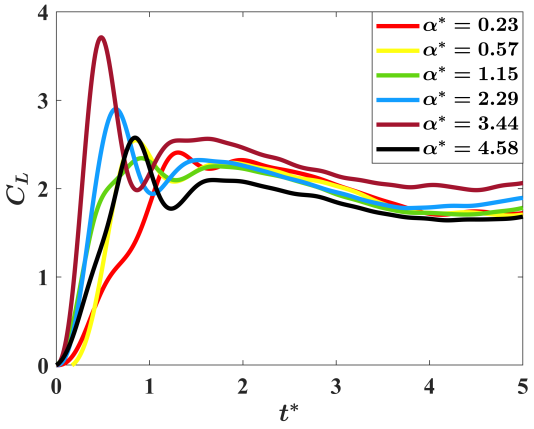

Figure 1: Variation of lift coefficient (C_L) with t^*.

Figure 2 shows the LEV structure for different α^* conditions. The flow field is represented in the figure by the non-dimensional spanwise vorticity ($\omega_z^* = \omega_z c/R_g$) and the velocity vectors. At $t^* = 1.5$, it can be observed that the LEV has formed for all $\dot{\Omega}$ conditions. In the case of the lowest α^* (lowest $\dot{\Omega}$), the LEV is much closer to the leading edge than $\alpha^* = 2.29$. However, the LEV is at a similar downstream position with a further increase in $\dot{\Omega}$. Therefore, increasing $\dot{\Omega}$ (α^*) results in the LEV to form faster and move further downstream at similar times. However, when the wing rotation approaches an impulsive start ($\dot{\Omega} > 1\, rad/s^2$), the LEV evolution and growth are not affected by $\dot{\Omega}$.

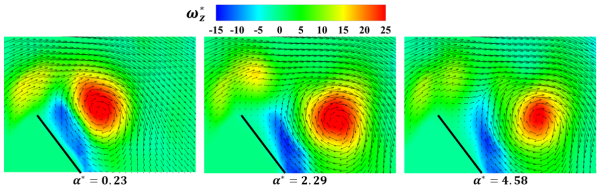

Figure 2: Evolution of the LEV represented by vorticity contours for different acceleration conditions at $t^* = 1.5$.

To further understand the influence of $\dot{\Omega}$ on LEV growth and evolution, the temporal evolution of the LEV circulation is plotted on the left of figure 3. From the circulation plot, a significant difference can be observed in the circulation values between $\alpha^* = 0.23$ and $\alpha^* = 2.29$. At any time, the circulation of $\alpha^* = 2.29$ is higher than $\alpha^* = 0.23$. However, the circulation distribution for $\alpha^* = 2.29$ and 4.58 does not appear to have a significant difference. Furthermore, it can be observed that the circulation suddenly drops down in all the cases. This drop in circulation is due to the separation of the LEV from the feeding shear layer. Hence, the LEV separation time was quantified to study the influence of $\dot{\Omega}$ on LEV separation. Right side plot of figure 3 shows the variation of non-dimensional separation time (t^*_{sep}) with α^*. It can be observed that increasing α^* ($\dot{\Omega}$) results in a decrease in the LEV separation time, which eventually asymptotes at higher α^*.

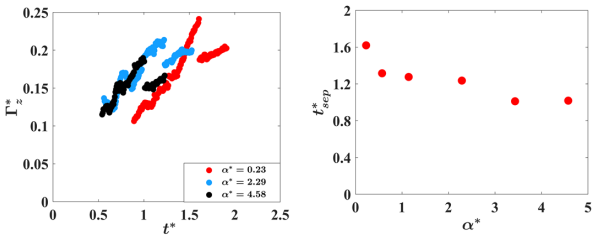

Figure 3: Left: Temporal evolution of the LEV circulation. Right: Variation of non-dimensional separation time (t^*_{sep}) with non-dimensional acceleration (α^*).

From the preceding discussions, it can be concluded that an increase in $\dot{\Omega}$ results in a faster vorticity growth in the LEV. Therefore, LEV growth is slower for lower $\dot{\Omega}$ cases compared to higher $\dot{\Omega}$ cases. This results in a higher LEV circulation for a higher $\dot{\Omega}$ at any given time. At higher $\dot{\Omega}$, the circulation (Γ_z) and the rate of change of circulation ($d\Gamma_z/dt$) is higher, resulting in a higher circulatory force. This, in addition to a higher non-circulatory lift, results in the total lift force growing quicker for higher $\dot{\Omega}$ conditions. As the LEV develops and grows quicker for higher $\dot{\Omega}$, it separates earlier (lower separation time). However, when the wing approaches an impulsive start (high $\dot{\Omega}$ (high α^*)), the effect of $\dot{\Omega}$ on the LEV dynamics is reduced. This results in the lift distribution, circulation distribution, and separation time not having a significant difference.

3 Conclusion

The influence of wing acceleration on LEV dynamics on a rotating wing is experimentally studied by varying wing acceleration at fixed Re_g, Ro_g, AR, and θ conditions. Force and PIV measurements were performed to understand the influence of acceleration on the loads experienced and flowfield over the rotating wing. An increase in $\dot{\Omega}$ resulted in a higher lift coefficient at any given time and a higher peak lift coefficient. The higher lift coefficient resulted from a stronger LEV at higher $\dot{\Omega}$. With an increase in $\dot{\Omega}$, the LEV is observed to be further downstream, has a higher circulation, and therefore has a lower separation time. From the observations mentioned, it is concluded that an increase in $\dot{\Omega}$ results in a faster vorticity growth in the LEV, which results in the LEV reaching maximum strength faster and separating earlier from the shear layer. More studies will be conducted in the future to understand the mechanisms responsible for the growth of LEVs under different $\dot{\Omega}$ conditions.

References

[1] Ellington, Charles P., et al. Leading-edge vortices in insect flight. *Nature*, 384.6610:626-630, 1996.

[2] Van Den Berg, Coen, and Charles P. Ellington. The three-dimensional leading-edge vortex of a 'hovering' model hawkmoth. *Philosophical Transactions of the Royal Society of London. Series B: Biological Sciences*, 325.1351:329-340, 1997.

[3] Birch, James M., and Michael H. Dickinson. Spanwise flow and the attachment of the leading-edge vortex on insect wings. *Nature*, 412.6848:729-733, 2001.

[4] Lentink, David, and Michael H. Dickinson. Rotational accelerations stabilize leading edge vortices on revolving fly wings. *Journal of Experimental Biology*, 212.16:2705-2719, 2009.

[5] Jardin, Thierry, and Laurent David. Spanwise gradients in flow speed help stabilize leading-edge vortices on revolving wings. *Physical Review E*, 90.1:013011, 2014.

[6] Werner, Nathaniel H., et al. Radial planetary vorticity tilting in the leading-edge vortex of revolving wings. *Physics of Fluids*, 31.4:041902, 2019.

[7] Chen, Long, et al. Effects of Reynolds number on leading-edge vortex formation dynamics and stability in revolving wings. *Journal of Fluid Mechanics*, 931, 2022.

[8] Wojcik, Craig J., and James HJ Buchholz. Vorticity transport in the leading-edge vortex on a rotating blade. *Journal of Fluid Mechanics*, 743:249-261, 2014.

[9] Gururaj, Abbishek, et al.. Rotating three-dimensional velocimetry. *Experiments in Fluids*, 62.7:1-20, 2021.

Effect of frequency on the hydrodynamic interactions between two pitching propulsors

Yuanhang Zhu* and Daniel Quinn
University of Virginia, Charlottesville, VA 22904, USA[1]
*Correspondence: *yz4kc@virginia.edu*

1 Introduction and Method

The hydrodynamic interactions between individual swimmers can lead to the formation of stable schools [1,2], and it has been shown that a fish can obtain energy and thrust benefits by swimming in such schools [3,4]. The interactions within a minimal school of two propulsors have been studied for in-line [5], side-by-side [6], and staggered configurations [7]. More recently, Kurt et al. [2] investigated the schooling stability and collective performance of two pitching propulsors, with the follower traversed around the leader in a two-dimensional plane. They discovered multiple stable and unstable equilibrium positions for the two-agent school which has not been reported in one-dimensional configurations. In these studies, it has been shown that a key phenomenon that governs schooling thrust/efficiency/stability is the interaction between fish bodies and leading-/trailing-edge vortices shed by other fishes, and the constructive/destructive nature of these interactions is further determined by the propulsor kinematics and spacing. However, these previous studies have mostly focused on a fixed Strouhal number - the effect of frequency on the hydrodynamic interactions has not been considered. Understanding this problem will potentially unveil the hydrodynamic effects involved in the schooling of high-speed fish species such as tuna, as well as benefit the design and control of future high-speed multi-agent bio-inspired robotic platforms.

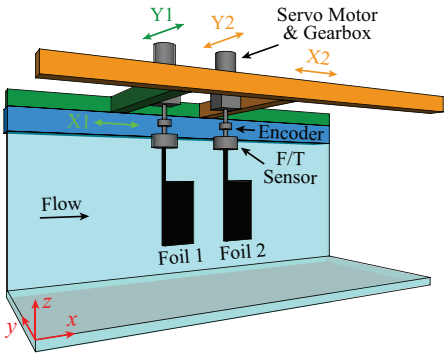

Figure 1: A schematic of the experimental setup.

To study the interactions between two pitching propulsors, we conduct experiments in a circulating water tunnel (Fig. 1). The two foils are 3D printed using ABS materials (chord: 6 mm, span: 12 mm) with a carbon fiber shaft (diameter: 7.94 mm) embedded at the leading edge. The flow speed is maintained at $U = 0.333$ m/s using an ultrasonic flow meter (Dynasonics Series TFXB), resulting in a chord-based Reynolds number $Re \equiv \rho U c/\mu = 20{,}000$, where ρ and μ are water density and dynamic viscosity, respectively. The shaft is further connected to a wireless six-axis force/torque transducer (Foil 1: ATI Mini40, Foil 2: ATI Mini45) to measure the hydrodynamic loads experienced by the foil, and an optical encoder (US Digital E2-5000) is used to record the pitching angle. The foils are driven by a servo motor (Teknic CPM-MCPV-2341S-ELN) with a 5:1 gearbox (SureGear PGCN23-0525) to pitch sinusoidally with a profile of $\theta = \theta_0 \sin(2\pi f t)$, where θ is the pitching angle, $\theta_0 = 12^\circ$ is the pitching amplitude, f is the pitching frequency, and t is time. We use three pitching frequencies, $f = 4$ Hz, 6 Hz and 8 Hz, to study the effect of frequency on the interactions of the two foils. These three frequencies result in three Strouhal numbers $St \equiv 2fc\sin\theta_0/U = 0.30$, 0.45 and 0.60, respectively. The pitching phase between the two foils is set to be $\phi = 180^\circ$ throughout the experiments. The automatic positioning of the two foils is enabled by a four-axis motorized traverse system, in which both foils can traverse in the x- and y-directions independently (Foil 1: X1 and Y1, green traverses, Foil 2: X2 and Y2, orange traverses). In the present study, Foil 1 is fixed at a position that is $2.5c$ from the wall. Foil 2 is traversed in the y-direction from zero to $1.4c$ away from Foil 1, with a step size of $0.2c$, and in the x-direction from zero to $2.0c$ away from Foil 1, with a step size of $0.25c$. There is a measurement void of size ($1c$, $0.8c$) near Foil 1 due to the geometry limitations of the pitching mechanism.

2 Results and Discussion

We measure the hydrodynamic forces experienced by the two foils as Foil 2 is traversed around Foil 1 at different spatial positions. The force vectors $\overrightarrow{F_1}$ and $\overrightarrow{F_2}$ are plotted in Fig. 2(a) and (b), respectively. In both subfigures, the thrusts produced by the two foils are observed to increase with the Strouhal number. In Fig. 2(a), we see that $\overrightarrow{F_1}$ is mostly not affected by the existence of Foil 2 when Foil 2 is swimming downstream of Foil 1. The hydrodynamic interactions between the two foils become more evident when they have spatial overlaps in the streamwise direction. As Foil 2 moves

[1]This work was supported by ONR, managed by Dr. Bob Brizzolara.

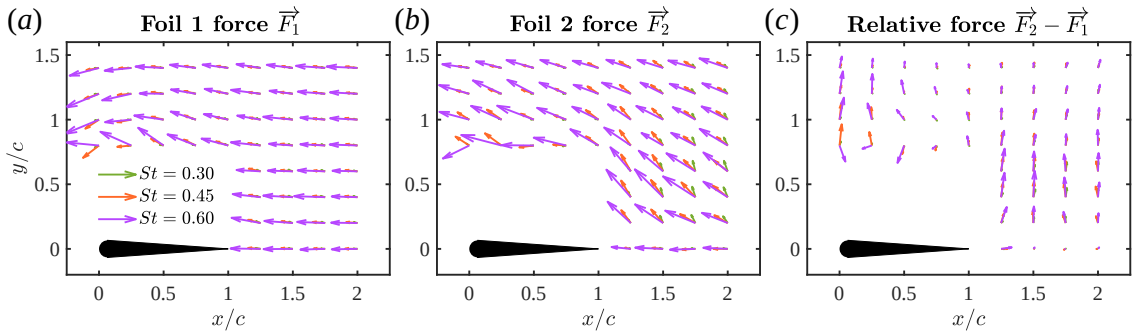

Figure 2: The hydrodynamic force vector (*a*) $\overrightarrow{F_1}$ exerted on Foil 1 and (*b*) $\overrightarrow{F_2}$ exerted on Foil 2 as Foil 2 is traversed around Foil 1 at different spatial positions for three different Strouhal numbers, $St = 0.30$, 0.45 and 0.60. (*c*) The relative force vector between the two foils, $\overrightarrow{F_2} - \overrightarrow{F_1}$.

more upstream, Foil 1 starts to experience a mild positive lift force, which pulls Foil 1 towards Foil 2 in the lateral direction. At lower Strouhal numbers ($St = 0.30$ and 0.45), this positive lift turns negative as Foil 2 moves further upstream and finally swims side-by-side with Foil 1. However, at the highest Strouhal number, $St = 0.60$, Foil 1 continues to feel an attractive (positive) force as Foil 2 moves upstream when the lateral gap between the two foils is small ($y/c = 0.8$). Fig. 2(*b*) shows that Foil 2 mostly feels a repelling force from Foil 1 for all the spatial positions tested, presumably due to its interactions with the vortex wake generated by Foil 1. Foil 2 experiences no lateral force when it is swimming right behind Foil 1 (i.e. $y/c = 0$). PIV experiments are in need to uncover the vortex-body interactions within the two-agent school.

We calculate the relative force $\overrightarrow{F_2} - \overrightarrow{F_1}$ to quantify the relative moving trend of Foil 2 with respect to Foil 1 [2], and plot the vectors in Fig. 2(*c*). Zero relative force vectors indicate equilibrium positions, with their stability determined by the force gradient. From the relative force vectors, we see that there is a trend of separation in general between the two foils. Increasing the Strouhal number can alter the relative force vectors, especially when the two foils are swimming side-by-side with the smallest gap. Comparing the relative force vector at $(x/c, y/c) = (0, 0.8)$ and $(0, 1.0)$ at $St = 0.60$, we see that the two vectors point to opposite lateral directions, indicating an *unstable* equilibrium. However, this unstable equilibrium is not shown at $St = 0.30$ and 0.45, presumably because they reside closer to Foil 1 (i.e. $y/c < 0.8$). This agrees with the observation of Zhong et al. [8] that the unstable equilibrium for a pitching foil moves farther from the ground as *St* increases. Since the phase difference between the two foils is kept at $\phi = 180^\circ$ in the present study, the interaction between two side-by-side foils ($x/c = 0$) is equivalent to that between one foil and a wall.

3 Conclusion and Outlook

In this study, we used laboratory experiments to examine the effect of frequency on the hydrodynamic interactions between two pitching propulsors. With the follower traversed around the leader, we measured and analyzed the hydrodynamic forces experienced by these two foils. We showed that the follower has minimal influence on the leader except when they overlap in the streamwise direction. By computing the relative forces between the two foils, we found an unstable equilibrium for the side-by-side configuration at the highest Strouhal number, but not at lower Strouhal numbers. This finding demonstrated the possibility of using frequency to manipulate the hydrodynamic interactions and schooling stabilities of a two-fish school.

We plan to perform more experiments with higher spatial resolutions to obtain a more complete understanding of the interactions within the two-fish school. In particular, we will improve the design of the pitching mechanism to enable measurements when the two propulsors are swimming in close proximity. In addition to force measurements, we plan to conduct PIV experiments to measure the flow field around two interacting foils, in order to unveil the underlying vortex dynamics.

References

[1] Newbolt, J. W., Zhang, J. and Ristroph, L. Flow interactions between uncoordinated flapping swimmers give rise to group cohesion. *Proc. Natl. Acad. Sci.*, 116(7):2419–2424, 2019.

[2] Kurt, M., Ormonde, P. C., Mivehchi, A. and Moored, K. W. Two-dimensionally stable self-organization arises in simple schooling swimmers through hydrodynamic interactions. *arXiv*, 2102.03571, 2021.

[3] Pan, Y. and Dong, H. Computational analysis of hydrodynamic interactions in a high-density fish school. *Phys. Fluids*, 32(12):121901, 2020.

[4] Saadat, M., Berlinger, F., Sheshmani, A., Nagpal, R., Lauder, G. V. and Haj-Hariri, H. Hydrodynamic advantages of in-line schooling. *Bioinspir. Biomim.*, 16(4):046002, 2021.

[5] Boschitsch, B. M., Dewey, P. A. and Smits, A. J. Propulsive performance of unsteady tandem hydrofoils in an in-line configuration. *Phys. Fluids*, 26(5):051901, 2014.

[6] Dewey, P. A., Quinn, D. B., Boschitsch, B. M. and Smits, A. J. Propulsive performance of unsteady tandem hydrofoils in a side-by-side configuration. *Phys. Fluids*, 26(4):041903, 2014.

[7] Huera-Huarte, F. J. Propulsive performance of a pair of pitching foils in staggered configurations. *J. Fluids Struct.*, 81:1–13, 2018.

[8] Zhong, Q., Han, T., Moored, K. W. and Quinn, D. B. Aspect ratio affects the equilibrium altitude of near-ground swimmers. *J. Fluid Mech.*, 917, A36, 2021.

Leading Edge Vortex Interactions on Generic Multi-Swept Wing Configurations

Casey Fagley[a], Mehdi Ghoreyshi[a], Jürgen Seidel[a] and Matthew Munson[a]
[a] United States Air Force Academy, Department of Aeronautics, USAF, USA[1]
*Correspondence: *matthew.munson@afacademy.af.edu*

1 Introduction

Leading Edge Vortex (LEV) development on swept wings is a key topic in aerodynamic design. The formation and behavior of these vortices have important implications for the design, control, and optimization of modern combat aircraft, including the integration of control surfaces and the development of flight stability and control algorithms. Many factors influence the stability and behavior of LEVs, including the wing planform shape, as well as the Reynolds number of the flow. Several studies have shown that LEV stability is highly sensitive to these factors, but the consensus in the literature is that three-dimensional effects in the base flow, such as wing sweep, play a dominant role in the stabilization of LEVs. Non-swept stationary wings are prone to stalling at moderate angles of attack; in contrast, LEVs have been observed to be stably attached to swept, rotating and pitching wings even at post-stall angles. One proposed mechanism for this stabilization is spanwise convection of vorticity, which arises from spanwise pressure gradients and balances the flux of vorticity transported into the vortex at the leading edge, allowing the LEV to reach a quasi-equilibrium state [1, 2]. Strong LEVs stabilized by spanwise flow common on delta-wing aircraft result in delayed stall at higher angles and generate a non-linear, vortex induced lift until vortex breakdown occurs as a result of a structural change from LEV to reversed-flow bubble.

Many modern fighter aircraft feature wing sweep variations that result in a wing configuration with a highly swept strake at the upstream portion, transitioning to a delta wing shape downstream. The strake portion of the wing acts as a vortex generator, producing a strong LEV that convects over the primary lifting surface of the wing. However, at the point where the wing sweep changes, a secondary LEV is also formed. The interactions between the primary and secondary LEVs can have significant effects on the aerodynamic performance of the aircraft. These interactions are highly dependent on the size, strength, and location of the vortices, and can include vortex braiding (where the vortices intertwine with each other), vortex merging (where the vortices combine into a single vortex), and vortex breakdown (where the resulting vortex dissipates or becomes unstable). Understanding and predicting the behavior of these interactions is therefore an important aspect of aircraft design and optimization.

[1]This work was supported by AFOSR under project number 21RT0010
[2]This material is based on research sponsored by the US Air Force Academy under agreement number FA7000-18-2-0008. The U.S. Government is authorized to reproduce and distribute reprints for Governmental purposes notwithstanding any copyright notation thereon.
The views and conclusions contained herein are those of the authors and should not be interpreted as necessarily representing the official policies or endorsements, either expressed or implied, of the US Air Force Academy or the U.S. Government.

2 Results

In this talk/poster, we will present the results of our ongoing research on vortex-vortex interactions in generic multi-swept wing configurations in the subsonic flight regime (Mach=0.15). Our approach involves combining computational simulations with experimental measurements to provide a comprehensive understanding of these interactions. As part of this study, we have identified two cases that demonstrate contrasting patterns of vortex breakdown in the LEV. The first case exhibits a gradual breakdown of the LEV, while the second case shows a rapid breakdown of the LEV. Our analysis has revealed that vortex merging or entrainment can lead to destabilization of the vortex system, while vortex braiding creates a more stable vortex system and significantly delays breakdown. Further investigations suggest that the extent of vortex merging and braiding is influenced by the size, strength, and location of the vortices, as well as by the kinematics of the wing and the flow conditions.

Figure 1 presents a comparison of experimental and simulation results for two models at an angle of attack of 28 degrees. The models are differentiated by the location at which the leading-edge sweep angle changes. The left column corresponds to a model in which the angle changes from 80 degrees to 50 degrees at 40% of the root chord location, termed as *C4*. The right column corresponds to a model in which the sweep angle transitions at the 60% location, termed as *C6*. The C6 model exhibits two distinct LEVs that interweave around one another, forming a stable vortex system. In contrast, the C4 model exhibits a weaker secondary LEV with more dispersed vorticity being shed along the secondary sweep angle, which leads to the coalescence of the two vortices. This results in vortex breakdown, as evidenced by the rapid onset of turbulent diffusion into small scale structures.

The coefficient of lift for the C4 and C6 models is shown in

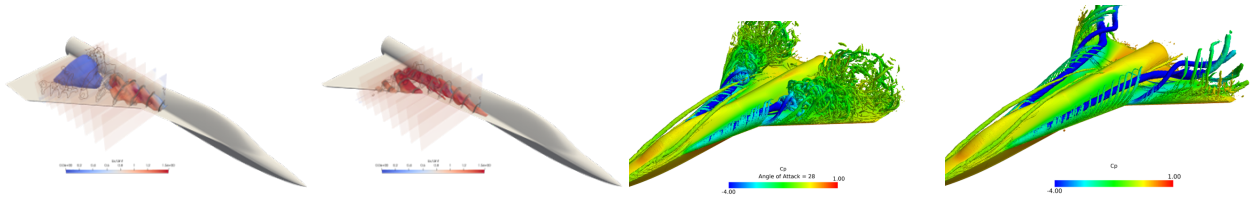

(a) C4 Exp (b) C6 Exp (c) C4 CFD (d) C6 CFD

Figure 1: Comparison of SPIV experiments and computational simulations of C4 and C6 wing planforms. Experiments show isosurface of streamwise vorticity colored by the freestream velocity where as simulations show an isosurface of Q-criterion colored by the coefficient of pressure.

Figure 2 over an angle of attack range of 0°to 40°. The C4 model exhibits a gradual transition from a linear lift region (corresponding to a stable vortex configuration) to a fully stalled configuration. In contrast, the C6 model exhibits a delay in stall up to an angle of attack of 28°, followed by a rapid breakdown. The magnitude of the lift difference between the two models is approximately 40%. Furthermore, good agreement is observed between the simulation and experimental measurements for both models."

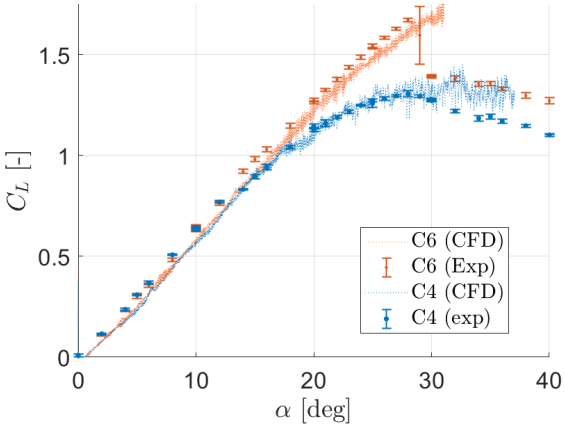

Figure 2: Lift force comparison between models C4 and C6 for experiments and simultions.

Stereoscopic particle image velocimetry (SPIV) measurements were conducted over a range of angles of attack from 20°to 32°, and corresponding simulations were performed under the wind tunnel test conditions. The location of vortex breakdown, as indicated by the first occurrence of flow reversal ($U_\infty < 0$), was determined and plotted in Figure 3 for the C4 and C6 models. As depicted, the C4 model exhibits a nearly linear breakdown starting at 80% of the root chord and progressing towards the 55% location. In contrast, the C6 model does not exhibit any breakdown until the highest angle of attack (32°), at which point the vortex configuration breaks down at the 80% location. In all cases, the CFD simulations show a slight delay in vortex breakdown compared to the experimental measurements which may be attributed to temporal-spatial discretization or turbulence model selection.

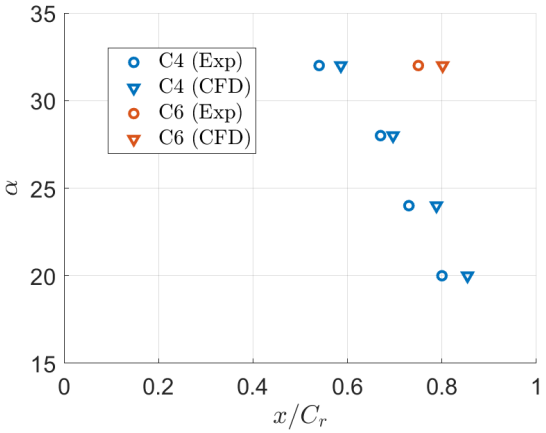

Figure 3: Resulting breakdown location (x/C_R versus angle of attack for models of interest

3 Conclusion

Our research has uncovered an intriguing connection between the location of sweep transition and the stability of leading-edge vortices (LEVs). Further investigation is needed to fully grasp the intricate dynamics of LEV interactions and their effect on aircraft performance. By performing vorticity flux analyses and quantifying vortex strength, size, and location, we may gain a deeper understanding of the braiding and mixing of vortices. Nevertheless, our findings offer valuable insights that can guide the design and optimization of multi-swept wing aircraft, ultimately improving their aerodynamic performance.

References

[1] Colin Hartloper and David E Rival. Vortex development on pitching plates with lunate and truncate planforms. *Journal of Fluid Mechanics*, 732:332–344, 2013.

[2] Robert Richard Harbig, John Sheridan, and Mark Christopher Thompson. Reynolds number and aspect ratio effects on the leading-edge vortex for rotating insect wing planforms. *Journal of Fluid Mechanics*, 717:166–192, 2013.

Slow Your Roll (Up): Studying Dynamic Stall Development with Variable Density Experiments

Nick Conlin[a], Claudia Brunner[b], and Marcus Hultmark[a]
[a] Department of Mechanical and Aerospace Engineering, Princeton University, Princeton, NJ, USA [1]
[b] Max Planck Institute for Dynamics and Self-Organization, Göttingen, Germany
*Correspondence: *nconlin@princeton.edu*

1 Introduction

Dynamic stall is an aerodynamic phenomenon experienced by lifting surfaces undergoing large amplitude unsteady maneuvers. For an airfoil operating below its static stall angle, small variations in the angle of attack leave the flow attached, resulting in aerodynamic loads that can be reasonably predicted by thin airfoil theory. Conversely, maneuvers dynamically exceeding the static stall angle induce delayed flow separation and drastic load changes. In classical deep dynamic stall a transient lift enhancement is achieved, followed by massive flow separation and the formation of a spanwise coherent vortex, referred to as the dynamic stall vortex. As the dynamic stall vortex convects over the airfoil trailing edge a large nose down moment occurs and is accompanied by a drop in lift and increase in drag. This highly variable loading during the stall process has the potential to cause structural fatigue on turbomachinery and limit the performance of agile aircraft.

A consistent description of the key stages and characteristic features of dynamic stall has been established [1], but a coherent quantitative physical description has yet to emerge. Progress towards a generalized physical description is stymied by the large parameter space. Dynamic stall mechanisms depend on the motion kinematics, airfoil geometry, and freestream flow conditions. Two key non-dimensional parameters are the Reynolds number, $Re_c = \rho U_\infty c/\mu$, and the reduced frequency, $k = \pi f c/U_\infty$. The present study aims to decouple the effects of Re_c and k for an airfoil undergoing a pitch-up maneuver by systematic experimental variation of each parameter.

2 Experimental Setup

Experiments were conducted in the High Reynolds Number Test Facility (HRTF) at Princeton University. High Reynolds numbers are achieved with freestream velocities less than 5 m/s by using air pressurized up to 220 bar as the working fluid. The resulting increase in density is used to manipulate the Reynolds number with no effect on the reduced frequency. This decouples the parameters and allows for systematic investigation of a broad parameter space. Furthermore, the dimensional pitching frequency of the airfoil remains below 1.4 Hz even for $k = 0.4$. This allows unsteady flow development to be studied with high time resolution. Experiments were conducted in the Reynolds number range $0.5 \times 10^6 \leq Re_c \leq 5.5 \times 10^6$ and reduced frequency range $0.01 \leq k \leq 0.4$. Data from these experiments were previously reported in Kiefer et al. (2022).

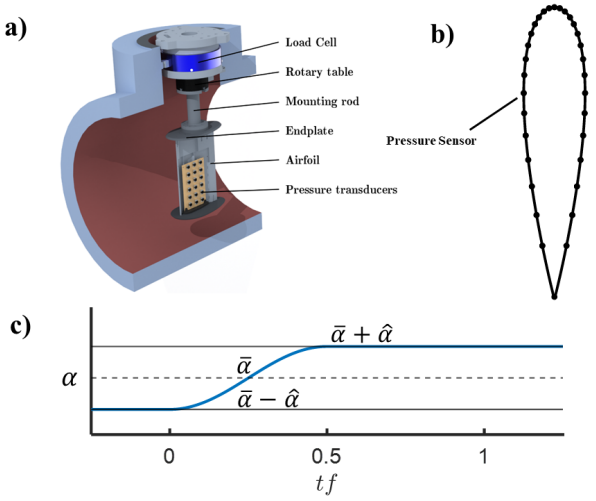

Figure 1: Overview of Experiments. a) Airfoil installed in the test section. b) Airfoil geometry (NACA0021) with pressure tap locations. c) Angle of attack for ramp-up pitching motion, plotted against time non-dimensionalized by pitching frequency.

An overview of the experimental setup is shown in fig. 1. A NACA 0021 airfoil of chord length $c = 0.17$ m was equipped with elliptical endplates and installed in the 0.45 m diameter test section as shown in fig. 1a. Time-resolved surface pressure distributions were obtained using 32 differential pressure sensors with locations indicated in fig. 1b. A temporal Savitzky–Golay filter with window size $tU_\infty/c = 2.8$ was applied to the raw data. Filtered pressure distributions were integrated to yield forces on the airfoil while pitching.

Ramp-up pitching motions about the airfoil mid-chord were considered. The angle of attack follows a half-sinusoidal cy-

[1]This work was supported by the National Science Foundation of the United States under grant number CBET 1652583

cle with amplitude $\hat{\alpha}$ about a mean angle $\bar{\alpha}$. A sketch of the ramp-up maneuver is shown in Figure 1c. The results presented below are phase-averaged over 150 individual half-cycles for all test cases. Further details on the experimental setup can be found in [2, 3].

3 Results

Results from two different parameter sweeps are shown in fig. 2 (varying Re_c) and fig. 3 (varying k). Each plot shows the lift coefficient versus time non-dimensionalized by the pitching frequency. Note motion begins at $tf = 0$ and ends at $tf = 0.5$, as indicated in fig. 1c. For all parameter combinations there is a transient increase in lift above the static maximum lift coefficient, followed by a rapid drop off due to stall. All test cases exhibit gradual trailing edge stall with the dynamic stall vortex forming near mid-chord [3]. This stall mechanism is consistent with previous studies considering the high Reynolds number [4] and moderate airfoil thickness [5].

Reynolds number effects on the lift curve can be deduced from fig. 2. For identical reduced frequency, mean angle, and amplitude ($k = 0.1$, $\bar{\alpha} = 24°$, and $\hat{\alpha} = 5°$) the onset of stall is delayed with increasing Reynolds number. Correspondingly, the maximum lift coefficient attained also increases from approximately $C_l = 1.6$ to $C_l = 1.9$. Furthermore the total drop in lift due to stall increases with increasing Reynolds number, indicating a growth in stall severity.

Lift curves for varying reduced frequency at $Re_c = 10^6$ are shown in fig. 3. The mean angle and amplitude are fixed at $\bar{\alpha} = 24°$ and $\hat{\alpha} = 5°$. From this data, two regimes can be identified. In the low reduced frequency regime, $(k < 0.1)$ stall occurs prior to reaching the maximum angle of attack at $tf = 0.5$. Within this regime, the maximum lift coefficient increases because the flow remains attached at higher angles of attack as the reduced frequency is increased. In the second regime $(k > 0.2)$, the maximum lift coefficient is nearly constant and stall occurs after the ramp-up motion has concluded. Previous analysis has shown that the lift, drag, and moment curves approach reduced frequency independence in the second regime, and thus the curves can be collapsed when plotted against tU_∞/c with the introduction of a stall delay offset [3].

4 Conclusion

A complete physical explanation of the trends in stall development with changing Re_c and k lies in the complex interplay of boundary layer transition and separation over the suction surface of the airfoil. Future analysis is aimed at determining scaling behavior of the stall delay with non-dimensional parameters.

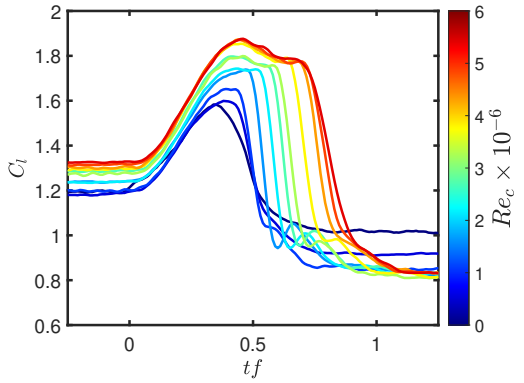

Figure 2: Reynolds number sweep with reduced frequency held constant at $k = 0.1$. The mean angle of attack and amplitude are fixed at $\bar{\alpha} = 24°$ and $\hat{\alpha} = 5°$.

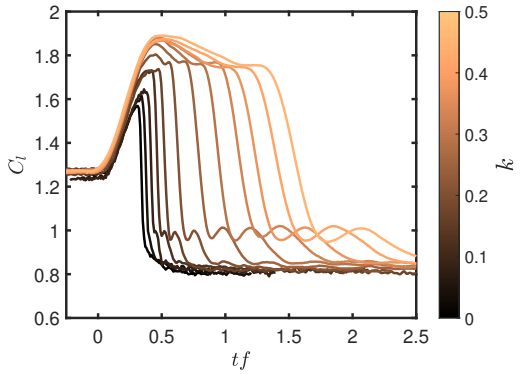

Figure 3: Reduced frequency sweep with Reynolds number held constant at $Re_c = 1 \times 10^6$. The mean angle and amplitude are fixed at $\bar{\alpha} = 24°$ and $\hat{\alpha} = 5°$.

References

[1] L. W. Carr, K. W. McAlister, and W. J. McCroskey. Analysis of the development of dynamic stall based on oscillating airfoil experiments. Technical Report January, 1977.

[2] Claudia E. Brunner, Janik Kiefer, Martin O. L. Hansen, and Marcus Hultmark. Study of Reynolds number effects on the aerodynamics of a moderately thick airfoil using a high-pressure wind tunnel. *Experiments in Fluids*, 62(8):178, aug 2021.

[3] Janik Kiefer, Claudia E. Brunner, Martin O.L. Hansen, and Marcus Hultmark. Dynamic stall at high Reynolds numbers induced by ramp-type pitching motions. *Journal of Fluid Mechanics*, 938:A10, may 2022.

[4] S. I. Benton and M. R. Visbal. The onset of dynamic stall at a high, transitional Reynolds number. *Journal of Fluid Mechanics*, 861:860–885, feb 2019.

[5] Anupam Sharma and Miguel Visbal. Numerical investigation of the effect of airfoil thickness on onset of dynamic stall. *Journal of Fluid Mechanics*, 870:870–900, jul 2019.

Wake Interference Effect on Large Amplitude Flapping of an Inverted Flexible Foil

Aarshana Parekh[a*] and Rajeev Jaiman[a]
[a] The University of British Columbia, Department of Mechanical Engineering, Vancouver, Canada[1]
[*]Correspondence: *arparekh@student.ubc.ca*

1 Introduction

Renewable energy devices using cantilevered flexible foils have been actively studied in recent years due to the foil's ability to undergo self-sustained flapping motion when subject to fluid flow [1-2]. Through flapping movement, fluid kinetic energy can be harnessed, then converted to electric energy via piezoelectric materials. The inverted foil, a flexible foil cantilevered at the leading edge, has shown superior abilities in harvesting electrical energy. Because, compared to their traditional counterparts, cantilevered at the leading edge, inverted foils become unstable at much lower flow speeds and undergo large amplitude flapping for a range of velocities in air and water [3].

However, the desired flapping mode only occurs for a narrow range of flow conditions. One way to increase this range and maximize energy harvesting is by using multiple foils in arrays, particularly in tandem. Previous work on isolated inverted foils has shown that the physics behind its large amplitude flapping response is due to both vortex shedding and the foil's fluid-elastic instability [4]. When placed in tandem, one foil is subject to the perturbed wake flow of the other. As a result of this wake-body interaction, the foil's dynamics become intricate and governed by the proximity of the upstream body. Much akin to the wake-induced-vibration dynamics observed for two tandem circular cylinders [5]. A complete understanding of these complex dynamics is necessary to design efficient array systems. In particular, the underlying physics leading to a flexible foil's self-excited flapping response when placed in the wake flow requires further investigation.

In this study, we consider a flexible inverted foil and numerically investigate its flapping dynamics wake flow. Our goal is to help answer the following key questions: (i) How do proximity and wake interference influence the foil's flapping response at various separation distances, (ii) what is the intrinsic relationship between the wake vortices and different flapping modes, (iii) What is the optimal range of bending stiffness to sustain LAF response. The knowledge gained through this study could be leveraged to develop novel and robust energy harvesting systems. Our model consists of a flexible foil of length L and thickness h with its trailing edge fixed and leading edge left free to oscillate. The foil is placed downstream a circular cylindrical bluff body with a diameter D. The separation between the foil's leading edge and the cylinder surface is defined as g. This setup is subject to a uniform axial incompressible flow with free stream velocity U_∞ The dynamics of the flexible foil are determined on the basis of four key non-dimensional parameters, i.e., Reynolds number Re, bending rigidity K_B mass ratio m^*, and reduced velocity U^*, defined as:

$$Re = \frac{\rho^f U_0 L}{\mu^f}, K_B = \frac{B}{\rho^f U_0^2 L^3}, m^* = \frac{\rho^s h}{\rho^f L}, U^* = \sqrt{\frac{m^*}{K_b}}. \quad (1)$$

Here ρ_f and ρ_s are densities of the fluid and structure, respectively. μ_f denotes the fluid's dynamic viscosity. E is Young's modulus, and ν is the Poisson's ratio of the foil. B represents the flexural rigidity defined as $B = Eh^3/12\left(1-\nu^2\right)$. K_B represents the ratio of the foil's bending force to the fluid's inertial force. Utilizing a higher-order coupled fluid-structure solver based on fully coupled three-dimensional Navier Stokes and nonlinear structural dynamic equations, we investigate the fluid-structure interaction of an inverted foil when placed behind a cylindrical bluff body.

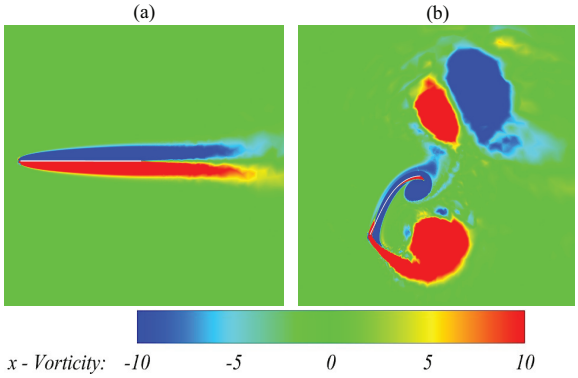

Figure 1: Spanwise vorticity contour for an isolated inverted foil at $Re = 1000$ and $m^* = 0.1$, when (a) $K_B = 0.4$, (b) $K_B = 0.2$

2 Results

To identify the flapping modes of an inverted foil in wake flow, we perform a preliminary comparative study on its dynamics with and without the presence of an upstream circular cylinder. Simulations are conducted for both setups at

[1]This work was supported by NSERC Discovery Grant.

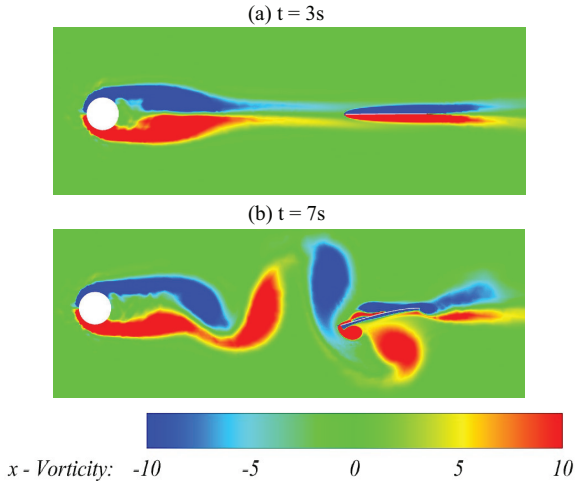

Figure 2: Spanwise vorticity contour for an inverted foil placed behind an upstream cylinder of $D = 0.4L$ at $g = 2.5L$, when $Re = 1000$, $m^* = 0.1$ and $K_B = 0.4$.

constant $Re = 1000$ and mass ratio, given as $m^* = 0.1$. The flapping modes are identified by varying the foil's flexibility measured using K_B. The spanwise vorticity contours in the fluid for an isolated inverted foil $K_B = 0.4$ and 0.2 are shown in Fig 1a. and Fig 1b., respectively. For $K_B = 0.4$, the flow field represents the boundary layer flow over the plate. As flow travels downstream, symmetric opposite signed boundary layers are observed on the foil sides, which form a narrow steady wake as seen in Fig. 1a. The foil is in a stable stationary position wherein the structure's elastic forces balance the fluid loading. As observed in Fig. 1b. when the flexibility of the foil is increased, i.e., $K_B = 0.2$, it experiences an onset of flapping instability as expected. The foil undergoes large amplitude flapping (LAF) mode where oscillations are symmetric, regular periodic with a single frequency and a large constant amplitude.

Figure 2 (a-b) show the spanwise vorticity contours for the inverted foil when placed behind a circular cylinder with $D = 0.4L$ at a separation distance $g = 2.5L$ and $K_B = 0.4$ at different instances in time. The foil's dynamics vary as compared to the isolated case. Initially, like the isolated case, boundary layers are formed on each side of the foil, as observed in Fig. 2a. As the flow progresses downstream, oppositely signed regular von Karman vortices shed in the wake interfere with the foil's boundary layers. The energetic upstream wake vortices merge with the same signed leading edge vortex (LEV), as shown in Fig 2b, and induce the foil's flapping instability. This result suggests that the flapping motion is wake induced, meaning that the oscillations are sustained by the balance between fluid loading induced by the wake vortices and the foil's elastic forces. Fig 3 shows the inverted foil's variation of maximum cross-stream tip displacement with respect to K_B for the isolated and tandem setups. It can be seen that, due to interaction with upcoming wake flow, the flapping instability is initiated at high foil stiffness (i.e., lower flow velocity)compared

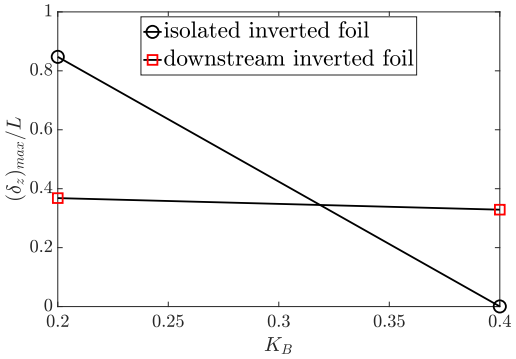

Figure 3: Maximum cross-stream leading edge tip-displacement for an isolated inverted foil (-○-) and with an upstream circular cylinder(-□-) for $m^* = 0.1$, $Re = 1000$ and $K_B \in [0.2, 0.4]$.

to the isolated case.

3 Conclusion and outlook

In this work, we have investigated the fluid-structure interaction of a flexible inverted foil with the wake of an upstream cylindrical bluff body. Of particular interest was exploring the foil's complex flow-induced flapping responses in this configuration. Our analysis shows that due to its interaction with the upstream cylinder's unsteady wake, the foil undergoes sustained oscillations at lower flow velocity than the isolated case. These results show that placing a bluff body upstream of an inverted foil can increase desired flapping range for energy harvesting. In our upcoming work, the differences in fluid load generation on the inverted foil in the presence and the absence of an upstream bluff body will be studied systematically for a more extensive range of K_B through force decomposition, phase relations, and corresponding wake contours. These results will provide an understanding of the underlying physics leading to flapping instability in inverted foils and its intrinsic relationship with the wake vortices. The influence of wake interference on the foil's response will also be studied for various separation distances. These findings can eventually be leveraged to design efficient and robust energy-harvesting array systems.

References

[1] Allen, J. J., and A. J. Smits. Energy harvesting eel. *Journal of fluids and structures*, 15(3-4): 629-640, 2001.

[2] Kim, Daegyoum, et al. Flapping dynamics of an inverted flag. *Journal of Fluid Mechanics*, 736, 2013.

[3] Gurugubelli, Pardha S., and Rajeev K. Jaiman. Self-induced flapping dynamics of a flexible inverted foil in a uniform flow. *Journal of Fluid Mechanics*, 781:657-694, 2015.

[4] Gurugubelli, Pardha S., and Rajeev K. Jaiman. Large amplitude flapping of an inverted elastic foil in uniform flow with spanwise periodicity. *Journal of Fluids and Structures*, 90:139-163, 2019.

[5] Mysa, Ravi Chaithanya, Abouzar Kaboudian, and Rajeev K. Jaiman. On the origin of wake-induced vibration in two tandem circular cylinders at low Reynolds number. *Journal of Fluids and Structures*, 61:76-98, 2016.

A systematic investigation into the effect of roughness on self-propelled swimming plates

Jonathan Massey[a,b*], Gabriel Weymouth[a,b] and Bharathram Ganapathisubramani[a]
[a] Faculty of Engineering and Physical Sciences, University of Southampton, UK[1]
[b] Faculty of Mechanical, Maritime, and Materials Engineering, TU Delft, NL
[*]Correspondence: *jmom1n15@soton.ac.uk*

1 Introduction

The kinematics have the most significant effect on the locomotive properties of marine animals; however, some intricacies of animal evolution, such as shark skin, have sparked research into the benefits of aquatic surface textures.

Previous work identified important non-dimensional kinematic parameters for efficient swimming such as the Strouhal number (St) and the amplitude to length ratio but these are not the only factors affecting the locomotive performance. Many studies have identified drag-reducing surface textures such as riblets although most are applied to static geometries. There is some suggestion the effect transfers to unsteady, aquatic propulsion however, if riblets are not viscous scaled and/or have other larger-scale features they can increase drag. Similarly, when the denticles do not entirely interlock, the three-dimensionality of denticles can be detrimental and increase drag.

During a swim cycle, denticles predominantly lie outside of the ideal conditions required for riblet induced drag reduction because of the morphing of the body and fluctuating viscous scales. However, some research focuses on the interaction between the denticles and kinematics in terms of a larger dynamical system, for example, this body morphing causes the denticles to bristle which has been shown to keep the flow attached in areas of flow reversal. The interaction with the kinematics and the hydrodynamic effect of surface texture remains under-studied and unclear in part, due to the complicated shape of the denticles which do not lend themselves to systematic investigation. To this end, we use an egg-carton type roughness function popular with rough-wall turbulence research because we can change important roughness scalings with a single parameter.

In this work, we study the interaction between kinematics and roughness topologies through high-resolution simulations. We fix the Reynolds number (Re) of these simulations to $12,000$ to access moderate Reynolds numbers for these types of flows and we fix the kinematics of the plate to a travelling waveform with $St = 0.3$. As denticle geometries are complex with several potentially important length scales, we focus on a simple roughness texture with a single-length scale to assess how the topology interacts with the kinematics and impacts the hydrodynamic properties of the swimmer. By combining information from two different, but, well-established topics we hope to understand the influence of one on the other.

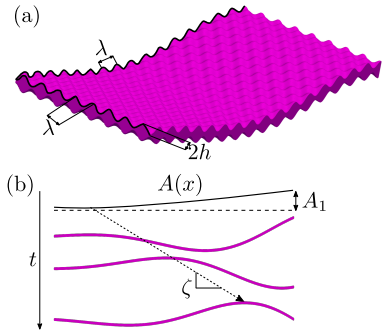

Figure 1: (a), the geometry used, which has two defining parameters λ, the wavelength of the roughness, and h, the roughness amplitude. (b), a visual representation of the parameters that define the plate motion.

2 Results

Scaling all length scales by the body length (L), and all time scales by L/U. We use a flat plate with an egg-carton type roughness defined by its wavelength, λ and the bump amplitude, h (figure 1a). In this study we fix $h = 0.01$ and restrict $\lambda[1/4, 1/52]$. Figure 1b illustrates the kinematics were we use $St = 0.3$, $A = 0.1$, a generalised amplitude envelope and change the wave speed ζ to achieve SPS.

Figure 2 shows the flow structure visualised by isosurfaces of the Q-Criterion. The flow exhibits a distinguishable transition as ζ increases. For low ζ the bumps dominate the flow structure and we see distinct horseshoe vortices shed from each element. These vortices persist downstream into counter-rotating streaks that compose the near wake. The flow structures get smaller as ζ increases and the horseshoe vortex around each element becomes less distinct. For figure 2c, we can see the near wake collects into a wavy vortex tube similar to those that categorise a two-dimensional flow

[1]This work was supported by the Office of Naval Research Global Award N62909-18-1-2091.

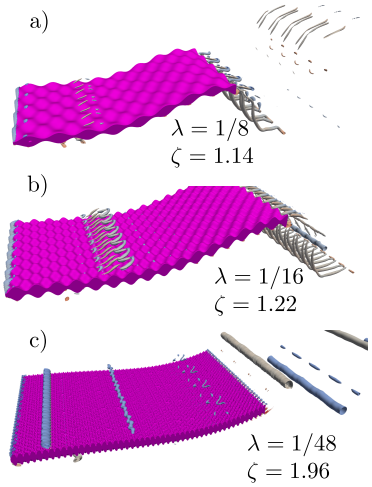

Figure 2: The Q-Criterion of the flow around a flat plate with a decreasing roughness wavelength.

driven by kinematics [1].

To identify the separate fluid dynamic contribution of ζ and λ we look at scaled enstrophy of the rough surface and its smooth kinematic counterpart. Figure 3a shows the results of E against ζ, where the black and grey lines are the rough and smooth plate results respectively. The positive gradient of both the lines shows that increasing ζ increases enstrophy, and the offset between the grey and the black line indicates that adding roughness also increases enstrophy. As we increase ζ, the enstrophy increases for both the smooth and the rough cases. At the upper limit of ζ, the smooth and the rough lines start converging as the rough flow also becomes two-dimensional (figure 2).

In figure 3a there is the peak in enstrophy at $\zeta \approx 1.2$ corresponding to a wavelength $\lambda = 1/16$. The peak coincides with the superposition of the flow features associated with both the roughness and kinematics (figure 2b). This is evident as surfaces with shorter λ are increasingly dominated by the two-dimensional vortex tubes associated with the kinematic flow as the structures shed off the roughness elements decrease in size (figure 2c), and surfaces with longer λ are dominated by the flow off the the roughness elements (figure 2b). We can relate this peak in enstrophy to an amplification of turbulent flow structures similar to those found in Prandtl's Secondary Motions of the Second Kind [2] where secondary currents were induced when the surface texture has features that scale with the outer length-scale of the flow.

In figure 3b we plot the difference in enstrophy between the smooth and the rough plate (ΔE) against λ/δ where $\delta = 0.06$ is the average accelerated boundary layer height at the trailing edge of the smooth plate. The peak in ΔE occurs when $\lambda/\delta \approx 1$. Finally, in our study, the power increases almost linearly until $\zeta \approx 1.8$, and our enstrophy peak lies within this regime. This means that the accentuation of these secondary flows truly is a boundary layer scaling, and

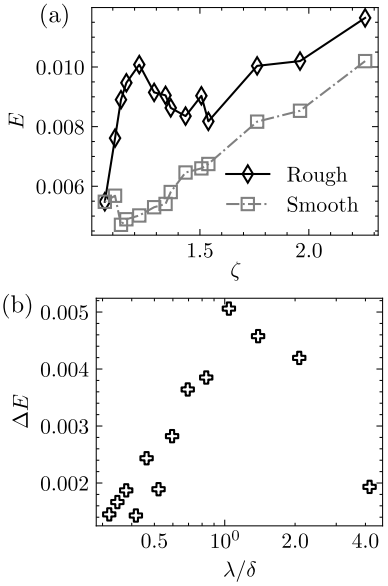

Figure 3: (a), the enstrophy (E) of the system depending on ζ of the plate. The black line is the rough plate with decreasing λ and the grey line is a smooth plate with identical kinematics. (b), the difference between the smooth and the rough E scaled by λ/δ.

not a result of increased vorticity production at the wall (due to kinematics). Therefore, we can relate the system's increase in mixing to scaling arguments previously defined in turbulent wall-flows.

3 Conclusion

We examined the effect of an egg-carton-type rough surface on a Self Propelled Swimming Body and found a decrease in the roughness wavelength requires an increase in the wave speed to maintain SPS. Increasing the wave speed changed the vortex structures and consolidated the vorticity into two-dimensional packets with a distinct leading edge vortex propagating down the body. To decouple the effects of roughness and kinematics we compared the forces and enstrophy to a smooth swimmer with identical kinematics. We saw there was a peak in enstrophy which coincided with a superposition of two flow modes, one dominated by three-dimensional structures and the other by the two-dimensional tubes. The peak in enstrophy was observed when the roughness wavelength matches the boundary layer thickness which is in line with scaling arguments defined for turbulent wall-flows ([3]).

References

[1] AN Zurman-Nasution, Bharathram Ganapathisubramani, and GD Weymouth. Influence of three-dimensionality on propulsive flapping. *Journal of Fluid Mechanics*, 886, 2020.

[2] Ludwig Prandtl. Über die ausgebildete Turbulenz. *Verhandl. des II. Int. Kongr. für Techn. Mech.*, pages 62–75, 1926.

[3] Christina Vanderwel and Bharathram Ganapathisubramani. Effects of spanwise spacing on large-scale secondary flows in rough-wall turbulent boundary layers. *Journal of Fluid Mechanics*, 774, 2015.

Volumetric PTV/PIV measurements of a Turbulent Separation Bubble

Ross Richardson[a*]
[a] Florida State University, Mechanical Engineering, Tallahassee, USA[1]
Yang Zhang and Louis Cattafesta[b]
[b] Illinois Institute of Technology, Mechanical, Materials, and Aerospace Engineering, Chicago, USA
[*]Correspondence: *rbr11@fsu.edu*

1 Introduction

Turbulent boundary layer separation and reattachement, otherwise referred to as turbulent separation bubbles (TSBs), occur across a wide variety of practical engineering applications. Present in both low- and high-speed flows, TSBs impact the performance of a multitude of fluidic devices and systems (i.e., wings at high angles of attack, diffusers, shock-wave boundary layer interactions, external protuberances, engine intakes, etc.) [1]. The dynamics of TSBs have been shown to be dependent on the means of their formation. Separation and reattachment caused by an adverse pressure gradient as opposed to a geometric singularity (i.e., backward-facing step) has been observed to significantly effect the dynamics of the flow and produces a pressure distribution that more closely resembles those occurring over airfoils and in diffusers [2]. Pressure-gradient-induced TSBs are documented to possess two distinct timescales associated to the shear layer 'vortex shedding' and contraction/expansion (i.e., 'breathing') of the separated region, which are separated by a factor on the order of 10 to 100 times [3]. In our recent studies, we investigated the flow features associated with these two different time scales using time-resolved Particle Image Velocimetry (PIV)[4].

TSBs are three-dimensional in nature. Advancements in modern optical based diagnostic techniques enable the non-intrusive volumetric measurement of these complex flow fields. As a continued study of our previous work [4], we further investigate the three-dimensionality of pressure-gradient-induced TSBs using Tomographic Particle Image Velocimetry (Tomo-PIV) and multi-pulse Particle Tracking Velocimetry (PTV) in the current study. The surface pressure properties and dimensionality of the flow field are explored to better understand the fundamental flow physics that occur in TSBs. Insights from this work seek to gain a better understanding on the three-dimensional flow structures associated with different time scales in pressure-gradient-induced TSBs.

[1]This work was supported by AFOSR under grant number FA9550-17-1-0084, and the Emil Buehler Fund

2 Experimental configuration

The experiments are carried out in the Florida State flow control wind tunnel. The flat plate model is illustrated in Figure 1. A suction fan is mounted on the top of the test section to impose an adverse pressure gradient on the flat plate model. There are 20 HCLA02X5EB pressure sensors with a 2.8 cm streamwise spacing, 6.35 mm from the model centerline. These sensors have a bandwidth from dc up to 2 kHz, thus providing both steady C_p and spectra of the surface pressure fluctuations in the current study. Details regarding the model and the pressure measurements are provided in [4].

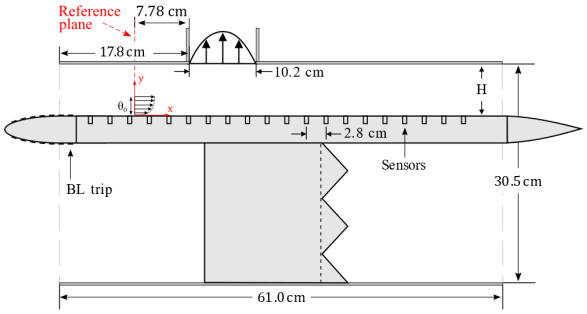

Figure 1: Flat plate model. Flow direction is left to right.

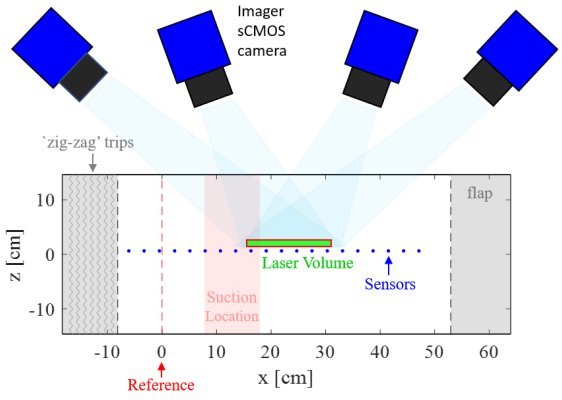

Figure 2: Tomo-PIV camera setup. Top view.

Tomo-PIV is performed using 4 sCMOS cameras on a rail located at one side of the wind tunnel (Figure 2). The cal-

ibration is first performed with a 3D calibration plate, and then volumetric self-calibration is performed. The laser volume is introduced into the test section slightly off the centerline at an angle with a dimension of $150 \times 50 \times 10$ mm. The data acquisition and processing are performed using LaVision DaVis 10.2. The final voxel size is $2490 \times 831 \times 167$ resulting in a vector resolution of approximately 2 vectors/mm.

3 Results

The results shown herein are obtained at a free stream speed of approximately 13.5 m/s corresponding to a Reynolds number based on the incoming turbulent boundary layer momentum thickness of $Re_\theta \approx 750$. The Cp distribution is shown in Figure 3. After the large adverse pressure gradient imposed by the suction fan, there is an abrupt relaxation followed by a mild adverse pressure gradient downstream. The $C_{p'}$ distribution clearly shows two local maxima with high variance in the surface pressure coefficient. The regions of higher variance in the surface pressure are associated with the elevated unsteadiness of the separation and reattachment points of the TSB.

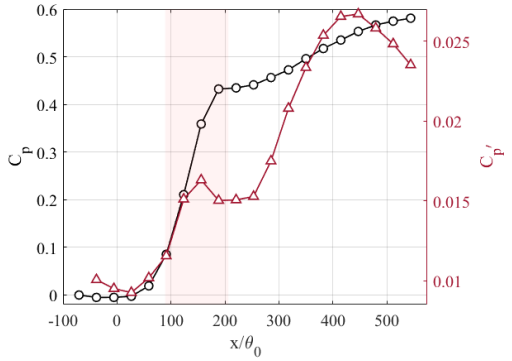

Figure 3: Mean surface pressure coefficient and fluctuating surface pressure coefficient. Shaded red band indicates the location of the suction.

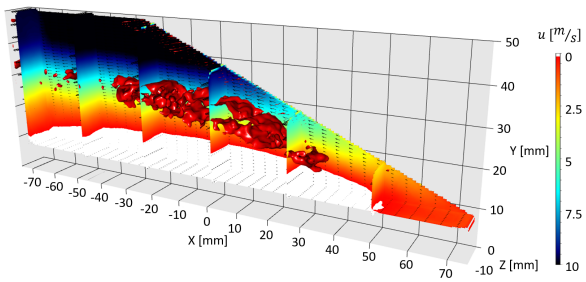

Figure 4: Mean TSB shown with streamwise velocity field and a red isosurface of vorticity

.

Preliminary results of the flow field are obtained from 500 snapshots. We will provide statistically converged results with longer data samples in the full paper. The flow field of the u-component with an isosurface of spanwise vorticity is shown in Figure 4. The separation and reattachment of the flow are clearly observed. Figure 5 displays the spanwise vorticity component with the isosurface of $\bar{u} = 0$. Elevated levels of spanwise vorticity are observed in the shear layer and on the surface of the flat plate, within the separated region.

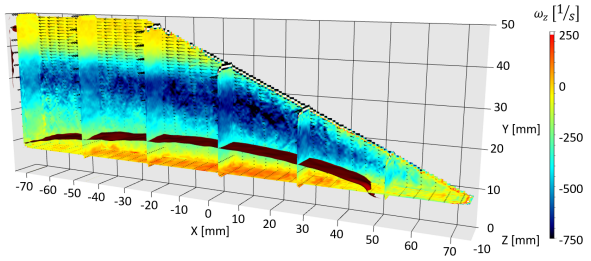

Figure 5: Mean TSB shown with the spanwise vorticity component and a red isosurface of streamwise velocity showing the edge of the reverse-flow region

.

4 Conclusion

Preliminary results of surface pressure and velocity fields from Tomo-PIV are shown to demonstrate the TSB induced by a suction imposed pressure gradient in the current study. In the full paper, more flow properties will be processed and provided from a longer data record. Besides the Tomo-PIV measurements, the laser timing scheme will be changed to a 4-pulse configuration to enable the 'state-of-art' PTV measurements. With this multi-pulse PTV configuration, in addition to flow velocity, material acceleration information can also be obtained. With the Spectral Modal Analysis Method [5], we will be able to calculate the three-dimensional coherent flow structures associated with different time scales.

References

[1] RL Simpson. A review of some phenomena in turbulent flow separation. 1981.

[2] Wen Wu, Charles Meneveau, and Rajat Mittal. Spatio-temporal dynamics of turbulent separation bubbles. *Journal of Fluid Mechanics*, 883, 2020.

[3] Julien Weiss, Abdelouahab Mohammed-Taifour, and Quentin Schwaab. Unsteady behavior of a pressure-induced turbulent separation bubble. *AIAA Journal*, 53(9):2634–2645, 2015.

[4] Ross Richardson, Yang Zhang, and Louis N Cattafesta. Low frequency characteristics of a pressure-gradient induced turbulent separation bubble. In *AIAA SCITECH 2023 Forum*, page 0079, 2023.

[5] Yang Zhang, Louis N Cattafesta, and Lawrence Ukeiley. Spectral analysis modal methods (samms) using non-time-resolved piv. *Experiments in Fluids*, 61(11):1–12, 2020.

7 Session G: Vortex Dynamics - 2

A weak coupling between near-wall Eulerian solvers and a Vortex Particle-Mesh method for efficient simulation of 2D external flows

P. Billuart[a], Y. Marchal[a], G. Lartigue[b], P. Bénard[b], M. Duponcheel[a], P. Chatelain[a] and G. Winckelmans[a*]
[a] Université catholique de Louvain (UCLouvain), iMMC, Louvain-la-Neuve, Belgium
[b] Institut National des Sciences Appliquées (INSA) Rouen Normandie
Complexe de Recherche Interprofessionnel en Aérothermochimie (CORIA) - UMR 6614
*Correspondence: *gregoire.winckelmans@uclouvain.be*

1 Introduction

External flow simulations are ubiquitous in both research and industry, spanning e.g. vehicle aero- or hydrodynamics, wind energy, civil engineering, etc. The targeted problems remain quite challenging as they usually require an accurate capture of (1) the near-wall region in order to compute accurately the forces at the wall device, and also of (2) the wake; especially when this wake interacts with another device downstream.

The research and industry currently offer various solutions to simulate such flows. Among those are so-called "vortex methods" that rely on the vorticity-velocity formulation of the Navier-Stokes equations. They offer several computational assets that are particularly interesting for the wake regions. The formulation also accommodates quite naturally the enforcement of unbounded conditions for external flows. Secondly, the discretization of the vorticity using Lagrangian "vortex particles" for the convection step also allows to waive the classical CFL condition, thereby allowing to use larger time steps. Their accuracy for long time simulations is also maintained thanks to the particle redistribution step (also called remeshing step), which consists in replacing the distorted set of vortex particles by a new well-order set every few time steps, by using high order interpolants. In the vortex particle-mesh (VPM) variant of the method, only the convection is done in a Lagrangian way; all otther operations are done on the mesh. The method also entails low dispersion and diffusion errors, which allows to accurately advect complex vortical structures over large distances [1–3].

Vortex methods are however less suited to capture high Reynolds number wall-bounded flows, because the computational elements (particles and underlying mesh) are intrinsically isotropic. This quickly leads to a very large number of particles, and thus a prohibitive computational cost, to capture the near-wall gradients. This limitation can be mitigated by the use of Multi-Resolution methods or Adaptive Mesh Refinement (AMR) [4]; yet this does not lift the local mesh isotropy constraint. This characteristic also implies that the body surface must be treated as an immersed boundary; i.e., using panel-based methods [5, 6], or penalization methods [7–9], or the more accurate immersed interface method [10].

Another possibility is to use an Eulerian body-fitted grid solver, e.g. using finite differences, finite volumes, finite elements, etc. Thanks to their anisotropic elements, conformal meshes that fit the body surface can be used to properly capture the thin boundary layers that develop near the walls. Such Eulerian methods are nevertheless not as efficient as remeshed vortex methods when it comes to simulating wakes, due to their common Eulerian-related dispersion and diffusion errors. Those solvers are also not enforcing naturally unbounded flow conditions. The proper capture of the wake over long distances and with similar accuracy hence requires a computational domain larger than that of the vortex method, and also with a finer grid.

This naturally leads to the idea that one could exploit the advantages of vortex methods and of body-fitted grid solvers in a coupled approach: use an Eulerian solver to resolve the near-wall region, and a vortex method to handle the convection-dominated part of the flow, such as the wake.

2 Methodology and Results

We consider here a weak coupling strategy, as that developed in [11–13]. In such a coupling, the Lagrangian method solves the flow over the entire domain that contains vorticity (yet in a highly under-resolved way near the wall), while the body-fitted Eulerian solver properly resolves the near-wall boundary layers and solves, using the primitive velocity-pressure variables, the near-wall region within a subdomain that contains the body and its neighborhoud. There is thus a full overlapping of the two computational domains over the near-wall region. In such coupling, the vortex method drives the Eulerian solver by providing the boundary conditions on the outer boundary of its domain, whereas the Eulerian solution is used to correct the vorticity of the vortex method in the near-wall region.

The weak couplings developed until now [11–13] enforce Dirichlet boundary conditions for the velocity components

[1] P. Billuart PhD research was funded by UCLouvain as Research Assistant. Y. Marchal PhD research is also funded by UCLouvain as Research Assistant.

at the outer boundary of the Eulerian solver domain. As these velocity values are obtained from the velocity field provided by the vortex method, any velocity mismatch between the solvers is translated into spurious vorticity. These works also utilise a non-conservative scheme for the transfer of vorticity from the near-wall solver to the vortex method; i.e., the circulation is not conserved. These works attempt to mitigate the circulation error by adding a vortex panel method on the body surface. The recourse to a panel method however proves counterproductive as it leads to oscillations in the near-wall velocity field. Those oscillations can even be exacerbated by the distortion of the computational elements typical of Lagrangian vortex methods. Those two symptoms lead to a noisy evaluation of the wall stresses, that are unexploitable toward the computation of accurate aerodynamic forces.

The novel approaches presented in [14] address the shortcomings identified above. The new coupling scheme uses mixed boundary conditions for the near-wall solver, so as to also properly match the vorticity field of both solvers on the outer boundary of the near-wall region, thereby avoiding the generation of spurious vorticity there. In addition, the correction scheme of the VPM vorticity field by the near-wall Eulerian field guarantees a global conservation of the circulation (within interpolation and discretisation errors), without requiring a complex vorticity integration method. No additional near-wall treatment technique (panel method or penalisation method or immersed interface method) is used here in the VPM method. To also mitigate the pressure oscillations in the body-fitted solver due to the common flow distortion errors of vortex methods, we use two sets of particles, each remeshed at different time intervals (the set closest to the body being remeshed more often).

The new coupling methodology has been developed, and validated, for two types of body-fitted solvers: (1) a solver developed on purpose and that uses finite differences on a staggered grid; the grid being everywhere orthogonal and obtained using a conformal mapping; (2) the industry-oriented solver YALES2 developed at CORIA and that uses finite volumes and unstructured meshes. We demonstrate the correct performance of the coupling on classical benchmarks: the flow past an impulsively started cylinder (see Fig. 1) and the flow past a cylinder with established vortex shedding. As application, we present the case of an airfoil at a high angle of attack. The method is also being extended to handle moving bodies, and results from [15] for the flow past a horizontally oscillating cylinder are also presented.

3 Conclusion

The coupling approach presented in [14] allows for accurate and efficient simulations in 2D external flow aerodynamics at high Reynolds numbers. Coupling of the VPM solver with the industry-oriented solver YALES2 for the near-body region was also achieved with success. The next step will be to achieve the coupling in 3D.

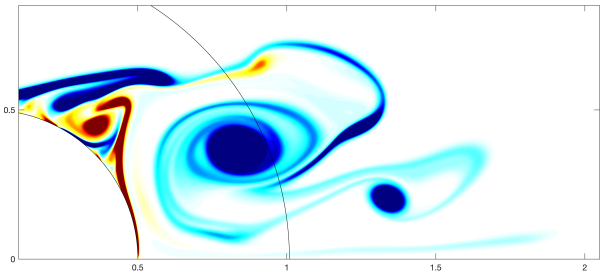

Figure 1: Impulsively started cylinder at $Re = 9500$: zoom on the vorticity field at $t^* = 4$. The black line shows the outer boundary of the near-wall solver (here YALES2).

References

[1] G.-H. Cottet and P. Koumoutsakos. *Vortex methods: theory and practice*, Cambridge University Press, 2000.

[2] G. Winckelmans. *Vortex Methods*, in *Encyclopedia of Computational Mechanics*, Volume 3 *Fluids*, John Wiley & Sons, 2004.

[3] D.-G. Caprace, P. Chatelain, G. Winckelmans. Wakes of rotorcraft in advancing flight: A large eddy simulation study, *Phys. Fluids* 32, 087107 (2020).

[4] D. Rossinelli, B. Hejazialhosseini, W. van Rees, M. Gazzola, M. Bergdorf, P. Koumoutsakos, MRAG-I2D: Multi-resolution adapted grids for remeshed vortex methods on multicore architectures, *Journal of Computational Physics* 288 (2015) 1?18.

[5] P. Koumoutsakos, A. Leonard, F. Pépin. Boundary conditions for viscous vortex methods, *Journal of Computational Physics*, 113-1 (1994) 52-61.

[6] G. Winckelmans, P. Ploumhans. Vortex methods for high-resolution simulations of viscous flow past bluff bodies of general geometry, *Journal of Computational Physics*, 165-2 (2000) 354-406.

[7] , M. Coquerelle, G.-H. Cottet. A vortex level set method for the two-way coupling of an incompressible fluid with colliding rigid bodies, *Journal of Computational Physics* 227 (2008) 9121-9137.

[8] , M. Gazzola, P. Chatelain, W. van Rees, P. Koumoutsakos. Simulations of single and multiple swimmers with non-divergence free deforming geometries, *Journal of Computational Physics* 230 (2011) 7093-7114.

[9] T. Gillis, G. Winckelmans, P. Chatelain. An efficient iterative penalization method using recycled Krylov subspaces and its application to impulsively started flows, *Journal of Computational Physics* 347 (2017) 490-505.

[10] T. Gillis, Y. Marichal, G. Winckelmans, P. Chatelain. A 2D immersed interface Vortex Particle-Mesh method, *Journal of Computational Physics* 394 (2019) 700-718.

[11] G. Daeninck. *Developments in hybrid approaches: Vortex method with known separation location; Vortex method with near-wall Eulerian solver; RANS-LES coupling*, PhD thesis, Université catholique de Louvain, 2006.

[12] Y. Marichal. Chapter in *An immersed interface vortex particle-mesh method*, PhD thesis, Université catholique de Louvain, 2014.

[13] M. Stock, A. Gharakhani, C. Stone. Modeling rotor wakes with a hybrid OVERFLOW-vortex method on a GPU Cluster, American Institute of Aeronautics and Astronautics, 2015/08/11 2010.

[14] P. Billuart, M. Duponcheel, G. Winckelmans, P. Chatelain. A weak coupling between a near-wall Eulerian solver and a Vortex Particle-Mesh method for the efficient simulation of 2D external flows, *Journal of Computational Physics* 473 (2023) 111726.

[15] Y. Marchal. *Efficient and accurate simulation of the flow past moving bodies*, Master thesis, Université catholique de Louvain, 2022.

Schlieren Visualization of Flow around Square Cylinders in Tandem Arrangement at a Reynolds Number 2.0×10^3 in Compressible Flows

Miku Kasai[a*], Takayuki Nagata [a], Keisuke Asai[a], Yuta Ozawa[a], and Taku Nonomura[a].
[a] Tohoku University, Department of Aerospace Engineering, Miyagi, Japan[1,2]
[*]Correspondence: *miku.kasai.p8@dc.tohoku.ac.jp*

1 Introduction

In recent years, high-altitude unmanned aerial vehicles and aircraft and helicopters for the exploration of Mars [1] have been attracting a great deal of attention. These fluid machines are exposed to low-pressure, high-speed airflow, that is, compressible low-Reynolds-number flow. It is necessary to elucidate the compressible low-Reynolds-number flow to design a fluid machine in such an extreme condition. Several researches have been conducted on the flow around fundamental shapes such as a cylinder [2–4], a square cylinder [2], and a flat plate [5, 6] at low Reynolds numbers. In contrast, research has not progressed on unsteady flow in which two or more objects fluid-dynamically interfere with each other. The flow around two cylinders arranged in tandem is one of the unsteady flows in which aerodynamic interference becomes important. Sakamoto et al. [7] experimentally evaluated the flow around two square cylinders in incompressible region at $Re = 2.76 \times 10^4$. The dimensionless distance s/W obtained by dividing the distance s between two cylinders by the height W of the cylinder was changed. On the basis of the discontinuous change in drag coefficient, Sakamoto et al. [7] categorized flow fields into two modes across the particular distance, that is the critical spacing, $s/W = 3$: Mode I where vortex is shed only from the downstream cylinder and Mode II where synchronous vortices are shed from both cylinders. In Mode I, the steady recirculation region between the two cylinders causes a negative drag on the downstream cylinder and a smaller drag coefficient on the upstream cylinder than that of a single cylinder. In Mode II, the drag of the downstream cylinder increases sharply and becomes positive because the separated shear layer rolls up strongly behind the upstream cylinder. Liu et al. [8] suggested that Mode I can be further divided into two modes from the pressure distribution at $Re = 2,700$. There are a flow field in which the separated shear layer from the leading edge of the upstream cylinder behaves as a single slender object without reattaching to the downstream one for shorter space, and a flow field in which the shear layer reattaches.

It is known that compressibility affects the length of the recirculation region around a circular cylinder [4]. This implies that the interference flow between objects may be strongly changed by the compressible effect. The purpose of this study is to elucidate how the flow around two square cylinders arranged in a tandem arrangement is influenced by compressibility.

2 Methods

The wind tunnel test is conducted in a low-density wind tunnel [5]. A duct with a butterfly valve connects a main tank which has a suction-type wind tunnel with a cross-section of 150 mm $\times$ 100 mm and a buffer tank. A high-pressure gas is injected downstream by an ejector located on the downstream side of the measurement unit. By adjusting the pressure in the main tank and the pressure of the gas supplied to the ejector, and the Reynolds number $Re = 2.0 \times 10^3$ and Mach number $M = 0.1$–0.7 except for $M = 0.3$ can be changed independently.

The schlieren visualization in the low-density wind tunnel was performed and analyzed according to the method by Shigeta et al. [9]. A model is a square cylinder of 10 mm on each side without chamfer and the span length l of 100 mm. When the space between the trailing edge of the upstream cylinder and the leading edge of the downstream one is s, the measurement was performed with the dimensionless space $s/d = 0.5, 1.5, 2.5, 3.1$, and 4 divided by a width d of the cylinder. The blockage rate is approximately 6.7%. Randomized singular value decomposition (RSVD) was applied to the time-series images after background subtraction. The size of the random sketch was set to 1200, the upper mode was selected so that the sum of the singular values was 90% of the total, and the time series data was reconstructed. The drag was also measured according to the method by Nagata et al. [4].

3 Results

Figure 1 shows the drag coefficient for dimensionless space at each Mach number. Below Mach 0.2, the drag coefficients of both cylinders increases sharply at critical spacing. In contrast, at Mach 0.4 and above, the drag coefficient of both cylinders gradually increases as the space increases. Figures 2, 3, and 4 show the effect of the Mach number on the instantaneous flow filed of tandem cylinders at $s/d = 0.5$, 2.5, and 4.0, respectively. The flow fields change signifi-

[1]This work was supported by the Japan Society for the Promotion of Science, KAKENHI under grant numbers JP21J20324 and JP21K14071.
[2]T. Nagata was supported by the Japan Science and Technology Agency, CREST grant JPMJCR1763.

cantly as the Mach number increases. In a tandem arrangement at $s/d = 0.5$, flow fields are classified into Mode I.

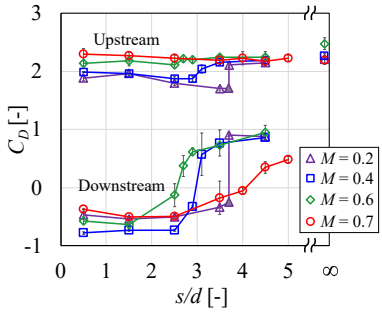

Figure 1: Variation of drag coefficient with space.

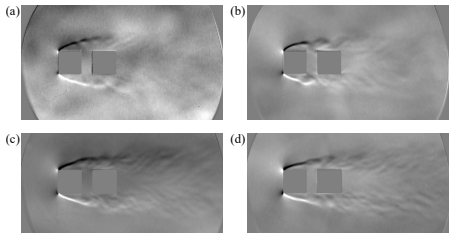

Figure 2: Instantaneous flow fields at $s/d = 0.5$. (a)$M = 0.2$; (b)$M = 0.4$; (c)$M = 0.6$; (d)$M = 0.7$.

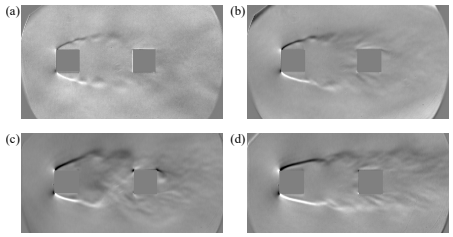

Figure 3: Instantaneous flow fields at $s/d = 2.5$. (a)$M = 0.2$; (b)$M = 0.4$; (c)$M = 0.6$; (d)$M = 0.7$.

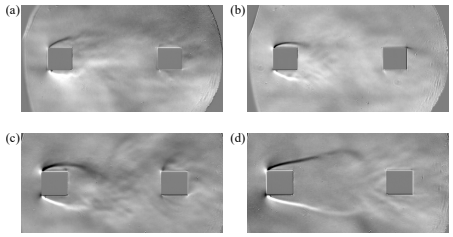

Figure 4: Instantaneous flow fields at $s/d = 4.0$. (a)$M = 0.2$; (b)$M = 0.4$; (c)$M = 0.6$; (d)$M = 0.7$.

For $M = 0.2$, the shear layer separated from the leading edge of the upstream cylinder extends to the rear of the downstream one. At $M = 0.4$, the shear layer strongly rolls between the sides of two cylinders, and relatively large eddies advect alternately on the downstream side of the cylinder. The flow fields at $M = 0.6$ and 0.7 are similar, and the shear layer rolls up symmetrically between the two cylinders on the sides of two cylinders, and the vortices advect downstream. In a tandem arrangement at $s/d = 2.5$ for $M = 0.2$, the small vortices in the shear layer due to the Kelvin–Helmholtz instability develop asymmetrically and extend to the downstream side of the cylinder. At $M = 0.4$, small vortices in the shear layer asymmetrically grow larger than $M = 0.2$ and are shed near the front surface of the downstream cylinder. At $M = 0.6$, the flow field transits to the Mode II, and large-scale vortex shedding begins between the cylinders. On the other hand, symmetrical vortices are emitted between the cylinders at $M = 0.7$. In a tandem arrangement at $s/d = 4.0$, Kármán vortices are emitted from both cylinders from $M = 0.2$ to 0.6. At $M = 0.7$, larger symmetrical vortex shedding begins between cylinders than $s/d = 2.5$. The increase in the Mach number reduces the growth rate of the instability of the shear layer and extends the recirculation region of a single cylinder significantly at $Re = 2.0 \times 10^3$. The transition to the Karman vortex (Mode II) does not occur even at $s/d = 4.0$ for $M = 0.7$ because the growth rate of the instability of the shear layer decreases. The instability of the shear layer is affected by the widening of the space, and the scale of the vortices formed between the cylinders increases at Mach 0.7.

4 Conclusion

In this study, the flow around two square cylinders in a tandem arrangement were visualized by Schlieren at $Re = 2.0 \times 10^3, M = 0.1$–$0.7$, and the effect of compressibility on interference flow was evaluated. The flow field changed with increasing space and Mach number. The higher the Mach number, the faster the flow field transitions from Mode I to Mode II below $M = 0.6$. At $M = 0.7$, the flow field did not transit to Mode II even at $s/d = 4$ due to the slow growth rate of the shear layer, and symmetrical large-scale vortex shedding is observed.

References

[1] David W. Hall, et al. Airplane for Mars Exploration. *Technical Report, NASA Ames Research Center*, 1977.

[2] William F. Lindsey, et al. Drag of cylinders of simple shapes. *National Advisory Committee for Aeronautics*, NACA-TN-3038, 1938.

[3] Daniel Canuto and Taira Kunihiko. Two-dimensional compressible viscous flow around a circular cylinder. *J. Fluid Mech.*, 785:349–371, 2015.

[4] Takayuki Nagata, et al. Experimental investigation on compressible flow over a circular cylinder at Reynolds number of between 1000 and 5000. *J. Fluid Mech.*, 893:A13, 2020.

[5] Masayuki Anyoji, et al. Effects of Mach number and specific heat ratio on low-Reynolds-number airfoil flows. *AIAA J.*, 53(6):1640–1654, 2015.

[6] Kensuke Kusama, et al. Investigation of Mach number effects on flow over a flat plate at Reynolds number of 1.0× 104 by schlieren visualization. *Fluid Dyn Res*, 53(1):015513, 2021.

[7] Hiroshi. Sakamoto, et al. Fluctuating forces acting on two square prisms in a tandem arrangement. *J. Wind. Eng. Ind.*, 26(1):85–103, 1987.

[8] Chia-Hung Liu and Jerry M. Chen. Observations of hysteresis in flow around two square cylinders in a tandem arrangement. *J. Wind. Eng. Ind.*, 90(9):1019–1050, 2002.

[9] Tsuyoshi Shigeta, et al. Enhancement of signal-to-noise ratio of schlieren visualization measurements in low-density wind tunnel tests using modal decomposition. *J Vis*, 1–16, 2022.

Bursting on helical vortices with small radius-to-pitch ratios

L. Ji [a] and W. M. van Rees[a*]
[a] Massachussetts Institute of Technology, Department of Mechanical Engineering, Cambridge, USA[1]
*Correspondence: *wvanrees@mit.edu*

1 Introduction

Flying and swimming in nature often involves flapping wings or fins, which can produce helical vortical structures whose evolution affects the generation of lift and drag [1,2], as well as the wake signature. The stability of such vortices to perturbation is thus relevant to biological propulsion, as well as other areas of fluid dynamics like free-space turbulence, wall-bounded turbulence, and swirling jets [5,8,11]. Existing stability analyses have identified various instability types on helical vortices, such as the long and short wave instability and the mutual induction instability [12]. However, these studies did not include the possible destabilizing effect of core-size variations on helical vortices. Such core-size variations can appear on trailing vortices in unsteady conditions [9], and lead to the propagation of twist waves [3,6,7] and subsequent vortex bursting. On straight vortex tubes, vortex bursting has been associated with a strong increase in energy dissipation and destabilization of the vortex core [4,10]. On helical vortices with initial core-size variations, we expect the generation and propagation of twist waves to interact with the axial velocity and core dynamics associated with the chirality of the tube. It is unclear how this specifically affects the bursting and possible subsequent destabilization of the bursting structure and vortex core.

To address these open questions, we simulate and analyze helical vortex tubes with small radius (R) to pitch (p) ratios at circulation-based Reynolds number 5000 with initial finite core-size perturbation amplitudes. We set-up initial conditions of helical vortex tubes with Gaussian core profile and radius-to-pitch ratios $0 \leq R/p \leq 0.0625$. This range of R/p values corresponds to helical vortices that are close to straight and the interaction between the neighbouring turns of the helical vortex is weak. A localized core-size perturbation of sinusoidal form (same as in [4]) is considered, where the perturbation amplitude is defined through the ratio of the maximum to minimum core-size (A). The computational domain is a rectangular box, where the helical centerline of the tube winds around the z axis and the length of the domain in z direction is $L_z = p$. The mean vortex core-size is chosen to be $\sigma_0/p = 0.05$. Time is non-dimensionalized with σ_0^2/Γ_0, where Γ_0 is the initial circulation. The boundary conditions are periodic in the z direction and unbounded in x and y directions. The flow evolution is solved by discretizing the 3D incompressible Navier-Stokes equations in vorticity-velocity form using a remeshed vortex method, as in [4,10].

[1]This work was supported by the U.S. Army Research Office under Award No. W911NF-21-1-0332.

2 Results

For the small radius-to-pitch ratio considered, the helical vortex tubes with no core-size perturbations undergo self-induced translation and rotation while the core diffuses, and remain stable during the time period considered. When finite core-size variations are imposed on such helical vortex tubes, the vortex tube undergoes a series of dynamics reminiscent of the straight tube case discussed in [4,10], but with some significant differences that we discuss below.

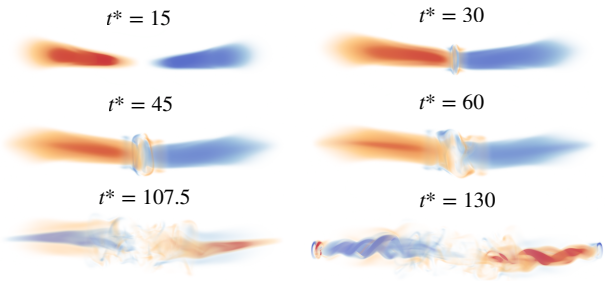

Figure 1: Volume rendering of helicity density field $h = \boldsymbol{u}\cdot\boldsymbol{\omega}$ for a helical vortex tube with $R/p = 0.02$ and $A = 4.3$ at different times.

Twist wave propagation Starting from $t^* = 0$, the differential rotation rates along the centerline of the vortex tube lead to the generation of a left-handed and a right-handed twist wave packet which propagate along the curved vortex tube. The helicity density field $h = \boldsymbol{u}\cdot\boldsymbol{\omega}$, for a helical vortex tube with a small R/p value is visualized in Fig. 1, which indicates the right-handed and left-handed twist waves (red and blue color, respectively) at $t^* = 15$. For a straight vortex tube with the type of core-size variation considered, the left-handed and right-handed twist waves propagate at the same speed due to symmetry. When the centerline of the vortex tube has non-zero torsion, as in the current case of a helix, there is a non-zero self-induced velocity component tangent to the centerline. For the current right-handed helix, this velocity component is positive and magnitude is small due to the small R/p ratios considered. This indicates that the symmetry between the left- and right-propagating twist waves is broken and there is a small but finite difference in their speeds in the lab frame.

Bursting events The twist wave packets propagate along the curved vortex centerline and their collision leads to the appearance of a pancake-like bursting structure starting at around $t^* = 30$, The bursting structure can be clearly visualized through the vorticity magnitude field and is shown in Fig. 2. The characteristic vortical structure that appears are formed by two interconnected vortex rings of opposite signs. As the core-size ratio increases, multiple ring pairs can be generated. The stability of the bursting structure at the late stage of bursting is different between the straight and helical vortex tubes. As shown in Fig. 2, for the same core-size ratio $A = 4.3$, for the straight tube case the bursting structure remains axisymmetric and no apparent instability sets in at the late stage of bursting. In contrast, the bursting structure for the helical vortex tubes becomes non-axisymmetric and unstable around $t^* = 45$, disintegrating into small scale structures. The instability originates from the shear arising in the bursting structure due to the vortex centerline dynamics, and thus sets in earlier for a higher R/p.

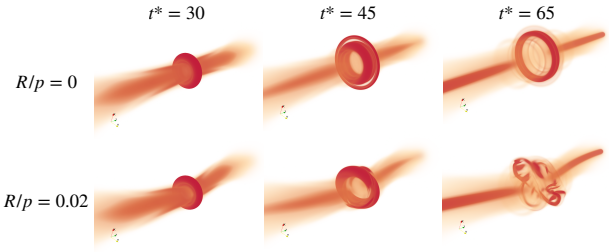

Figure 2: Volume rendering of vorticity magnitude field in the bursting region for $A = 4.3$ at three different times for a straight vortex tube (top row) and a helical vortex tube with $R/p = 0.02$ (bottom row).

Long-time flow evolution Despite the break-up of the bursting structure, the bursting process leads to twist wave reversal as in [4]. As indicated in Fig. 1, the cascading instabilities arising from bursting eventually disintegrate the vortex core at $t^* = 130$. This is associated with long-wave instabilities that manifest themselves as helical strands of stronger vorticity winding around the remnant of the centerline. This was also observed in the straight-line case [4], and the evolution of global energy and energy of the helical vortex tubes follows a similar trend to that of the straight vortex tubes with the same core-size ratio (see Fig. 3). As in the straight-line case, repeated bursting events and instabilities lead to a significant increase in global enstrophy and thus accelerate energy dissipation. Eventually, starting around $t^* = 200$, the twist waves and instabilities gradually dissipate and the vortex tubes undergo a relatively smooth viscous decay.

3 Conclusion

The analysis of the simulation results suggest that core-size perturbations on helical vortices can generate twist waves, which propagate along the vortex axis and their collision leads to the bursting events. The basic mechanisms underlying bursting appear to be similar between helical vortices and straight vortices. However, as helical vortex tubes are characterized by a self-induced axial flow along centerline of the vortex tube, the symmetry of the left- and right-propagating twist waves is broken. The associated difference in wave speeds shifts successive axial bursting locations in the lab frame. Further, the self-induced flow also shears and distorts the bursting structure, leading to instability and the generation of small scale vortical structures at the late stage of bursting. Overall, our results suggest that the twist wave propagation and bursting effects associated with core-size variations are robust phenomena for destabilizing vortex tubes within a wide range of centerline geometries.

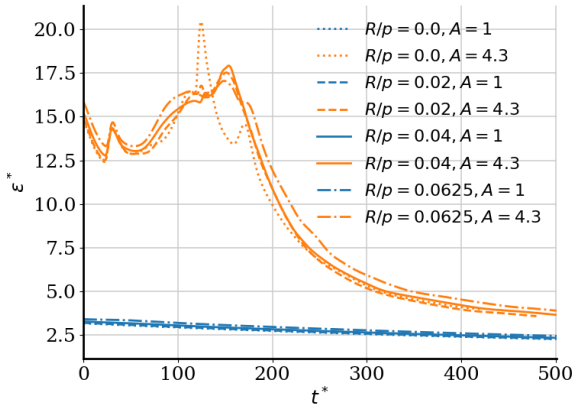

Figure 3: The time evolution of global enstrophy $\varepsilon^*(\Gamma_0^2/\sigma_0) = \int_V \boldsymbol{\omega} \cdot \boldsymbol{\omega} dV$ for cases with different R/p values. Here $R/p = 0$ is associated with a straight tube, and $A = 1$ denotes the absence of initial core-size variations.

References

[1] P. Chakraborty and A. Roy Energy dynamics in the helical wakes of flapping systems. *Physics of Fluids*, 34(10):103111, 2022.

[2] T. Engels, et al. Helical vortices generated by flapping wings of bumblebees. *The Japan Society of Fluid Mechanics*, 50(1):011419, 2018.

[3] D. Fabre, et al. Kelvin waves and the singular modes of the Lamb–Oseen vortex. *Journal of Fluid Mechanics*, 551:235–274, 2006.

[4] L. Ji and W. M. van Rees. Bursting on a vortex tube with initial axial core-size perturbations. *Journal of Fluid Mechanics*, 7(4):044704, 2022.

[5] W. Liu and B. Bai. A numerical study on helical vortices induced by a short twisted tape in a circular pipe. *Case Studies in Thermal Engineering*, 5:134–142, 2015.

[6] M. V. Melander and F. Hussain. Core dynamics on a vortex column. *Fluid Dynamics Research*, 13(1):1–37, 1994.

[7] H. Moet et al. Wave propagation in vortices and vortex bursting. *Physics of Fluids*, 17(5):054109, 2005.

[8] M. R. Ruith et al. Three-dimensional vortex breakdown in swirling jets and wakes: direct numerical simulation. *Journal of Fluid Mechanics*, 486:331-378, 2003.

[9] P. R. Spalart. Airplane trailing vortices. *Annual Review of Fluid Mechanics*, 30(1):107–138, 1998.

[10] W. M. van Rees. Vortex bursting. *Physicical Review Fluids*, 5(11):110504, 2020.

[11] C. M. Velte et al. Alteration of helical vortex core without change in flow topology. *Physicical of Fluids*, 23(5):051707, 2011.

[12] S. Widnall The stability of a helical vortex filament. *Journal of Fluid Mechanics*, 54(4):641–663, 1972.

Vortex Dynamics of Planar Flows at Extreme Reynolds numbers

Michail Chatzimanolakis[a] and Petros Koumoutsakos[b*]
[a] ETH Zurich, Switzeralnd[1]
[b] Harvard University, USA
[*]Correspondence: *petros@seas.harvard.edu*

1 Introduction

We present a series of Direct Numerical Simulations of the planar flow past an impulsively started cylinder at Reynolds numbers up to $1,000,000$. An intriguing portrait of unsteady separation is revealed; vorticity generation and vortex shedding entail a cascade of separation events on the cylinder surface that are reminiscent of Kelvin-Helmholtz instabilities. Primary vortices roll-up along the cylinder surface as a result of instabilities of the initially attached vortex sheets, followed by vortex eruptions, creation of secondary vorticity and formation of dipole structures that are subsequently ejected from the surface of the cylinder. The vortical structures and their relationship to the forces experienced by the cylinder are analyzed.

2 Results

Our high resolution simulations employ Adaptive Mesh Refinement (AMR), in order to keep the computational cost manageable [1, 2]. To ensure converged results, a refinement study was performed and the resolution of each simulation was selected such that the early pressure and viscous drag history given by the analytical results from [3] are captured with less than 1% error. This is shown at the top of fig. 1 for the flow at $Re = 100,000$. Note that time is non-dimensionalised as $T = \frac{D}{2U}$, where D is the cylinder diameter and U its velocity. We identify four phases in our simulations: (i) the early times of diffusion-dominated evolution of the vortex sheet, (ii) the vorticity eruption, (iii) the re-impingement on the cylinder surface of the wake dipole and (iv) the wake development stage. They are highlighted with different colors at the bottom of fig. 1, which shows the drag coefficient as a function of time, for the flow at $Re = 100,000$.

The vorticity field is shown at the last timestep of our simulations in fig. 2, for several Reynolds numbers and in fig. 3 for $Re = 1,000,000$. At the present Reynolds numbers it is known that symmetric flow conditions can be lost by tiny perturbations, such as numerical round-off errors. In our simulations we confirm a previous finding from [4], where it was found that fixing the order of operations through the inclusion of parentheses in the source code can preserve symmetry. The presence of symmetry without explicitly enforcing it is a manifestation of minimal numerical noise in the computations of the flow past an impulsively started cylinder [5].

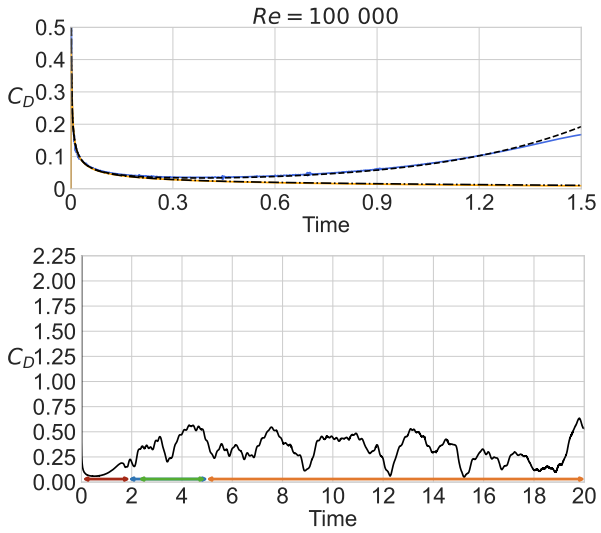

FIGURE 1. Top: computed pressure (—) and viscous (—) drag coefficients and analytical pressure (- - - -) and viscous (— · —) drag coefficients from [3]. Bottom: drag coefficient as a function of time. On the time axis we indicate the early vorticity diffusion regime (—), the vorticity eruption (—), the re-impingement on the cylinder surface of the wake dipole (—), and the wake development stage (—).

3 Conclusion

We performed high resolution simulations of the planar flow past an impulsively started cylinder at extreme Reynolds numbers up to $1,000,000$. Our numerical method manages to capture the analytical solutions for early times (that are even singular at $t = 0$) and to preserve a very fragile symmetry. We study unsteady separation mechanisms not present at lower Reynolds numbers and explore how they develop with time. Four distinct stages are identified: the early times of diffusion-dominated evolution of the vortex sheet, the vorticity eruption, the re-impingement on the cylinder surface of the wake dipole and the wake development stage. A strong dependence of drag on the vortex patterns observed

[1]We gratefully acknowledge resources by the Swiss Supercomputing Center (CSCS) ...

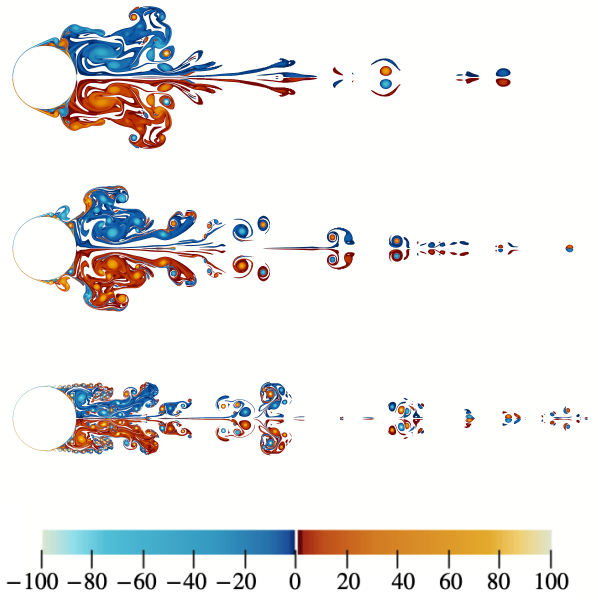

FIGURE 2. From top to bottom: vorticity field for the impulsively started cylinder at $Re = 25,000$, $Re = 50,000$, $Re = 100,000$. All snapshots correspond to $t = 20T$.

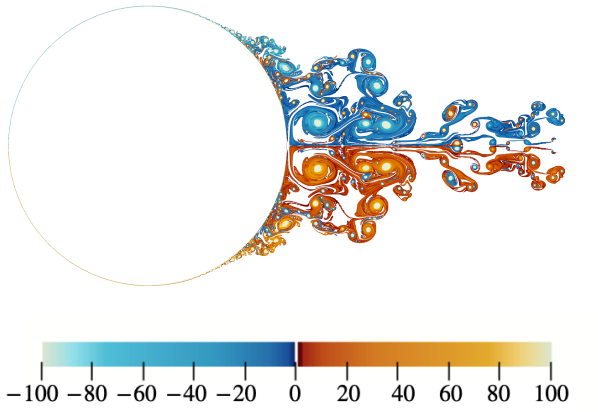

FIGURE 3. Vorticity field for the impulsively started cylinder at $Re = 1,000,000$ at time $t = 6.35T$.

during these stages is thoroughly analyzed. Commencing of separation leads to a significant increase in drag, whereas vortex re-impingement on the cylinder surface leads to local drag minima. At $Re = 100,000$, drag reduction seems to occur when the primary separation angle becomes acute, a situation reminiscent of the well-known drag crisis [6]. By comparing the flows at different Reynolds numbers, we find that the mechanisms of wake formation involve a cascade of separation events and merging of small primary vortices and the annihilation of secondary vorticity that erupts in the form of tight dipoles from the cylinder surface. Inducing such dipole eruptions may be an effective mechanism for control of turbulent, unsteady separated flows.

References

[1] Michail Chatzimanolakis, Pascal Weber, and Petros Koumoutsakos. CubismAMR – a C++ library for distributed block-structured adaptive mesh refinement, 2022.

[2] Michail Chatzimanolakis, Pascal Weber, and Petros Koumoutsakos. Vortex separation cascades in simulations of the planar flow past an impulsively started cylinder up to $Re = 100\,000$. *Journal of Fluid Mechanics*, 953:R2, 2022.

[3] W. M. Collins and S. C. R. Dennis. Flow past an impulsively started circular cylinder. *Journal of Fluid Mechanics*, 60(1):105–127, 1973.

[4] Nico Fleischmann, Stefan Adami, and Nikolaus A. Adams. Numerical symmetry-preserving techniques for low-dissipation shock-capturing schemes. *Computers & Fluids*, 189:94–107, 2019.

[5] P. Koumoutsakos and A. Leonard. High-resolution simulations of the flow around an impulsively started cylinder using vortex methods. *Journal of Fluid Mechanics*, 296:1–38, 1995.

[6] S. P. Singh and S. Mittal. Flow past a cylinder: shear layer instability and drag crisis. *International Journal for Numerical Methods in Fluids*, 47(1):75–98, 2005.

Vortex Dynamics of Free-Falling Porous Plates and Discs in Discrete Transverse Gust

Chandan Bose and Ignazio Maria Viola*
School of Engineering, Insititute for Energy Systems, University of Edinburgh
*Correspondence: *i.m.viola@ed.ac.uk*

1 Introduction

Some natural plant seeds exhibit long-distance dispersal by enabling the formation of vortical flow structures associated with a lowered terminal velocity. Understanding the aerodynamics underpinning their dispersal can inspire the design of novel unpowered flying devices with high endurance and range. The diaspore of the dandelion, for example, employs a bundle of bristles called pappus, which gives way to the formation of a steady Separated Vortex Ring (SVR) in their wake when they fall steadily [1]. Because the formation of the SVR is due to the low pressure in the near wake of the pappus, it has been associated with drag enhancement.

The flight of seeds is susceptible to wind gusts. However, it is not yet understood how the vortex dynamics around these free-falling diaspores gets altered by the effect of gusts. This is taken up in this study. It has recently been shown by Cummins *et al.* [2] that the SVR, seen in the wake of dandelion diaspores, also exists in the wake of porous discs. Hence, we model the flight behavior of dandelion diaspores as free-falling porous discs. Furthermore, we first focus on the vortex dynamics of two-dimensional permeable plates, as the two-dimensionality of the flow simplifies the interpretation of the vortex dynamics. Within the talk, however, we aim to discuss how the phenomenon demonstrated in this abstract for two-dimensional porous plates extends to porous three-dimensional disks.

We study the changes in the wake topology of free falling plates and disks during the transient due to a horizontal discrete gust. Furthermore, we extend the study to periodic gusts to investigate whether the optimal flight condition is related to the natural frequency of the free-falling body.

2 Computational Methodology

High-fidelity simulations are performed by solving the Darcy equation in the porous disk, and the incompressible Navier-Stokes equations or Newtonian fluids in the clear fluid region around the disk. We use a finite volume approach with an overset mesh-based flow solver, `overPimpleDyMFoam`, available within the open-source library `OpenFOAM`. The *inverse distance* overset interpolation technique is used to facilitate interpolation between the *donor* and *acceptor* cells.

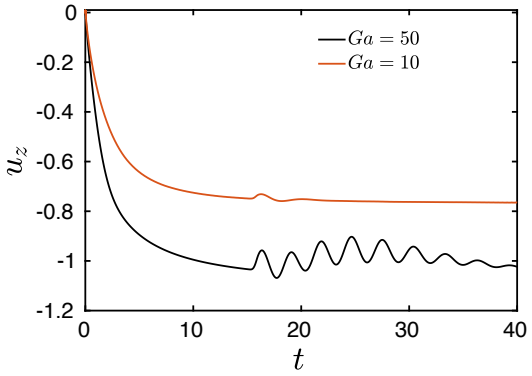

Figure 1: Vertical velocity of a free-falling porous plate experiencing a horizontal gust with $Ga = 10$ and 50.

To solve the fluid-structure interaction, a partitioned weak coupling strategy-based 6-DoF solver is used, where the fluid and solid solvers interact in a staggered manner. The fluid governing equations are weakly coupled with the Newton-Euler equations of motion using a partitioned approach. The structural solver uses a Newmark-beta time integration scheme.

We solve this set of equations in a nondimensional form using the fluid density $\hat{\rho}$, the plate length (or the disk diameter) $\hat{L}$ and the gravitational velocity $\hat{U}$ as reference density, length and velocity, where the hat over the symbols identifies dimensional quantities. The gravitational velocity is computed as $\hat{U} = \sqrt{\hat{m}\hat{g}/(\hat{\rho}\hat{L}^2)}$, where $\hat{m}$ is the mass of the solid body, and $\hat{g}$ is the gravitational acceleration. The nondimensional governing equations in an inertial frame of reference with origin at the centre of mass of the body are

$$\nabla \cdot \mathbf{u} = 0, \tag{1}$$

$$\frac{\partial \mathbf{u}}{\partial t} + \mathbf{u} \cdot \nabla \mathbf{u} = -\nabla p + \frac{1}{Ga}\nabla^2 \mathbf{u} - \frac{1}{GaDa}\mathbf{u}, \tag{2}$$

$$m\dot{\mathbf{u}}_\mathbf{b} + \boldsymbol{\omega}_b \times m\mathbf{u}_b = \mathbf{F} + \boldsymbol{\gamma}, \tag{3}$$

$$\mathbb{I}_\mathrm{o}\dot{\boldsymbol{\omega}}_b + \boldsymbol{\omega}_b \times \mathbb{I}_\mathrm{o}\boldsymbol{\omega}_b = \mathbf{T} + e\mathbf{r} \times \boldsymbol{\gamma}, \tag{4}$$

This work was supported by the European Research Council through the Consolidator Grant 2020 "Dandidrone," H2020 ERC-2020-COG 101001499.

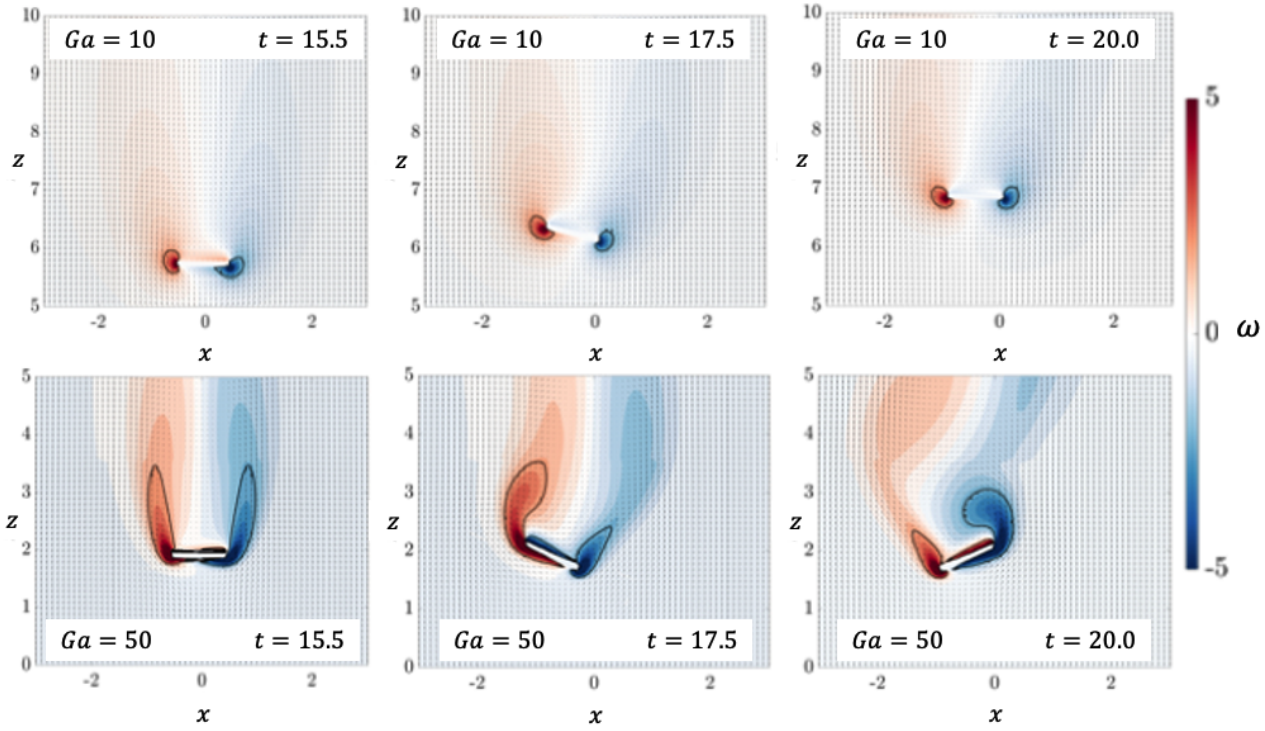

Figure 2: Vorticity contours in the wake of a porous plate experiencing a gust at $Ga = 10$ and 50.

where u is the fluid velocity; t is time, p is the kinematic pressure; $Ga \equiv \hat{U}_g \hat{L}/\hat{\nu}$ is the Galilei number; $Da = \hat{\kappa}/\hat{L}^2$ is the Darcy number, with $\hat{\kappa}$ the dimensional permeability; m is the solid mass; $\mathbf{u}_b$ is the solid body velocity vector; ω_b is the angular velocity of the solid body; $\mathbb{I}_o$ is the inertia tensor; $\mathbf{F}$ and $\mathbf{T}$ are the fluid force and torque vectors; γ is a unit vector in the direction of the gravity force; $\mathbf{r}$ is a unit vector from the centre of gravity to the centre of buoyancy; and e is the distance between the two centres.

To decrease the dimension of the computational domain and tototal computational effort, the fluid equations 1 and 2 are re-written for a noninertial frame of reference translating vertically at the gravitational velocity U, and horizontally at the gust velocity u_G. The horizontal gust speed is described by a cosine ramp: the gust speed is $u_G = 0$ up to time $t_0 = 15$ to allow the body to settle at a constant terminal velocity, then between t from $t_0 = 15$ and $t_1 = 16$, it is $u_G = \frac{1}{2}\left[1 - \cos\left(\frac{\pi(t-t_0)}{t_1-t_0}\right)\right] G_R$, where $G_R = 1$ is the gust ratio. After t_1, the horizontal velocity is $u_G = 1$. The plate has a thickness of $1/10$ and a mass $m = 0.5$.

3 Results

Figure 1 presents the comparison of the vertical velocity time history of a porous plate for two different Ga values of 10 and 50. At $Ga = 10$, the transient regime of the plate dynamics after the gust is damped within few convective times. On the contrary, at $Ga = 50$, the porous plate exhibits a longer transient regime, resulting in a substantial temporary reduction in the vertical velocity. This reveals that the gust results in an overall reduction in the mean terminal velocity from, for example, $t = 0$ and 40, and thus in a lower vertical distance travelled over this period of time. It is to be noted that in both cases, the initial condition at $t = o$ is that of a horizontal plate with zero vertical velocity, and the kinematics of these plates in the absence of gust was determined to be a steady fall asymptotically reaching the terminal velocity.

Figure 2 presents the vortex dynamics of the both these cases. It is seen that the vortex cores manifested at the end of the porous plates at $Ga = 10$ are of considerably lower strength than that of $Ga = 50$ and remains almost attached without having much deformation. On the other hand, at $Ga = 50$, the transient flow regime is seen to be completely unsteady with strong vortex interactions. In the presentation, we will discuss how this transient flow interaction reduces the overall vertical descent of the porous plate. We will also extend these results to three-dimensional porous discs.

References

[1] Cathal Cummins, Madeleine Seale, Alice Macente, Daniele Certini, Enrico Mastropaolo, Ignazio Maria Viola, and Naomi Nakayama. A separated vortex ring underlies the flight of the dandelion. *Nature*, 562:414–418, 2018.

[2] C. Cummins, I.M. Viola, E. Mastropaolo, and N. Nakayama. The effect of permeability on the flow past permeable disks at low Reynolds numbers. *Physics of Fluids*, 29(9), 2017.

Leading-edge vortex dynamics of high-amplitude pitching swept wings

Alex Cavanagh[a], Chandan Bose[b] and Kiran Ramesh[a*]
[a] University of Glasgow, Autonomous Systems and Connectivity, Glasgow, UK[1]
[b] School of Engineering, Insititute for Energy Systems, University of Edinburgh, Edinburgh, UK
[*]Correspondence: *kiran.ramesh@glasgow.ac.uk*

1 Introduction

Swept wings are of significance over a vast array of aerospace engineering applications, from micro-aerial vehicles to passenger aircraft design. The leading-edge vortex (LEV) is the key unsteady flow feature that underpins the enhanced lift generation, especially in flapping flight. The LEV dynamics of swept wings are extensively studied in the existing literature due to the significant effects the planform geometry has on LEV characteristics as well as interactions with the tip vortex and LEV stability. However, a complete understanding of LEV formation, growth and shedding in swept wings is yet to be achieved.

The latest work by Chiereghin *et al.* [1] experimentally investigated the LEV's 3D nature by comparing unswept and swept (40°) AR = 10 wings, undergoing plunging kinematics at Re = 2×10^4 with reduced frequency k $\leq$ 1.1. Significant 3D flow occurred where the outer LEV leg connects to the wing surface, which was found not to be due to wing tip interactions. The swept case had a larger bending moment due to outboard movement of the inner LEV leg. Bending moment and lift increased with increasing reduced frequency, due to increased LEV and tip vortex circulation that cause greater LEV filament deformation. Vortex breakdown was gradual, unlike in classical cases.

Zhang *et. al* [2] used direct numerical simulation (DNS) to simulate swept AR = 1-8 wings at Re = 400 at constant angles of attack between 16-30°. Unsteady wake features were considerably more complex in swept wing cases. At low sweep angles and aspect ratios tip vortex downwash stabilises the wake. For moderately swept wings, midspan effects are more significant than tip flow effects. This results in stationary vortices over the inboard section, the downwash of which increases the steady wake to higher aspect ratio and acts as a lift enhancement mechanism for low to medium aspect ratio wings. At AR = 8, midspan effects are small over outboard sections and unsteady vortex shedding occurs near the tip. At high sweep angles, stabilising streamwise finger-like structures form across the span.

Hammer *et. al* [3] studied aspect ratio effects on dynamic stall by simulating AR = 4, 8 swept wings (30°) at Re = 2×10^5 undergoing harmonic pitching from 4° to 22° at a reduced frequency of k $\approx$ 0.2. Visbal and Garmann [4] extended this to look at the effect of varying sweep angle by considering a sweep angle of 15°. Arch vortices centred at the half span and three-quarter span for 15° and 30° sweep respectively were found. At 30° sweep, the outer LEV leg interacts strongly with the tip flow and sudden tip stall occurs. At AR = 8, 30° sweep, wall-induced instabilities cause the vortex core to twist and a secondary stall region to form that merges with the stalled near-tip flow. This results in stall over the outer three-quarters of the leading-edge. The trailing-edge vortex (TEV) was stronger and motion-induced effects caused earlier formation and propagation of unsteady flow features. Increased aspect ratio increased mean and peak loads, with an earlier onset of stall.

Despite these advances, there is research lacking regarding high-fidelity simulations (in particular hybrid RANS-LES) in the Re = $O(10^4)$ regime. Transient kinematics have been limited to small amplitude plunging [1] and pitching up to a maximum of 22° [3,4]. These will be addressed in this study by performing improved delayed detached-eddy simulations (IDDES) of high-amplitude pitching swept wings to assess how LEV stability, structure and convection vary as functions of aspect ratio and sweep angle.

2 Methodology

An in-house setup of the open-source CFD software OpenFOAM is being used to conduct simulations. A non-orthogonal coordinate body-fitted mesh is applied to the aerofoil and extended into the farfield to a distance of 12c. The finite volume method is used to solve the time-dependent, incompressible Navier-Stokes equations. Discretisation of the time derivatives is achieved using the backward scheme, which was chosen for its second-order accuracy. Second-order accurate Gaussian integration schemes are also chosen for the gradient, divergence and Laplacian terms. The pressure implicit with splitting of operators (PISO) algorithm is used to achieve pressure-velocity coupling. The Spalart-Allmaras model is used for turbulence closure, as its effectiveness has been demonstrated

[1]This work was supported by the UK Engineering and Physical Sciences Research Council (EPSRC) through a DTA scholarship, grant EP/T517896/1.

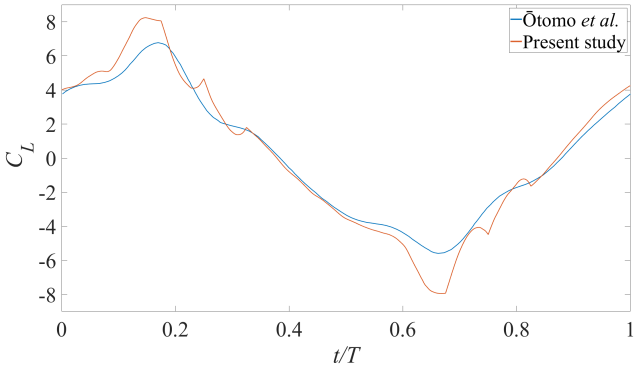

Figure 1: Results of Ōtomo *et al.* [5], compared to results from the present study after 3 pitching cycles.

for a wide range of unsteady separated external aerodynamics flows. The no-slip boundary condition is applied to the aerofoil surface and the farfield is given the freestream (inlet/outlet) boundary condition. This acts as a zero-gradient condition when fluid is exiting the domain and as a fixed value condition, equal to the freestream value, otherwise.

3 Results

The experimental results of Ōtomo *et al.* [5] were compared to preliminary results for a cyclic 2D aerofoil case as a means of validating the IDDES solver. The validation case considered underwent symmetric triangular pitching up to a maximum angle of attack of $\alpha = 64°$ at a reduced frequency of $k = 0.88$.

The graph in figure 1 demonstrates good overall agreement between experiment and simulation. At the maximum and minimum values of lift, the overshoot by computational results is likely due to 3D effects in the experimental results reducing the lift peak. The discontinuities in computational results at $t/T \approx 0.18, 0.25, 0.33, 0.68, 0.76, 0.82$ have been observed to be a feature of the reduced frequency considered, as results for $k = 0.22$ did not show this behaviour.

Figure 2 demonstrates the fine vortical scales that can be captured by hybrid RANS-LES, which is a key motivation for pursuing these simulations. Due to the majority of the flowfield being resolved by LES, rather than modelled like in traditional RANS simulations, smaller flow features can be resolved. This will be particularly important when considering swept wing cases, as the three-dimensionality of the vortical flow field due to the geometry will be better captured and further insights into the nature of LEV dynamics over swept wing geometries can be ascertained.

4 Conclusion

To conclude, the preliminary results of this investigation demonstrate the need to conduct high-fidelity simulations to accurately resolve the flow field in the case of high-amplitude pitching aerofoils. Hybrid RANS-LES methods

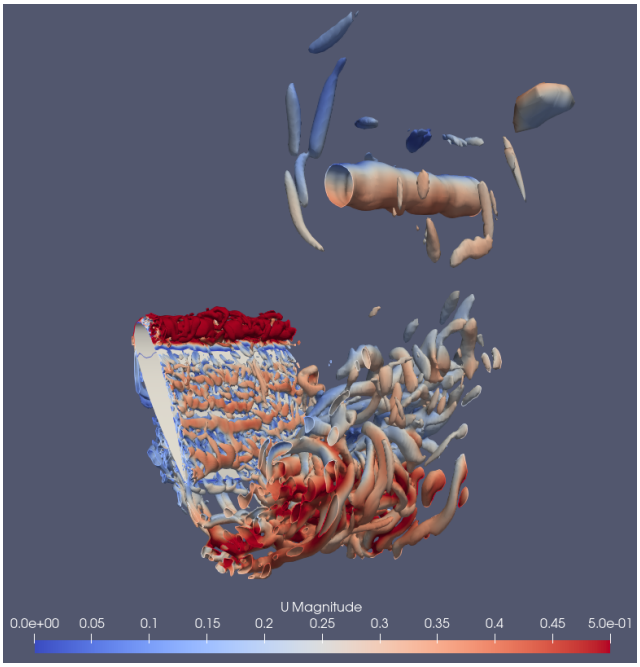

Figure 2: Q = 1 isosurface, coloured by streamwise velocity magnitude at $\alpha = 64°$.

are promising due to the compromise between improved accuracy over RANS simulations and lower computational cost than LES. This is particularly important for cases undergoing complex transient kinematics.

The aim of this research is to investigate the relationship between LEV formation, growth, stability and breakdown and swept wing planforms of varying aspect ratio and sweep angles. Additional novel post-processing techniques are under development to augment understanding of LEV dynamics in these cases. Results will be compared to existing LOMs to assess their capability for predicting forces and moments for these cases.

References

[1] Chiereghin, N., Bull, S., Cleaver, D. J. and Gursul, I., Three-dimensionality of leading-edge vortices on high aspect ratio plunging wings. *Physical Review of Fluids*, 5(6):064701, 2020.

[2] Zhang, K., Hayostek, S., Amitay, M., Burtsev, A., Theofilis, V. and Taira, K., Laminar separated flows over finite-aspect-ratio swept wings. *Journal of Fluid Mechanics*, 905:R1, 2020.

[3] Hammer, P. R., Garmann, D. J. and Visbal, M. R., Effect of Aspect Ratio on Swept Wing Dynamic Stall. *AIAA Aviation 2021 Forum*, 2948, 2021.

[4] Garmann, D. J. and Visbal, M. R., Effect of Sweep on Dynamic Stall of a Pitching Finite-Aspect-Ratio Wing *AIAA Journal*, 57(8):3274–3289, 2019.

[5] Ōtomo, S., Henne, S., Mulleners, K., Ramesh, K. and Viola, I. M., Unsteady lift on a high-amplitude pitching aerofoil. *Experiments in Fluids*, 62(6), 2021.

Third Generation of Vortex Definition and Identification

Chaoqun Liu[a*]
[a] University of Texas at Arlington, Arlington, Department of Mathematics, Arlington, USA[1]
*Correspondence: *cliu@uta.edu*

1 Three generations of vortex definition and identification

Vortex is omnipresent in the universe but is also a major threat to human life and the human environment. It is a major cause of heart diseases, respiratory system diseases, extreme climate change, air pollution, noise generation, in addition to turbulence, etc. Vortex is intuitively recognized as a rotational/swirling motion of fluids. It is ubiquitous in nature and viewed as the building blocks, muscles, and sinews of turbulent flows [1]. Quantitative research of vortex is essential for scientific research. However, there was no quantified definition for vortex which is a major bottleneck of vortex science and turbulence research.

There are three generations of vortex identification methods [9]. Helmholtz (1858) [2] defined vortex as vortex filament which is infinitesimal vorticity tube. Helmholtz's definition of vortex is classified as the first generation. During the past four decades, several vortex identification criteria, such as Q,$\triangle$, λ_2, and λ_{ci} methods, have been developed [3-6] and are classified as the second generation of vortex identification. They are all based on eigenvalues of the velocity gradient tensor; however, they are scalars and thus strongly dependent on the arbitrary thresholds. They cannot show the vortex rotation axis, which is critical for vortex structure. Furthermore, they are all contaminated by shearing. Rotational axis and uniqueness in strength are two important issues for vortex definition that cannot be solved by either the first or second vortex identification methods.

Liutex, the third generation of vortex definition and identification, was introduced by Liu at the University of Texas at Arlington (UTA) [7-9]. It is defined as a vector that uses the real eigenvector of velocity gradient tensor as its direction and twice the local angular speed of the rigid rotation as its magnitude. The major idea of Liutex is to extract the rigid rotation part from velocity gradient tensor to represent vortex, which is a mathematically rigorous tool suitable for vortex characterization. The location of the rotation axis is then the local maxima of Liutex (not vorticity), and the Liutex magnitude is twice the vortex angular speed, which is uniquely defined.

[1]This work was under the support of NSF EAGER Grant #2300052, Development and Application of Liutex and Third Generation of Vortex Definition and Identification.

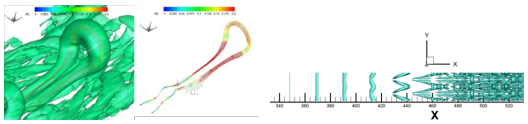

(a) (b)

Figure 1: (a) Liutex iso-surface and Liutex lines (color represents the rotation strength), and (b) Liutex iso-surface for the vortex structure in early transition (R = 0.1)

2 Liutex

Liutex is defined as the rigid rotation part of fluid motion [7-9]. The mathematical definition of Liutex is presented by Eq. 1-2:

$$\vec{R} = R\vec{r} \tag{1}$$

$$R = (\vec{\omega}\cdot\vec{r}) - \sqrt{(\vec{\omega}\cdot\vec{r})^2 - 4\lambda_{ci}^2} \tag{2}$$

where $\vec{R}$ and R are Liutex vector and magnitude, $\vec{r}$ is the real eigenvector of $grad\vec{v}$, $\vec{\omega} = \nabla\times\vec{v}$ is vorticity, and λ_{ci} is the imaginary part of the conjugate complex eigenvalues of $grad\vec{v}$. The condition $\vec{\omega}\cdot\vec{r} > 0$ is used to keep the definition unique and consistent when the fluid motion is pure rotation.

3 Liutex-based Vortex Identification Methods

Liutex Iso-surface. Since Liutex is the rigid rotational part that is extracted from fluid motion, the Liutex vector, Liutex vector lines, Liutex tubes, and Liutex iso-surface can all be applied to display the vortex structure (Fig. 1). The advantage of the Liutex method is that Liutex is a vector, unlike others which are all scalar. Another benefit of Liutex is that it represents pure rotation without contamination by shears, while all other vortex identification methods are contaminated by shears.

Modified Liutex-Omega Method. The modified Liutex-Omega method combines the ideas of both the Liutex and Omega method, which is normalized, not contaminated by shear, and is insensitive to threshold selection. The modified Liutex-Omega method is defined by Eq. 3.

$$\tilde{\Omega_R} = \frac{(\vec{\omega}\cdot\vec{r})^2}{2[(\vec{\omega}\cdot\vec{r})^2 - 2\lambda_{ci}^2 + 2\lambda_{cr}^2 + \lambda_r^2] + \varepsilon} \tag{3}$$

Liutex Core Line Method. All iso-surface methods are threshold-dependent. A Liutex core line is defined as the rotation axis of each vortex and is unique and threshold-free.

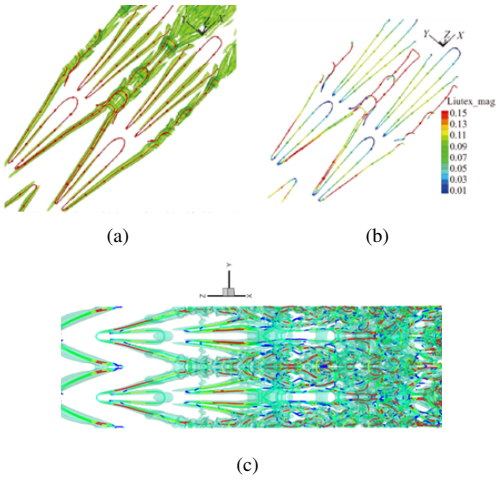

(a) (b)

(c)

Figure 2: Vortex structure in flow transition displayed by Liutex core line methods (color represents Liutex strength): (a) Liutex iso-surface and core lines, (b) Liutex core lines, (c) Liutex core lines for flow transition (preliminary results)

The vortex core line is defined as a special Liutex line that passes through the points satisfying the condition expressed by Eq. 4.

$$\nabla \mathrm{R} \times \vec{r} = 0 \quad \vec{r} \neq 0 \tag{4}$$

where $\vec{r}$ represents the direction of the Liutex vector. The Liutex (vortex) rotation core lines are uniquely defined without any threshold requirement (Fig. 2). Therefore, the Liutex core rotation axis lines with Liutex strength are derived uniquely and are believed to be the only entity capable of cleanly and unambiguously representing vortex structures. Fig 2c shows that it is possible to use the automatic Liutex-core-line method to show the vortex structure.

References

[1] D. Kuchemann Report on the IUTAM symposium on concentrated vortex motions in fluids. J. Fluid Mech., 21 (1965), 1-20.

[2] H. Helmholtz Über Integrale der hydrodynamischen Gleichungen, welche den Wirbelbewegungen entsprechen. Journal fur die reine und angewandte Mathematik 55, 25–55 (1858)

[3] J. Hunt, A. Wray and P. Moin, "Eddies, streams, and convergence zones in turbulent flows," Center for Turbulence Research Proceedings of the Summer Program, 193, (1988).

[4] M. Chong, A. Perry and B. Cantwell, "A general classification of three-dimensional flow fields," Phys. Fluids A 2, 765-777 (1990).

[5] J. Jeong and F. Hussain, "On the identification of a vortices," . Fluid Mech. 285, 69-94 (1995).

[6] J. Zhou, R. Adrian, S. Balachandar and T. Kendall, "Mechanisms for generating coherent packets of hairpin vortices in channel flow," J. Fluid Mech. 387, 353-396 (1999).

[7] C. Liu, Y. Gao, S. Tian, and X. Dong, Rortex—A new vortex vector definition and vorticity tensor and vector decompositions, Physics of Fluids 30, 035103 (2018); doi: 10.1063/1.5023001

[8] Y. Gao and C. Liu, Rortex and comparison with eigenvalue-based vortex identification criteria, Physics of Fluids, Volume 30, 085107 (2018), https://doi.org/10.1063/1.5040112

[9] C. Liu, Y. Gao, X. Dong, J. Liu, Y. Zhang, X. Cai, N. Gui Third generation of vortex identification methods: Omega and Liutex/Rortex based systems, Journal of Hydrodynamics, 31(2): 1-19 (2019) https://doi.org/10.1007/s42241-019-0022-4

8 Session P: Posters

Active heaving and passive pitching of a foil in a wavy stream

Abdur Rehman[a] and Daniel Floryan[a*]
[a] University of Houston, Department of Mechanical Engineering, Houston, TX, USA
[*]Correspondence: *dfloryan@uh.edu*

1 Introduction

Swimming and flying animals encounter a wide variety of flow conditions in their environments. They adapt their flapping motions accordingly and may even use the environmental conditions to their favour. For example, Beal *et al.* [4] reported an experiment where a dead trout propelled itself against a vortical flow, showing that a body can follow another body without expending energy. We are interested in how swimmers and flyers make take advantage of heterogeneous flow conditions in their environments. As an initial step, this study focuses on an actively heaving and passively pitching rigid foil placed in a wavy fluid stream.

We consider a thin foil of chord c, thickness b, span s, and density ρ_s, as sketched in Figure 1. The foil is driven at its leading edge by a periodic heaving motion of amplitude h_0 and frequency f, and held against a freestream velocity consisting of a uniform flow U_∞ of density ρ_f, and a wavy flow with amplitude V_w, frequency f_w, and wavenumber k. At the leading edge, a torsional spring of stiffness κ allows the foil to pitch passively with pitch angle θ in response to the heaving motion and wavy stream.

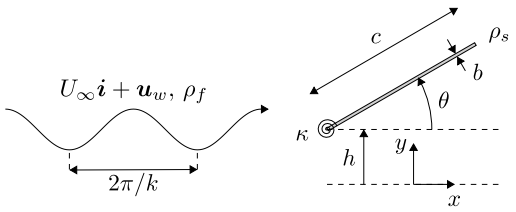

Figure 1: Schematic of the problem.

2 Methodology

We restrict ourselves to the small-amplitude limit of $h_0/c \ll 1$, $\theta \ll 1$, and $fh_0/U_\infty \ll 1$. In this limit, the non-dimensional equation of motion for the pitch angle is

$$\frac{16}{3}R\ddot{\theta} = -4K\theta - 4R\ddot{h}^* + C_M, \tag{1}$$

similar to [2]. Above,

$$R = \frac{\rho_s b}{\rho_f c}, \quad K = \frac{\kappa}{\rho_f U_\infty^2 c^2 s}, \quad h^* = \frac{2h}{c}, \quad C_M = \frac{4M_f}{\rho_f U_\infty^2 c^2 s}. \tag{2}$$

R is the ratio of a characteristic mass of the foil to a characteristic mass of the fluid, and K is the ratio of a characteristic moment from the torsional spring to a characteristic moment from the fluid. C_M is the non-dimensional moment that the inviscid fluid exerts on the foil, calculated as in [1, 3].

The mean thrust, power, and energy coefficients are defined as

$$C_T = \frac{2\langle T\rangle}{\rho_f U_\infty^2 cs}, \quad C_P = \frac{2\langle P\rangle}{\rho_f U_\infty^3 cs}, \quad C_E = \frac{2\langle E\rangle}{\rho_f U_\infty^3 cs}. \tag{3}$$

Above, $\langle\cdot\rangle$ denotes time-averaging. C_T and C_P have the usual interpretations, and C_E is the mean rate of power imparted to the fluid.

3 Results and discussion

The foil is forced by two independent mechanisms: the applied heaving at the leading edge and the moment generated by the oncoming wavy stream. The kinematic response is directly related to the propulsive performance [2] and it also helps us understand the underlying physics. We start by analysing the kinematic response under each type of forcing separately.

The magnitude and phase of the pitch angle are shown in Figure 2 (only heave; no wavy stream) and Figure 3 (only wavy stream; no heave) as functions of the reduced frequency $\sigma = \pi fc/U_\infty$. To gain intuition, we compare the responses to those without a fluid.

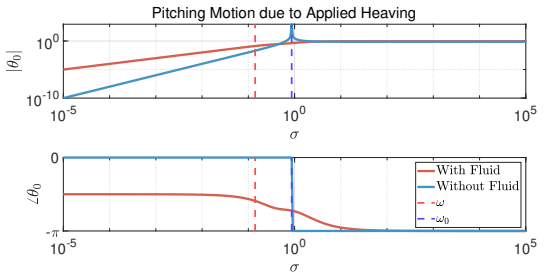

Figure 2: Bode plot for kinematic response under applied heaving at the leading edge for $K = 0.01$, $R = 0.01$, and $h_0^* = 1$.

The fluid adds damping to the system, which eliminates the resonant peak for the weak torsional spring used here. Furthermore, the fluid creates moments proportional to σ in both cases, leading to modified asymptotic behaviour.

Comparing the two types of forcing, we see that wavy forcing dominates at low frequencies while the applied heaving dominates at high frequencies. The natural frequency of the system ω_0 is shifted down to ω due to the added inertia offered by the fluid.

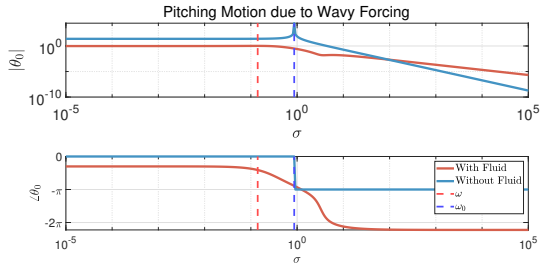

Figure 3: Bode plot for kinematic response under wavy forcing for $k^* = \pi$, $V_w = 1$, $K = 0.01$, and $R = 0.01$.

As the response for the applied heaving case has been discussed in detail in [2], we focus on the wavy forcing. In Figures 4 and 5, we show the how the kinematics depend on the non-dimensional stiffness and wavenumber.

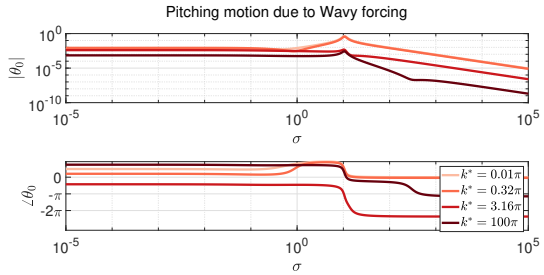

Figure 4: Bode plot for kinematic response for different wavenumbers at $K = 100$, $R = 0.01$, and $h_0^* = 0$.

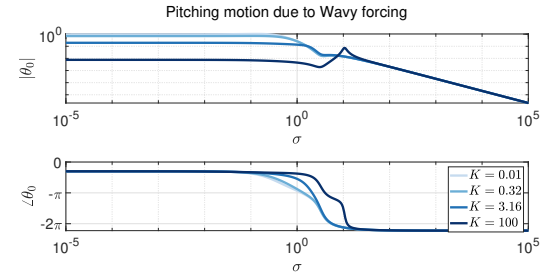

Figure 5: Bode plot for kinematics response for different non-dimensional stiffnesses at $k^* = \pi$, $V_w = 1$, $K = 0.01$, and $R = 0.01$.

In general, a lower non-dimensional stiffness or wavenumber lead to a greater pitch amplitude, although this may not be the case near a natural frequency of the system. The physical picture is as follows. Far from a natural frequency, a stiffer spring offers greater resistance to applied moments, yielding a lower pitch angle. When the wavenumber is large, the wavelength of the wavy stream is much smaller than the chord. As a result, successive peaks and troughs virtually nullify each other's contributions to the net moment on the foil. We also bring to the reader's attention a dip in the amplitude of the pitch angle when the reduced frequency and wavenumber are equal. Physically, this condition corresponds to the phase speed of the wavy stream being equal to the freestream speed. It can be shown that the non-circulatory moment is zero in this case.

In Figures 6 and 7, we show the mean thrust coefficient. The trends differ from those for the amplitude of the pitch angle, and we even observe a non-monotonic relation with the wavenumber in an asymptotic regime. Of note, the foil produces thrust despite the kinematics being purely passive.

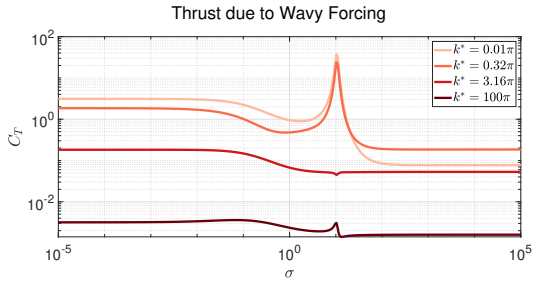

Figure 6: Frequency response for C_T for a range of wavenumbers at $K = 100$, $R = 0.01$, and $h_0^* = 0$.

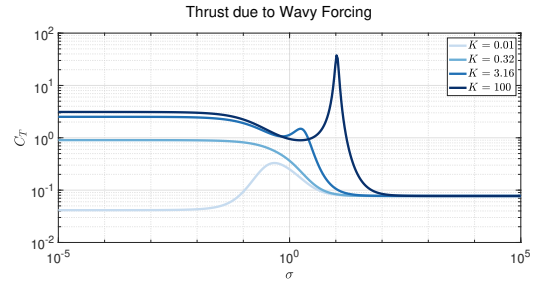

Figure 7: Frequency response for C_T for a range of spring stiffness values at $k^* = 0.01\pi$, $V - w = 1$, $K = 0.01$, and $R = 0.01$.

To summarize, the wavy forcing plays a dominant role (at least for the pitch kinematics) for lower forcing frequencies. Despite purely passive kinematics, the foil can produce thrust in a wavy stream. At the colloquium, we will expand on the physical origins of our observations and characterize the propulsive performance when the forcing is mixed.

References

[1] T. Y.-T. Wu. Extraction of flow energy by a wing oscillating in waves. *Journal of Ship Research*, 16(01):66–78, 1972.

[2] M. N. J. Moore. Analytical results on the role of flexibility in flapping propulsion. *Journal of Fluid Mechanics*, 757:599–612, 2014.

[3] T. Y. Wu and A. T. Chwang. Extraction of flow energy by fish and birds in a wavy stream. In *Swimming and Flying in Nature*, 687–702, Springer, Boston, MA, 1975.

[4] D. N. Beal, F. S. Hover, M. S. Triantafyllou, J. C. Liao, and G. V. Lauder. Passive propulsion in vortex wakes. *Journal of Fluid Mechanics*, 549:385–402, 2006.

Application of topological data analysis to vortex-dominated fluid flows

A. Yiran[a] and M. Green[a*] and M. Budišić[b]
[a] University of Minnesota, Aerospace Engineering and Mechanics, GreenFluids Lab, Minneapolis, MN, USA
[b] Clarkson University, Mathematics, Potsdam, NY, USA
[*]Correspondence: *magreen@umn.edu*

1 Introduction

The application of topological data analysis (TDA) to detect patterns in fluid dynamics evolving under an unsteady or vortex-dominated flow field is a relatively new endeavor. TDA quantifies the shape of data in a multiscale manner, and can be used to both detect large-scale features in data, and to filter out the noise in the shape. The particular TDA technique used here is called persistent homology (PH) and it tracks connections between data points as they appear and disappear at different spatial scales. For example, analysis of persistent features of the vorticity field identifies vortex core centers and vortex boundaries as representatives of the zeroth (H_0) and first (H_1) homology groups. We apply PH to the vortex wakes generated by pitching and heaving flat plates as models of bio-inspired propulsion with data sets obtained via velocity fields from stereoscopic particle image velocimetry (PIV). The vorticity fields are analyzed using PH to quantify the topology of the fields, and then the results, that is the time evolution of numbers and boundaries of vortices detected in this way, are correlated with the dynamic fluid phenomena.

The basic workflow of PH takes in the data set of interest, forms local connections between data points based on the value of the chosen scale parameter (filtration), computes and counts global features such as connected sets and loops formed from local connections (homology), and then visualizes the results of this analysis across the values of the scale parameter using the persistence diagram (PD). In general, PH represents local connections using simplices, the simplest possible polytopes in a given dimension, such as vertices, edges, triangles, etc., resulting in the data set stored using the simplicial complex. Since our PIV data is already represented on a uniformly-spaced and structured rectangular grid, we instead use cubical complexes that are better adapted to such structures. We denote a vertex (the data point itself) as a 0-cube, an edge between two vertices as a 1-cube, a face formed by four bounding edges as a 2-cube (pixel), and a volume enclosed by six bounding faces as a 3-cube, as shown in figure 1. These complexes, whether simplicial or cubical, can reach up to any n-dimension needed. The cubical complex itself is the composition of these individual pieces to create a large object of these n-cubes.

To form connections between grid points, this analysis method uses a filtration technique called lower-star filtration

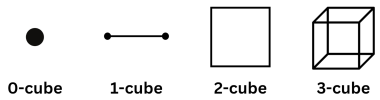

Figure 1: Building blocks of cubical complexes visualized in three dimensions.

(or sublevelset filtration). Each grid point (0-cube) is assigned the vorticity value; the edges (1-cubes) are assigned the larger of the two values of their endpoints, the pixels (2-cubes) the largest of the values of their edges, and so on. To filter according to vorticity, a vorticity value (level) is chosen and all n-cubes with values larger than the chosen level are temporarily removed— the remaining cubes form connected components and loops. Threshold values at which a particular feature appears and disappears are recorded as, respectively, the "birth" and "death" of a feature; where the subset of cubes in a feature needed to still recognize the connectivity of the feature is called its "representative". Changing the threshold value from minimum to maximum can be imagined as a three dimensional surface formed by the vorticity distribution that is intersected with a horizontal plane to form level-set contours. As this threshold plane is swept, we record the threshold values at which contours appear, merge, or disappear.

The persistent homology can be represented as a persistence diagram (PD), which encodes topological features as points in the birth-death plane. The larger the difference between death and birth, called persistence, the more robust is the feature across scales. Points close to the diagonal represent trivial features of near-zero persistence, disappearing almost as quickly as they appear. They are interpreted as topological noise and can be removed to simplify the topology of the data. Points further from the diagonal represent points that may be of interest, i.e., persist for a longer interval. PDs are created for both zeroth and first-order features, respectively detecting vortex cores and vortex boundaries in our case.

To compare two snapshots quantitatively, we can compute distances (metrics) between their PDs as the optimal transportation of points in one PD to the other. Based on the distance of transportation, the *bottleneck metric* measures only the single largest difference between persistence diagrams and ignores the rest, whereas the *Wasserstein metrics* add up all distances. PD distance of consecutive snapshots can

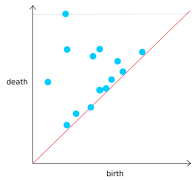

Figure 2: An example of a persistence diagram. Points along the diagonal represent noisy data, and points further from the diagonal represent data points that are more likely of interest as they persist longer. The most persisting feature is the topmost data point in the graph, with a death value of ∞, intersecting the grey line.

be interpreted as "topological speed" and, when high, could be an indicator when the topology of the flow is changing dramatically.

Our goal is to capture and parameterize structures of the flow field through the application of persistent homology in the analysis of vortex topology. Specifically, we will analyze the wake structures produced by a bio-inspired panel undergoing three different cases: pure pitching, pure heaving, and a combined pitching and heaving motion. We know that fish and aquatic mammals demonstrate high power, efficiency, and maneuverability using similar actuators, and significant research has been conducted to study their 2D/3D flow structures and their effects on the time-averaged performance. From these reconstructed 2D phase-averaged vortex wakes we explore whether different kinematics of fish-like panels produce different patterns of vorticity in the wake, and how we can encode the persistent and/or dynamically important features of those patterns using PH.

2 Results

Using persistent homology on the varying kinematic cases of the moving panel results in identification of persistent maxima and minima of the flow field as vortex cores of the positive- and negative-signed respective vortices, as well as loops around both the maxima and minima as vortex boundaries.

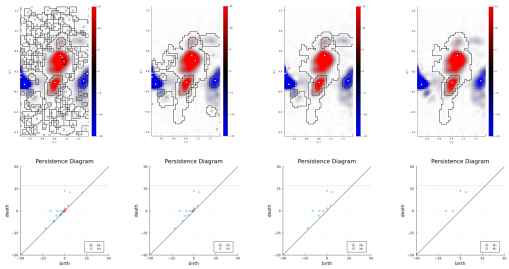

Figure 3: Visualization of adjusting the cutoff value of the PH function. Starting from the left, the cutoff is set to 0.01 and is subsequently increased to 0.5, 2.0, and finally 5.0

As the cutoff value is adjusted in the function that computes the persistent homology of the space, we see a reduction in the amount of persistent H_0 points and H_1 loops identified, which is also reflected in the respective PD, shown in figure 3. As the cutoff value is increased, the number of persistent points (H_0) and loops (H_1) that are identified decreases, i.e., there is a reduction of the effects of noise in the analysis.

Furthermore, a step through of the PDs for a given case exhibits a periodic nature that corresponds to a new vortex being shed behind the plate. In the example of the heaving plate below, we see that as a new positively-signed vortex is shed behind the plate, the relevant persistent maximum (H_0) and vortex boundary (H_1) peaks in persistence on the PD. The same is observed for each negatively-signed vortex that is shed as well, where a persistent minimum value and vortex boundary loop peaks in the respective PD.

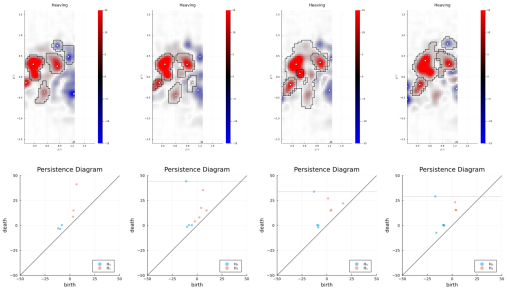

Figure 4: These four figures are subsequent snapshots of the vorticity field and their corresponding PDs for the positive vorticity only. Starting from the left, we observe that as a new vortex is fully shed, both the H_0 and H_1 groups acquire a new maximally-persistent feature (second in from the left). The persistence intervals of these features will continue to decrease per snapshot as the vortices move towards the right and out of the frame, and a new feature will appear with the shedding of the next positively-signed vortex.

3 Conclusion

In conclusion, we see that persistent homology yields a consistent framework to deal with vorticity fields. It filters noisy data via a cutoff value, without changing the most persistent representatives of both the H_0 and H_1 homology groups. It can be applied directly to field data, and can be n-dimensional. Additionally, we anticipate that the bottleneck and Wasserstein distances are metrics that will help measure the similarity between two persistence diagrams. Implementing this technique to describe the similarity of PDs of a fluid flow is an attempt to extend on previous work [1]. Future objectives with this work are to use this persistent homology framework to implement machine learning on trackable vortex topology features, exploring three-dimensional topological data analysis, and using zigzag persistence and multi-parameter persistent to track how persistence diagrams evolve in time-varying metric spaces.

References

[1] Miroslav Kramár, Rachel Levanger, Jeffrey Tithof, Balachandra Suri, Mu Xu, Mark Paul, Michael F. Schatz, and Konstantin Mischaikow. Analysis of Kolmogorov flow and Rayleigh–Bénard convection using persistent homology. *Physica D: Nonlinear Phenomena*, 334:82–98, 2016.

Effectiveness of Facemasks for Large Virtual Cohort of Population

Akshay Anand,[a] Tomas Solano,[a] and Kourosh Shoele[a*]
[a] Florida State University-Florida A&M University, Department of Mechanical Engineering, Tallahassee, USA[1]
*Correspondence: *kshoele@eng.famu.fsu.edu*

1 Introduction

Although facemasks have been widely accepted as a must-have tool for reducing COVID-19 transmission (caused by the SARS-CoV-2 Coronavirus), their effectiveness in reducing airborne transmission due to several respiratory actions (breathing, coughing, talking, sneezing, etc.) is obscure. The efficacy of the facemasks depends on how well it fits on the wearer's face, respiratory aerodynamics, filtration flow physics, droplet dynamics, and their interaction with the porous mask's material [1]. Poor fit of masks enables flow leakage around the periphery of the mask where it does not make a seal with the face, and thereby reduces the effectiveness of the facemask. Peripheral leakages are significantly impacted by facial features, therefore, fitting of facemasks should be thoroughly investigated to understand how and where the leakage sites are present to ensure higher protection efficacy of facemasks.

Recent studies have demonstrated that the flow produced during routine daily activities such as talking, breathing, and laughing has the potential to spread the SARS-CoV-2 virus. Droplets generated during everyday speech may act as a stimulant in the transmission of COVID-19. We focus on investigating how the pronunciation of some syllables and induced mouth movement may result in deformation of the facemask, therefore reducing the protection efficiency. A novel analytical integral boundary layer solution is devised to quantify the flow in the interface regions between the face and the mask. The mask is deployed on the faces based on a previously developed model [2]. Face and mask are modeled mathematically using a series of linearly interconnected channels with porous top boundary. The region of the face covered by the mask is discretized into channels beginning at the mouth and ending at the mask edge. The channels' height varies and depends on the distance between the face and mask at every location. The fluid dynamics inside the channels are driven by the compatibility condition of the inlet pressure. The model is validated with a detailed flow simulation and employed to find the interconnected relation between fitness during talking, porosity, and leakage through the mask. We quantify the effectiveness of face masks during talking in a large cohort of faces and diverse probable talking scenarios to quantify the leakage pattern and mask efficacy in talking activities.

[1]This work is supported by National Science Foundation under grant number Number: CBET-2034992.

2 Results

2.1 Outward and Inward Protection Model

We focus on the fluid phenomenon behind a breathing person wearing a face mask. The first step in this study involves creating a large virtual cohort of faces; a popular approach for building morphable faces is via principal component analysis (PCA) representing the face as a function of shape vectors; through different combinations of these vectors, the face can be morphed into different geometries [2,3]. Further broadening the approach the PCA can even be applied to a specific facial feature (nose, cheek, chin, zygomatic bone, eyes, ears) while keeping other regions of the face unchanged. The next, step involves mask deployment on virtually generated faces. In the end, pass the face and mask deployed geometry to the analytical boundary layer solver coupled with Darcy's porosity term to estimate the flow field in the interface region between the face and the mask. The pressure drop inside each i channel can is determined as,

$$P(x^*) = P_o - \beta\mu v_{inj}(x^*) \tag{1}$$

where P_o is the outside pressure, μ is kinematic viscosity, β is the Darcy's porosity coefficient, v_{inj} is the inflow breathing flux to the model. The simplest velocity profile is to assume the Poiseuille flow parabolic profile. Using the Kármán-Pohlhausen momentum integral technique we can obtain the solution for v_x and v_y such that [4]

$$v_x(x^*,y^*) = u_e[1+f(x^*)][6y^*(1-y^*)] \tag{2}$$

$$v_y(x^*,y^*) = -u_e\frac{df}{dx^*}\left[3y^{*2}-2y^{*3}\right] \tag{3}$$

On substituting the equation 3 into 1 we can calculate the pressure at injection surface as,

$$P(x^*) = P_o - \beta\mu u_e\frac{df}{dx^*} \tag{4}$$

Figure 1 shows the non-dimensionalized through-mask flux for facial features chin and cheek, α represents the shape coefficients for example α = -1.2 and 1.2 represents maximum deformation on the chin while keeping other facial features unchanged. As the flow involves suction in the (b) inward model there we incorporated the effect of head-loss coefficient k with this model. The through-mask leakages for each face are different signifying seemingly insignificant changes in facial features can induce different leakage behavior. Furthermore, when the porosity increases the through-mask flow increases, and on the contrary when peripheral leakage increases the through-mask flow decreases.

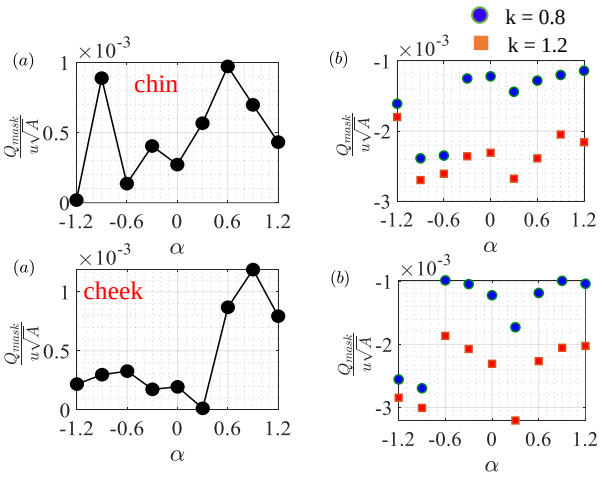

Figure 1: Statistics of non-dimensionalized through-mask leakage for facial feature chin and cheek for a) outward and b) inward protection model; α is the shape coefficient.

2.2 Full-Scale 3D Simulation

Here, direct numerical simulations (DNS) of the Navier-Stokes equations are used to study, in more detail, the flow physics of a person coughing while wearing a facemask. The immersed boundary method (IBM) is implemented to enforce the boundary conditions at the face and facemask as follows,

$$\nabla \cdot \mathbf{u} = 0, \tag{5}$$

$$\frac{\partial \mathbf{u}}{\partial t} + \nabla \cdot (\mathbf{u}\mathbf{u}) = -\frac{1}{\rho}\nabla p + \nu \nabla^2 \mathbf{u} - \mathbf{f}, \tag{6}$$

where $\mathbf{u}(\mathbf{x},t)$ is the velocity field, $p(\mathbf{x},t)$ is the pressure and $\mathbf{f}(\mathbf{x},t)$ is a forcing term added to enforce the effect of porous mask. Here $\mathbf{x} = (x,y,z)$ is the Cartesian coordinate vector.

The mask is considered to be thin enough to be represented as a membrane, and the Darcy law is used to model it's porosity. The Darcy law, integrated through the thickness of the mask is given as

$$[p]\,\mathbf{n} = -\frac{\mu}{k}\mathbf{v} = -c_k \mathbf{v}, \tag{7}$$

where $\mathbf{v}(s,t)$ is the through-mask velocity and $[p] = p^+ - p^-$ is the pressure jump over the mask. The mask's porosity is described by k, however, we use the parameter $c_k = \mu/k$, the effective flow resistance coefficient.

A representative face is selected based on the integral boundary layer model results and a preliminary simulation is shown here to validate the model capabilities. A cough jet with a peak velocity of 10 m/s is simulated. Figure 2 shows the flow structures and velocity magnitude leading up to the time of peak coughing velocity for a facemask with a porosity coefficient of $c_k = 1000$.

In figure 2 the predominant leakage jet is the upward-flowing leakages around the periphery of the nose due to larger gaps; leakages at the sides are minuscule. A part of through-mask leakage is filtered and the filtration extent depends on the mask material. We used fitted filtration efficiency (FFE) as a metric to quantify how much of the flow is filtered which correlates directly with how much protection the mask offers. FFE consider the nominal FE for instance the FE on N95 mask is 95% but FFE is lower depending on fit [5].

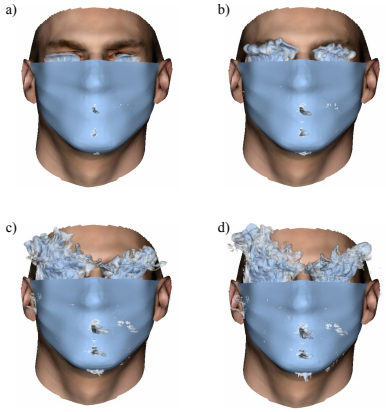

Figure 2: Time evolution of the flow during a coughing episode; front view of iso-surface of velocity magnitude a) 25% b) b) 50% c) 75% of peak velocity time d) peak time.

3 Conclusion

We focus on understanding how the changes in facial features may lead to mask leakages. A geometrically weighted PCA algorithm is proposed to generate a large virtual population. The flow physics of a person breathing while wearing the mask is investigated from outward and inward protection perspectives. We noted that the gap profile varies for each face even with seemingly insignificant changes in facial topology resulting in unique trends of peripheral leakages. We simulated a coughing jet from a full-scale 3D CFD for representative faces. It is observed that male and child faces have almost similar gaps in the mask fit; the female face showed larger gaps at both the top and bottom edge of the mask therefore leakage was significant. As a future direction, the model and simulations are extended to the dynamic case of a talking person with diverse probable talking scenarios to advise simple metrics that can quantify the leakage pattern and mask efficacy in talking activities.

References

[1] Rajat Mittal, et al. The Flow Physics of Face Masks. *Annual Review of Fluid Mechanics*, 55.1 (2023).

[2] Tomas Solano et al. One size fits all?: A simulation framework for face-mask fit on population-based faces. *PloS one*, 16.6 : e0252143 (2021).

[3] Tso-Kang Wang, et al. Bridge the gap: Correlate face mask leakage and facial features with 3D morphable face models. *JESEE* , 32.5 (2022).

[4] Jason Hartwig, et al. Analytical model for steady flow through a finite channel with one porous wall with arbitrary variable suction or injection. *Physics of Fluids*, 26:12 123603 (2014).

[5] Tomas Solano, et al. Perimeter leakage of face masks and its effect on the mask's efficacy. *Physics of Fluids*, 34.5 : 051902 (2022).

Effects of Sweep Angle on Flow Over Seal Whisker Inspired Geometry

Trevor Dunt[a*], Jennifer Franck[a], Raúl Bayoán Cal[b], Christin Murphy[c]
[a]University of Wisconsin - Madison, Department of Mechanical Engineering, Madison, WI, USA[1]
[b]Portland State University, Mechanical and Materials Engineering Department, Portland, OR, USA
[c]Naval Undersea Warfare Center-Newport,Newport, RI, USA
[*]Correspondence: *dunt@wisc.edu*

1 Introduction

Seals have keen hydrodynamic tracking abilities attributed to their uniquely shaped whiskers that have two sets of opposing undulations in the spanwise direction. In controlled experiments, the undulated whiskers experience reduced drag and near-elimination of vortex induced vibration when compared to smooth cylindrical shapes [1]. In span-perpendicular flow, the undulated geometry is responsible for a three-dimensional vortex shedding pattern and modification of the shedding frequency response in comparison to a circular cylinder. These effects enhance sensitivity and elimination of signal noise for seals as their whiskers remain relatively still in flow. Similarly, this geometry may lend benefits to engineering applications that benefit from sensing and reduction of forces.

Existing research focuses primarily on geometric parameters describing the whisker surface such as thickness, aspect ratio, and undulation wavelength, phase and amplitudes [2, 3]. Generally, studies involving whisker geometry focus on flow perpendicular to geometry span. With the exception of angle of attack [4], other orientations remain mostly unexplored, though the complexity of shedding behavior from surface undulations is likely compounded by orientation changes. Sweep angle variation is pertinent to many potential uses of seal whisker geometry such as force reduction on wind turbine bases, drilling risers, or pipelines.

In this research, flow simulations are performed on a periodic section of whisker-inspired geometry at a biologically relevant Reynolds number of 500. Direct numerical simulation (DNS) of flow over the geometry is performed alongside models with circular and elliptical smooth cross sections for comparison. Simulations are performed through a range of sweep angles and, from this data, flow structures, shedding frequency changes, and spanwise distribution of fluid forces are analyzed. These metrics are used to evaluate the effect of sweep angles from the perspective of force reduction and identify important trends in the resulting flow physics.

[1]This work was supported by the National Science Foundation under grant numbers CBET-2035789 and CBET-2037582, and the Department of Defense SMART Fellowship

2 Methods

The whisker model is defined by a repeatable analytical definition and generated by a dynamic mesh morphing algorithm that generates the undulations from a structured cylinder mesh [5]. Sweep angle, Λ, is prescribed about the whisker geometry yaw axis, and is modified in 15 degree increments from 0 to 60 degrees, achieved by altering the prescribed inlet velocity direction. End-effects are not investigated due to periodic spanwise boundary conditions. Finally, forces are computed along the surface and defined by the coefficients of drag and lift,

$$C_D(z,t) = \frac{2F_D(z,t)}{\rho U_\infty^2 T(z) L_z} \quad \text{and} \quad C_L(z,t) = \frac{2F_L(z,t)}{\rho U_\infty^2 C(z) L_z}, \quad (1)$$

which are functions of time, t and spanwise location z, and defined using the spanwise dependent thickness $T(z)$ and chordlength $C(z)$.

3 Results

Figure 1(a) portrays the instantaneous flow structures (Q-criterion) from $\Lambda = 0$, 15, and 30 degrees. At this Reynolds number the baseline smooth geometry with matching aspect ratio (not shown) displays a vortex street with shed structures remaining connected across the span. In all cases presented in the aforementioned figure, there is noticeable breakup of vortices about the center of the whisker geometry. However, the perpendicular flow (top) demonstrates a shedding pattern both separated in space and alternating in time. This feature is responsible for cancelling out a portion of what would otherwise be a large instantaneous net force on the model in a single direction.

The alternating shedding pattern is gradually lost as sweep angle increases. The implications of this trend are seen on the unsteady lift coefficient, shown in the spatiotemporal plot with respect to spanwise position and time in Figure 1(b). At $\lambda = 0$ positive and negative peaks in lift force alternate clearly with respect to time and spanwise position, reducing the $C_{L,RMS}$ by 91.1% with respect to a smooth ellipse of equivalent aspect ratio, as well as near-elimination of a clear and dominant shedding frequency. As sweep angle

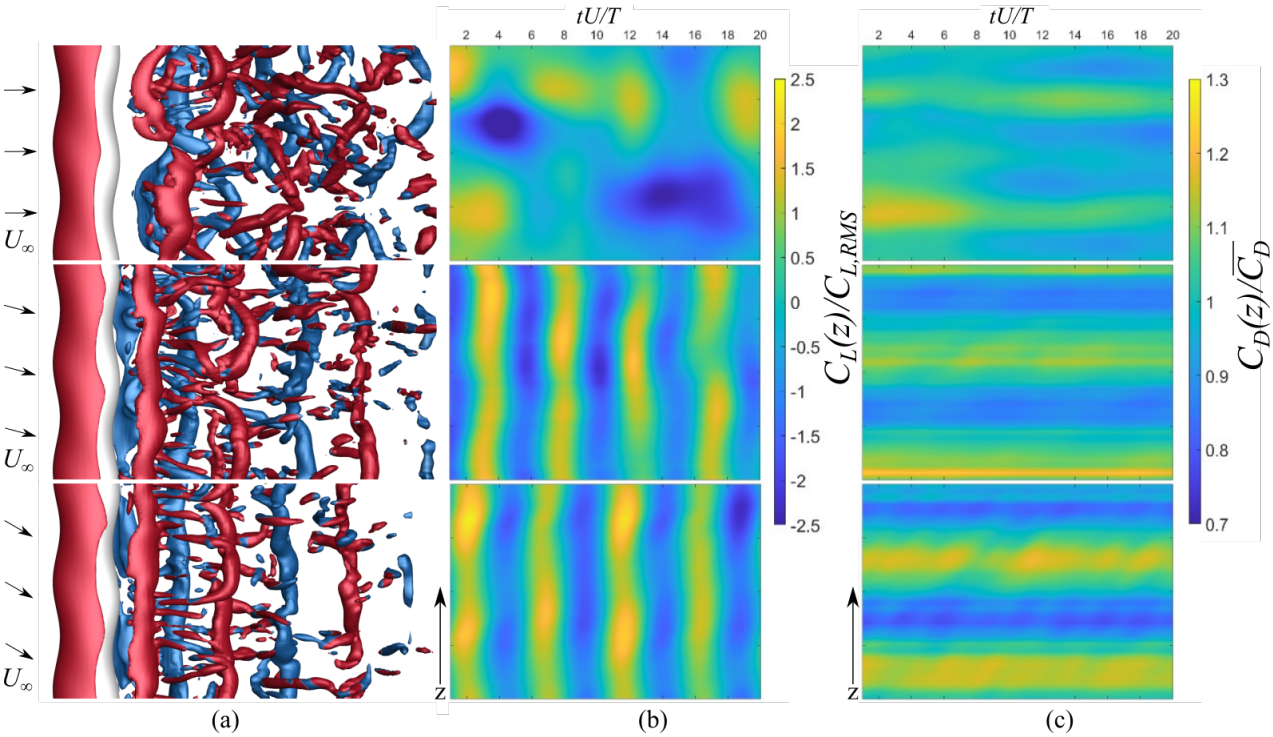

Figure 1: (a) Instantaneous flow structures plotted by Q-criterion (b) Lift force with respect to spanwise location over whisker geometry at 0, 15, and 30 degrees (descending) (c) Drag force with respect to spanwise location for the same cases.

increases, a strong shedding frequency returns and decreases in descending order on Figure 1(b). The formerly separated peak forces merge together on the time axis resulting in a smaller reduction in lift from ellipse to whisker of 75.4% at 15 degrees and 49.8% at 30 degrees. These downward trends in smooth ellipse coefficients and upward trend for whisker geometry continue at larger angles. The two geometries converge at 45 degrees with similar $C_{L,RMS}$ values of 0.11, and then diverge again at $\lambda = 60$ degrees when the undulated geometry has a higher root-mean-square lift than the smooth ellipse.

Lastly, to explain the reduction in drag forces, it is best to look at the behavior of the flow at various locations along the span in 1(c). Flow structures interact with the model through forces that vary with respect to location due to surface undulations since the local aspect ratio changes periodically. As λ increases, the *relative* chord length and aspect ratio seen by the streamlines increase. As a result, localized forces become increasingly concentrated at specific locations, and the overall drag forces decrease with sweep angle for whisker geometry. There is a 10.4% decrease in coefficient of drag from that of a smooth ellipse at 0 degrees, a 7.4% decrease at 15 degrees, and a 1.8% decrease at 30 degrees. Beyond this, values of drag coefficient are nearly identical at 0.381 and 0.222 for whisker geometry at 45 and 60 degrees, compared to 0.377 and 0.222 for an ellipse. The reduction in drag forces is significantly smaller percentage-wise than was seen for lift forces, and at 45 to 60 degrees, both geometries result in nearly identical values which indicates little significance of surface undulations on drag force reduction at or beyond the 45 degree threshold.

4 Summary and Future Work

Results of flow simulations indicate potential for the utility of whisker-inspired geometries for angled flow applications when sweep angle is less than 45 degrees. Further research could explore coupled orientation and geometric parameter changes and may yield optimization of desired force-reduction effects or improve efficacy of this geometry for larger sweep angles.

References

[1] Hanke, et al. Harbor Seal vibrissa morphology suppresses vortex-induced vibrations. *Journal of Experimental Biology*, 213(15), 2010.

[2] Lyons, et al. Flow over seal whiskers: Importance of geometric features for force and frequency response. *PLOS ONE*, 15(10), 2020.

[3] Liu, et al. Phase-difference on seal whisker surface induces hairpin vortices in the wake to suppress force oscillation. *Bioinspiration & Biomimetics*, 14(6), 2019.

[4] Murphy, et al. Effect of Angle on Flow-Induced Vibrations of Pinniped Vibrissae. *PLOS ONE*, 8(7), 2013.

[5] Yuasa, et al. Simulations of flow over a bio-inspired undulated cylinder with dynamically morphing topography. *Journal of Fluids and Structures*, 211, 2022.

Experimental study on covert-inspired flow control using time-resolved flowfield measurements

Girguis Sedky*, Chengfang Duan, Ahmed Othman, and Aimy Wissa

Princeton University, Princeton, NJ, USA
**Correspondence: gs7362@princeton.edu*

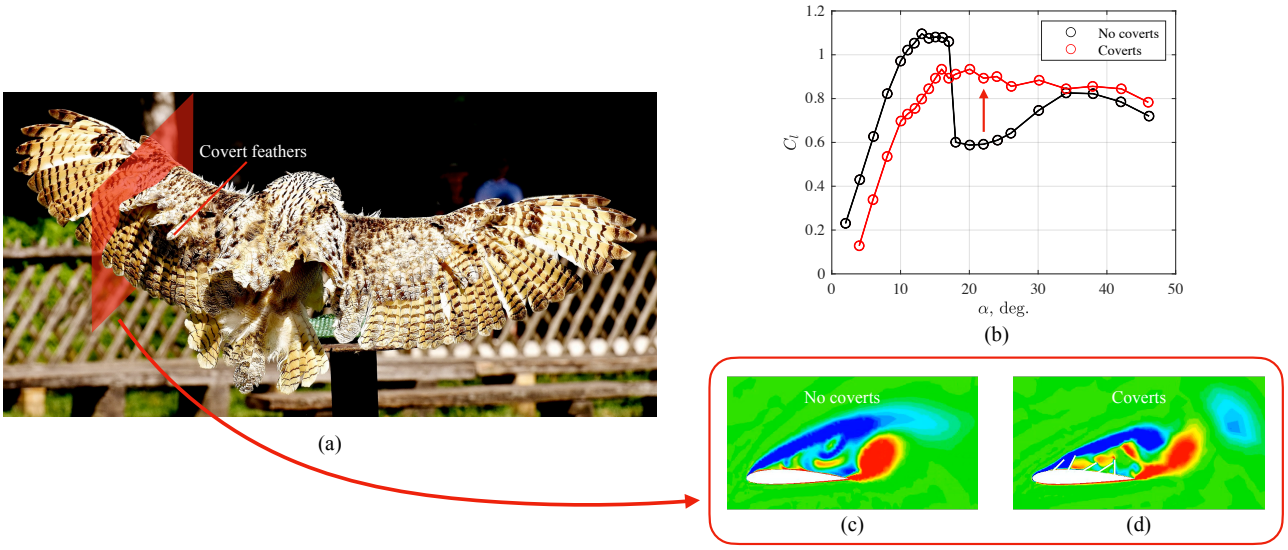

Figure 1: (a)Bird undergoing a high angle-of-attack maneuver with deployed covert feathers. (b) Experimental coefficient of lift C_l measurements as a function of angle of attack α for a NACA 2412 airfoil with and without covert-inspired flaps. Instantaneous vorticity fields of the NACA 2412 airfoil obtained using Detached-Eddy simulations for the no-covert configuration (c), and the covert configuration (d).

Recent years have seen the deployment of unmanned aerial vehicles (UAVs) and small electric vertical take-off and landing (eVTOL) aircraft for a variety of operations, including extended surveillance, logistics support, and urban air mobility. Many of these operations require air vehicles to navigate, hover, and land in urban environments and complex terrain dominated by unsteady flow conditions that significantly increase the risk of stall [1, 2]. While mitigating the risk of sudden stall and flow separation in these environments remains a major challenge for vehicle design [3], birds have long been able to navigate and maneuver in obstacle-filled environments and gusty conditions [4]. Thus, incorporating bird-inspired elements in vehicle design presents a possible solution for engineering stall-resistant air vehicles.

Birds feathers have been reported to aid in stall mitigation by modulating and modifying the flow field around the wings. One of such feather systems is known as the covert feathers or coverts (Figure 1a). Coverts are contour feathers found on the upper and lower surfaces of birds' wings. There are multiple rows of covert feathers, and each has been observed to deploy during flight, especially during high angle-of-attack-maneuvers and gust encounters [5, 6].

The authors' prior work explored the aerodynamic impact of incorporating a single covert-inspired flaps on a NACA 2414 airfoil in wind tunnel experiments at a Reynolds number of 200,000. They demonstrated a large average lift gain ($\approx 12\% - 23\%$) in the post-stall regime, showcasing the efficacy of the flap in delaying stall and mitigation of flow separation [7, 8]. These studies were limited to one covert-inspired flap, while bird wings have multiple rows of covert feathers. Most recently, we investigated the impact of using multiple flaps on the aerodynamic forces and the flow field using wind tunnel experiments and Detached-Eddy simulations (DES). Figures 1b-1d summarize recent findings for a 5-flap configuration. Wind tunnel lift measurements showed up to a 57.6% improvement in the coefficient of lift C_l in the post-stall regime for five freely moving flaps distributed along the suction side of an NACA2414 airfoil. DES was then used to visualize the flow field around the same airfoil with five flaps located at the same chord-wise locations as the experiments. The vorticity snapshot of the 5-flap configuration shown in figure 1d shows a portion of the leading-edge vortex trapped between the first and second flaps, which results in increased suction over the wing's upper surface. In addition, the covert configuration prevents recirculating flow from propagating upstream, reducing the

adverse-pressure gradient and allowing the flow to remain attached until the first covert flap. While the simulation results represent the first evidence for the benefit of having multiple covert-inspired flaps at this Reynolds number, the simulations ignored the effect of the flap dynamics by fixing the flaps' deflection angle at the mean value observed during the wind tunnel experiment.

Thus, the overall aims of this study are to a) validate the simulation results and b) investigate the effect of the flap dynamics on the flow field. More specifically, we will present results from two experiments. In the first experiment, the static-flap simulation will be re-created, and time-resolved flow field measurements will be acquired using planar particle image velocimetry (PIV). In the second study, the covert flaps will be allowed to move freely in response to the aerodynamic loads, similar to the wind tunnel experiments, and the resulting unsteady flow fields will be visualized and quantified. The measurements will be used to validate the static-flap assumption made in the simulations and improve our understanding of the physical mechanisms governing the lift-enhancing role of covert feathers in birds. The results will include lift and drag measurements from the aforementioned wind tunnel experiments, and the experimental flow fields for high-resolution time-resolved PIV measurements.

References

[1] Abdulghani Mohamed, Matthew Marino, Simon Watkins, Justin Jaworski, and Anya Jones. Gusts encountered by flying vehicles in proximity to buildings. *Drones*, 7(1):22, 2022.

[2] Anya R Jones, Oksan Cetiner, and Marilyn J Smith. Physics and modeling of large flow disturbances: Discrete gust encounters for modern air vehicles. *Annual Review of Fluid Mechanics*, 54:469–493, 2022.

[3] Darryll J Pines and Felipe Bohorquez. Challenges facing future micro-air-vehicle development. *Journal of Aircraft*, 43(2):290–305, 2006.

[4] Johnny H Evers. Biological inspiration for agile autonomous air vehicles. Technical report, AIR FORCE RESEARCH LAB EGLIN AFB FL MUNITIONS DIRECTORATE, 2007.

[5] Graham K Taylor, Anna C Carruthers, Tatjana Y Hubel, and Simon M Walker. Wing morphing in insects, birds and bats: mechanism and function. *Morphing Aerospace vehicles and structures*, pages 11–40, 2012.

[6] Anna C. Carruthers, Adrian L. R. Thomas, and Graham K. Taylor. Automatic aeroelastic devices in the wings of a steppe eagle Aquila nipalensis. *Journal of Experimental Biology*, 210(23):4136–4149, 12 2007.

[7] Chengfang Duan and Aimy Wissa. Covert-inspired flaps for lift enhancement and stall mitigation. *Bioinspiration & biomimetics*, 16(4):046020, 2021.

[8] Ahmed K. Othman, Nirmal J. Nair, Anushka Sandeep, Andres Goza, and Aimy Wissa. *Numerical and Experimental Study of a Covert-Inspired Passively Deployable Flap for Aerodynamic Lift Enhancement.*

Experimental study on the development of wakes past perforated plates

M.M. Cicolin [a], I.P. Castro[a], and B. Ganapathisubramani[a]
[a] Aero & Astro Department, University of Southampton, UK[1]
*Correspondence: *mmc1c21@soton.ac.uk*

1 Introduction

The flow past a solid plate is one of the most common situations in fluid mechanics, in which the interaction of two shear layers carrying concentrated vorticity of opposite signs results in the classical von Karman vortex street. Is is well know that this classical wake pattern can be altered by interfering with the wake by adding a splitter plate, for example, letting the base to bleed or simply making the body porous. The changes induced in the wake can delay the onset of vortex shedding or even completely remove it. Early works using plates with different porosity values have shown that the removal of vortex shedding is accompanied by a fall in drag, and it is possible if the porosity level reaches certain level [1,3]. Another reported effect of porosity is the movement of the recirculation bubble, leading the vortices to form and shed further downstream when compared to a solid bluff body [1,5]. In addition to experimental works, simulations and theoretical models have been published recently. However, the former are still restricted to low Reynolds number [2], and the latter is only available for steady models [4]. There are a series of questions that remain open. For example, how fast is the "switch-off" of the vortex shedding as the porosity increases; can vortex shedding occur even in the absence of a recirculating bubble; what is the impact on drag forces. In an attempt to answer these and other questions, we carried out a series of experiments in water channel and wind tunnel using hot wire anemometer, force measurements, and PIV. In this work, we present preliminary results focusing on the vortex shedding evolution as the porosity increases at the moderate range of Reynolds number.

2 Experimental setup

Experiments were carried out with a series of rectangular plates made out of acrylic sheets with width $D = 66$mm and height $H = 740$mm. The porosity $\beta = A_o/A_T$, defined as the ratio between the open and the total area of the plate, varied between 0% - the solid plate - and 35%. The Reynolds number varied in the range $15,000 \leq Re \leq 65,000$. Two series of experiments were carried out - one in the wind tunnel and another in the water channel. The experiments in air used hot wire anemometers to obtain the time series of two points, located next to each shear layer separating from the plate at a distance $x/D = 6$ and $y/D = \pm 1.5$. These velocity signals were then used to obtain the coherence between the layers, which is an indication of vortex shedding. In the same series, force measurements were acquired using two independent load cells, one at each extremity of the model. The experiments in the water channel focused on planar PIV measurements in the middle cross section of the model, as illustrated in figure 1.

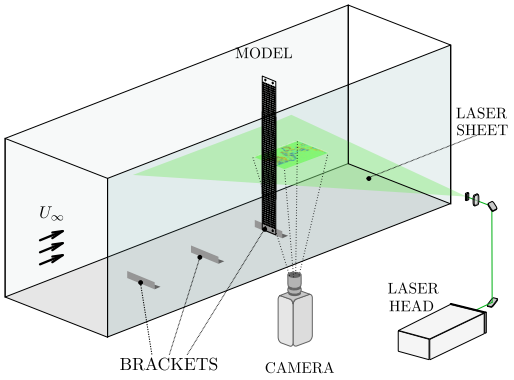

Figure 1: Experimental setup for PIV measurements in the water channel

3 Results

Figure 2 shows the mean field for the u component (parallel to the incoming flow), obtained from the PIV measurements. In addition, the streamlines are superimposed in the figures, and the yellow line marks up the recirculation bubble for each porosity value. It is possible to observe that the recirculation bubble moves dowstream as the porosity increases, similarly to what [1] observed. The bubble starts to decrease in extent from $\beta \approx 15\%$ and, for $\beta \geq 30\%$ it is no longer observable in the mean fields.

The velocity signals were used to calculate the coherence between the two shear layers. Figure 3 illustrates the position of the probes (u_1, u_2) and the typical plot for $\beta = 18\%$. C indicates the coherence and ϕ is the phase difference between the two signals. The figure shows a clear peak in coherence at the frequency $fD/U_\infty \approx 0.14$, which is an indication of vortex shedding. In addition, the correspondent phase difference between the signals is consistently close to 180°, whereas it is scattered for other frequency values. The second peak at $fD/U_\infty \approx 0.14$ and phase difference around 0° indicates an harmonic of the same phenomenon. Figure 4

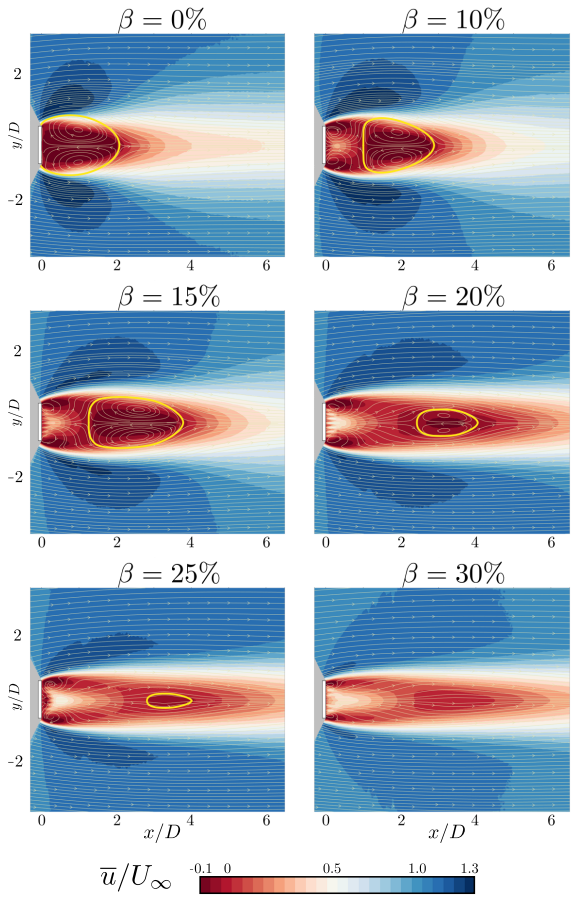

Figure 2: Mean velocity fields ($\overline{u}/U_\infty$) an streamlines for different values of β. $Re = 25,000$

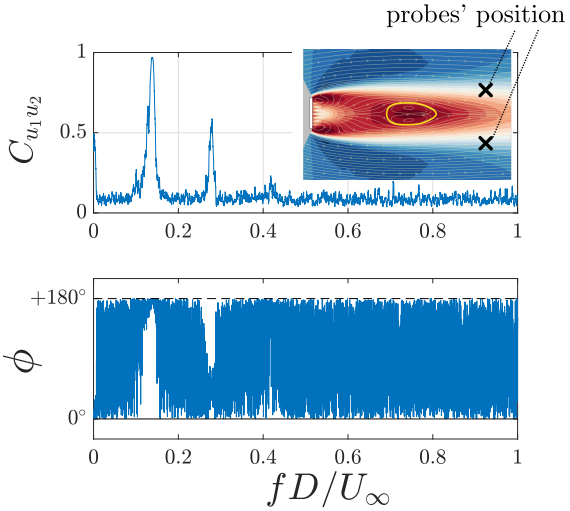

Figure 3: Coherence and absolute phase difference between the two velocity signals (u_1, u_2) at $(x/D, y/D) = (6, \pm 1.5)$. $\beta = 18\%$ and $Re = 60,000$

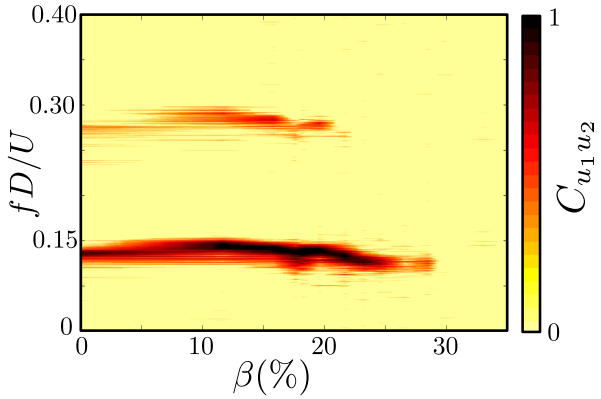

Figure 4: Coherence between the two velocity signals versus β. Probes location: $(x/D, y/D) = (6.0; \pm 1.5)$ and $Re = 60,000$

was produced by using the same approach as figure 3 for all porosities β. There is a clear frequency signature delimited by high values of coherence around $fD/U_\infty \approx 0.14$ and its harmonic around 0.3. From $\beta \approx 22\%$, the peak of coherence starts to fall, disappearing completely at $\beta = 30\%$.

4 Conclusion and Future work

Experiments were carried out in the wind tunnel and water channel to investigate the wake development of the flow past porous plates varying the porosity β for moderate values of Reynolds number. The focus was on the formation of the regular vortex shedding mechanism. The results have shown that the recirculation bubble dettaches from the plate as β increases, then reduces in size and vanish for $\beta \geq 30\%$. The transition from the regime with regular vortex shedding to the regime without it occurs from $20\% \leq \beta \leq 30\%$, and in this range the vortex shedding is intermittent as the coherence value oscillates across the acquisition period. Next steps involve the characterisation of the vortex shedding period for the range $20\% \leq \beta \leq 30\%$ and the analysis of the drag force.

References

[1] Castro, I.P. Wake characteristics of two-dimensional perforated plates normal to an air stream. *J. Fluid Mech.*, 46,599, 1971.

[2] Singh, A. and Narasimhamurthy,V.D. Perforation effects on the wake dynamics of normal flat plates. *J. Fluid Mech.*, 947,A23, 2023.

[3] Steiros, K. and Hultmark, M. Drag on flat plates of arbitrary porosity. *J. Fluid Mech.*, 853,R3, 2018.

[4] Steiros, K. *et al.* Recirculation regions in wakes with base bleed. *Phys. Rev. Fluids.*, 6034608, 2021.

[5] Steiros, K. *et al.* An analytical blockage correction model for high-solidity turbines. *J. Fluid Mech.*, 948, A57, 2022.

Flow-induced-vibration control using superhydrophobic surfaces

Fuwang Zhao[#], Lingwei Zeng[#], Yang Liu, Hui Tang[*]
Department of Mechanical Engineering, The Hong Kong Polytechnic University, Kowloon, Hong Kong[1]
[#]These authors contributed equally to this work
[*]Correspondence: *h.tang@polyu.edu.hk*

1 Introduction

Flow-induced vibration (FIV) of bluff bodies is frequently encountered in many engineering applications, such as cooling towers, high-rise buildings, heat exchangers, etc. The vibration may cause structure fatigue and catastrophic consequences. To better control the FIV of bluff bodies, various methods were developed, such as modifying the surface and installing appendages. Originally inspired by lotus leaves' unique water-repellent feature, superhydrophobic surfaces have been successfully applied for drag reduction on fixed bluff bodies (Kim et al. 2015; Zhang et al. 2019; Sooraj et al. 2020). However, rare literature has focused on their effects on the FIV of elastically supported bodies (Daniello et al. 2013).

A previous study on wavy cylinders have revealed that the best drag reduction and lift fluctuation mitigation occur at the mean-diameter normalized wavelength of 1.8 due to the spanwise flow induced on the cylinder surface (Lam and Lin 2009). This motivated us to conduct the current study, in which the FIV of a cylinder was controlled by coating the surface with different superhydrophobic bands, a much simpler way to create spanwise property variations.

The study was conducted in a closed-loop water tunnel. As shown in Fig.1(a), A circular cylinder was elastically supported with air bearings and springs, such that it can move transversely in a crossflow. The diameter and length of the cylinder are D = 22 mm, L = 440 mm, respectively. Five cylinders, including a normal (i.e., without coating) cylinder, three cylinders coated with superhydrophobic bands of wavelength $\lambda = D$, $1.8D$ and $3.6D$, and a fully coated cylinder ($\lambda = \infty$) were selected for comparison (see Fig.1b). To pin down the near wake of the cylinders, PIV measurements were conducted in the central horizontal plane of the normal and fully coated cylinders; For the cylinders with patterned bands, three horizontal planes were measured, covering a normal surface band, the superhydrophobic surface band and their interface.

[1]This work was supported by Natural Science Foundation of Guangdong Province (Project No. 2021A1515010337) and partially supported by Natural Science Foundation of China (Project No. 91952107)

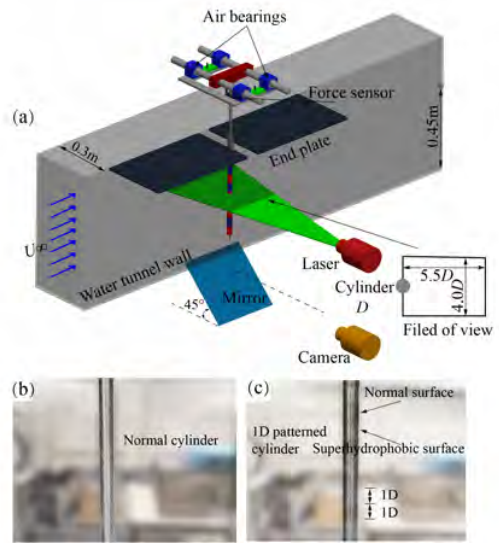

Figure 1: (a) Schematic of the water-channel test rig; (b) a picture of the normal cylinder; and (c) a representative cylinder with superhydrophobic surface bands where $\lambda = D$.

2 Results

Fig. 2 exhibits the root-mean-square values of the FIV amplitude A versus the reduced velocity U_r for the selected cylinders. Only two FIV branches were observed, i.e., the initial branch and the lower branch. All cylinders achieved their maximum oscillation amplitude at about $U_r = 5.3$. At $U_r = 5.0$ (corresponding to the Reynolds number of about 2660) in the initial branch, $A \approx 0.19D$ for the fully coated cylinder, roughly a 38.9% reduction if compared to $A \approx 0.31D$ for the normal cylinder. As for the patternedly coated cylinders, A values for the $\lambda = D$ and $3.6D$ cylinders do not deviate too much from the normal cylinder's values. However, the $\lambda = 1.8D$ cylinder exhibits quite different dynamics: its A values are largest in the initial branch and smallest in the lower branch. Similar trends were also observed for the measured transverse forces.

To uncover the reasons behind the above observations, Figs. 3 and 4 present the evolution of wakes behind the normal, fully coated and $\lambda = 1.8D$ cylinders at U_r = 5.0 and 8.4, respectively. The 2S vortex mode is observed for all the cylinders at U_r = 5.0 in the initial branch (see Fig.3). It seems that, compared to the normal cylinder, the vortex de-

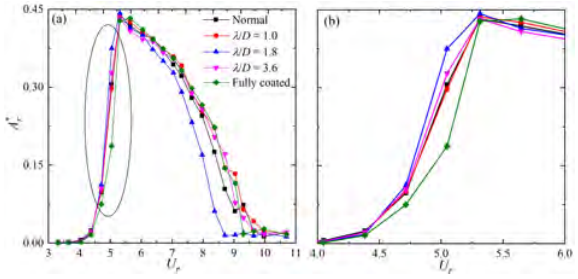

Figure 2: FIV oscillation amplitude A comparison of selected cases: (a) a global view (b) a local view in the initial branch

velopment for the fully coated cylinder is suppressed and delayed. In addition, the lateral distance between its negative and positive vortex cores is also significantly smaller than that for the normal cylinder. As such, less pressure difference is then produced in the lateral direction, leading to smaller A. For the $\lambda = 1.8D$ cylinder, the vortex structures are different in both strength and position among all three cross-sections, reflecting the three-dimensionality of the wake. At $U_r = 8.4$ in the lower branch, due to the increase of incoming flow velocity and the resulting Reynolds number, the vortices become more dissipative. Only two main eddies can be observed in Fig. 4. The difference between the normal and fully coated cylinder is not so noticeable, while both show stronger vortices than those shed from the $\lambda = 1.8D$ cylinder, which echoes the observation of the oscillation amplitude in Fig. 2.

3 Conclusion

We investigated the FIV control of a circular cylinder using superhydrophobic surface bands. It was found that the fully coated cylinder can suppress the FIV in the initial branch. In the lower branch, only the $\lambda = 1.8D$ cylinder could achieve FIV mitigation. The fluid-structure interaction analysis further revealed some physical insights. More detailed results will be presented in our poster.

References

[1] Lam K, and Lin Y. Effects of wavelength and amplitude of a wavy cylinder in cross-flow at low Reynolds numbers. *Journal of Fluid Mechanics*, 620: 195-220, 2009.

[2] Daniello R, Muralidhar P, Carron N, et al. Influence of slip on vortex-induced motion of a superhydrophobic cylinder. *Journal of Fluids and structures*, 42: 358-368, 2013.

[3] Kim N, Kim H, Park H. An experimental study on the effects of rough hydrophobic surfaces on the flow around a circular cylinder. *Physics of Fluids*, 27(8): 085113, 2015.

[4] Zhang H, Yi X, Du Y, et al. Dynamic behavior of water drops impacting on cylindrical superhydrophobic surfaces. *Physics of Fluids*, 31(3): 032104, 2019.

[5] Sooraj P, Ramagya M, Khan M, et al. Effect of superhydrophobicity on the flow past a circular cylinder in various flow regimes. *Journal of Fluid Mechanics*, 897: A21, 2020.

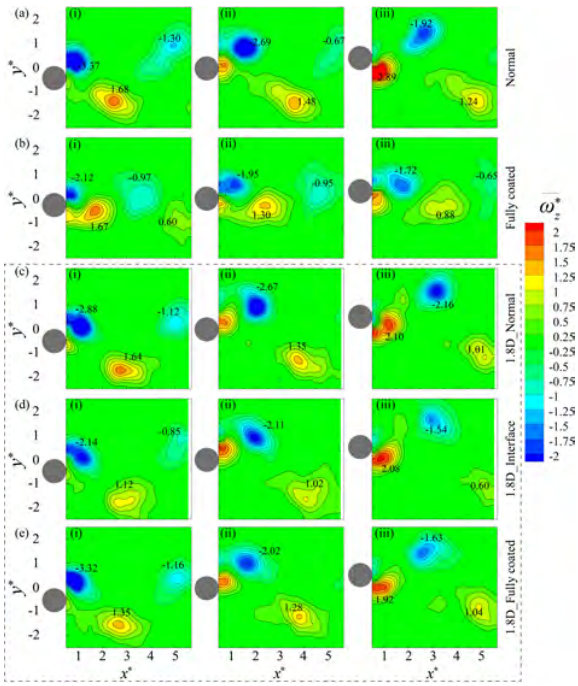

Figure 3: Phase-averaged vortex patterns behind selected cylinders: (a) normal, (b) fully coated, and (c-e) $\lambda = 1.8D$ at $U_r = 5.0$ in the initial branch. (i) to (iii) correspond to the location of the oscillating cylinder at $y^* = 0$, $0.5A_{max}$ and A_{max}.

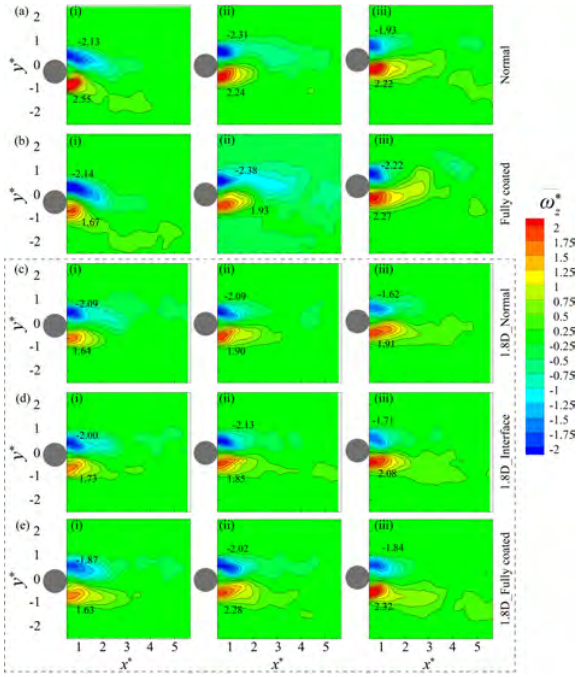

Figure 4: Phase-averaged vortex patterns behind selected cylinders: (a) normal, (b) fully coated, and (c-e) $\lambda = 1.8D$ at $U_r = 8.4$ in the lower branch. (i) to (iii) correspond to the location of the oscillating cylinder at $y^* = 0$, $0.5A_{max}$ and A_{max}.

Force models for a flapping foil under unsteady upstream conditions

R. Vilumbrales-Garcia[a], G.D. Weymouth[b], and B. Ganapathisubramani [a]
[a] Faculty of Engineering and Physical Sciences, University of Southampton, UK,
[b] Faculty of Mechanical, Maritime and Materials Engineering (3mE), TU Delft, NL
*Correspondence: *r.vilumbrales-garcia@soton.ac.uk*

1 Introduction

Coordinated controlled manoeuvring through upstream wakes is important for a wide range of applications; from surface ships to autonomous underwater vehicles. A proper understanding of the unsteadiness of the surrounding flow is essential, and it is a requirement to develop operations involving several autonomous vehicles. Previous work has shown that animals can greatly improve their performance in terms of thrust production or efficiency if their kinematics and paths are properly adapted to the incoming flow [1], but the physics behind the performance augmentation are still not well understood.

With the use of flapping foils to replicate fish-schooling, it has been seen that the performance of a foil immersed in a thrust-producing wake is highly dependant on the interactions between its path and the incoming vorticity structures. An important thrust augmentation can be achieved, but also a large detriment if the kinematics are not adapted to the upstream flow [2]. This points out to the importance of adapting to any upstream condition changes in real time to maximise and maintain gains.

With the use of Reinforcement Learning, a foil can learn to keep the location that maximises performance [3], but those tools usually require a large amount of computational data. It has been shown that the use of physically relevant parameters can help to reduce the training cost, and to improve generalisation [4]. In this line, [5] proposed a method called "SINDy" to identify sparse governing equations by providing relevant input data to the system. The approach provides 'human-interpretable' outputs, which would lead to a better understanding of the mechanism behind the fish-schooling gains. Also, another concept that needs attention is the manoeuvring motion required to locate the foil in the optimum route. Those kinematics changes can impose a large amount of unsteadiness in the forces evolution that has to be addressed in the prediction stage.

Here, we construct a sparse database of cases where a foil is executing manoeuvres inside an incoming thrust-producing wake. Next, we develop several forces predictive models with different inputs, to determine what components of the surrounding flow are relevant to the performance of the foil. We use physically relevant parameters, in order to reduce the amount of data required, and to improve generalisation. Finally, we will evaluate the governing equations discovered by the models to gain knowledge about the physics behind the performance augmentation.

2 Methodology

To develop the forces predictive models we use the tool SINDy (Sparse Identification of Nonlinear Dynamics) [5]. The approach relies on the control equation presented next: $X_{t+1} = f(X_t, U_{t+1})$, where X is the state vector, U are the control inputs, and f is the predictive function that advances the state vector from t to $t+1$. To find f, we develop a database of cases of tandem foil simulations, as depicted in Figure 1A. Both foils follow similar sinusoidal heaving ($h = Asin(2\pi ft)$) and pitching motions ($\theta = \theta_A cos(2\pi ft)$), where $A = 2C$ is the peak-to-peak heaving amplitude, θ_A is the maximum pitching angle, and f is the kinematics frequency. The Strouhal $St = 2Af/U$ value is set as $St = 0.36$. The foils are located at a longitudinal distance of three chords ($X = 3c$). We also add a phase delay to the kinematics of the hind foil, ϕ. As part of its manoeuvre, the follower foil executes a motion as presented in Figure 1B, inside the wake generated by the leader. The path of the foil can be defined as follows: one flapping cycle at a given ϕ_0, one transition cycle to a new ϕ_1, and a last cycle at ϕ_1. We include 64 cases in the training database, with 8 different ϕ_0 and ϕ_1, both ranging from 0π to 2π.

Table 1 introduces the three predictive models considered in this study. In each of the models, we increase the complexity of the inputs, in an effort to gain knowledge of the mechanisms behind the performance augmentation. All the models have as state vector X, the instantaneous C_L and its first derivative. For the control parameters U, the first one, "Delay" uses the delay component ϕ. Next, we include in the second model, "Kinematics", the ϕ inside its basis functions, h and θ, motivated by the importance of both parameters on other theoretical approaches, like [6]. In the last model we include physical knowledge about the incoming flow, in the shape of the relative distance between the foil and the incoming vortices (x_1, y_1) and (x_2, y_2). With the use of a predetermined library of functions, the approach will find the governing equations that best represent the training data. To improve the sparsity, we have selected a LASSO regressor. Finally, to evaluate the predictive capabilities of the models, we use 150 cases not seen in the training phase,

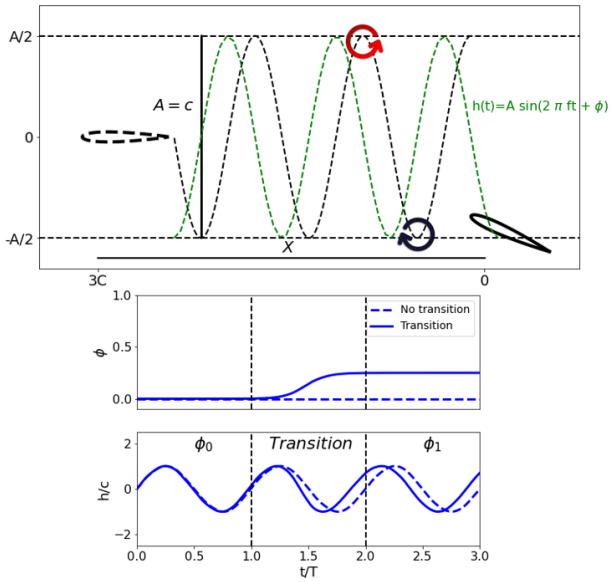

Figure 1: A) Schematics of the tandem simulations followed in this study. The rotating arrows represent the incoming vortices of the thrust producing wake. B) Transition motions executed by the hind foil.

Table 1: Inputs for the three predictive models. X is the state vector, and U are the control inputs. The first derivative of all the components is also included as an input.

	X	U
Delay	C_L	ϕ
Kinematics	C_L	ϕ, h, θ
Wake info	C_L	$\phi, h, \theta, x_1, x_2, y_1, y_2$

consisting of a combination of 10 starting phase-delays (ϕ_0) and 15 final phase-delays (ϕ_1).

3 Results

Figure 2 introduces the forces prediction achieved by the three models ("Delay" in green, "Kinematics" in red, and "Wake info" in purple) for one of the validation cases. The prediction starts at X_t, located at $t/T = 1$ and is projected for two flapping cycles, the transition ($t/T = 1-2$), and the new state, ϕ_1 ($t/T = 2-3$). It can be seen by looking at the model "Delay" that including the control parameter ϕ by itself is not enough to account for the unsteadiness presented in the system, resulting in a poor approximation of the target. Adding the kinematics information reduces the predictive error, but it is still not capturing neither the transition nor the ϕ_1 cycle. The model that contains information about the upstream flow achieves the best approximation, highlighting the importance of adding physically relevant parameters into any system identification approach. The results presented in Figure 2 are consistent through the whole evaluation database: the model "Delay" generating an overall error of 32%, reduced to 25% for the kinematics, and 19% for the wake info. Still, it can be seen that, even

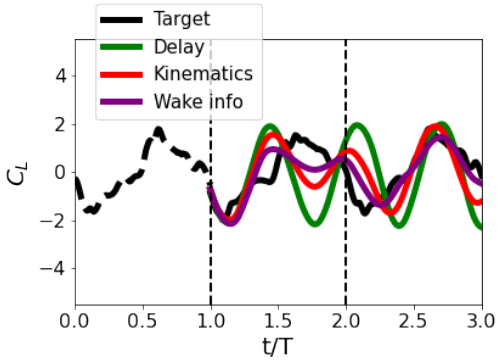

Figure 2: Forces prediction by the three models: Delay (green), kinematics (red), wake info (purple), and the target data (black).

with the more complex model ,there are areas of the forces evolution not being captured, mainly at the transition phase.

4 Conclusion and Future Work

In this work, we have develop three different forces prediction models for a flapping foil executing transition manoeuvres inside an unsteady incoming flow. By carefully selecting the inputs of the system identification tool, we have seen that the use of the control parameter is not enough to account for the unsteadiness and interactions between the foil and the wake, with an overall predictive error in the validation cases of 32%. After incorporating the ϕ inside its basis functions, the kinematics, the error was reduced to 25%. Finally, by adding the relative distance between the foil and the incoming vortices as control inputs, we achieve the most accurate prediction, with an error of 19%. Still, all the models struggle with the most unsteady part of the motion, the transition. More analysis is required to understand this, and a different transition strategy will be develop to reduce the sudden change in forces and to increase the efficiency of the operation. Finally, in order to assess the generalisation of the models, we will evaluate them under several types of wakes/conditions.

References

[1] Weihs, D Hydromechanics of fish schooling *Nature*, 5387:290–291, 1973.

[2] Muscutt, LE and Weymouth, GD and Ganapathisubramani, Bharathram Performance augmentation mechanism of in-line tandem flapping foils. *Journal of Fluid Mechanics*, 827:484–505, 2017.

[3] Verma, Siddhartha and Novati, Guido and Koumoutsakos, Petros Efficient collective swimming by harnessing vortices through deep reinforcement learning *Proceedings of the National Academy of Sciences*, 115.23:5849–5854, 2018.

[4] Weymouth, GD and Yue, D. K. P. Physics-Based Learning Models for Ship Hydrodynamics *Journal of Ship Research*, 57.1:1-12, 2013.

[5] Brunton, Steven L and Proctor, Joshua L and Kutz, J Nathan Sparse identification of nonlinear dynamics with control (SINDYc) *IFAC-PapersOnLine*, 49.18:710–715, 2021.

[6] Theodorsen, Theodore, and I. E. Garrick. Mechanism of flutter a theoretical and experimental investigation of the flutter problem. *NATIONAL AERONAUTICS AND SPACE ADMINISTRATION WASHINGTON DC*, 1940

Generalizing the surface layer, modulation of turbulence eddies near surfaces

S. Sheppard[a], J. Farnsworth[a], J.G. Brasseur[a],
J.C. Vassilicos[b], P. Braganca[b], and C. Cuvier[b]
[a]University of Colorado Boulder, Boulder, Colorado, USA [1]
[b] Laboratoire de Mécanique des Fluides de Lille, Lille, France
*Correspondence: *samantha.sheppard@colorado.edu*

1 Introduction

The classical description of the surface layer is the inertia-dominated wall-adjacent region within the high Reynolds number turbulent boundary layer (TBL) in which integral scales scale linearly on the distance from the surface, z, and where law-of-the-wall scaling applies, when appropriate. Typically the surface layer encompasses the lower 15-20% of the boundary layer thickness. In this work we generalize the surface layer concept beyond shear-dominated boundary layer flows to wall-adjacent inertia-dominated regions in any wall-bounded turbulent flow where the vertical velocity fluctuations w' are directly modified by surface impermeability in such a way that integral scales involving w' scale linearly with z. To do so, we compare analysis of two classes of wind tunnel experiments: (1) the interaction between grid turbulence and an impermeable flat-plate in the generation of a shear-free surface layer outside the surface viscous layer and (2) the classical flat-plate turbulent boundary layer within which exists a shear-dominated surface layer.

Prior research directed at the interactions between a turbulent boundary layer and free-stream turbulence has focused on the impact of the turbulence on the boundary layer structure [1]. In the present research our interest is the generation of a surface layer outside the viscous boundary layer in the inertia-dominated region with zero mean shear-rate in order to investigate the impact of surface impermeability on the grid turbulence structure. The interaction of shear-free turbulent flows with impermeable surfaces has been studied experimentally with moving walls [2,3] and with oscillating grid turbulence adjacent to surfaces [4]. Shear-free turbulent boundary layers have also been explored computationally [5].

The present work examines the impact of an impermeable surface on grid turbulence structure outside the viscous wall layer as it evolves along a flat-plate leading to the creation of a shear-free surface layer, as illustrated in Figure 1. We look for relationships between the shear-free surface layer and the shear-dominated surface layer within the TBL.

[1]This work was supported by the Lille Turbulence Program and the DoD NDSEG fellowship program.

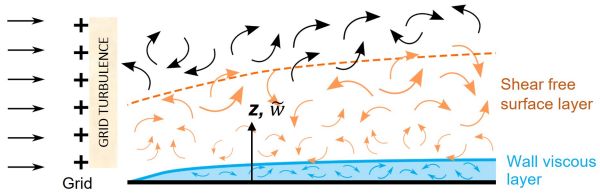

Figure 1: Schematic depicting the development of a shear-free surface layer.

2 Methods

The grid turbulence study was conducted in the University of Colorado Boulder low-speed unsteady wind tunnel facility. Three different passive grids were used as shown in Figure 2(b-d), at two wind tunnel speeds, $U_\infty = 5$ and 10 m/s. A flat-plate was installed in the test section with the leading edge downstream of the development region of the grid-generated turbulence. A schematic of the experimental setup is given in Figure 2(a).

Two-component (u,w) velocity fields were measured with time-resolved planar particle image velocimetry (TR-PIV) over the $x-z$ (longitudinal) plane. The measurement domain was located 0.58 m downstream from the leading edge to allow the grid turbulence sufficient distance (and time) to interact with the surface, while ensuring that the boundary layer remained thin compared with the integral length scales of the grid turbulence. The measurement field of view extended from the top edge of the wall viscous layer up to a distance of approximately four times the grid turbulence streamwise integral length scale, to encompass the shear-free surface layer region that is the focus of this study.

To enable the comparison of the shear-free surface layer with the shear-dominated surface layer that develops within the TBL, a second data set was acquired in the Lille TBL wind tunnel. The boundary layer thickness was $\delta_{99} = 0.28\,m$ at the nominal wind tunnel speed of 3 m/s and $Re_\tau = 2260$. The velocity fields were measured with time-resolved, stereoscopic particle image velocimetry (TR-sPIV) in two perpendicular ($x-z$, $y-z$) planes, sampled independently. The field of view extended from the surface to slightly above the surface layer region ($FOV_z \approx 0.3\delta_{99}$).

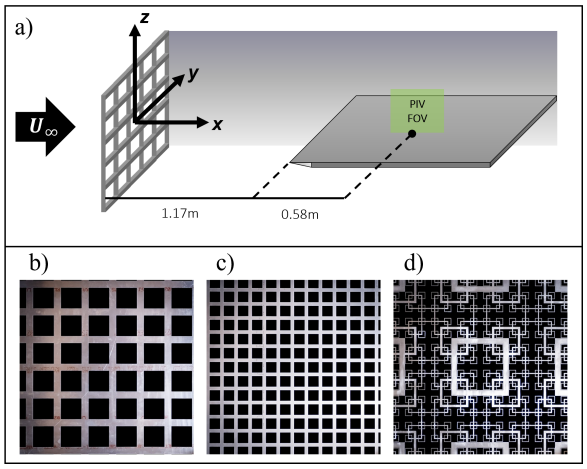

Figure 2: (a) Schematic of the grid turbulence wind tunnel experiment. Photographs of the three passive grids studied: (b) A "large" rectilinear grid ($M = 0.102\ m$), (c) A "small" rectilinear grid ($M = 0.052\ m$), (d) A square fractal grid.

3 Results

The integral length scales were calculated from two-point autocorrelations of each of the two velocity components u' and w' in the streamwise (x) and wall normal (z) directions. Of particular interest is the integral length scale of the vertical velocity component in the streamwise direction, $l_{ww,x}$. This is because the vertical velocity component w' is directly impacted by surface impermeability and is therefore where the blockage effects of the surface on the structure and coherence of the grid turbulence in the shear-free region is expected to be most directly observed. Figure 3(a) presents this integral length scale at $U_\infty = 10\ m/s$ for the rectilinear grid with mesh size $M = 0.102\ m$, which is pictured in Figure 2(b). The corresponding mean shear-rate profile is shown in Figure 3(b). Outside the wall viscous region ($z > \delta_{99}$) $l_{ww,x}$ grows linearly with z. The linear growth of the integral length scale in the region with zero shear defines the shear-free surface layer, indicated in Figure 3 by the orange region.

The linear fits of the $l_{ww,x}(z)$ profiles and the bounds of the shear-free surface layers were iteratively determined until the deviation from the linear fit was within 1% over the defined surface layer region. The upper bound of the shear-free surface layer was found to be of order the far-field value of $l_{uu,x}$, while the far-field value of $l_{ww,x}$ is not recovered until twice this distance. A region of linear growth in $l_{ww,x}(z)$ (i.e. a shear-free surface layer) was found and quantified for all three grids. In all cases the upper bound of the shear-free surface layer was found to scale on the streamwise integral scale of horizontal velocity fluctuations in the far field (i.e., outside the surface layer as defined above).

The same fitting procedure was applied to identify a linear growth in $l_{ww,x}$ within the TBL. A distinct linear growth is identified over a region extending to $0.15\delta_{99}$.

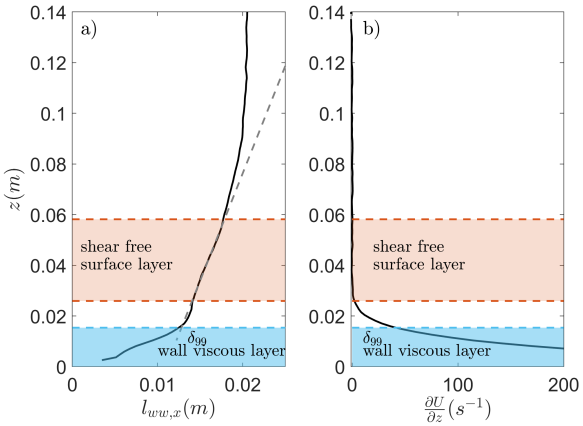

Figure 3: (a) Variation in $l_{ww,x}$ with vertical distance z above the flat-plate for the $M = 0.102\ m$ rectilinear grid at $10\ m/s$. The dashed gray line represents the linear fit over the shear-free surface layer. (b) Corresponding variation of $\partial U/\partial z$ with z.

4 Conclusion

This study examined the impact of an impermeable surface on grid turbulence convected over a flat-plate and the formation of a shear-free surface layer to contrast with the canonical shear-dominate surface layer in the flat-plate TBL. The growth of a surface layer was identified in the region with zero mean shear-rate outside of the viscous layer adjacent to the wall. In the shear-free inertia-dominated region of grid turbulence, the horizontal integral scale of the vertical velocity fluctuations was found to grow linearly with distance from the surface, mirroring the behavior of the shear-dominated surface layer within the flat-plate TBL.

In continued analysis, the grid turbulence shear-free surface layer will be further related to that found in the classical TBL in order to generalize the surface layer concept. Ultimately, the understanding gained from this research will be used to improve wall models in large-eddy simulation of wall bounded turbulent flows by accurately incorporating the vertical correlations established by blockage effects on turbulent structures by impermeable surfaces.

References

[1] Hearst, J.R, Dogan, E. & Ganapathisubramani, B.. Robust features of a turbulent boundary layer subjected to high-intensity free-stream turbulence. *Journal of Fluid Mechanics*, 851, 416-435, 2018.

[2] Thomas, N.H. & Hancock, P.E.. Grid turbulence near a moving wall. *Journal of Fluid Mechanics*, 82(3), 481-496, 1977.

[3] Hunt, J.C.R & Graham, J.M.R.. Free-stream turbulence near plane boundaries. *Journal of Fluid Mechanics*, 84(2): 209-235, 1978.

[4] McCorquodale, M.W. & Munro, J.R.. Experimental study of oscillating-grid turbulence interacting with a solid boundary. *Journal of Fluid Mechanics*, 813, 768-798, 2017.

[5] Perot, B. & Moin, P.. Shear-free turbulent boundary layers. Part 1. Physical insights into near wall turbulence. *Journal of Fluid Mechanics*, 295, 199-227, 1995.

How does the Darcy-Forchheimer law perform in high-Re porous media flows?

Mostafa Aghaei-Jouybari[a], Jung-Hee Seo[a], Charles Meneveau[a] and Rajat Mittal[a*]
[a] Department of Mechanical Engineering, Johns Hopkins University, Baltimore, USA[1]
*Correspondence: *mittal@jhu.edu*

1 Introduction

The Darcy law [1, 2], where the bulk pressure drop within a porous medium is related to the bulk velocity and fluid viscosity, still is one of the most effective and conventional ways of modeling flow through a porous substrate in low Reynolds number (Re) flows. This law, however, captures only the viscous effects and needs extra corrections to accommodate for flows at medium or relatively high pore-scale Reynolds number, where the inertial effects dominate the viscous ones. A well-known extension to the Darcy law is the Forchheimer [3, 4] correction. It tries to capture the inertial effects by adding a nonlinear term to the Darcy law. Most numerical and theoretical studies on porous media rely on modeling the porous substrate via the Darcy-Forchheimer (DF) law. This is particularly important when the interstitial Re is not low and the inertial effects are dominant. All the associated results, accordingly, are trustworthy and correct only when the assumptions and preconditions of the DF law are satisfied. Especially, at the intermediate and high Re flows, due to vortex shedding and other nonlinear effects, the performance of the DF law is expected to change. In this study, we examine the performance of the DF law for different random (isotropic) and arranged (anisotropic) porous lattices, for a wide range of Reynolds numbers (from almost Stokes flows, exhaustively to high Re flows) and will quantify the DF law accuracy for different lattices and flow Reynolds numbers.

2 Results

Figure 1 shows the five porous media used in this study. Medium C1 consists of aligned square inclusions, medium C2 of staggered square inclusions, medium C3 of square inclusions with low degree of randomness (only inclusions' position is chosen randomly), medium C4 of square inclusions with high degree of randomness (there both position and orientation are chosen randomly), and medium C5 of random circular inclusions. All five media are designed to have porosity of $\varepsilon = A_f/A_t = 0.75$, where A_f and A_t are the fluid occupied and the total domain area, respectively. For all cases, the simulations sweep over 14 values of Reynolds number, $\mathrm{Re} \equiv U_B a/\nu$, where $U_B = \frac{1}{A_f}\int_{A_f} u dA$ is the bulk velocity vector (u being the fluid velocity vector), a being the inclusion length scale (i.e. squares height for cases C1-4, and the circles diameter for C5), and ν being the fluid kinematic viscosity. The set of Re is chosen as $\mathrm{Re} = \{1, 5, 10, 20, 40, 60, 80, 100, 140, 180, 250, 400, 750, 1000\}$, capturing the fluid dynamics from almost Stokes flow at low Re's, exhaustively to highly nonlinear dynamics at high Re flows. The flow is pressure driven– the pressure gradient angle α (with respect to the horizontal direction) is prescribed, but the pressure gradient magnitude is adjusted in each time step such that it yields $U_B = 1$, i.e. constant mass mode. For each medium and at each Re, the flow is simulated for 7 values of $\alpha = \{0, 15, 30, 45, 60, 75, 90\}$ degrees. Figure 2 shows vorticity contours for case C1 at $\alpha = 0$ and Re=1, Re=100 and Re=1000. Given true pressure gradient vector and the predicted tensors for K and F, obtained by simple regression analysis on the simulations result, the DF law prediction of velocity vector U can be obtained using equation 1 as

$$U = -\left(\frac{1}{\mathrm{Re}}K^{-1} + F^{-1}\right)^{-1}\nabla P. \qquad (1)$$

The DF law performance, then, can be assessed by com-

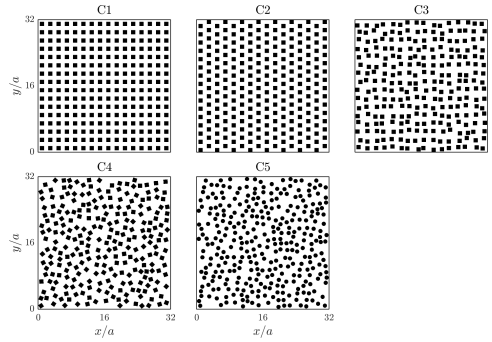

Figure 1: Porous media geometries.

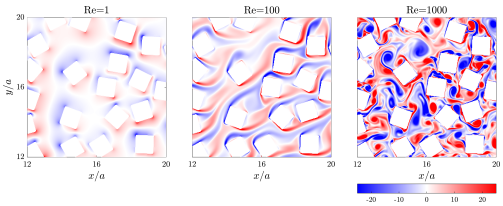

Figure 2: Contours of vorticity ω_3 for case C1 at $\alpha = 0$ and Re=1, Re=100 and Re=1000.

[1]This work was supported by the US Air Force Office of Scientific Research (AFOSR) under grant number FA9550-21-1-0286.

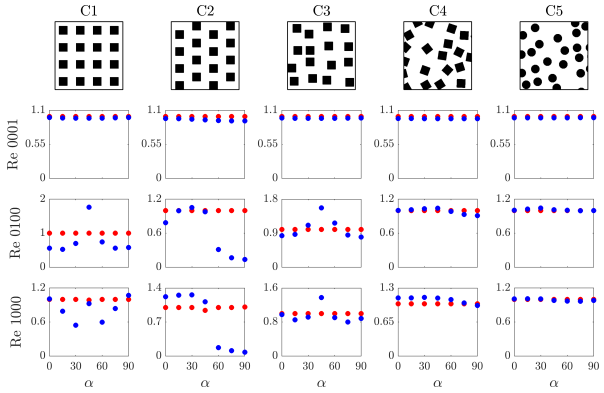

Figure 3: The DF law prediction of U at Re $= 1$, 100 and 1000. True U (red dots), predicted U (blue dots).

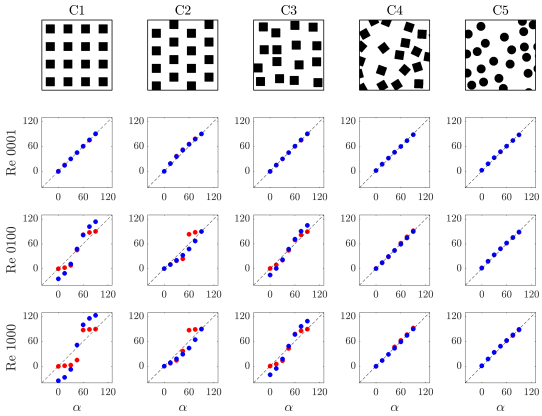

Figure 4: The DF law prediction of β at Re $= 1$, 100 and 1000. True β (red dots), predicted β (blue dots).

paring the magnitude and phase of the true and predicted U vectors. Figures 3 and 4, respectively, show the profiles of U and β (phase of U) comparing the true values with the predicted one at different α and Re values. There, the true values are shown by red dots and the predicted ones are shown by the blue dots. At a low Reynolds number of Re $= 1$ the predicted U vectors (both in magnitude and phase) match very well with the true vectors for all geometries, with the maximum error of less than 3%. At the intermediate and high Reynolds numbers of Re $= 100$ and 1000, however, the predicted U vectors match with the true vectors only for highly random geometries, cases C4 and C5, and for less random or arranged geometries C1, C2 and C3, the predicted U vectors deviate from the true vectors significantly. In some cases U is not predicted accurately (such as case C2 at $\alpha = 60$ in figure 3) and in some others β is out of phase (such as case C1 at $\alpha = 90$ in figure 4). The prediction results are slightly better for Re $= 100$ (the onset of vortex shedding regime) compared to Re $= 1000$ (fully vortex shedding regime), though at both Re's, the DF law is considered to perform poorly for C1, C2 and C3.

An important observation in the true β profiles (figure 4) is the flow refraction at high-Re regime for the regularized geometries. At the intermediate and high Re $= 100$ and 1000, the direction of the bulk velocity vector complies with the direction of the applied pressure gradient only for the highly random geometries C4 and C5 for all values of α, and the regularized geometry C2 if $\alpha \leq 45$. For these cases $\beta \approx \alpha$ for Re $= 100$ and 1000. For the regularized geometries C1, C2 and C3, on the other hand, there exist stable directions for the flow, i.e. if the imposed α is less than 45, the fluid tends to flow in the x-direction ($\beta \approx 0$ for any $\alpha < 45$) for C1 and C3, and if the imposed α is greater than 45, the fluid tends to flow in the y-direction ($\beta \approx 90$ for any $\alpha > 45$) for C1, C2 and C3. These phenomena are called flow channeling or refraction. The flow directions swings around 45 degree if $\alpha = 45$ for these cases. All these trends can be easily explained by considering the sheltering effects– for highly random geometries C4 and C5 there is no preferred geometrical axis for the medium, imparting same flow sheltering from upstream elements on the downstream elements in all directions. Therefore the fluid simply flows in the direction that the pressure gradient is imposed, i.e. $\beta \approx \alpha$. For cases C1 and C3 in both x and y directions and case C2 in the y direction, as explained before, the downstream elements are strongly sheltered by the upstream elements, imparting less drag to the flow. Therefore the fluid tends to flow in these directions at high Re, even though the normal component of $-\nabla P$ might be considerable. For these cases and α's, the direction of the bulk velocity vector does not comply with the direction of the pressure gradient.

3 Conclusion

According to the DF law prediction results in figures 3 and 4, we therefore conclude that the DF law is accurate as long as U complies with the direction of $-\nabla P$, otherwise its accuracy deteriorates significantly. For those cases that U does not comply with the direction of $-\nabla P$, we also notice that $U = \text{function}(-\nabla P)$ does not have a unique solution for $-\nabla P$. For example in figure 4, case C1 at Re $= 1000$, one notices $\beta \approx 90$ for three differernt values of $\alpha = 60$, 75 and 90. This happens due to flow refraction for this medium at high Re. It immediately translates that there are multiple vectors for $-\nabla P$ that result in same vector U. A simple mathematical analysis shows that the DF law, equation 1, ensures a unique solution for $U = \text{function}(-\nabla P)$, simply because both tensors K and F are positive definite and thus invertible. This fundamental contradiction between the mathematics of the DF law and the physics results in a deteriorated prediction accuracy for this law, that depends on the porous media geometry and the flow Reynolds number.

References

[1] Henry Darcy. *Les fontaines publiques de la ville de Dijon*. Paris: Dalmont., 1856.

[2] Stephen Whitaker. Flow in porous media i: A theoretical derivation of darcy's law. *Transport in Porous Media*, 1(1):3–25, 1986.

[3] PH Forchheimer. Wasserbewegung durch boden: Zeitschrift des vereines deutscher ingenieure, v. 45. 1901.

[4] Stephen Whitaker. The forchheimer equation: A theoretical development. *Transport in Porous Media*, 25(1):27–61, 1996.

Measuring the surface waves produced by a swimming snake

V. Stin[a,b], G. Polly[a], A. Mérigaud[a], X. Bonnet[c], A. Herrel[b] and R. Godoy-Diana[a]
[a] PMMH, CNRS, ESPCI Paris-PSL, Sorbonne Université, Université de Paris, Paris, France [1]
[b] MECADEV, Département Adaptation du Vivant, MNHN, CNRS, Paris, France
[c] Centre d'Études Biologiques de Chizé, CNRS, Villiers-en-Bois, France

1 Introduction

Snakes display multiple swimming behaviours. Some will swim with the body fully submerged to forage but some will be more likely to swim on the surface, like the garter snake *Thamnophis saurita*. Animals swimming at the water surface face more challenges compared to fully submerged swimming. On top of inertial and viscous drag, surface swimming must battle wave drag. Similar to what happens during the displacement of the hull of a ship, animals swimming at the surface must overcome waves generated from their own forward locomotion. The differences in pressure around the body of the swimmer created by its movements produce capillary-gravity waves called bow and stern waves. Research on surface swimmers has focused on animals using limb-surface interactions for propulsion such as ducks [1], geckos [2] and muskrats [3]. Nevertheless, some animals like snakes won't use any limbs and will travel at the water surface using continuous oscillation of the body. Waves formed by a swimming snake have been briefly described [4] but the fluid-structure interaction during surface swimming of a limbless swimmer is not well understood.

2 Results

Surface waves produced by a captive garter snake (*Thamnophis saurita*, length : 64cm, diameter : 0.94cm, weight : 33.8g) swimming at the surface of a water tank (dimensions: 2.5m long, 0.48m width, water depth: 0.1m) were measured using a synthetic Schlieren technique [5] (Fig. 1). The snake swimming kinematics were measured by tracking the snake's body with an in-house program. The snake was typically swimming at a speed of $0.4BL.s^{-1}$. The computed Strouhal number, often used to evaluate the swimming performances of aquatic animals [6] is $St = 0.92$. Its high value suggests that the swimming kinematics is theoretically not optimal.

The reconstruction of the waves generated by the swimming garter snake clearly show bow waves near the upper part of the body (Fig. 2.A). The bow waves spread out at an angle of $\pm 19.3^{\circ}$ with a wavelength of 4.73cm and a frequency of 7.14Hz. These waves are moving in the same direction as the swimmer and produce wave drag which may be the reason why the Strouhal is not optimal.

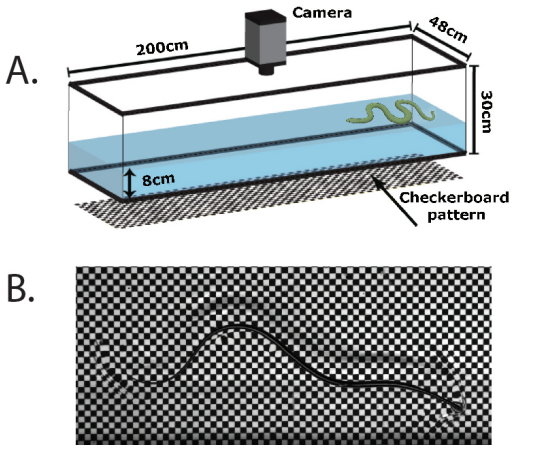

Figure 1: (A) Experimental setup for measuring the wave generated by snake surface swimming using Schlieren imaging technique. (B) Snapshot during surface swimming of *Thamnophis saurita*.

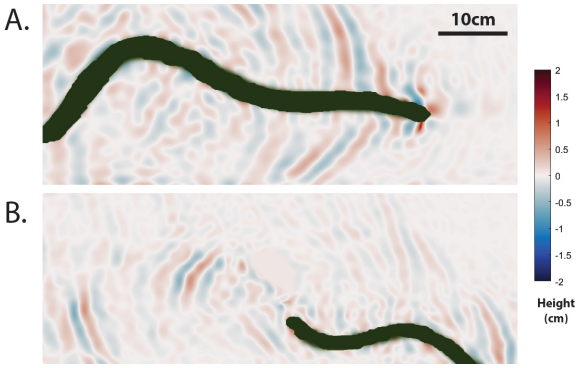

Figure 2: Reconstruction of the waves produced by the swimming snake. (A) Bow waves generated by the forward locomotion. (B) Capillary-gravity waves generated by the oscillation of the body.

We also witnessed that the continuous oscillation of the snake body produced coherent packs of waves at a frequency close to the tailbeat frequency of the swimming snake. These capillary-gravity wave have properties (f,λ)

[1] This work was supported by the Paris Sorbonne IPV doctorate program and the ANR DRAGON2 (ANR-20-CE02-0010)

similar to the bow waves but are traveling in the direction of the snake path. These waves could therefore help the propulsion via radiation stress [7] which is the motivation for us to continue to investigate this phenomenon and measure how much these waves help the propulsion of the swimmer.

3 Conclusion

These preliminary results are first steps toward the measurement of the energy balance during limbless surface swimming using quantitative real-time measurements of the surface wave pattern. This may help future developments of simple bio-inspired aquatic systems.

References

[1] Gough, et al. Aquatic burst locomotion by hydroplaning and paddling in common eiders (Somateria mollissima). *J Exp Biol*, 218 (11): 1632–1638, 2015.

[2] Nirody, et al. Geckos Race Across the Water's Surface Using Multiple Mechanisms. *Current Biology*, 28 (24), 4046-4051.e2, 2018.

[3] Fish, et al. Mechanics, power output and efficiency of the swimming muskrat (Ondatra zibethicus). *J Exp Biol*, 110(1), 183-201, 1984.

[4] H. Hertel. Structure, form, movement. 1966.

[5] S. Wildeman Real-time quantitative schlieren imaging by fast fourier demodulation of a checkered backdrop. *Experiments in Fluids*, 59 (6), 1–13, 2018.

[6] C. Eloy Optimal Strouhal number for swimming animals. *Journal of Fluids and Structures*, 30, 205-218, 2012.

[7] M.S. Longuet-Higgins The mean forces exerted by waves on floating or submerged bodies with applications to sand bars and wave power machines. *Proceedings of the Royal Society of London. A. Mathematical and Physical Sciences*, 352(1671), 463-480, 1977.

Modal Force Partitioning Method (mFPM) with Application to Aeroacoustic Noise from Rotating Wings

Suryansh Prakhar[a], Jung-Hee Seo[a] and Rajat Mittal[a*]
[a] Johns Hopkins University, Mechanical Department, Baltimore, USA[1]
[*]Correspondence: *mittal@jhu.edu*

1 Introduction

Drones are finding ever-increasing use in a variety of applications such as wildlife monitoring, product delivery, security, rescue operations, etc. However, one of the major factors limiting their widescale use is the noise that they generate. Drone noise, apart from being annoying to humans, can also negatively affect the health of humans and wildlife. However, despite these challenges, due to the benefits they offer, drone market is growing rapidly but it has been acknowledged that the noise problem must be addressed (Ref [1]).

The two main categories of aeroacoustic noise from drones are tonal noise and broadband noise. The tonal component of noise is generated primarily due to periodic variation in aerodynamic force vector due to the rotation of the mean drag force, advancing/retreating rotors in translational flight, while the broadband component consists of noise components like blade vortex interaction, blade gust interaction, boundary layer trailing edge interaction, stall and flow separation noise. Determining the relative importance of these various mechanisms is difficult since the surface pressure variations that are the source of this noise are induced simultaneously by all these mechanisms. Vortex induced pressure fluctuations are particularly important, but the vorticity field in these flows is highly complex, making it difficult to pinpoint the flow structures that are important for noise generation.

In complex flows such as those generated by a drone, a standard way to decompose the flow is via techniques such as Reynolds (RD) or triple decomposition (TD, Ref [2]). Proper orthogonal decomposition (POD), dynamic mode decomposition (DMD) and spectral POD (sPOD) are also being increasingly used for the decomposition of flows and for determining the dominant modes in the flow. While these methods provide a kinematic decomposition of the flow field, the pressure and associated forces induced by these modes are generally not available. In the current work, we describe the modal force partitioning method (mFPM), an extension of the force partitioning method (Ref [3]) which enables us to determine the pressure forces induced by the various modes in the flow, irrespective of the modal decomposition technique. We combine mFPM with the compact source form of the Ffowcs Williams-Hawkings equation-based acoustic partitioning method (APM, Ref [4]) to obtain the loading noise due to the various modes in the flow. The method is applied to fine-aspect ratio flow past a stationary wing and rotating wing to gain insight into the modes and vortex structures that dominate the aeroacoustic noise from such wings.

[1]This work was supported by ARO via Cooperative Agreement W911NF2120087

2 Results

Any time-dependent flow field can be decomposed into modes and can be generally expressed as,

$$\boldsymbol{u}(\boldsymbol{x},t) = \boldsymbol{u_0}(\boldsymbol{x}) + \boldsymbol{u_1}(\boldsymbol{x},t) + ... + \boldsymbol{u_i}(\boldsymbol{x},t) + ... + \boldsymbol{u_N}(\boldsymbol{x},t), \quad (1)$$

where $\boldsymbol{u_0}$ is the mean mode. For RD, $N = 1$, and $\boldsymbol{u_1}$ is the velocity fluctuation about the mean. For TD, $N = 2$, and $\boldsymbol{u_1}$ and $\boldsymbol{u_2}$ are the coherent and incoherent components of the velocity field. For POD, $i = 1, N$ correspond to the N POD modes of the flow. To compute the pressure forces due to each mode, we resort to FPM, according to which, the vortex induced pressure force induced by a velocity field is given by

$$F_Q = -2\rho \int Q\phi dV, \quad (2)$$

where ϕ is the influence field associated with the force component under consideration (Ref [3]). In the above expression, $Q = \frac{1}{2}(||\boldsymbol{\Omega}||^2 - ||\boldsymbol{S}||^2) = -\frac{1}{2}\boldsymbol{\nabla}\cdot(\boldsymbol{u}\cdot\boldsymbol{\nabla}\boldsymbol{u})$, where $\boldsymbol{\Omega}$ and $\boldsymbol{S}$ denote rotation and strain rate tensor respectively (see Hunt et. al., 1998). By substituting the modal decomposition into Eq. 2, we can obtain the force induced by the interaction between mode i and mode j as

$$F_{Qi,j} = -2\rho \int Q_{i,j}\phi dV, \quad (3)$$

where

$$Q_{i,j} = \frac{1}{2}(||\boldsymbol{\Omega_i}\boldsymbol{\Omega_j}|| - ||\boldsymbol{S_i}\boldsymbol{S_j}||) = -\frac{1}{2}\boldsymbol{\nabla}\cdot(\boldsymbol{u_i}\cdot\boldsymbol{\nabla}\boldsymbol{u_j}). \quad (4)$$

With the above formulation, we can compute the forces generated by inter-modal and intra-modal interactions. We can further obtain the aeroacoustic noise associated with each of these modal interaction via the Ffowcs Williams-Hawkings model as follows:

$$p'_{Qi,j} = \frac{\boldsymbol{r}}{4\pi r^2}\left[\left(\frac{1}{c}\frac{\partial}{\partial t} + \frac{1}{r}\right)\cdot \boldsymbol{F_{Qi,j}}\right]_{(t-\frac{r}{c})}. \quad (5)$$

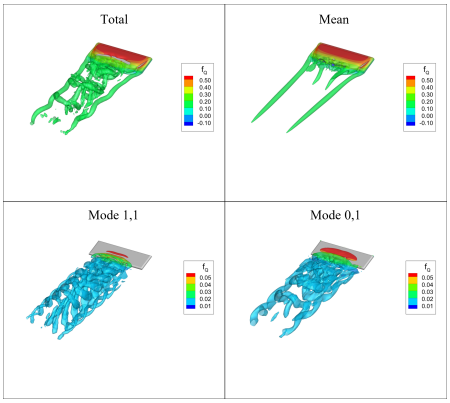

Figure 1: Isosurface of vortices for flat plate (shown using Q), colored by lift.

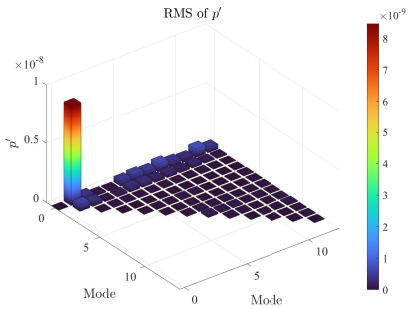

Figure 2: RMS of sound pressure for modal interactions of flat plate 50C away in negative lift direction.

The above methodology is first applied to the POD of data from DNS of flow past a stationary flat plate with aspect-ratio=3, an angle-of-attack of 15 deg, and a Reynolds number of 1000. The resulting vortical structures and their interaction are shown for mean and mode-1 in Figure 1. We see that the effect of tip vortices is captured by the mean mode and wake shedding is captured by the first mode. The RMS value of sound pressure corresponding to different modal interactions computed using equation 5 for the flat plate is shown in Figure 2. The mean mode produces most of the lift but does not contribute to noise as it does not vary with time. The interaction of the mean and first mode captures almost all the amplitude for fluctuation of vortex induced force and hence this mode alone can predict most of the loading noise.

We have also applied the method to a rotating wing. The rotor was simulated in a rotating reference frame at Reynolds number (based on tip speed and chord) of 3300. The vortical structure for the mean and the first POD mode and their interaction is shown in Figure 3. For this case, even though we need O(10) modes to predict lift force, we see that the interaction of these modes with just the mean mode can predict most of the noise. The cumulative sound pressure level for this case is calculated 50C away in the negative lift direction and is shown in Figure 4.

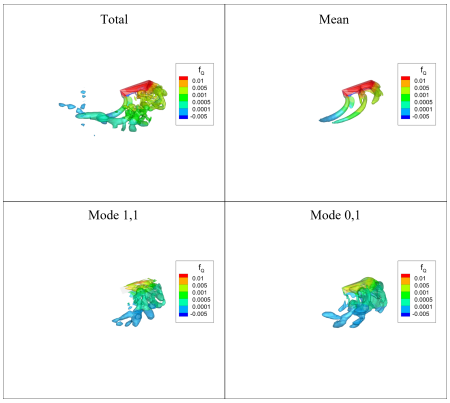

Figure 3: Isosurface of vortices for drone rotor (shown using Q), colored by lift.

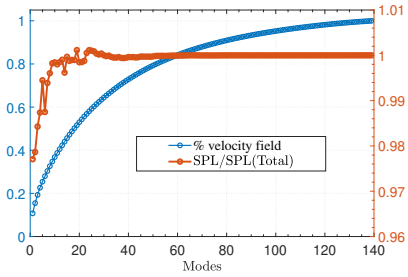

Figure 4: Flow field reconstruction using velocity vs acoustic partitioning method (Eq. 5) to predict noise (shown using sound pressure level) for drone rotor blade.

3 Conclusion

We have described the modal force partitioning method (mFPM) which enables us to compute the pressure forces associated with modes that result from the application of modal decomposition techniques to flow-field data. The method is extended to compute the far-field noise associated with these modes and applied to the POD modal decomposition of two flows – flow past a finite wing and flow associated with a rotating wing. This method shows that while a large number of POD modes are required for an accurate representation of the flow field, the aeroacoustic sound is associated with very few modes.

References

[1] Candeloro, P. and Ragni, D. Small-Scale Rotor Aeroacoustics for Drone Propulsion: A Review of Noise Sources and Control Strategies. *Fluids*, 7(8):279, 2022.

[2] Kotapati, R., Mittal, R., and Cattafesta III, L. Numerical study of a transitional synthetic jet in quiescent external flow. *JFM*, 581:287-321, 2007.

[3] Menon, K., and Mittal, R On the initiation and sustenance of flow-induced vibration of cylinders: Insights from force partitioning. *JFM*, 907:A37, 2021.

[4] Seo, J.H. , Menon, K., and Mittal, R. A method for partitioning the sources of aerodynamic loading noise in vortex dominated flows. *Phys. Fluids*, 34(5):053607, 2022.

Optimal waveform for fast synchronization of periodic airfoil wakes

Vedasri Godavarthi[a*], Yoji Kawamura[b] and Kunihiko Taira[a]
[a]Department of Mechanical and Aerospace Engineering, University of California, Los Angeles, USA[1]
[b] Center for Mathematical Science and Advanced Technology,
Japan Agency for Marine-Earth Science and Technology, Japan
[*]Correspondence: *vedasrig@g.ucla.edu*

1 Introduction

Unsteady periodic fluid flows are common in both nature and engineering, being observed over flapping wings, bluff bodies, and airfoils. In such applications, flow control is challenging owing to their periodically-varying base states [1]. For this purpose, it is important to characterize the perturbation dynamics and synchronization properties about the time-periodic base state which can be achieved using a phase reduction technique. The insights from synchronization support the design of a phase-dynamics-based optimal control to modify the shedding behavior [2]. This so-called vortex lock-in phenomenon has been studied using a sinusoidal waveform. However, an optimal waveform could be determined to maximize the speed of synchronization (entrainment speed) which is paramount for efficient flow control.

In this work, we provide a theoretical framework to obtain the optimal waveform for fast entrainment for laminar flow over airfoils at post-stall angles of attack. We then compare the entrainment speed obtained using the theoretical optimal waveform with a sinusoidal waveform by numerically actuating the flow. These results show tremendous potential for efficient unsteady wake control.

2 Phase description and entrainment of airfoil wakes

The periodic flows over NACA0012 airfoil at various angles of attack and at a chord-based Reynolds number of 100 are obtained using immersed boundary projection method. The phase reduction approach reduces this high-dimensional unsteady flowfield to perturbation dynamics about the time-periodic base states in terms of a single scalar phase variable. The phase for this system is defined based on the lift coefficient C_L and its time derivative $\dot{C}_L$. (see figure 1(a)), where each θ describes the corresponding flow state. The phase dynamics is given by $\dot{\theta} = \omega_n$, where ω_n is the natural frequency of the system. The phase dynamics when the flowfield is actuated with external periodic forcing $\mathbf{f}(\boldsymbol{x},t)$ with forcing frequency ω_f can be obtained as

$$\dot{\theta}(t) = \omega_n + \varepsilon \int \mathbf{Z}(\boldsymbol{x},\theta)\cdot\mathbf{f}(\boldsymbol{x},\omega_f t)d\boldsymbol{x}, \qquad (1)$$

where $\mathbf{Z}(\boldsymbol{x},\theta)$ is the phase sensitivity field that quantifies the phase response to any given forcing. The spatial phase sensitivity field for airfoil wakes with respect to the velocity perturbations (see figure 1(b)) is obtained using an adjoint-based approach [3]. The speed of synchronization to external pointwise forcing $\mathbf{f}(\boldsymbol{x}_0,\omega_f t)$, where $\boldsymbol{x}_0$ is the location of the force can be maximized by posing it as an optimization problem [4]. The optimal waveform for maximizing the speed of entrainment can be theoretically obtained as,

$$\mathbf{f}_{opt}(\boldsymbol{x}_0,\theta) = \frac{\mathbf{Z}'(\boldsymbol{x}_0,\theta)}{2\lambda} - \frac{\Delta\omega\mathbf{Z}(\boldsymbol{x}_0,\theta)}{\langle\mathbf{Z}^2\rangle}, \qquad (2)$$

where $\Delta\omega = \omega_n - \omega_f$, $\langle\cdot\rangle$ denotes a phase averaged variable and λ is a constant. Hence, the optimal waveform for fast entrainment could be identified theoretically from the phase sensitivity fields (see figure 1(c)).

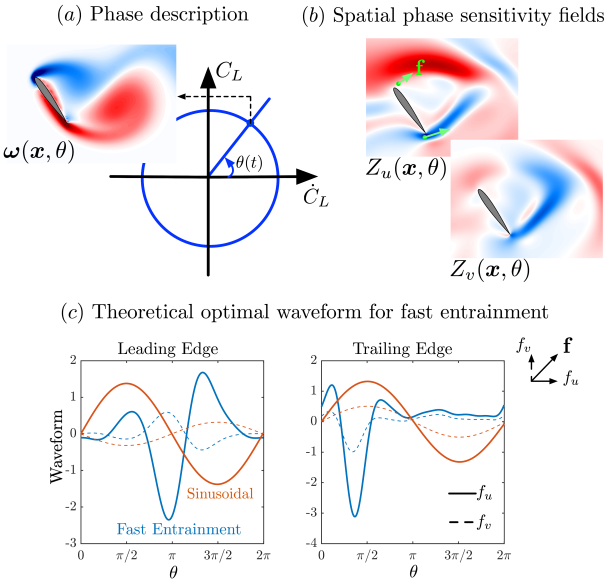

Figure 1: Overview of phase synchronization analysis of flow over NACA0012 airfoil at $\alpha = 55°$. (a) Phase description based on $C_L - \dot{C}_L$ plane. (b) Spatial phase sensitivity fields with velocity perturbation. (c) Theoretical optimal waveform for fast entrainment (in blue) and sinusoidal waveform (in red) for pointwise forcing at leading and trailing edges.

[1]This work is supported by the US Air Force Office of Scientific Research (FA9550-21-1-0178) and the US National Science Foundation (2129639).

3 Synchronization characteristics of airfoil wakes

We investigate the effect of the angle of attack on the entrainment properties of NACA0012 airfoil wakes, as shown in figure 2. The spatial distribution of entrainment speed around the airfoil for $\alpha = 35°, 45°, 55°$, as depicted in figure 2(a)-(c), suggests the increased difficulty in modification of wake shedding frequency as the angle of attack increases. Further, the theoretical optimal waveform for fast entrainment using pointwise forcing at the leading and trailing edges (highlighted using black dots) for $\alpha = 35°, 45°, 55°$ are shown in figure 2(d). We observe that as the angle of attack increases, the optimal waveform becomes increasingly non-sinusoidal. This non-sinusoidal behaviour could be attributed to the asymmetry in the shedding process at leading and trailing edges observed at higher angles of attack. The theoretical entrainment speed increases by 2.5 times when actuated with the optimal waveform in comparison with sinusoidal forcing for $\alpha = 55°$. The numerical verification of these results is then performed by introducing pointwise external forcing at the leading and trailing edges of NACA0012 airfoil at $\alpha = 55°$ in the direct numerical simulation using optimal and sinusoidal waveforms as shown in figure 1(c). The entrainment characteristics are observed for various forcing frequencies, $\omega_f = 0.9\omega_f, 0.95\omega_f, 1.05\omega_f$ and $\varepsilon = 0.3$. The entrainment, measured by the convergence of k^{th} oscillation period to forcing frequency, $\Delta\theta_k$, occurs significantly faster for the optimal waveform actuation (within as low as 2 shedding cycles (see figure 3(a))). The modification in wake dynamics is shown using the instantaneous vorticity fields, when actuated with optimal waveform with $\omega_f = 0.9\omega_n, 1.05\omega_n$ in comparison to the baseline case show longer streamwise elongated vortical structures at lower frequencies and more localized structures with an increased roll-up at higher frequencies, thereby modifying the time period of vortex shedding cycle, as shown in figure 3(b).

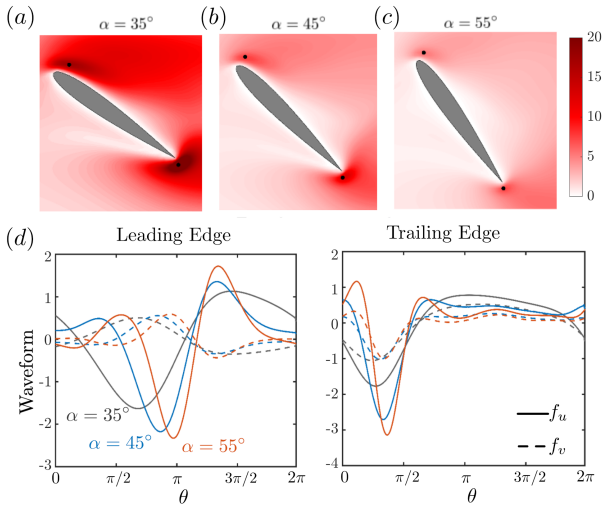

Figure 2: (a)-(c) Entrainment speed around NACA0012 airfoil at $\alpha = 35°, 45°, 55°$. The black dots indicate the locations of local maxima. (d) Theoretical optimal waveform for fast entrainment for pointwise forcing.

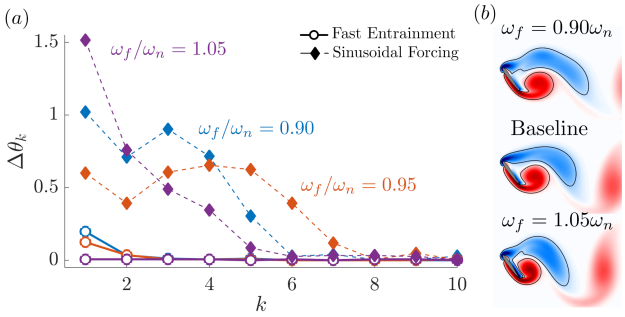

Figure 3: Numerical results for fast entrainment of NACA0012 airfoil at $\alpha = 55°$. (a) Convergence of difference between oscillation frequency for each cycle to the forcing frequency using sinusoidal and optimal waveforms. (b) Instantaneous entrained vorticity fields for $\omega_f = 0.9\omega_n, \omega_f = 1.05\omega_n$ and baseline flowfield.

4 Conclusions

We discussed the framework to theoretically obtain the actuation waveform for optimizing the speed of synchronization of post-stall airfoil wakes to external forcing frequency. For this purpose, we leveraged the phase reduction approach to obtain the sensitivity fields to external perturbations. The optimal waveform for fast entrainment is then theoretically obtained from the phase sensitivity fields. We investigated the influence of the angle of attack and observed that a higher actuation is needed to achieve entrainment at a high angle of attack and the corresponding optimal actuation waveform is non-sinusoidal. These results are verified using direct numerical simulations and we observed a significant improvement in the entrainment speed when actuated using optimal waveform in comparison with sinusoidal forcing. The wake shedding could be efficiently modified by modifying the timing of leading and trailing edge vortex shedding, which we will discuss in the presentation.

References

[1] Tim Colonius and David R Williams. Control of vortex shedding on two-and three-dimensional aerofoils. *Philos. Trans. Royal Soc.*, 369(1940):1525, 2011.

[2] Aditya G Nair, Kunihiko Taira, Bingni W Brunton, and Steven L Brunton. Phase-based control of periodic flows. *J. Fluid Mech.*, 927:A30, 2021.

[3] Yoji Kawamura, Vedasri Godavarthi, and Kunihiko Taira. Adjoint-based phase reduction analysis of incompressible periodic flows. *Phys. Rev. Fluids*, 7:104401, 2022.

[4] Anatoly Zlotnik, Yifei Chen, István Z Kiss, Hisa-Aki Tanaka, and Jr-Shin Li. Optimal waveform for fast entrainment of weakly forced nonlinear oscillators. *Phys. Rev. Lett.*, 111(2):024102, 2013.

Side-by-side swimming: A building block for studying higher-complexity fish schools

P. Ormonde* and K. Moored
Lehigh University, Mech. Eng. Dept., Bethlehem, PA, USA[1]
*Correspondence: *pco218@lehigh.edu*

1 Introduction

The hydrodynamics of schools of swimming animals are not fully understood. Studies have shown that schooling fish can experience performance benefits by swimming in a group when compared to swimming in isolation [1–8]. In addition, the spatial arrangement and synchronization of the undulatory motion of one individual relative to another are key to determine the stability of schooling arrangements [8–11].

In a recent study [8] it was demonstrated that self-organization of two unconstrained swimmers can arise spontaneously, leading to a stable side-by-side schooling formation. The results show that a side-by-side schooling formation emerges from hydrodynamic interactions alone, without any changes made to the kinematics of the two swimmers. The swimmers were modeled as wings of aspect ratio 3, NACA0012 profile and prescribed sinusoidal pitching motion around the leading edge.

The present work is designed to explore the hydrodynamics of schools of slightly higher complexity in water channel experiments. We take the stable side-by-side schooling arrangement (proved to exist by Kurt et al. [8]) as a starting point, and increase the complexity of the system in two distinct ways:

In one experiment we substitute the NACA0012 wings for two fish-like robots (Tunabots) based on the shape of real fish (yellowfin tuna and Atlantic mackerel). The objective is to understand how the stability and performance of the side-by-side schooling arrangement is affected by a more realistic representation of the two swimmers.

In a second experiment we use NACA0012 wings of $AR = 3$ to explore a school of three swimmers. Two upstream wings positioned in a side-by-side stable configuration are the *leaders* and the third wing (the *follower*) is placed downstream of the leaders. The objective here is to understand how a third swimmer placed downstream of a stable side-by-side school interacts with the oncoming wake.

2 Methods

In the first experimental investigation we study a minimal school of two swimmers. Instead of using NACA0012 wings of $AR = 3$ (as done by Kurt et al. [8]) we represent the swimmers by two fish-like robots similar a yellow-fin tuna, with a body, tail and caudal fin. The tail of the robotic fish pitches with a prescribed sinusoidal motion of known frequency and amplitude. Figure 1 shows two Tunabots in the waterchannel. Please see [12] for the Tunabot features.

Figure 1: Schematic of positions of the follower hydrofoil relative to the leader. Blue dots represent the position of the follower's leading edge placed downstream of the two leaders.

The second experiment uses three wings of aspect ratio $AR = 3$ and NACA0012 profile. The chord-based Reynolds number $Re_c \approx 10,000$. Two wings are positioned side-by-side forming a stable, side-by-side schooling arrangement. These two wings are named as the *leaders*, and remain at the same position for the entire experimental campaign. The third wing, named as the *follower*, is placed at different locations downstream of the two *leaders*. Figure 2 shows a representation of the different spatial arrangements for the three-swimmer school. Each blue dot represents a different location for the leading edge of the follower. The follower kinematics is in-phase with leader 1 and out-of-phase with leader 2.

The thrust (C_T), lift (C_L), power (C_P) and efficiency (η) of each wing is measured using a 6-axis force and torque sensor. The quantities are defined below.

$$C_T = \frac{\overline{T}_{\text{net}}}{\frac{1}{2}\rho U^2 cs}, \quad C_L = \frac{\overline{L}}{\frac{1}{2}\rho U^2 cs}, \quad C_P = \frac{\overline{P}}{\frac{1}{2}\rho U^3 cs}, \quad \eta = \frac{C_T}{C_P}, \tag{1}$$

[1]This work was supported by funding_agency under grant number ...

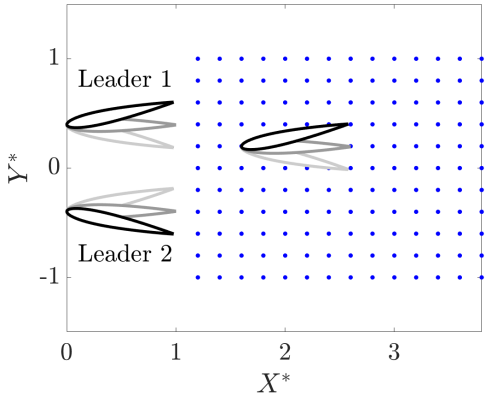

Figure 2: Schematic of positions of the follower hydrofoil relative to the leader. Blue dots represent the position of the follower's leading edge placed downstream of the two leaders.

3 Preliminary Findings and Expected Results

Figure 3 shows preliminary results from the 3-swimmers schooling experiment. The normalized efficiency η^* of the follower is plotted as a function of its position (X^*, Y^*). Results show that the efficiency of the follower is substantially affected by the presence of the leaders. At some locations there is an increase of almost 100% whereas other in other locations the efficiency decreases more than 90%. We also found that the follower can obtain high thrust improvements depending on where it is located.

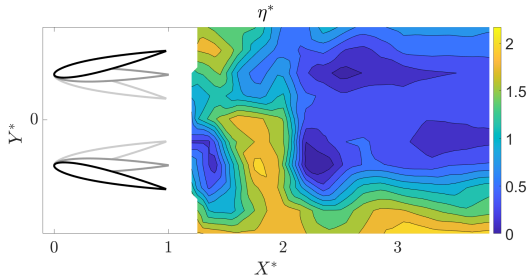

Figure 3: Efficiency of the follower normalized by an isolated swimmer. Efficiency improvements of over 100% can be achieved behind the leaders.

As for the experiments with two Tunabots, we expect to see a change in the lateral equilibrium distance between the two swimmers when compared to the pitching wings due to the presence of the fish body upstream of the propulsive caudal fin.

References

[1] Brian L Partridge. The structure and function of fish schools. *Scientific american*, 246(6):114–123, 1982.

[2] Ichiro Aoki. A simulation study on the schooling mechanism in fish. *Bulletin of the Japanese Society of Scientific Fisheries*, 48(8):1081–1088, 1982.

[3] Siddhartha Verma, Guido Novati, and Petros Koumoutsakos. Efficient collective swimming by harnessing vortices through deep reinforcement learning. *Proceedings of the National Academy of Sciences*, 115(23):5849–5854, 2018.

[4] Sophie Ramananarivo, Fang Fang, Anand Oza, Jun Zhang, and Leif Ristroph. Flow interactions lead to orderly formations of flapping wings in forward flight. *Physical Review Fluids*, 1(7):071201, 2016.

[5] Longzhen Dai, Guowei He, Xiang Zhang, and Xing Zhang. Stable formations of self-propelled fish-like swimmers induced by hydrodynamic interactions. *Journal of The Royal Society Interface*, 15(147):20180490, 2018.

[6] Joel W Newbolt, Jun Zhang, and Leif Ristroph. Flow interactions between uncoordinated flapping swimmers give rise to group cohesion. *Proceedings of the National Academy of Sciences*, 116(7):2419–2424, 2019.

[7] Ze-Rui Peng, Haibo Huang, and Xi-Yun Lu. Collective locomotion of two closely spaced self-propelled flapping plates. *Journal of Fluid Mechanics*, 849:1068–1095, 2018.

[8] Melike Kurt, Pedro Ormonde, Amin Mivehchi, and Keith Moored. Two-dimensionally stable self-organization arises in simple schooling swimmers through hydrodynamic interactions. *arXiV preprint arXiV:2102.03571*, 0(0):1–11, 2021.

[9] Intesaaf Ashraf, Hanaé Bradshaw, Thanh-Tung Ha, José Halloy, Ramiro Godoy-Diana, and Benjamin Thiria. Simple phalanx pattern leads to energy saving in cohesive fish schooling. *Proceedings of the National Academy of Sciences*, 114(36):9599–9604, 2017.

[10] Melike Kurt and Keith W Moored. Flow interactions of two-and three-dimensional networked bio-inspired control elements in an in-line arrangement. *Bioinspiration & biomimetics*, 13(4):045002, 2018.

[11] Liang Li, Máté Nagy, Jacob M Graving, Joseph Bak-Coleman, Guangming Xie, and Iain D Couzin. Vortex phase matching as a strategy for schooling in robots and in fish. *Nature communications*, 11(1):1–9, 2020.

[12] Joseph Zhu, Carl White, Dylan K Wainwright, Valentina Di Santo, George V Lauder, and Hilary Bart-Smith. Tuna robotics: A high-frequency experimental platform exploring the performance space of swimming fishes. *Science Robotics*, 4(34):eaax4615, 2019.

Solidity and Length Scale Effects on Porous Disk Wind Turbine Wake Characteristics

J. W. Kurelek[a,*], A. Piqué[a], and M. Hultmark[a]
[a] Princeton University, Department of Mechanical and Aerospace Engineering, Princeton NJ 08540, USA[1]
[*]Correspondence: *john.kurelek@princeton.edu*

1 Introduction

A common approach used to simplify the numerical modelling of a horizontal axis wind turbine (HAWT) is the actuator disk concept [1], where a turbine's rotor is replaced with a stationary drag source. Popular due in part to its simplicity, the method has been well validated through its experimental analogue, the porous disk. When using an actuator or porous disk model, the goal is to match the self-similar, far-wake velocity profile of a given HAWT, which is most often accomplished by matching the disk's thrust coefficient to the turbine at a given Reynolds number. This approach yields relatively few design constraints, and has lead investigators to develop a wide variety of different porous disk designs [2] (*e.g.*, metal mesh, perforated plate, and 'hub-and-spoke' designs), all of which can be well-matched to a turbine through careful, iterative tuning. However, this is time consuming and can be infeasible if turbine wake characteristics are not known *a priori*. In this investigation, a new design for porous disks that does not require iterative tuning is tested, where a disk is matched to a HAWT based on two new criteria (radial solidity distribution and length scale), in addition to matching the thrust coefficient. Notably, the inclusion of these two new criteria significantly improves porous disk performance in the far-wake, however, these model are not capable of accurately re-creating the all important turbine tip vortices in the near-wake region.

2 Experimental Setup

Experiments were conducted in the High Reynolds Number Test Facility (HRTF) at Princeton University, where high Reynolds numbers are achieved at relatively low flow velocities ($<$ 10 m/s) by using air pressurized up to 238 bar as the working fluid. The facility has a 4.88 m long, 49 cm diameter test section, within which a 20 cm diameter (D, radius R) turbine or porous disk model can be installed along with a measurement and control stack that enables direct thrust force measurements and control over the turbine's rotational speed. The flow conditions for study were $Re_D = 4 \times 10^6$ at free-stream turbulent intensity of 1.2%. Wake measurements were performed via hot-wire anemometry using a nano-scale probe (NSTAP, sensing element size $60 \times 2 \times 0.1$ µm) and a Dantec StreamLine Pro system. Sampling was performed at 200 kHz with 2^{21} samples collected per measurement location. Probe positioning was controlled by a 3-axis traverse mounted inside the test section. Calibration was performed *in situ* against a pitot-static tube. A cylindrical coordinate system (radius r, azimuth θ, and streamwise x) is used throughout, with the origin located at the turbine hub.

[1]This work was supported by the Natural Sciences and Engineering Research Council of Canada and the National Science Foundation under Grant No. CBET 1652583 (Program Manager Ron Joslin)

3 Results

Three porous disk designs are considered for modelling the wake of a three-bladed turbine rotor, all shown in fig. 1a. The disks include one with a uniform solidity distribution (UD), and two with non-uniform distributions (ND1 and

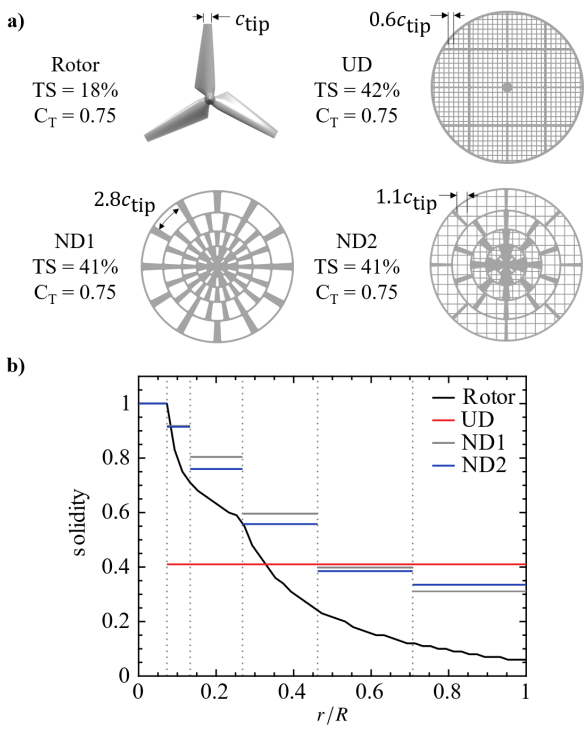

Figure 1: a) Rotor and porous disks, and **b)** their radial solidity distributions. Total solidity (TS) is calculated as the projected model solid area over rotor swept area. C_T and c_{tip} are thrust coefficient and rotor tip chord length, respectively.

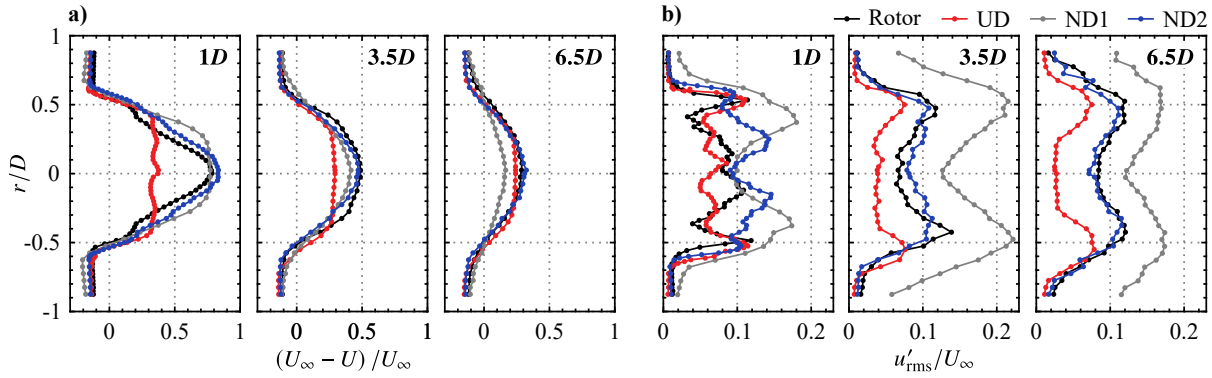

Figure 2: Wake profiles of **a)** mean streamwise velocity deficit and **b)** root-mean-square of streamwise velocity fluctuations. Top-right labels indicate streamwise position.

ND2). ND2 incorporates all three design criteria, while ND1 and UD intentionally lack specific features (length scale and solidity distribution matching, respectively) in order to isolate the effect of each feature on wake characteristics. Key disk and rotor parameters are summarized in fig. 1a. All disks feature a total solidity (TS) of 41–42%, needed in order to matched the thrust coefficient, C_T, of the rotor at $Re_D = 4 \times 10^6$ and a tip-speed ratio of 7. The radial solidity distributions of the rotor and disks are plotted in fig. 1b. Disks ND1 and ND2 feature non-uniform distributions, designed to mimic the radial profile of the rotor. The disks are designed in six annular segments (marked by the grey dotted lines in fig. 1b), where within each segment the disk solidity is set to the average rotor solidity plus a positive offset. The offsets are required to increased the total solidity of the disks to 41%. ND1 and ND2 differ in their predominant length scale, as ND2 has a layer of mesh added to match its length scale to the rotor's tip chord length, c_{tip}.

Figures 2a and b present the wake development of the turbine and disks in terms of the mean streamwise velocity deficit, $(U_\infty - U)/U_\infty$, and the profiles of the root-mean-square of streamwise velocity fluctuations, u'_{rms}, respectively. Comparing the disk wakes to the rotor in fig. 2a, the uniform porous disk (UD) creates a strong 'top hat'-like mean velocity profile at $x/D = 1$, with a centerline magnitude that is significantly less than that of the rotor. This effect can be attributed to the disk's uniform solidity distribution (fig. 1b), yielding a model that performs relatively poorly. By comparison, the ND1 and ND2 wakes are much better matched to the rotor profile at this location. Moving downstream, the ND2 wake in particular remains well-matched to the rotor profile at both $x/D = 3.5$ and 6.5, while the ND1 wakes over-recovers toward the free-stream velocity which is evident by the $x/D = 6.5$ mark.

The faster recovery of the ND1 wake is due to the turbulence generated within its wake, which is examined in fig. 2b. Comparing the rotor and ND1 cases, the expected peaks in the near-wake at $r/D = \pm 0.5$ are seen in the rotor profile and correspond to the tip vortices. The ND1 profile shows a double peak structure (peaks at $r/D = \pm 0.6$ and ± 0.4 at $x/D = 1$), which likely correspond to an annular shear layer shed from the disk edge and large coherent structures shed from the large openings near the disk edge, respectively. These two peaks eventually collapse into one further downstream, however, their magnitude is significantly higher than the rotor case, and so the faster wake recovery of ND1 is driven by large, energetic structures shed from the relatively large openings of ND1 that dominate the wake and its recovery process. In contrast, the added layer of mesh to ND2 reduces the size of the openings at the disk edge to the order of the rotor's tip chord length, presumably resulting in reduced integral length scales introduced into the flow. These effects are seen through the comparison of ND1 and ND2 in fig. 2b, where at $x/D = 1$ the inner peak of ND1 at $r/D = \pm 0.4$ is shifted further inward and reduced in magnitude signficantly by the mesh layer of ND2, indicating that the inner wake of ND2 consists of smaller, less energetic structures. Overall, the ND2 results better approximate the rotor's profile of turbulent fluctuations in the near-wake, with the agreement improving downstream, as the turbulence from the disk shear layer and inner wake diffuse to form a profile that is well-matched to the rotor at $x/D = 3.5$ and 6.

4 Conclusion

By incorporating new radial solidity distribution and length scale criteria, alongside existing thrust coefficient matching, a new porous disk design (ND2) was developed and tested, showing significantly improved performance over designs that do not utilize these new criteria. Further results to be presented at DisCoVor 2023 will include a look at Reynolds number effects on porous disk performance ($0.5 \times 10^6 \leq Re_D \leq 8 \times 10^6$), in addition to exploring the inability of porous disk models to accurately re-create the rotor tip vortices in the near-wake region.

References

[1] B. Sanderse, S. Pijl and B. Koren Review of computational fluid dynamics for wind turbines. *Wind Energy*, 14:799–819, 2011.

[2] S. Aubrun *et al.* Round-robin tests of porous disc models. *J. Phys. Conf. Ser.*, 1256, 2019.

Sound radiation from a wing hovering near a wall

Xueyu Ji[a], Bruce Jin[a], Qiuxiang[a], Li Wang[a], Sridhar Ravi[a], and Fang-Bao Tian[a*]
[a] School of Engineering and Information Technology, UNSW Canberra, ACT 2612, Australia
[*]Correspondence: *f.tian@adfa.edu.au*.

1 Introduction

The aerodynamic noise of flapping wings has been studied extensively during last few years, but very few studies have considered its control strategies [1, 2]. For stationary foils, some of the control strategies include trailing edge serrations (see e.g., [3,4]), leading edge serrations (see e.g., [5,6]) and flexible structures (see e.g., [7]). The flexibility effects have been considered for the flapping wings by Wang and Tian [8]. Previous studies on the sound of flapping wings have been confined to the free space, and the interference caused by non-compact obstacle in the path of wave propagation has not been considered. In practice, the sound generated by flapping wings could be reflected by obstacles (e.g. a wall), yielding a different radiation pattern compared with the free-space case [9].This work studies the effects of an infinite rigid wall on the noise generated by a flapping wing.

2 Numerical method

A rectangular wing with an AR of 1.5 undergoes both flapping and pitching motions (see Fig. 1) according to

$$\alpha(t) = \frac{\pi}{5}\sin(2\pi f_o t + \frac{\pi}{2}), \beta(t) = \frac{\pi}{6}\sin(2\pi f_o t), \qquad (1)$$

where α is the flapping angle, β is the pitching angle, and f_o is the flapping frequency. In the simulation, $f^* = f_o c/U_{ref} = 0.25$, $Re = U_{ref}c/\nu = 10^3$ and $M = U_{ref}/c_o = 0.04$, where $U_{ref} = 2\pi/5 f_o(1.5c + 0.1c) \approx 4cf_o$ is the mean tip velocity. An infinite rigid wall is considered by being located with a distance of $5c$-$195c$ away from the wing.

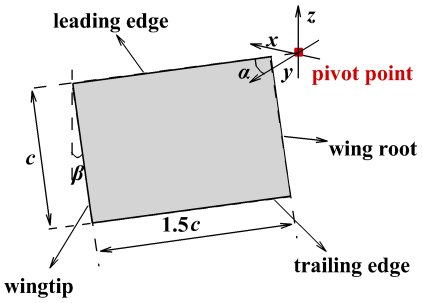

Figure 1: Schematic of the flapping wing.

The study is conducted by combining an immersed boundary method (IBM) for fluid solver and an acoustic analogy for acoustics. The fluid solver employs a feed-back diffusion interface IBM based on the three-dimensional incompressible Navier-Stokes equations in curvilinear coordinate [1, 10]. As shown in Fig. 2, the sound pressure at an arbitrary observer with the presence of an infinite rigid wall is decomposed into the sound pressure p'_{di} directly propagate from the noise source y and the sound pressure p'_{rl} reflected by the infinite wall, e.g.,

$$\begin{aligned} p'(x,\omega) &= p'_{di}(x,\omega) + p'_{rl}(x,\omega) \\ &\approx \frac{e^{ik|r|}r_i}{4\pi|r|^2 c_o}\dot{f}_{p_i}(y,\omega) + \frac{e^{ik|\widetilde{r}|}\widetilde{r}_i}{4\pi|\widetilde{r}|^2 c_o}\widetilde{\dot{f}_{p_i}}(\widetilde{y},\omega), \end{aligned} \qquad (2)$$

$$\Delta\phi = |\widetilde{r} - r|k, \quad \dot{f}_{p_i} = \oint \dot{p} n_i dA, \qquad (3)$$

where $\widetilde{y}$ is the location of the mirror source, $\widetilde{r} = x - \widetilde{y}$ and $\widetilde{r}_i$ is the i-th component of $\widetilde{r}$.

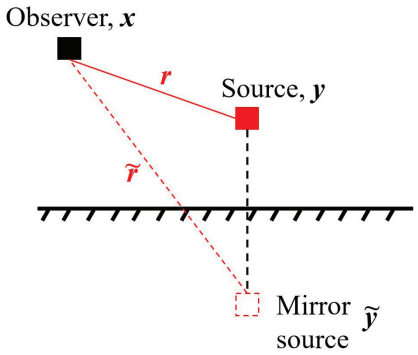

Figure 2: Schematic of sound propagation for a hovering flapping wing with the presence of an infinite rigid wall.

3 Results

Two infinite rigid walls located at $x = -100c$ (case I) and $z = -100c$ (case II) are chosen to investigate its effects on the acoustics. Here the flapping wing (sound source) for case I and II is set to move along the x-axis and z-axis, respectively. To evaluate the contributions from p'_{di} and p'_{fl}, two observers are chosen for each case [$(0, 100c, 0)$ & $(0, 0, 100c)$ for case I, and $(0, 100c, 0)$ & $(100c, 0, 0)$ for case II).

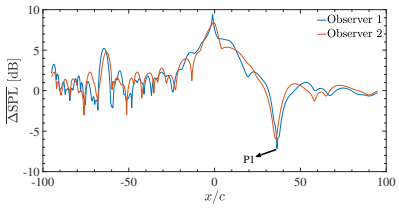

(a)

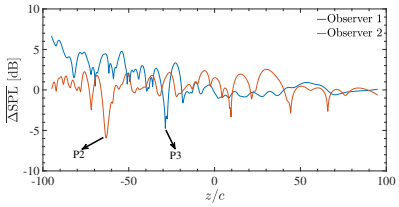

(b)

Figure 3: Average sound pressure level difference for: (a) case I and (b) case II, at observer 1 and 2.

For case I, $\overline{\Delta \mathrm{SPL}}$ over x from $-95c$ to $95c$ is shown in Fig. 3a. At $x < 0$, the magnitude of $\overline{\Delta \mathrm{SPL}}$ is not significant while $\overline{\Delta \mathrm{SPL}}$ achieve its maximum and minimum value near $x = 0$ and $x = 36.4c$, respectively, for observer 1. The minimum value of $\overline{\Delta \mathrm{SPL}}$ (-7.1 dB) occurs at $x = 36.4c$ (denoted as P1). For case II, a noticeable variation of $\overline{\Delta \mathrm{SPL}}$ around 5 dB occurs at P3 ($z = -28.7c$ (Fig. 3b) for observer 1. $\overline{\Delta \mathrm{SPL}}$ of case II is close to zero with some insignificant fluctuation at $z > 0$. For observer 2, the minimum $\overline{\Delta \mathrm{SPL}}$ of 5.93 dB occurring at $z = -63.2c$, denoted as P2.

A destructive interference between the direct propagation and reflection for the first harmonic f_o and other higher harmonics is observed, and can be analyzed by,

$$\begin{aligned} \Delta\phi(f_o) &= \frac{2\pi f_o \Delta r}{c_o} = \Phi + 2k_o\pi, \\ k_o &= 0,\ \pm 1,\ \pm 2, ..., \pm N,\ \Phi \in [-\pi, \pi], \quad (4) \\ \Delta\phi(jf_o) &= \frac{2\pi f_o \Delta r}{c_o} + \frac{2\pi f_o (j-1)\Delta r}{c_o} \\ &= \Delta\phi(f_o) + \Delta\phi(f_o)(j-1),\ j \geq 2, \quad (5) \end{aligned}$$

where $\Delta r = |\widetilde{r} - r|$, and k_o is an integer. Therefore, the phase angle at the higher harmonics $\Delta\phi(jf_o)$ is the summation of the phase angle of the first harmonic $\Delta\phi(f_o)$ and $\Delta\phi(f_o)(j-1)$. For P1, Φ of f_o is close to $-\pi$. To achieve the destructive interference for the higher harmonics, $\Delta\phi(f_o)(j-1)$ should be the multiples of 2π, which can only occur if j is an odd number. Meanwhile, the constructive interference is expected if j is an even number. Overall, the infinite wall can reduce the noise associated with the odd harmonics if the out of phase between p'_{di} and p'_{rl} occurs at the first harmonic.

It is noted that the sound pressure is dependent on the time derivative of forces on the wing [2, 11], which is dominated by the time derivative of the surface pressure. The time derivative of the surface pressure is affected by the time derivative of the Q-criterion and Coriolis acceleration. The vortex convection of the leading edge vortex at around a chord from the wing root leads to the intense variation of the vorticity and Q-criterion, which results in the high time derivative of the surface pressure and is further verified in a non-inertial reference frame.

4 Conclusion

The effects of a wall on the sound property from a rectangular flapping wing are studied by a hybrid method coupling an incompressible flow solver and a simplified acoustic model. It is found that the presence of a wall in the x and z directions can reduce the sound pressure level for a given observer by more than 7 dB via the destructive interference. Moreover, the sound pressure from the wing and that reflected by the wall are out of phase at the odd harmonics if they are out of phase at the first harmonic, which is further verified by the theoretical analysis.

Acknowledgement

This work was partially supported by Australian Research Council Discovery Project (project number DP200101500) and conducted with the assistance of resources from the NCI, which is supported by the Australian Government.

References

[1] X. Ji, L. Wang, S. Ravi, F.-B. Tian, J. Young, and J. C. S. Lai. Influences of serrated trailing edge on the aerodynamic and aeroacoustic performance of a flapping wing during hovering flight. *Physics of Fluids*, 34(1):011902, 2022.

[2] J.-H. Seo, T. L. Hedrick, and R. Mittal. Mechanism and scaling of wing tone generation in mosquitoes. *Bioinspiration & Biomimetics*, 15:016008, 2019.

[3] M. S. Howe. Aerodynamic noise of a serrated trailing edge. *Journal of Fluids and Structures*, 5:33–45, 1991.

[4] A. S. H. Lau and X. Huang. The control of aerodynamic sound due to boundary layer pressure gust scattering by trailing edge serrations. *Journal of Sound and Vibration*, 432:133–154, 2018.

[5] X. Huang. Theoretical model of acoustic scattering from a flat plate with serrations. *Journal of Fluid Mechanics*, 819:228–257, 2017.

[6] J. Rong and H. Liu. Aeroacoustic interaction between owl-inspired trailing-edge fringes and leading-edge serrations. *Physics of Fluids*, 34:011907, 2022.

[7] M. Nardini, R. D. Sandberg, and S. C. Schlanderer. Computational study of the effect of structural compliance on the noise radiated from an elastic trailing-edge. *Journal of Sound and Vibration*, 485:115533, 2020.

[8] L. Wang and F.-B. Tian. Numerical study of sound generation by three-dimensional flexible flapping wings during hovering flight. *Journal of Fluids and Structures*, 99:103165, 2020.

[9] A. Powell. Aerodynamic noise and the plane boundary. *Journal of the Acoustical Society of America*, 32:982–990, 1960.

[10] T. J. Chung. *Computational Fluid Dynamics*. Cambridge University Press, 2002.

[11] F.-B. Tian. Hydrodynamic effects of mucus on swimming performance of an undulatory foil by using the DSD/SST method. *Computational Mechanics*, 65:751–761, 2020.

Starting vortex formation by a surging airfoil

Anushka Goyal[a] and Jovan Nedić[b*]
[a] McGill University, Department of Mechanical Engineering, Montréal, Canada
[b] McGill University, Department of Mechanical Engineering, Montréal, Canada
[*]Correspondence: *jovan.nedic@mcgill.ca*

1 Introduction

It is well established that an airfoil impulsively set into linear motion will result in the formation of a clockwise vortex, also known as the starting vortex, and an unsteady mixing layer, as shown in Figure 1. The circulation generated over the wing increases over time and eventually settles to its steady state value, which is characteristic of a dynamic response to a system. This dynamic response was first solved analytically by Wagner, who modelled the system as a line of vortex centers shed from the trailing edge of an impulsively accelerated wing, with the last vortex center being the starting vortex [1]. As the wing surges through some distance (called the surge distance), the circulation over it increases. Using Kelvin's circulation theorem, the circulation in the rest of the flow field (excluding the wing) would also increase. This allows us to postulate that the circulation within the starting vortex and the mixing layer would be equal to Wagner's prediction. As the surge distance increases, the bound circulation over the wing increases and so does that in the flow field, which consists of the shear layer and starting vortex. From studies on vortex rings, we know that vortex size and strength are limited [2]. Vortex rings generated by pushing a column of fluid with a piston through an orifice had an upper limit on growth and circulation for piston stroke to orifice diameter ratios (L/D) of 4. This critical ratio was termed the formation number. In subsequent studies, it has been shown that the formation number is not universal and depends on the geometry generating the vortex ring [3,4]. The objective of this study is to investigate if the principle of the formation number can be applied to an isolated vortex and the value it will assume. Further, we would like to characterise the starting vortex by measuring its circulation and size and link these to the initial conditions of the surging airfoil, namely, the angle of attack, (α), surge speed (U) and surge distance (Δx).

2 Experimental Setup and Limits of Initial Conditions

The experiment is designed for a 30 inches long, 12.5 inches wide and 19 inches deep water tank. The vortex generating airfoil has a NACA0010 profile with a span of 26 inches and chord length 3 inches. It is attached with end plates to suppress the formation of end vortices. The angle of attack of the plate can be altered from 1° to 10° in 1° increments. The velocity field is obtained by using time resolved planar particle image velocimetry.

Since the primary objective of the apparatus is to create and characterise an isolated vortex, it is important to define the limiting values of the initial conditions. Large angles of attack (above 8°) result in a strong leading edge vortex and flow separation. As a result, in this study, the angles of attack are below 8°. For a given angle of attack, surge speeds below a critical surge speed ($U_{critical}$) result in secondary vortices. This critical speed depends on the angle of attack- an increase in the angle of attack decreases the critical speed. In vortex ring formation studies, it was found that additional circulation (beyond a critical L/D of four) was 'rejected' by the vortex ring and resulted in the formation of Kelvin-Helmholtz type instabilities. In the present study, we hypothesise that increasing the surge speed at a fixed angle of attack would result in additional circulation and the secondary vortices observed at surge speeds greater than $U_{critical}$ may be attributed to this.

When an airfoil is impulsively started from rest, a starting vortex is formed. Consequently, when the airfoil is impulsively stopped, an equal strength counter rotating stopping vortex is formed. Since the objective of this study to characterise roll up, a large enough surge distance ensures minimal influence of the stopping vortex on the starting vortex roll up. As a result, surge distances of 0.5c and 1c were chosen for this study. Ideally, the surge distance would be beyond a critical formation time for a single vortex. Since this is not known at present, the upper limit on the surge distance is chosen based on wall effects (which would occur at $\Delta x >$1c). The lower limit is chosen arbitrarily.

3 Circulation of the Starting Vortex

The net circulation in the field was found to be equal to Wagner's prediciton. However, the starting vortex only entrained half of the net circulation, as shown in Figure 3. At an angle of attack of 6°, $U_{critical}$ was found to be close to 0.6c/s. At surge speeds beyond $U_{critical}$, the formation of secondary vortices was observed. However, the circulation of the primary vortex for these cases was also approximately half of Wagners prediction. Similar results were observed for α=8°.

It is hypothesized that the circulation of the starting vortex is always half of the net circulation in the flow field because it

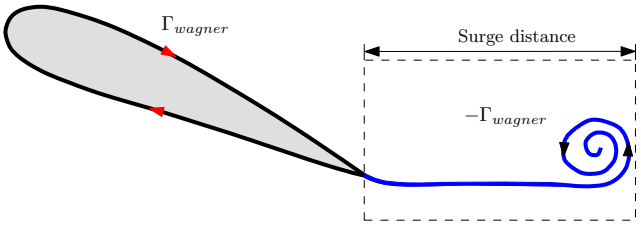

Figure 1: Net circulation for an impulsively started airfoil

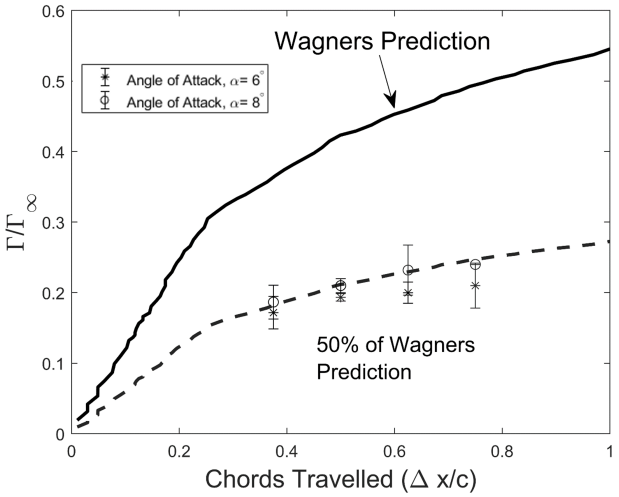

Figure 2

Figure 3: Circulation of the starting vortex as compared to Wagner's function

attains an 'optimal' size and strength. Thus, the next step of this study is to investigate if the formation number concept can be applied to the starting vortex.

4 Conclusion

Based on preliminary results, it can be asserted that the circulation of a starting vortex in an impulsively started airfoil is 50% of Wagners function. The aim of future experiments is to characterise the vortex size and link it to the initial conditions of surge speed, angle of attack and surge distance. Finally, it is hypothesized that there may be a critical strength and size, beyond which the starting vortex does not entrain any additional circulation. The future goal of this study is to investigate this critical parameter.

References

[1] Wagner, Herbert Über die Entstehung des dynamischen Auftriebes von Tragflügeln *ZAMM - Journal of Applied Mathematics and Mechanics*, 5 (1), 17–35, 1925.

[2] Gharib, Morteza and Rambod, Edmond and Shariff, Karim A universal time scale for vortex ring formation *Journal of Fluid Mechanics*, 360, 121-140, 1998.

[3] Limbourg, R., and Nedić An extension to the universal time scale for vortex ring formation *Journal of Fluid Mechanics*, 915, p. A46, 2021

[4] Dabiri, John O Optimal Vortex Formation as a Unifying Principle in Biological Propulsion *Annual Review of Fluid Mechanics*, 360, 17-33, 2009.

Strouhal and Membrane Elasticity Effects on Bat Flight

Marin Lauber[a*], Gabriel D. Weymouth[b,a] and Georges Limbert[a,c]
[a] University of Southampton, Faculty of Engineering and Physical Sciences, Southampton, UK[1]
[b] Delft Univesrity of Technology, Ship Hydromechanics, Delft, The Nederlands
[c] University of Cape Town, Faculty of Health Science, Cape Town, South Africa
[*]Correspondence: *M.Lauber@soton.ac.uk*

1 Introduction

Bats are the only mammal on the planet able to perform powered flight and feature characteristic membrane wings that give them astonishing agility [1]. There have been several studies measuring the kinematics of bats in forward flight such as those shown in Figure 1 from [2]. The flapping amplitude A during a cycle is linearly dependent on flight speed U [3] across numerous bats, and wingbeat frequency f stays relatively constant across flight speeds, regardless of body size and bat families [1,3]. This means that bats operate at a fairly constant Strouhal number $St = fA/U$. Using this data we find bats operate from $St = 0.5-0.7$ (not shown), but this is significantly higher than the $St = 0.2-0.4$ optimal range associated with insect and bird flight.

Additionally, the effect of membrane elasticity on the flight characteristics of bats is not clearly understood. It is suspected that the non-linear membrane allows bats to use elasticity to induce camber while limiting the maximum deformation [4]. The fibrous structure of the membrane is also believed to improve the folding of the wing and limit flutter [4] but such studies cannot directly investigate the impact of changing membrane properties on bat flight.

In this paper, we use high-resolution fluid-structure interaction simulations to investigate the influence of St and elasticity on bat flight. We use our immersed boundary fluid-structure interaction solver [5] to perform fully-coupled simulations of a simplified geometrical bat wing. The model consist of the handwing part of the wing and uses parametric kinematics over various Strouhal and membrane Cauchy numbers

$$Ca = \frac{Et_m}{12(1-\nu^2)\rho_f U_{ref}^2 L},$$

where we choose to use the maximum wing velocity during the cycle U_{ref} instead of the forward speed U to ensure the membrane stiffness is scaled consistently as St is varied. We use a simple linear isotropic material model for the membranes and bones in the wing. The kinematics are derived from a simplified model that considers five degrees of freedom movements around the *carpus*. The resulting kinematics are shown in Figure 1. To mimic the folding and feathering of the wing during the upstroke, the pitch profile is optimized for each Strouhal number using an apparent angle of attack approach, where we minimize the mean apparent angle of attack during the upstroke and target a specific value in the downstroke.

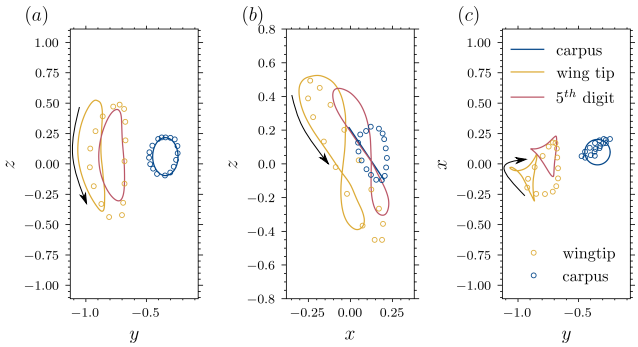

Figure 1: Comparison of simplified kinematics for 3 points on the wing (lines) and experimental measurements (dots) from [2].

2 Results

Figure 2 shows the flow around the wing for three Strouhal numbers for an elastic wing with $Ca = 0.5$. The flow is represented by isosurfaces of vorticity magnitude ($\|\boldsymbol{\omega}\|$). We observe significantly different wake behaviours for the different Strouhal numbers. At a low Strouhal number ($St = 0.3$), strong vorticity is generated near the tip of the wing, and a shear layer covers most of the upper surface of the wing. A medium Strouhal number ($St = 0.5$) results in a coherent wake, with packs of vorticity being shed from the trailing edge of the wing. A shear layer is also observed on the upper surface of the wing, similar to the lower Strouhal number wing. For a high Strouhal number ($St = 0.7$), the wake becomes severely chaotic, large packs of vorticity are shed from the shear layer of the wing.

Results, in terms of the standard thrust, lift, and power coefficients, for the whole Strouhal range and two Cauchy numbers are presented in Figure 3. Our method of optimizing the pitching kinematics has ensured that the cycle-averaged thrust is positive over the whole Strouhal number range and for both Cauchy numbers (Figure 3a). Both membrane elasticities produce similar thrust at low Strouhal numbers,

[1]This work was supported by the UKRI under grant number EP/L015382/1

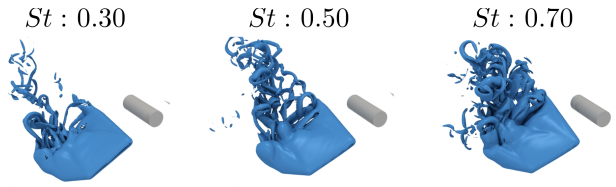

Figure 2: Isosurface of vorticity magnitude during the downstroke for three Strouhal numbers. Bat's body is shown for visualization purposes.

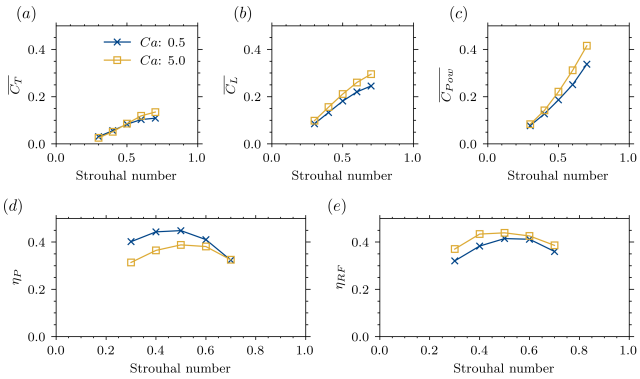

Figure 3: Cycle-averaged force coefficients and efficiencies at various Strouhal numbers.

while the stiffer membrane produces more thrust at the high $St = 0.7$. Cycle-average lift and power coefficients constantly increase with increased stiffness, Figure 3b-c.

To quantify the aerodynamic efficiency of the wing, we use the propulsive and *Rankine-Froude* efficiency [6]

$$\eta_{\mathrm{P}} = \frac{\overline{F_x} U_\infty}{\overline{P}} = \frac{\overline{C_T}}{\overline{C_{\mathrm{Pow}}}}, \qquad \eta_{\mathrm{RF}} = \frac{\overline{C_L}^{3/2}}{\overline{C_{\mathrm{Pow}}}}.$$

The standard propulsive efficiency is studied for swimmers and flyers alike, but flyers also need to maintain weight support. This is not included in the propulsive efficiency; the Rankine-Froude efficiency provides this measure. The resulting propulsive and Rankine-Froude efficiencies are presented in Figure 3d-e. Propulsive efficiency is improved for elastic wings over stiffer ones for the whole Strouhal range, and they are almost equal for $St = 0.7$. On the other hand, Rankine-Froude efficiency is larger for the stiffer wing over the whole Strouhal range. A clear peak in both efficiencies for both Cauchy numbers occurs near $St \sim 0.5$. This peak in efficiency occurs at the Strouhal number where the wake generated by the wing is most coherent, see Figure 2f, whereas

The effects of varying Cauchy numbers for fixed kinematics at the optimum (from the results above) Strouhal number of $St = 0.5$ are shown in Figure 4, on a logarithmic scale. While lift and power steadily increase with the Cauchy number, thrust remains relatively constant. This results in a peak in propulsive efficiency near $Ca \sim 0.1$, whereas Rankine-Froude efficiency steadily increases with the Cauchy number. This is to be expected since we have seen previously

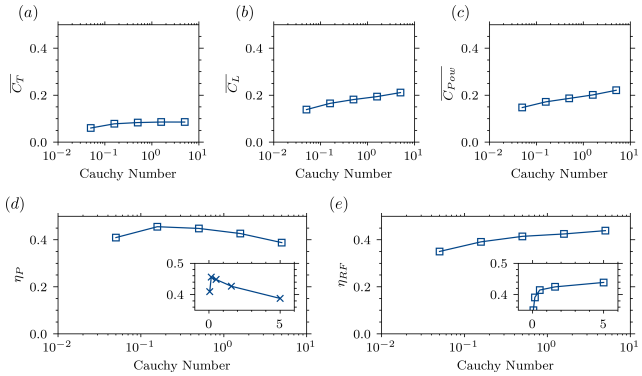

Figure 4: Cycle-averaged force coefficients and efficiencies at various Cauchy numbers.

that power and lift increase with Cauchy number. There is a sharp drop in efficiencies for very low Cauchy numbers; with the help of modal analysis techniques (not shown here), we relate this drop in efficiencies to the fluttering of the wing's membrane. Finally, we will show that by reinforcing our (linear) isotropic membrane with two (non-linear) fibre families, forming an orthogonal net on the wing, that the flutter can be reduced, even for (initially) equally elastic membranes.

3 Conclusion

We perform coupled numerical simulation of bat flight using a simplified geometrical and a parametric kinematical model to show that, although bats operate at significantly higher Strouhal numbers than insects or birds, this corresponds to a peak both in propulsive and Rankine-Froude efficiency. We are able to relate these peaks in efficiencies to specific structures in the wake of the bat. We then show that membrane elasticity plays a less important role in the aerodynamic efficiency of bats, although flutter can severely penalise it when it occurs. Finally, we demonstrate that by reinforcing isotropic membranes with anisotropic non-linear fibres, we are able to passively control flutter and recover the aerodynamic performances of stiffer wings.

References

[1] S. M. Swartz and N. Konow. Advances in the study of bat flight: The wing and the wind. *Canadian Journal of Zoology*, 93:977-990, 2015.

[2] M. Wolf and L. C. Johansson and R. Von Busse and Y. Winter and A. Hedenström. Kinematics of flight and the relationship to the vortex wake of a Pallas' long tongued bat (Glossophaga soricina). *The Journal of Experimental Biology*, 213:2142-2153, 2010.

[3] R. D. Bullen and N. L. McKenzie. Scaling bat wingbeat frequency and amplitude. *Journal of Experimental Biology*, 205:2615–2626, 2002.

[4] J. A. Cheney and N. Konow and A. Bearnot and S. M. Swartz. A wrinkle in flight: The role of elastin fibres in the mechanical behaviour of bat wing membranes. *Journal of the Royal Society Interface*, 12, 2015.

[5] M. Lauber and G. D. Weymouth and G. Limbert. Immersed-Boundary Fluid-Structure Interaction of Shells and Membranes. *XII International Conference on Structural Dynamics*, 2023.

[6] T. Engels and H. N. Wehmann and F. O. Lehmann. Three-dimensional wing structure attenuates aerodynamic efficiency in flapping fly wings. *Journal of the Royal Society Interface*, 17(164), 2020.

Unsteady propulsion: Application to windsurfing

G. Bertrand[a], M. Fermigier[a], B. Thiria[a] and R. Godoy-Diana[a]
[a] PMMH, CNRS, ESPCI Paris-PSL, Sorbonne Université, Université Paris-Cité, Paris, France

1 Introduction

The competitive practice of sailing and windsurfing is evolving. It may be assigned to the willingness to break the records increasing the performances of the sailing boats. Thus, the development of new platforms using hydrofoils (Figure 1), capable of providing lift, is replacing the use of the so-called "classic" windsurf that relies only on buoyancy. Among these innovations are the new "iQFoil" class of windsurf which will be used in the next Olympic Games.

The interest of using a foil, and the passage from an Archimedean boat to a dynamically supported boat, is to obtain a considerable increase of speed during sail races. But at the same time, the air resistance becomes the main source of drag in relation to the wave drag or hydrodynamic drag against the board. Other parameters, besides the latter, must be taken into account to better understand the contributions of a foil. In this respect, an unsteady maneuver called "pumping" is essential [1].

For windsurfers, pumping consists in a periodic pitching of the sail with a certain kinematics and seems to be an efficient contribution to the propulsive force under certain wind conditions. It is used a lot in the beginning of the race to accelerate and after tack changes to stabilize the boat in flight mode. Understanding the details of the functioning of boats is complex like on a sailing yacht [2] and requires some measurements even more so difficult to do during navigation in a windsurf boat because of its size.

It is a complex mechanical structure with deformation associating the mast, the sail and the battens that stiffen it, but also geometrically complex by the camber and the helical torsion of the sail. It has a fairly clear analogy with insect wings [3]. Here we investigate a simplified model of a pumping sail in a wind-wall open aerodynamic tunnel.

2 Results

A 1:10-scale model of sail (or rig) is set up (length: $0.2m$, height: $0.5m$) in a wind wall tunnel (Figure 2), with a velocity between $2m/s$ and $8m/s$.

Figure 1: Chronophotography from top-left to bottom-right of a windsurfer during one oscillation period of a pumping phase.

The first studies of pumping are done in pitching with a rigid airfoil and on a reconstructed shape of a windsurf sail varying different parameters: The velocity of the flow, the frequency of pitching, the range of the flapping and the average angle of incidence.

Figure 2: Wind-wall tunnel.

A multiple axis load sensor allow us to investigate the propulsion and the drag forces.
A preliminary study of an elastic sail is done to examine the role of some geometrical parameters: the camber and the twist angle of the sail (Figure 3).

Figure 3: Left: Some battens with different cambers,
Right: Top view of the elastic sail on the wind-wall tunnel.

3 Conclusion

I will present my first results toward the characterisation and optimisation of the unsteady propulsion of an elastic sail. Ongoing work is dedicated analysing the deformation of the sail during pitching with 3D shape reconstruction by stereo photographic recording. Full-scale experiments in the sea will be compared to our result with a 1:10-scale model of sail.

References

[1] Aubin N., Augier B., Sacher M., Bot P., Hauville F., Flay R. Wind tunnel investigation of dynamic trimming on upwind sail aerodynamics. *Journal of Sailing Technology*, 2010-2011.

[2] Deparday J. Experimental studies of Fluid-Structure Interaction on Downwind sails. *PhD thesis*, Université de Bretagne Occidentale/IRENav, 2016.

[3] R. J. Wootton, R. C. Herbert, P. G. Young and K. E. Evans. Approaches to the structural modelling of insect wings. *Phil. Trans. R. Soc. Lond. B: Biological Sciences*, 358 (1437) 1577-1587, 2003.

Vortex induced vibration of a seal whisker-like cylinder at different angles of attack

Biao Geng, Xudong Zheng and Qian Xue*
Rochester Institute of Technology, Department of Mechanical Engineering, Rochester, USA[1]
*Correspondence: *qxxeme@rit.edu*

1 Introduction

Habor seal whiskers (HSWs) are excellent hydrodynamic sensors that enable the seals to prey in turbid underwater conditions. The shape of HSWs is roughly a slender cylinder featuring an elliptical cross-section and undulation along the shaft. The undulation of the major and minor axis of the elliptical cross section has a 180° phase difference (Figure 1b). The specialized shape of HSWs has been shown to suppress hydrodynamic force oscillation and vortex induced vibration (VIV) by breaking the coherence of the Kármán vortices when its long cross section axis is oriented streamwise. This essentially reduces the self-induced noise in the sensory system for the seals during forward swimming. In the mean time, HSWs are sensitive to wakes left behind by other swimming objects, which incide upon the whiskers at various angle of attacks (AoAs). In addition, seals have an array of whiskers attached next to either nostril. The orientation of each whisker can also be actively controlled. However, knowledge on how seals actively orient their arrays of whiskers during preying is very limited. Therefore, it is important to understand the hydrodynamic characteristics of the HSW shape at different AoAs.

Kim and Yoon [1] used large eddy simulation to study the effect of AoA on flow characteristis around a static HSW for the Reynolds number of 500. They showed that for small AoAs ($< 15°$) the lift force oscillation of the HSW was almost negligible. When AoA increased beyond 15°, the amplitude of the lift force oscillation increased, reached a plateau of about 0.2 (RMS[2]) at 50°, and then remained almost constant up to 90°. The authors concluded that as AOA increases, the bluffbody flow overcomes the flow induced by the HSW shape, resulting in almost the same flow as the elliptic cylinder. Murphy et al. [2] tested VIV responses of real seal whiskers oriented at 0°, 45°, and 90° against an incoming flow of 0.5 m/s. Vibration velocity was up to 60 times higher when AoA was 90° compared to 0°. Song et al. [3] experimentally studied the single degree of freedom (DOF) VIV response of a scaled up harbor seal whisker model with AoA ranging from 0° to 90°. The density ratio of the model was about 10. The HSW model started to show significant VIV when AoA reached 30° and reached a peak amplitute as high as 3 diameters when AoA was 90°.

Despite previous research, many aspects of the VIV of HSWs remained to to be explored. This study aims to quantify the single DOF VIV response of seal-whisker-like cylinders with density ratio close to that of real seal whiskers under low Reynolds number. This is an effort toward providing normative data for seal-whisker inspired sensor designs.

2 Method

The flow field is solved using an inhouse, immersed-boundary-method based flow solver. The vibration of the whisker is solved using the average acceleration Newark scheme. The flow and solid vibration is implicitly coupled. For brevity, the formulations are not listed here. The implementation of this solver setup has been validated in Ref [4] for canonical flow-structure interaction (FSI) problems with solid/fluid density ratios of 1 and 10.

The simulation setup is shown in Figure 1. Only one segment of an idealized whisker is included, which allows the use of periodic boundary conidtions at the top and bottom of the domain. The domain is discretized using Cartesian grid with high resolution ($\sim 0.025\bar{D}$) around the whisker body. The whisker is set as a single DOF rigid body with spring K and damper C. Variation of the reduced velocity U_r (see definition in Table 1) is implemented by changing the stiffness of the spring. By default, U_r is varied from 2 to 15. For AoAs where the VIV remains significant in the default range, larger U_r (up to 50) is tested. The AoA is varied from 0° to 90° at 15° increment. Simulation setup parameters are summarized in Table 1. The solution of a test case (AoA= 60° and U_r=8) shows good grid independence with the adopted grid resolution. For cases with large VIV amplitude, the grid number in the transverse direction is doubled to increase the size of the high resolution region to cover the range of VIV.

For most cases, the simulation was run long enough to have 10∼20 cycles in steady vibration. However, for some cases there seemed no sign of reaching steady vibration even after extended simulation time. These cases were not run further due to limited computational resources.

[1]This work was supported by NSF under grant number 2144217. The computation was supported by XSEDE project TG-CTS180004. This work is submitted to DISCOVOR as a poster presentation.

[2]Root Mean Square

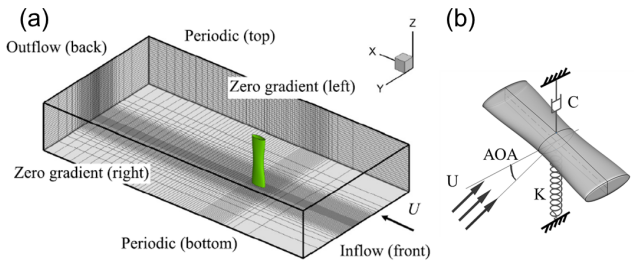

Figure 1: Simulation setup. (a) The simulation domain (schematic). The domain size is $40\times60\times6$, nondimensionalized with respect to the mean hydraulic diameter of the whisker $\bar{D}(0.533mm)$. (b) Whisker segment with one degree of freedom in the transverse direction. Note that in simulation, the whisker geometry instead of the flow is rotated to form the angle of attack.

Table 1: Simulation setup parameters

FSI	Re	m^*	$m^*\xi$	U_r	AoA
parameter	300	1.0	0.02	$2\sim15(50)$	$0^\circ\sim90^\circ$
whisker	λ	A	a	B	b
parameter	6	0.882	0.1	0.373	0.043

Note: m^* is the mass ratio of the whisker to the displaced fluid. The mass-damping coefficient $m^*\xi$ is kept constant. U_r is reduced velocity, defined as $U_r = U/(f_n\bar{D})$, where U is the uniform flow speed and $f_n = 2\pi\sqrt{M/K}$ is the in vacuum natural frequency of the mass-spring system. λ is the wavelength of the whisker shape undulation. A and B are the mean length of the semi major and minor axis, respectively, and a and b are the corresponding undulation amplitude (all length normalized by $\bar{D}$).

3 Results

Figure 2 shows the VIV amplitude for different AoAs. The amplitude is quantified as $A^*_{rms} = \text{rms}(dy - \text{mean}(dy))$. The horizontal axis is the effective reduced velocity, U^*_r, which is defined as $U^*_r = U/(f_n D_\text{F})$, where D_F is the maximum width of the frontal projection of the whisker. Note that D_F increases with AoA for the whisker shape. Figure 3 shows the dominant VIV frequency for different AoAs. From Figure 2, the VIV amplitude increases substantially as AoA increases from 0° to 90°. At 0° AoA, the VIV amplitude is so small that the curve almost overlaps with the $y = 0$ line. When zoomed in, the curve is similar to that of typical forced system going through resonance, reaching a peak amplitude (~ 0.002) at $U^*_r \approx 5$. From Figure 3, the dominant VIV frequency for AoA$=0^\circ$ remains almost constant (~ 0.19) regardless of the reduced velocity. This shows that the VIV at 0° AoA is too small to affect the flow dynamics. At 15° AoA, the VIV amplitude remains considerably small (~ 0.02) except for the lowest tested reduced velocity where the VIV locked to the in water natural frequency (f_{nw}) of the whisker and the amplitude reached 0.05. VIV amplitude becomes significant at 30° AoA (~ 0.2) and keeps increasing with AoA. Observations of the trend include: 1. the U^*_r at which peak VIV amplitude is reached slightly increases with AoA. 2. the U^*_r at which VIV starts to occur for each AoA decreases with AoA. 3. at high AoAs, the VIV persists even for high U^*_r, which is different from cases with a mass ratio of ~ 10 [3]. And 4. the VIV is highly periodic before reaching the maximum amplitude, after which it becomes irregular.

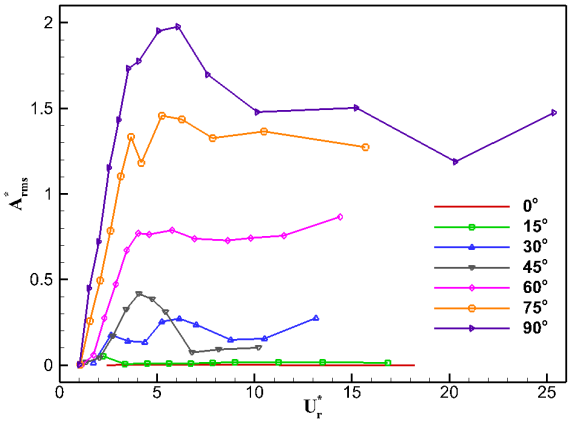

Figure 2: HSW VIV amplitude at different AoAs

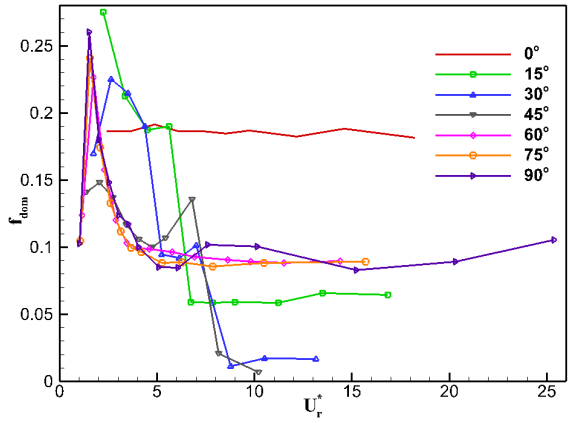

Figure 3: HSW VIV dominant frequency at different AoAs

The dominant VIV frequency at the lowest U^*_r roughly reflects the dominant vortex shedding frequency of the static cases, which can be seen to first increase (0° to 15°) and then decrease (15° to 90°) with AoA from Figure 3. Similar observation was reported previously [1]. For AoA$\geq 60^\circ$, VIV first locks to the in water natural frequency of the whisker until the peak amplitude is reached. After that, the dominant VIV frequency remains a constant that is slightly lower than the static vortex shedding frequency.

References

[1] Kim, H. J. and Yoon, H. S. Effect of the orientation of the harbor seal vibrissa based biomimetic cylinder on hydrodynamic forces and vortex induced frequency. *AIP Advances*, 7(10), 2017.

[2] Murphy, C. T., et al. Effect of Angle on Flow-Induced Vibrations of Pinniped Vibrissae. *PLoS ONE*, 8(7), 2013.

[3] Song, L., et al. Single degree-of-freedom flow-induced vibration of an elastically-supported harbor seal whisker model: an experimental study. *Lixue Xuebao*, 54(3), 653–668, 2022. (in Chinese)

[4] Liu, G., et al. An image-guided computational approach to inversely determine in vivo material properties and model flow-structure interactions of fish fins. *Journal of Computational Physics*, 392, 578–593, 2019.

Vortex interactions between tandem oscillating foil turbines and optimal system kinematics

Eric Handy-Cardenas* and Kenneth Breuer
Brown University, Center for Fluid Mechanics, School of Engineering, Providence, USA[1]
* Correspondence: *eric_handy–cardenas@brown.edu*

1 Introduction

Oscillating hydrofoil turbines can be used to extract energy from tidal and river flows. These kinds of turbines offer an alternative to the more common horizontal axis rotary turbines and it has been shown that they can achieve comparable efficiencies [1–3]. Although single foil performance has been well characterized, extending this to hydrofoil array configurations in order to extract more energy from a system is less well understood, and an area of active research [6–8]. Optimizing rotary turbine array configurations requires avoiding wake interactions in order to prevent detrimental effects on individual turbine performances. However, in the case of oscillating hydrofoil arrays arranged in a tandem configuration, interactions between the structured wake shed from the front foil and a downstream foil can lead to a constructive interference that maximizes the system efficiency [5, 8]. The operating kinematics of turbines in an array configuration (stroke amplitude, pitching angle, etc) might not be the same for as solo turbines, and the aim of the this study is to determine the optimal kinematics for one of these tandem hydrofoil arrays by using information about the structure of the wake behind the leading foil.

By correlating the effective angle of attack, $\alpha_{T/4}$, at mid downstroke of the leading foil to the performance of the foil, three wake regimes have been identified [8]. In the first regime - the shear layer regime - the wake consists of a continuous shear layer with very little vortex formation. The mid-range $\alpha_{T/4}$ wake regime is identified as the Leading Edge Vortex (LEV) regime, where a single LEV is formed and shed by the leading foil every half-cycle, and the highest and most unsteady wake regime is the Leading Edge Vortex plus Trailing Edge Vortex (LEV+TEV) regime, which is characterized by a stronger vortex pair shed every half cycle.

These three wake regimes can potentially lead to different constructive and destructive interactions between the leading foil wake and the trailing foil, and understanding how the trailing foil's kinematics must adapt in order to achieve optimal performance will give insight into what the optimal system kinematics should be. To study this, experiments were performed in a water flume at Brown University where foil kinematics were prescribed over a large range of parameters for the leading and trailing hydrofoils in a tandem configuration array. By prescribing leading foil kinematics with a desired $\alpha_{T/4}$, specific wake structures were created in each of the three wake regimes. For each wake regime, the kinematics of the trailing foil were varied over a range of pitch θ_0 and heave h_0 amplitudes, as well as the inter-foil phase ψ_{1-2} (phase shift between the motions of the two foils). The two foils shared the same frequency. Leading and trailing foil efficiencies were computed by measuring the flow-induced forces and torques on each foil and used to obtain the system efficiency. Particle Image Velocimetry (PIV) was used to measure the velocity fields of the optimal configurations in order to better understand the structure wake-foil interactions.

[1]This work was supported by NSF Grant 1921359

2 Results

System efficiency was obtained by calculating the ratio of the time-average power extracted by both foils and the power available in the flow considering the maximum foil swept area $\eta_{sys} = (\bar{P}_{\text{le}} + \bar{P}_{\text{tr}})/0.5\rho U^3 A_{s,\max}$. For all three cases of leading $\alpha_{T/4}$ the inter-foil phase, ψ_{1-2}, had the most influence on performance of the trailing foil by dictating the timing of the interactions between the shed vortices and the trailing foil. The shedding of vortex structures by the leading foil is directly dependent to its frequency of heaving and pitching, with it shedding a vortex every stroke reversal for the LEV and LEV+TEV regimes. Due to both foils having the same operating frequency, the relative position of the trailing foil with respect to the leading foil wake-structures it encounters is dependent only on ψ_{1-2}. Optimal and minimum values of efficiency were found to be around -120° and 60° respectively for all three regimes.

Having identified the parameters for optimal performance, examination of PIV velocity fields of these cases show that direct interactions between the wake structures and the trailing foil lead to a decrease in performance (Fig 1). This happens because these interactions produce lift enhancement on the trailing foil during parts of the cycle where either its heaving velocity vector is very small, or opposite to its lift force, leading to negative power extraction as shown in the blue highlighted case in figure 1. Conversely, cases where the system performs better are those where the trailing foil avoids direct interactions with the vortices, shown in the red highlighted case figure 1.

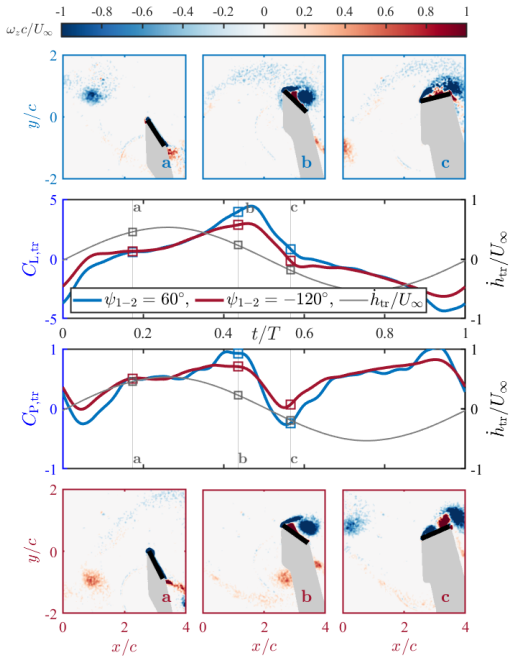

Figure 1: PIV snapshots of two different cases of wake foil interactions. The $\psi_{1-2} = 60°$ shows a destructive case and the constructive case is given by $\psi_{1-2} = -120°$. Each snapshot is referenced to a time during the cycle in the cycle-averaged Lift and Power curves.

Pitch and heave amplitudes have smaller but notable effects as compared to phase, ψ_{1-2}. Both parameters have a stronger effect on performance as the value of $\alpha_{T/4}$ increases, with optimal pitch amplitudes shifting to the highest value studied (75°), and the heave showing a more distinct optimal amplitude at $h_0 = 0.8c$. The maximal variations in system efficiency due to these two parameters is in the order of 3%, while for the phase it reaches 10%.

The heave amplitude was initially expected to have a significant effect on the performance of the trailing foil. However, as shown by [9] and confirmed in figure 2, in the LEV+TEV regime the shed vortex pair initially move outward but then, due to the opposite circulation of the LEV and TEV, they move back towards the centerline as they travel downstream. Thus, the optimal heave amplitude will change, depending on the streamwise separation of the two foils.

3 Conclusions

The system efficiency achieved by tandem foils can reach up to 57% in optimal cases, indicating that oscillating foil turbines have promising performance metrics when compared with rotary turbines. The power density for these types of turbine arrays can also be higher than for axial turbines due to the close proximity of the foils.

The parameter that most strongly influences the performance of the trailing foil is the inter-foil phase, as it determines the positioning of the trailing foil respect to the vortices in the wake.

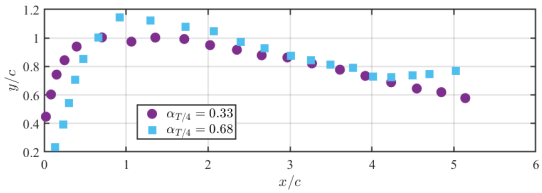

Figure 2: Trajectory of the primary vortex shed by the leading foil for two $\alpha_{T/4}$ cases. The leading foil's pitching axis is located at $x/c = 0$ and the trailing foil is at $x/c = 6$. Note the more curved trajectory that the vortex in the $\alpha_{T/4} = 0.68$ displays compared to that of the 0.33 case.

For the cases studied, direct interception of the trailing foil with vortices shed by the leading foil can lead to a drop in trailing foil performance due to lift enhancement at an undesirable part of the cycle. Optimal system performance occurs when the trailing foil avoids vortices in the wake.

High system efficiencies are achieved over a range of foil kinematics where neither foil in the system is necessarily operating at its maximal performance, but as an aggregate their contributions reach high system performances over optimal cases.

References

[1] J. Young, et al. A review of progress and challenges in flapping foil power generation. *Progress in Aerospace Sciences*, 67:2–28, (2014)

[2] McKinney and Delaurier. Wingmill: An oscillating-wing windmill. *J. Energy*, 5: 109, (1981)

[3] T. Kinsey and G. Dumas. Parametric study of an oscillating airfoil in a power-extraction regime. *AIAA J.*, 46: 1318, (2008)

[4] D. Kim et al. Energy harvesting performance and flow structure of an oscillating hydrofoil with finite span. *J. Fluids Struct.*, 70: 314, (2017)

[5] J. O. Dabiri Potential Order-of-Magnitude Enhancement of Wind Farm Power Density via Counter-Rotating Vertical-Axis Wind Turbine Arrays. *Journal of renewable and sustainable energy*, 3(4):043104–043104–12 (2011)

[6] Kinsey and G. Dumas Optimal tandem configuration for oscillating-foils hydrokinetic turbine. *J. Fluids Eng.*, 134: 031103 (2012)

[7] G. Xu and W. Xu, Energy extraction of two flapping foils with tandem configurations and vortex interactions *Eng. Anal. Bound. Elements*, 82: 202 (2017)

[8] B. Ribeiro et al, Wake-foil interactions and energy harvesting efficiency in tandem oscillating foils *Physical Review Fluids*, 6, 074703 (2021)

[9] H. Lee et al, Leading edge vortex formation and wake trajectory: Synthesizing measurements, analysis, and machine learning *Physical Review Fluids*, 7, 074704 (2022)

Vortices and mechanics around the swimmer

R. Guignabel*, A. Eon, A. Decatoire, T. Monnet, L. David and M. Samson
Pprime institute, CNRS – University of Poitiers – ENSMA, UPR 3346, Futuroscope Cedex, France[1]
*Correspondence: *raphael.guignabel01@univ-poitiers.fr*

1 Introduction

Performance in competitive swimming relies in part on the propulsive force that swimmers can generate. This force is mainly provided by arm movements [1]. Pioneering work in the evaluation of swimmer-generated forces is based on a quasi-static approach. The underlying assumption of this approach is that the kinematic parameters of the flow (in particular velocity and angle of attack) do not vary over time. However, it has now been demonstrated that the flow is unsteady [2–4]. It is therefore necessary to assess the flow from unsteady modelling. In recent years, devices and knowledge have been developed in ways that make such studies feasible. Our experimental and numerical studies carried out at the Prime Institute fall within this framework. The emphasis is on measurements of the propulsive force of the swimmers' upper limbs. Our methodology deals with flow measurements, which have been carried out with PIV methods and compared to CFD calculations. Nonetheless, experimental measurements of force and kinematics of the arm enables us to strengthen our understanding. The main unsteady mechanisms studied are the spatio-temporal analyses of vortex structures, but also the Kramer, axial flow, added mass or delayed stall effects [5]. Previous very promising studies have been carried out using a robotic arm to understand some of the propulsion mechanisms in swimming based on unsteady fluid studies [6]. We have also developed a robotic swimming arm device. This allows the kinematic parameters of the swimming motion to be varied such as the angle of attack or the velocity of the hand. A study using this device was carried out to investigate the relationship between propulsive force and swimming frequency [7]. Acceleration has been deemed important in the force generation process [3]. Which is why we would like to study its role in propulsion.

2 Methods

The robotic system described in Figure 1 is based on the swimmers' kinematics that we tend to reproduce by varying the angular acceleration of the arm $\ddot{\theta}$ in $rad.s^{-2}$. On the one hand, the aim is to produce a parametric study assessing key parameters such as arm angular accelerations and propulsive forces. On the other hand, to compare these parameters with various phenomena such as vortex development and detachment. The experimental study was carried out in a laboratory, in an open channel. The forearm and hand were molded on an elite swimmer's model and built in epoxy resin (density of 0.98 kg/L similar to the human body). The mold was attached to a motor that allowed the forearm to produce aquatic movements. The motor was attached to a frame resting on two rails with four guide rollers providing a virtually slippery connection. We used a level to align the $(\vec{X})$ axis and calibrated the system with a device comprised of weights, belt and pulley, identifying frictional forces of 2.3 N. The frame was held with a monoaxial force sensor, measuring the force generated by the reaction of water on the arm, which represents the arm's propulsive force $\vec{F}_p = F_p\vec{X}$ (Figure 1). The sensor was connected to the motor's servo-drive from where data were extracted. The results were obtained in the cartesian frame of reference related to the earth $R(\vec{X},\vec{Y},\vec{Z})$. The arm's angular acceleration $\ddot{\theta}$ varied between 1 to 15 $rad.s^{-2}$ with a step of 1 $rad.s^{-2}$. The relative flow of the flume regarding the cartesian frame of reference related to the earth was 0.3 m/s, although it should have been around 2 m/s [1], but we couldn't go higher at this stage. The experiments were coupled with PIV measurements in two planes. In the vertical laser sheet, we can follow and evaluate the behavior of the fluid around the arm in the median plane. For the horizontal plane, vortex slices can be observed at different depths of the laser sheet crossing the arm. Two Phantom v2640 cameras were used to reconstruct the image for the whole motion θ in degrees from 20 to 160.

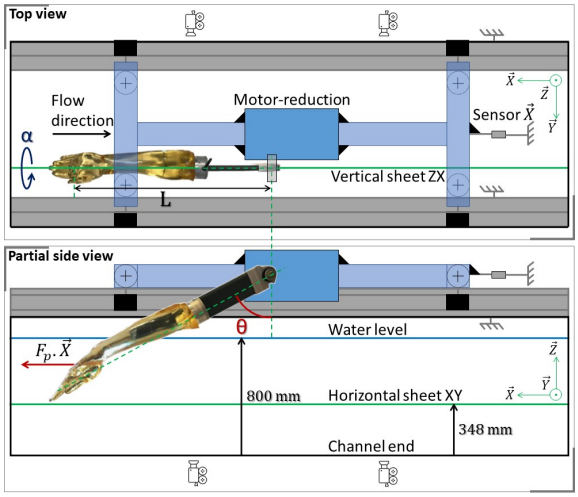

Figure 1: Schematic device of the robotic arm

[1]Authors would thank Patrick Braud, Jean-Carl Rousseau, Richard Tessier and Jessy Cantet as well as the Pprime Institute for the financial support provided (ACI project), and the French government aid managed by the National Research Agency (ANR) under the Future Investment Program (PIA) with the reference ANR-19-STHP-0001. This work pertains to the French government program "Investissements d'Avenir" (EUR INTREE, reference ANR-18-EURE-0010).

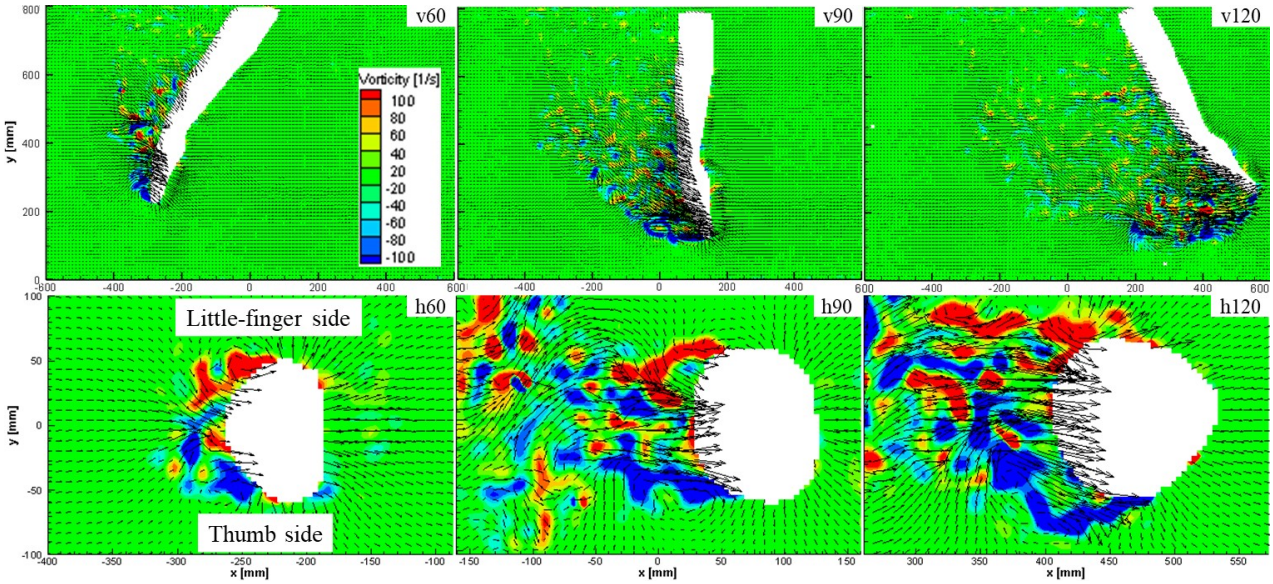

Figure 2: Experimental 2D PIV fields for $\ddot{\theta} = 10\ rad.s^{-2}$; θ = [60°,90°,120°] for the ZX and XY laser sheets

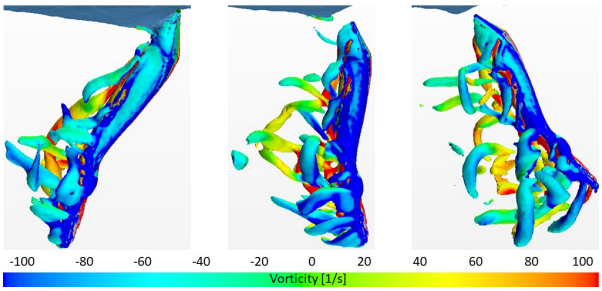

Figure 3: Spatio-temporal evolution of the vortex structures around the hand and the forearm, from the Q criterion and vorticity at different angles θ = [60°,90°,120°], for $\ddot{\theta} = 10\ rad.s^{-2}$

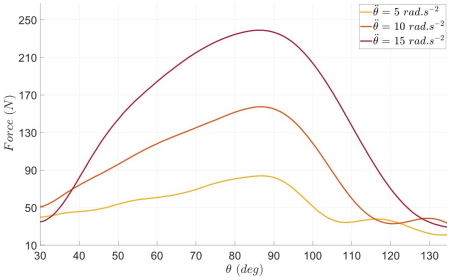

Figure 4: Evolution of the sensor's measured force according to the angular position of the arm. For three angular acceleration values

3 Results

Post-processing of the data clearly shows that the higher the angular acceleration, the greater the propulsive force (Figure 4). A peak of strength can be observed around 90 degrees which matches our former study [7]. These data are to be compared with PIV fields from both vertical and horizontal laser sheets (Figure 2). For θ = 60 degrees, we can see two vortex structures being formed on the edges of the thumb and little-finger (Figure 2). These leading-edge vortices grow and develop behind the hand and are then gradually shedded in the wake (θ = 90 deg). From θ = 90 to 120 degrees, the wake becomes increasingly turbulent. To strengthen our understanding of the flow, we performed the same tests under numerical conditions (Figure 3), using the URANS methodology [8]. This study is promising because of the unsteady model and its confrontation with the fluid's behavior. We will present the effects of the arm's angular acceleration on propulsion in front crawl swimming in unsteady condition. The evolution of the propulsive force regarding acceleration and vortex formation will be analyzed under several conditions.

References

[1] Ernest W. Maglischo. *Swimming fastest*. Human Kinetics, Champaign, IL, rev. edition edition, 2003.

[2] Huub M Toussaint, Coen Van den Berg, and Wiero J Beek. "Pumped-up propulsion" during front crawl swimming. *Medicine and science in sports and exercise*, 34(2):314–319, 2 2002.

[3] Shigetada Kudo, Ross Vennell, and Barry Wilson. The effect of unsteady flow due to acceleration on hydrodynamic forces acting on the hand in swimming. *Journal of Biomechanics*, 46(10):1697–1704, June 2013.

[4] Mathias Samson, Tony Monnet, Anthony Bernard, Patrick Lacouture, and Laurent David. Kinematic hand parameters in front crawl at different paces of swimming. *Journal of Biomechanics*, 48(14):3743–3750, 11 2015.

[5] Mathias Samson, Tony Monnet, Anthony Bernard, Patrick Lacouture, and Laurent David. Comparative study between fully tethered and free swimming at different paces of swimming in front crawl. *Sports Biomechanics*, 18(6):571–586, 11 2019.

[6] Hideki Takagi, Motomu Nakashima, Takashi Ozaki, and Kazuo Matsuuchi. Unsteady hydrodynamic forces acting on a robotic arm and its flow field: application to the crawl stroke. *Journal of Biomechanics*, 47(6):1401–1408, 4 2014.

[7] Raphaël Guignabel, Antoine Eon, Arnaud Decatoire, Achraf Outada, and Mathias Samson. Parametric study of propulsiveforces in front crawl swimming. *Computer Methods in Biomechanics and Biomedical Engineering*, 25(sup1), 8 2022.

[8] Mathias Samson, Anthony Bernard, Tony Monnet, Patrick Lacouture, and Laurent David. Unsteady computational fluid dynamics in front crawl swimming. *Computer Methods in Biomechanics and Biomedical Engineering*, 20(7), 5 2017.

Wake-Induced Vibration of Flexible Cantilevers: Application to Vortex Sensing

S. Heydari[a] and R. K. Jaiman[a]
The University of British Columbia, Department of Mechanical Engineering, Vancouver, Canada[1]
*Correspondence: *sheydari@mail.ubc.ca*

1 Introduction

Although humans do not have specialized flow-sensing abilities, many aquatic, terrestrial, and aerial animals, including seals [1], rats [2], and bats [3], possess unique flow-sensing capabilities that enable them to perform impressive behaviors such as identifying and locating prey, following trails, navigating in total darkness, and moving efficiently in turbulent flow conditions. These abilities are often achieved through the use of mechanosensory hairs, such as whiskers (Figure 1A), and hair-like structures, on different parts of the body. These mechanosensory hairs allow the animals to detect changes in flow patterns and respond quickly to potential predators, mates, or food sources. The specific placement and structure of these hairs enable directional selectivity, allowing the animal to not only detect changes in flow but also determine the location of these changes and how best to respond behaviorally.

The diverse array of biological sensors found among animals can be used to inform the design of artificial sensors for robots tasked with detecting and discriminating objects in novel environments. While many biological sensor specializations remain to be discovered, ongoing research into biological sensors continues to inspire and advance new technologies. In our current work, we utilize a high-fidelity numerical framework to examine the coupled fluid-structure dynamics of biological flow sensors relevant to the development of mechanosensing in artificial systems, such as robotics. We focus on the fluid-structure interaction (FSI) of mechanosensory hairs with upstream vortices (Figure 1B) to study the coupled mode response, also known as wake-induced vibration, of these structures. The presence of upstream vortices can significantly impact the local fluid behavior around a flexible body by altering factors such as amplitude, frequency, and phase of the vibrations. Therefore, studying the behavior of an array of flexible cylinders in various configurations is important to understand how multiple real sensory hairs create and interact with wake structures.

We take a flexible cylindrical cantilever of length L and diameter D as a representative model of mechanosensory hairs. As shown in Figure 1C, due to fluid forces acting on the cantilever, it initially deforms in the streamwise direction and, depending on the system parameters, it could exhibit an unsteady dynamic response leading to sustained large-amplitude vibrations. To examine the cantilever's vibrational behavior, we consider three non-dimensional parameters, namely mass ratio m^*, Reynolds number Re, and reduced velocity U^*, defined as

$$m^* = \frac{4m}{\pi D^2 \rho^f}, \qquad Re = \frac{\rho^f U_0 D}{\mu^f}, \qquad U^* = \frac{U_0}{f_n D}, \quad (1)$$

where m is the mass per unit length of the cantilever, ρ^f and μ^f are the density and dynamic viscosity of the fluid, respectively, U_0 is the magnitude of the flow velocity, and f_n is the first-mode natural frequency of the cantilever. Using a fully-coupled fluid-structure solver based on the three-dimensional Navier-Stokes and Euler-Bernoulli beam equations described in [4], we examine the unsteady dynamics of the flexible cantilever for $Re = 40$ and 60 for $U^* \in [5, 25]$

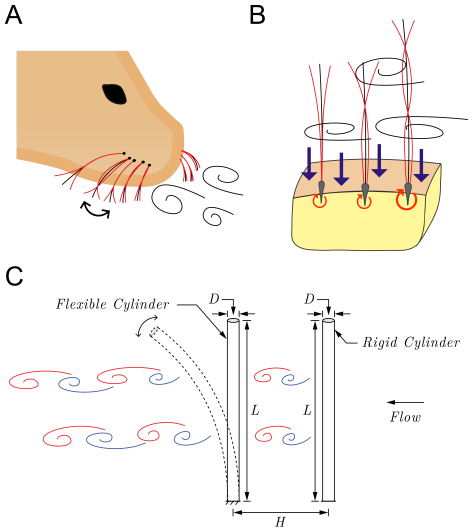

Figure 1: *(A)* Upstream vortices induce sustained vibrations in seal whiskers; *(B)* the forces and moments induced by the vortices are transmitted through the hair shaft and result in the deformation of the follicle, which is rooted underneath the skin. *(C)* Fluid-structure interaction model of the mechanosensory hairs, represented by a flexible circular cylinder, interacting with upstream vortices generated by a stationary rigid cylinder. The distance between the two cylinders is denoted by H.

[1]This work was supported by the Natural Sciences and Engineering Research Council of Canada.

at a mass ratio $m^* = 1$. Our key objective is to characterize the cantilever's oscillatory dynamics as a function of flow and structural parameters and examine how upstream wakes affect this dynamical behavior. All results have significant implications for the study of biologically-based flow sensing and engineered fluid sensors.

2 Results

For this study, the aspect ratio of the cantilever, defined as the ratio of the cantilever length L to diameter D, is set equal to $L/D = 100$. Figure 2A compares the root-mean-square (rms) value of the cantilever's transverse vibration amplitude, probed at its free end, in two different configurations. In one configuration, the cantilever is subjected to a uniform flow (i.e., isolated), while in the other configuration, the cantilever is positioned in the wake of a rigid stationary cylinder, with the same diameter D and length L, at a streamwise distance $H = 5D$ (i.e., tandem). Based on the results presented in Figure 2A, the two key observations are: (i) sustained oscillations are present at a subcritical Reynolds number $Re = 40$, where no periodic vortex shedding is expected; and (ii) the vibration amplitudes are sustained over a wider range of U^* for the tandem cylinder configuration compared to the isolated case. Figure 2B illustrates the superimposed images of the tandem cylinder's cross-flow motion at $U^* = 9$ and 25 at $Re = 60$. As it is seen, the cantilever's peak-to-peak vibration amplitude has a value of $\approx 2.5D$ at $U^* = 9$, reducing to $\approx 1D$ at $U^* = 25$. One notable finding here is that the cantilever's motion at $U^* = 9$ is primarily in its first natural vibration mode, becoming progressively complex and getting close to its second natural vibration mode at $U^* = 25$.

For all the studied cases, we find that the frequency of the cross-flow oscillation matches the frequency of the cross-flow (lift) force (Figure 2C), both being equal to the first-mode natural frequency of the cantilever for $U^* \in [6,9]$. This finding indicates that the synchronization (also called lock-in) phenomenon is the mechanism underlying the sustained oscillations. We find that the interactions between the upstream wake and the boundary layer of the downstream cylinder affect the flow features along the circumference of the cylinder (Figure 2D) and shift the position of the downstream cylinder's stagnation point, which plays a major role in the load generation mechanism [5]. Further stability analyses are underway to explain the origin and mechanism of wake-body interactions in flexible cantilevers and determine the significance of pressure and viscous forces in the composition of lift force and their phase relations with respect to structural velocity.

3 Conclusion

In this work, we examined the FSI of a flexible cantilever as a model of mechanosensory hairs. Of particular interest was exploring the vibrational characteristics of the cantilever in the presence of upstream wakes. We showed that compared

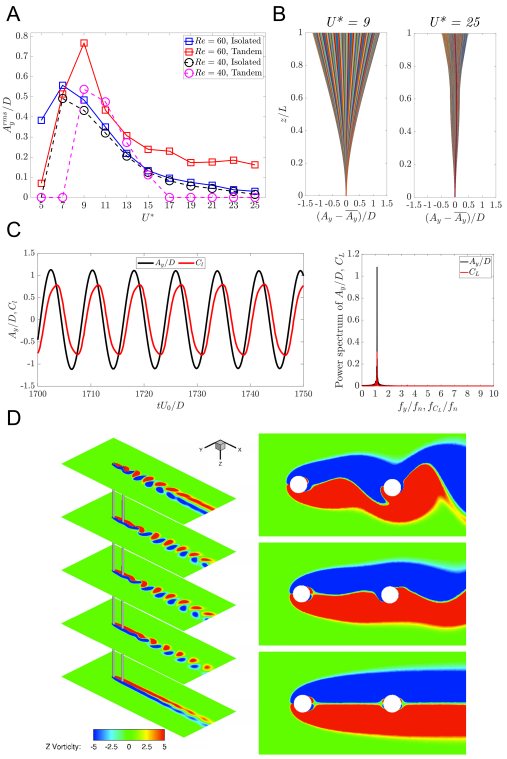

Figure 2: *(A)* Normalized values of cross-flow vibration amplitude. *(B)* Superimposed images of the cantilever's cross-flow motion in the tandem configuration at $Re = 60$. *(C)* Time history and power spectra of cross-flow vibration and lift force, denoted by C_l, at $(U^*, Re) = (9, 60)$ for the cylinder in the tandem configuration. *(D)* Isometric view of the z-vorticity contours alongside the x-y plane view of the contours at $(U^*, Re) = (9, 60)$; (top) at the free end, (middle) mid-section, and (bottom) fixed end of the cylinders.

to an isolated cylinder, the cantilevered cylinder positioned tandem to a rigid cylinder at a distance $5D$ has larger cross-flow vibration amplitudes and exhibits sustained oscillations for a broader range of U^*. These results emphasize the significance of wake-induced vibrations in providing vortex-sensing abilities to animals and have implications for the design of artificial flow sensors.

References

[1] Guido Dehnhardt, Björn Mauck, and Horst Bleckmann. Seal whiskers detect water movements. *Nature*, 394(6690):235–236, 1998.

[2] Y. S. W. Yu, N. E. Bush, and M. J. Z. Hartmann. Whisker vibrations and the activity of trigeminal primary afferents in response to airflow. *The Journal of Neuroscience*, 39(30):5881–5896, 2019.

[3] S. J. Sterbing-D'angelo, M. Chadha, K. L. Marshall, and C. F. Moss. Functional role of airflow-sensing hairs on the bat wing. *Journal of Neurophysiology*, 117(2):705–712, 2017.

[4] Shayan Heydari, Neelesh A. Patankar, Mitra J. Z. Hartmann, and Rajeev K. Jaiman. Fluid-structure interaction of a flexible cantilever cylinder at low reynolds numbers. *Phys. Rev. Fluids*, 7:024702, Feb 2022.

[5] Ravi Chaithanya Mysa, Abouzar Kaboudian, and Rajeev Kumar Jaiman. On the origin of wake-induced vibration in two tandem circular cylinders at low reynolds number. *Journal of Fluids and Structures*, 61:76–98, 2016.

Aerodynamics of bat-inspired flapping wings

Sushrut Kumar[a], Jung-Hee Seo[a] and Rajat Mittal[a,b]
[a] The Johns Hopkins University, Department of Mechanical Engineering, Baltimore, USA[1]
[b] The Johns Hopkins University, School of Medicine, Baltimore, USA
*Correspondence: *mittal@jhu.edu*

1 Introduction

Bio-inspired micro-aerial vehicles (MAVs) with flapping wings have been of great interest to the engineering community since they offer several advantages over rotary-wing MAVs. These include reduced aeroacoustic noise as well as improved power efficiency at small scales [1]. The aerodynamics involved in these systems is significantly different from those of a fixed-wing or a rotor drone. This has implications for flight stability and control, as well as the selection of materials for the wings and other control surfaces.

In developing these drones, inspiration can be drawn from the biological flapping wings of birds, flying insects, bats, etc. The wing structures and kinematics in these animals have evolved over millions of years and offer a myriad of unique design features that have not yet been considered in engineering design of MAVs. Bats are the only mammals known to employ powered flight, and several bat species are adapted to fly and navigate through very complex and tight environments. A bat's hand-wing is formed from an elastic membrane that is reinforced by relatively stiff bones. The wing flapping causes the interaction between the incoming flow and the highly flexible membrane. This fluid-structure interaction generates the aerodynamic forces that support the bat's flight.

In the past, several researchers have investigated the aerodynamics of bat's flight using both numerical [2] and experimental methods. Numerical simulations are a powerful tool that can be used to model and analyze the complex fluid-structure interaction involved in such flights. Most computational modeling efforts have relied on either wing kinematics extracted from high-speed videogrammetry [2] or performed FSI of simplified wing shapes [3]. Wing kinematics obtained from high-speed videogrammetry has mainly been restricted to exploring the aerodynamics of a single flight condition and the effects of modulating kinematics and wing material property of the elastic membrane, remain unexplored. The wing shapes and/or the kinematics also usually differ significantly from those of real bats and have left open questions regarding the effect of fluid-structure interaction (FSI) in the wing aerodynamics of bats. Thus, this work attempts to model, with a high level of fidelity, the complex fluid-structure interaction of the membrane wing of a bat in flight using the bone joint kinematics and material properties obtained from the experiments. The data generated is then subjected to examine the aerodynamic performance of these wings. The finite-element method is the most common method for modeling structural deformation in fluid-structure interaction simulations. However, the large deformations inherent in these problems require a complex computational infrastructure and significantly increase the computational cost of these simulations. In the current effort, we choose a spring-network model for the structural deformation of the membrane. These methods were initially proposed for rapid simulations of cloth deformation in computer animations but have been successfully used to perform complex FSI simulations of heart valves, membranes parachutes, etc. A significant advantage of this method is the relatively low computational cost and easy coupling with the fluid solver, especially with the sharp interface immersed boundary method (IBM) used in this work.

2 Results

The numerical simulations were performed using our in-house IBM code, ViCar3D [4], and the spring network model-based structural solver. The work was carried out in two phases. The first phase used a hovering flight model with simple kinematics and a membrane wing with three different flexibilities. The flexibilities were quantified using the Aeroelastic number, Ae and were chosen based on the aeroelastic characterization performed by Gehrke et al. [5]. In the second phase, simulations were performed using a model derived from experimental data for a bat in forward flight [6]. Instead of prescribing the kinematics of the whole wing as done by several other studies only the kinematics of the bone joints (red spheres in figure 1) were prescribed. Figure 1 shows the flow structures using the Q-criterion on the left wing and structural deformation on the right wing.

Table 1: Cycle-averaged force coefficients

	Upstroke	Downstroke
$\overline{C}_L$	-1.34	10.61
$\overline{C}_T$	1.16	0.98

The time evolution of normalized lift and thrust forces are shown in figures 2 and 3 respectively. The cycle-averaged force coefficients for this particular simulation are shown in

[1]This work was supported by NSF under CBET-2011619

table 1. The plots of the force coefficients present a highly complex profile in time with oscillations with a variety of time scales.

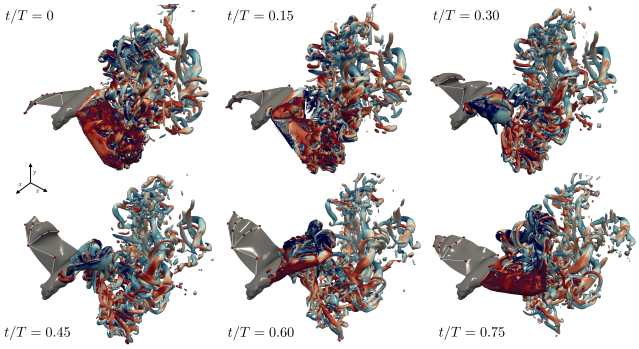

Figure 1: The left side of the bat model shows the flow structures using isosurfaces of Q colored with ω_z. The right side shows the wing structural deformation where red dots are the bone joints and white lines are the bones.

Different mechanisms are expected to contribute to the generation of the aerodynamic forces on a flapping wing. These include the influence of various vortices, added-mass effects, flow acceleration in the free stream, and possibly, viscous diffusion. The complex behavior of the lift and thrust curves can therefore be fully understood by decomposing the total force into these different contributions. Here, we employ the Force partitioning method (FPM) [7] for this purpose, and FPM decomposition of lift and thrust are also shown in figure 2 and 3 respectively. The various terms in FPM method applied to the pressure force on the wing in the i^{th} direction are:

$$\int_B p\, n_i\, dS = -\int_B \hat{n} \cdot \left(\frac{dU_B}{dt}\phi_i\right) dS \quad (1)$$

$$+\int_{V_f} \nabla \cdot (u \cdot \nabla u)\, \phi_i\, dV \quad (2)$$

$$+\frac{1}{Re}\int_{V_f} \left(\nabla^2 u\right) \cdot \nabla \phi_i\, dV \quad (3)$$

$$-\int_\Sigma \hat{n} \cdot \left(\frac{du}{dt}\phi_i\right) dS \quad (4)$$

The FPM reveals that the high-frequency oscillations in the lift and thrust are predominantly due to the added-mass effects (eq. 1) associated with the flutter of the membrane. The changes in the vortex-induced forces (eq. 2) are relatively smooth compared to the added-mass forces. The viscous diffusion-induced forces (Eq. 3) and freestream acceleration-induced forces (eq. 4) are negligible for this case. FPM also allows us to identify the mechanism responsible for generating lift or thrust in specific parts of the cycle. As seen in figure 3, added-mass effects produce thrust in the first quarter cycle followed by a vortex-induced thrust in the second quarter. In the third quarter, both added-mass and vortex-induced effects produce a net thrust. In the last quarter, vortices only generate a drag force.

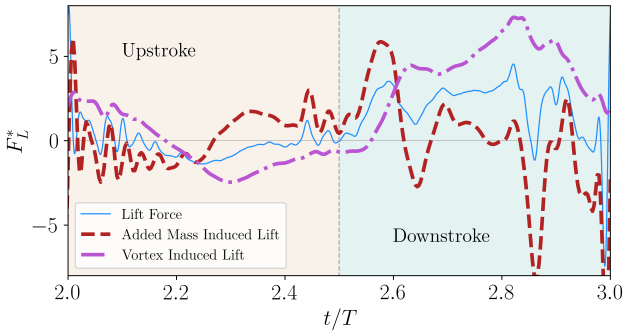

Figure 2: FPM decomposition of lift force

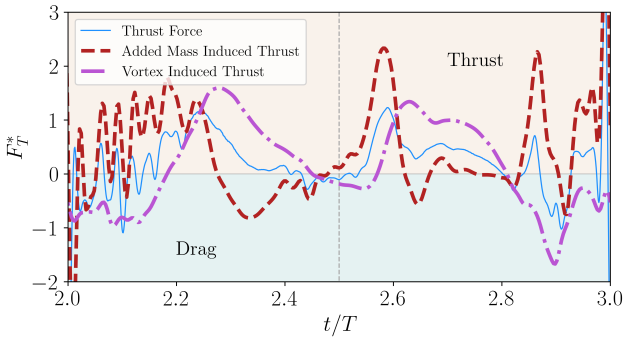

Figure 3: FPM decomposition of thrust force

3 Conclusion

In this work, we presented a fluid-structure interaction methodology for simulating bat-like flight with flexible membrane wings. The method was used to simulate flows around simple hovering membrane wing models and complex bat-like flight models. Further, the force partitioning method was used to dissect the complex fluid forces generated by the wing. Further details of the simulations and the FPM analysis will be presented in our presentation at the meeting.

References

[1] Alireza Ramezani, et al. A biomimetic robotic platform to study flight specializations of bats. *Science Robotics*, 2(3):eaal2505, 2017.

[2] Susheel Sekhar, et al. Canonical description of wing kinematics and dynamics for a straight flying insectivorous bat (Hipposideros pratti) *AIAA Journal*, 14(6):e0218672, 2019.

[3] Guojun Li, et al. A novel 3D variational aeroelastic framework for flexible multibody dynamics: Application to bat-like flapping dynamics. *Computers & Fluids*, 180:96–116, 2019.

[4] Rajat Mittal, et al. A versatile sharp interface immersed boundary method for incompressible flows with complex boundaries *Journal of computational physics*, 227(10):4825–4852, 2008.

[5] Alexander Gehrke, et al. Aeroelastic characterisation of a bio-inspired flapping membrane wing. *Bioinspir. Biomim*, 17 (6):065004, 2022

[6] Daniel Riskin, et al. Quantifying the complexity of bat wing kinematics. *Journal of theoretical biology*, 254(3):604–615, 2008.

[7] Karthik Menon, et al. Contribution of spanwise and cross-span vortices to the lift generation of low-aspect-ratio wings: Insights from force partitioning. *Physical Review Fluids*, 7(11):114102, 2022.